MAPPING THE INTERSTELLAR MAGNETIC FIELD: OBSERVATIONS OF THE GOLDREICH-KYLAFIS EFFECT TOWARDS LATE-TYPE EVOLVED STARS AND STAR-FORMING REGIONS

BY

KO-YUN HUANG

DISSERTATION

Submitted in partial fulfillment of the requirements
for the degree of Doctor of Philosophy in Astronomy
in the Graduate College of the
University of Illinois at Urbana-Champaign, 2020

Urbana, Illinois

Doctoral Committee:

Professor Athol Kemball, Chair
Professor Leslie Looney
Professor Tony Wong
Professor Paul Ricker

Abstract

Mapping magnetic fields is the key to resolving the yet unclear physical picture of circumstellar magnetic fields in both late-type evolved stars and star-forming regions. Observations of linearly polarized molecular line transitions arising from the Goldreich-Kylafis (G-K) effect provide valuable insight into the magnetic field geometry in these sources. Through observing with CARMA, the VLA, and ALMA, this dissertation addresses the questions concerning the dynamical role of magnetic fields in the environment of both the young and the late-type evolved stars.

In the circumstellar envelope (CSE) of AGB stars, the uncertainties concerning both the morphology and magnitude of circumstellar magnetic fields and the relative dynamical influence of magnetic fields in shaping AGB mass-loss outflows relative to other proposed mechanisms such as wind interaction models and binarity remain important open astrophysical questions. We examined the magnetic field morphology in the CSE of two Thermal Pulsating (TP-) AGB stars, R Crt and R Leo, revealed by the detected linear polarization of both thermal and maser lines with CARMA and VLA observations to understand the field morphology on multiple scales in the CSE. We detected both thermal (CO J=2-1) and maser (SiO v=1, J=5-4 and SiO v=0,1,2; J=1-0) line polarizations in these two TP-AGB stars. The observed fractional linear polarization due to the G-K effect in the CO emission is measured as $m_{\ell,p} \sim 3\%$ and $m_{\ell,p} \sim 9\%$ for R Crt and R Leo, respectively. We utilize a model of the CSE to estimate both circumstellar envelope (CSE) temperature and density profile to yield an estimated linear polarization from G-K modeling (Yang and Lai, 2010) and compare it with the detected CO $J = 2 - 1$ linear polarization signal. The observed thermal line polarization level is consistent with the predicted results from the model in the case of R Crt, and the missing flux density due to spatial filtering by the interferometer may explain the higher fractional linear polarization in R Leo if the polarized emission originates from a region of smaller spatial extent than the Stokes I emission. The compiled comparison between the inferred magnetic field orientation from our G-K mapping using the polarized $J = 2-1$ CO transition and other intrinsic alignments published for these sources in the literature suggested that there is a more confined magnetic field geometry in R Crt.

In star-forming regions, both the magnetic field and turbulence are considered the main agents that

support the cloud from collapsing against self gravity (Krumholz and Tan, 2007). We studied the massive star-forming region G10.6-0.4 in ALMA Band 3 polarization observation. G10.6-0.4 is one of the most luminous HII regions with embedded OB stars and thus is a good template for investigating massive star formation processes. In this dissertation, the observed dust continuum polarization mapping and G-K polarization mapping of the CO $J = 1-0$ transition are presented. The detected dust continuum polarization is at $m_{\ell,p} \sim 1.52\%$ with a fairly concentrated spatial structure and with an error-weighted PA $\sim 7.1°$. The peak fractional linear polarization measured in the $J = 1 - 0$ CO line ($m_{\ell,p} \sim 2.28\%$) is broadly consistent with the predicted signal strength from detailed G-K modeling. We also found a detailed spatial structure of emission and absorption features across this massive star-forming region, where the absorption region tends to concentrate at the phase center, with the emission originating prominently in the outer region. We discuss future avenues of investigation arising out of the work in this dissertation.

Acknowledgments

First, I would like to recognize and acknowledge that the work described herein was performed on the lands of the Peoria, Kaskaskia, Piankashaw, Wea, Miami, Mascoutin, Odawa, Sauk, Mesquaki, Kickapoo, Potawatomi, Ojibwe, and Chickasaw Nations. These lands were the traditional territory of these Native Nations prior to their forced removal; these lands continue to carry the stories of these Nations and their struggles for survival and identity. As a land-grant institution, the University of Illinois has a particular responsibility to acknowledge the peoples of these lands, as well as the histories of dispossession that have allowed for the growth of this institution for the past 150 years. We are also obligated to reflect on and actively address these histories and the role that this university has played in shaping them. This acknowledgement and the centering of Native peoples is a start as we move forward for the next 150 years.

This material is based upon work supported by the National Science Foundation Graduate Research Fellowship Program under Grant NSF-AST 1139950, and by the National Science Foundation through award SOSP18B-002 from the National Radio Astronomy Observatory. Observations presented here utilize the Combined Array for Research in Millimeter-wave Astronomy. Observations presented here also utilize the Karl G. Jansky Very Large Array and the Atacama Large Millimeter Array operated by the National Radio Astronomy Observatory. The National Radio Astronomy Observatory is a facility of the National Science Foundation operated under cooperative agreement by Associated Universities, Inc.

I would like to thank my advisor, Professor Athol Kemball, for his wise guidance and advice that led me out of trouble water at many moments. I would also like to express my thanks to Professor Richard Crutcher for the support in my research and many helpful discussions in between. In addition, I would like to thank the faculty members and staff in this department who are caring and offering support to graduate students. I thank our former colleague, Robert Harris, for his advice and assistance during this project. I would also like to express my thanks to the fellow graduate students of this department and my friends for being my mental support, especially in this peculiar year of 2020. Last but certainly not least, I would like to thank my parents, and my dear sister who has inspired me to be in this journey and showed support in many ways.

Table of Contents

List of Figures

List of Tables

List of Abbreviations

AGB Asymptotic Giant Branch (Star)

TP-AGB Thermal-Pulsating AGB (Star)

LPV Long-Period Variable (Star)

AGN Active Galactic Nucleus

ISM Interstellar Medium

EVPA Electric Vector Position Angle

G-K Goldreich-Kylafis (effect)

LVG Large Velocity Gradient

LOS Line-Of-Sight (direction)

CSE Circum-Stellar Envelope

CARMA Combined Array for Research in Millimeter-wave Astronomy

VLA Very Large Array

VLBA Very Long Baseline Array

VLBI Very Long Baseline Interferometry

ALMA Atacama Large Millimeter Array

MIRIAD Multichannel Image Reconstruction, Image Analysis and Display

CASA Common Astronomy Software Applications

FWHM Full Width at Half Maximum

RMS Root Mean Square

Chapter 1

Introduction

Magnetic fields are ubiquitous in the universe at various scales. Their importance has been heavily cited from driving AGN jets to weaving the interstellar medium (ISM) (Crutcher, 2012; Han, 2017) The evolved late-type stars are the major donors of heavy elements to the ISM via their mass-loss process (Habing and Olofsson, 2004). The details of the driving mechanism of the mass-loss process remains unclear (Decin et al., 2018), as well as the dynamical role of magnetic fields in shaping the circumstellar envelope (CSE) (Blackman et al., 2001; García-Segura et al., 2005, 2014). Magnetic fields are also critical in understanding the star formation process (Crutcher, 2012).

1.1 Magnetic Field of AGB Stars

1.1.1 AGB stars

Asymptotic giant branch (AGB) stars are known to be one of the remarkable cosmic chemistry labs in supplying heavier elements. These elements will eventually be injected into the interstellar medium through their significant stellar mass loss. Past the He-core burning stage when the C/O core inside the stellar center is built up, the low- and intermediate-mass ($0.8 - 8M_{\odot}$) stars enter into the AGB phase as the last phase before becoming planetary nebulae. The double shell burning (He-shell and H-shell burning) features early in the AGB phase, and it drives expanded convection between layers and the envelope above (i.e. the 3rd dredge-up). While the He shell and the H shell take turns as the dominant source for the stellar luminosity, the drastic energy deposit in the midst of this alternation and the resulting luminosity oscillation marks the onset of the late, thermal-pulsating AGB (TP-AGB) phase. At the end of this phase, the increasing mass loss of the AGB stars will eventually lead to the ejection of the envelope, and the core white dwarf (WD) will be exposed. There are three major spectral classes for AGB stars: M, S, and C stars, which are characterized by the chemical abundance ratio of carbon and oxygen in the stellar envelope. The M-giants are the oxygen-rich stars, the C stars are the carbon-rich stars, and the S stars have C/O$\sim$ 1. Factors including dredge-up efficiency and hot-bottom burning (HBB) are relevant to such diversity, and these factors are strongly correlated with the ZAMS mass range (Herwig, 2005). In general, the stellar size of AGB stars are a few hundred solar radii, or equivalently one to a few astronomical units.

AGB stars are known to be surrounded by an extended envelope due to their great mass loss of order $\dot{M} \sim 10^{-7} - 10^{-4} \mathrm{M}_{\odot} \mathrm{y} r^{-1}$. The size of such a circumstellar envelope (CSE) can extend to several hundred astronomical units. Overall the region (extending from stellar photospheric surface) is often divided into 2 parts: 1.) the dynamical atmosphere (or inner CSE), and 2.) the (intermediate and outer) CSE. Beneath the dynamical atmosphere is the defined stellar interior, including the stellar envelope and the stellar core. The outermost region of the CSE marks its boundary to the ISM. The dynamical and chemical properties of this CSE are known to be complex. The interplay of mechanisms such as convection, pulsation, radiation, molecular and dust formation, radiation absorption onto those particles, and stellar wind acceleration greatly complicates and impacts the evolution of chemical, dynamical, and physical properties (Habing and Olofsson, 2004). These contribute to the occurrence of the stellar wind, significant mass loss of the star, shock waves, and the formation and destruction of chemical species, amongst other effects.

The stellar wind is believed to arise from the radiation pressure on the dust grains that form in condensation at a few stellar radii. It is also known as the continuum-driven wind, a subtype of the dust-driven wind, given the radiation absorbed by dust grains is over a broad range of wavelengths. For launching the dust-driven wind, a few essential conditions are required (Lamers and Cassinelli, 1999a). First is that the hot dust grains have to survive against the sublimation. In addition, the momentum coupling between the grains and the gas molecules must be present. In the dynamical atmosphere of an AGB star, the dust grains are believed accelerated by the absorption of photons from the strong radiation field. As a dust grain obtains momentum from the absorption of photons and is driven outward, its collision with the gas molecules produces a drag force on the gas particles. [1] The outflow of gas is then triggered through the drift from the grains to the gas. This momentum coupling model also suggests that there is a radius beyond which the wind velocity will no longer increase (Kwok, 1975; Lamers and Cassinelli, 1999a). The drift velocity derived from the drag force is inversely proportional to the square root of the gas density. When the drift velocity is large, the kinetic energy of the gas might exceed the surface potential energy of the grain. Thus the surface atoms might be ejected from the grains. This suggests the destruction of the grains, and therefore the terminal point where the stellar wind is no longer accelerated and where the stellar wind settles down, to be a stable outflow.

The great mass-loss process of AGB stars is induced by both the stellar pulsation/oscillation and the dust-driven wind. The stellar pulsation raises the density scale height which levitates material in the stellar atmosphere through periodic shock propagation through the CSE (Bowen, 1988; Wittkowski et al., 2016). The stellar wind provides momentum moving outward. The combination of the pulsation and dust formation (thus the dust driven wind) is thus believed to produce very high mass-loss rates up to $10^{-5} \mathrm{M}_{\odot} \mathrm{y} r^{-1}$ or more (Lamers and Cassinelli, 1999a).

The CSE is also a region of complex chemical reactions. As the gaseous material of the star flows

[1] And in fact, the mean-free-path among the gas molecules is not too large ($\sim 10^7$ cm); thus the momentum transferred from the dust grains is also diffused throughout the gas by gas-gas collisions (Kwok, 1975).

into the CSE, the ambient temperature and density gradients, and the radiation field produce a complicated chemical environment. The hot, thermal-dynamically controlled synthesis, the "freeze-out" of molecules, the shock initiated reactions, and the photochemistry governed by radical mechanisms are all contributing to the complexity of this environment (Ziurys, 2006). Induced by the stellar oscillation/pulsation and convection, it is suggested that shock waves are able to induce the destruction and formation of molecules, as well as efficient dust grain condensation (Gail and Sedlmayr, 2013a). The parent species of molecules and dust grains are formed within the dynamical atmosphere, while some of the parent species will be eliminated due to the adsorption onto the dust grains. At the transition point of the dynamical atmosphere and intermediate CSE, the parent species elements are injected into the intermediate CSE. The photo-dissociation of molecules and the production of new molecules (the daughter species) due to the ion-molecule reactions take place in the intermediate and outer CSE (Decin et al., 2010). At the outer edge, the interstellar cosmic rays and the UV photons penetrating the outer envelope also influence the CSE chemistry (Decin et al., 2010; Cox et al., 2012). The wind-ISM bow shocks are occasionally present at the outer edge of the CSE, which is also evidence for the interaction of the stellar wind and the ISM (Cox et al., 2012).

1.1.2 Circumstellar Magnetic Field of AGB stars

The detailed role of magnetic fields in the circumstellar envelopes (CSEs) of asymptotic giant branch (AGB) stars remains an important open astrophysical question. Specifically, there are key uncertainties concerning both the morphology and magnitude of circumstellar magnetic fields around late-type evolved stars (Leal-Ferreira et al., 2013; Lèbre et al., 2014; Duthu et al., 2017) and the relative dynamical influence of magnetic fields in shaping AGB mass-loss outflows relative to other proposed mechanisms such as wind interaction models and binarity (García-Segura et al., 1999, 2014; Matt et al., 2000; Blackman et al., 2001; Soker, 2006; Kwok et al., 1978; Frank et al., 1993; Balick and Frank, 2002; Soker, 2004; García-Segura et al., 2018; Frank et al., 2018).

The radial dependence of the magnetic field strength in the CSE of AGB stars can be estimated from the Zeeman effect traced by various molecular species (e.g. SiO, H_2O, OH, CN)(Herpin et al., 2006; Leal-Ferreira et al., 2013; Duthu et al., 2017). The measured power-law index of the magnetic field strength dependence on R (the radial distance from the central star) has been used to model the global magnetic field morphology in the CSE and to constrain the field geometry, including possible dipole ($B \propto R^{-3}$), solar/poloidal ($B \propto R^{-2}$), and toroidal ($B \propto R^{-1}$) geometries (Reid et al., 1979; Reid, 1990; Leal-Ferreira et al., 2013). The literature contains competing arguments concerning the magnitude and origin of circumstellar fields around late-type evolved stars and their global or local morphology and dynamical influence (Blackman et al., 2001; Thomas et al., 1995; Nordhaus and Blackman, 2006; Soker, 2006; Soker and Zoabi, 2002; Soker, 2002). Lèbre et al. (2014) report optical spectropolarimetric observations of the S-type Mira star χ Cyg, enabled by recent advances in Zeeman techniques at optical wavelengths (Donati et al., 1997), that infer a magnetic

field strength of ~ 0.5 Gauss averaged over the stellar surface of the AGB star. The authors argue that this measurement weakens the case for global dipole and poloidal morphologies due to the field strengths ($B \sim 10^{2-3}$ G) implied at the stellar surface in these models. Combined with the associated measured magnetic field strength at the surface of the non-rotating RSG Betelgeuse using optical spectropolarimetry (Petit et al., 2013), they argue that magnetic fields formed by a local dynamo in the convective envelope of these giant stars (Soker, 2006; Dorch, 2004) are favored. It has also been proposed that the magnetic field can be locally enhanced at specific regions such as above stellar magnetic spots (Soker, 2002) or as a result from amplification of the tangential magnetic field due to shock compression around pulsating stars (Hartquist and Dyson, 1997; Kemball et al., 2009; Richter et al., 2016). The magnetic field strengths inferred from maser polarization observations imply a magnetic energy density greater than the thermal and ram pressure counterparts (Reid, 2007; Richter et al., 2016). Further, (Watson, 2009) argues that the measured circular SiO maser polarization may also arise from non-Zeeman effects. Both factors have been used to argue further against the hypothesis of a global dynamically-significant magnetic field. However, there is evidence from recent Goldreich-Kylafis effect (Goldreich and Kylafis, 1981) observations of CO emission toward OH17.7-2.0 (Vlemmings, 2019) that the magnetic field probed by prior OH maser observations is consistent with the global field morphology visible in the CO G-K observations. The morphology, magnitude, and dynamical influence of magnetic fields in late-type evolved stars remains a critical open question in both theory and observation (Vlemmings, 2019).

The uncertainty regarding AGB magnetic fields extends also to their role in shaping the physical conditions in later stages of stellar evolution including the planetary nebula (PN) phase. In particular, any role magnetic fields may play in transforming the initially spherically symmetric circumstellar winds of late-type evolved stars into the asymmetric morphology common in PNe is presently unclear (Blackman et al., 2001; Nordhaus and Blackman, 2006; García-Segura et al., 1999, 2014). Outflow collimation (van Marle et al., 2014) and direct shaping of the CSE material around isolated AGB stars (Rüdiger et al., 2005; Nordhaus et al., 2007) have both been attributed to the action of magnetic fields.

It is widely believed that the observed dense shell of gas in planetary nebula is formed from the colliding of the slow wind from the progenitor (i.e. AGB star) and the fast wind from the central star (i.e. the hot exposed core) (Kwok et al., 1978). However, over decades the causative agent for the commonly seen asymmetric planetary nebule (APN) has been under great debate. The APN that deviates from the spherical symmetry became a great challenge to explain to this isotropic interacting stellar wind (ISW) model (Balick and Frank, 2002). Two of the most popular candidates as the shaping agent are the magnetic field and the binary companion interaction.

Hinted by the observations, magnetic fields around late-type evolved stars at CSE scale have been suggested as playing a role in the APN shaping process. From theory, it has been shown that magnetic fields can possibly trigger the asymmetric shaping (Pascoli, 1997; García-Segura et al., 1999; Blackman et al., 2001; García-Segura et al., 2005). However, in the more recent consideration of these arguments, both the field

sustainability and the insufficient amount angular momentum transferred from the core to the CSE through the magnetic field are in question (Soker and Zoabi, 2002; Soker, 2002, 2006; García-Segura et al., 2014). In addition, the slow-rotating core and the angular momentum transport mechanisms such as the Tayler-Spruit dynamo (Spruit, 2002) are still not well understood yet (Cantiello et al., 2014; Leal Ferreira, 2014). The theory for inducing magnetic fields at CSE scale is therefore still a topic under active investigation. The existence of a companion has been suggested as an alternative means to generate most of the APN through binary interaction. It is suggested that if a sufficient amount of angular momentum is transferred through the common envelope evolution, the induced aspherical fast-slow wind interaction would lead to the APN morphology. In recent discussions, the proposed companion may be a star or planet. In recent observations, there is no direct detection of any close companions around late-type evolved stars as the possible progenitor system for the APN however. Based on a survey over 7 post-AGB stars, the unseen companion objects could possibly have a longer orbital period (> 30 years), be smaller in size ($< 0.2 M_{\odot}$), be embedded in the stellar atmosphere, or be absent in the PPNe evolution (i.e. it evolves as a single star) to take account for no direct detection so far (Hrivnak et al., 2017).

In summary, the APN shaping for isolated AGB stars remained unclear. Either the companion has remained undetected, or there is a mechanism, such as the magnetic field that dominates the full process. For general APN shaping, the balance of evidence suggests that low-mass binary companions are favored in playing a significant role in asymmetric PNe (Soker, 2004, 2006; Marco et al., 2004; Nordhaus et al., 2007; Chen et al., 2016; Hillwig et al., 2016; Hrivnak et al., 2017; Kim et al., 2017) while magnetic fields are still believed to be a complimentary factor of CSE evolution.

Concerning both the field's dynamic role in CSE shaping, and the field origin itself, high angular resolution studies of total intensity and magnetic field morphology in AGB stars pose critical tests on the properties of the proposed models and greatly constrain the problem.

Key science of interest

Our goal in the current work is to map the magnetic fields of TP-AGB stars (which are the precursors of post-AGB/pre-PNe and PNe) by combining the measured electric-vector polarization angles (EVPAs) and possibly the inferred B fields from various observational approaches in a joint analysis to develop a better understanding. The rich CSE chemistry offers abundant tracers for further field mapping with both continuum and spectral-line polarimetry. We have also mapped the observed EVPA and the magnetic field alignment with other observed features such as the proposed bipolar outflow, or whether it is in correlation with the spiral structures seen in some observational results. The link between the field alignment versus the CSE higher order structure would offer insight concerning the field geometry, for example whether it is toroidal or poloidal. This in turn might help us to inspect the field origin model as well. In the Section 1.3, the key techniques employed and the potential difficulties will be discussed.

1.2 Magnetic Field in Star-Forming Regions

The formation of stars is one of the fundamental questions in astrophysics (Shu et al., 1987). The process of star formation transforms gas into stars, which tap nuclear energy and illuminate the universe, synthesize heavy elements, and are indispensable in the formation and evolution of planetary systems (McKee and Ostriker, 2007). Therefore, understanding star formation remains one of the important astrophysical problems and is critical in understanding the structure and evolution of galaxies.

Magnetic fields are ubiquitous at all size scales and throughout evolutionary stages of star formation. In the sense that only $\sim 1\%$ of the gas forms stars every free-fall time, magnetic field and turbulence are considered the main agents that support the cloud from collapsing against the self gravity (Krumholz and Tan, 2007). It remains a matter of debate concerning which of the two agents governs the star-formation process. In the strong magnetic field scenario, the cloud is supported by the magnetic field (through ambipolar diffusion) against the gravitational collapse (e.g. Mouschovias (1991); Mouschovias and Ciolek (1999)). When the magnetic pressure is released through a process such as ambipolar diffusion, the formation of cores and protostars occur through gravitational collapse. In the weak field scenario, the interstellar turbulence regulates the process and via turbulent supersonic flow it forms the high-density regions that will either collapse if they are gravitational bounded when they were formed or dissipate back into the ISM (e.g. Padoan and Nordlund (1999); Mac Low and Klessen (2004)). More recent theoretical work has considered the importance of both magnetic fields and turbulent flows (e.g. Nakamura and Li (2005, 2008); Tilley and Pudritz (2007); Kudoh and Basu (2008); Vázquez-Semadeni et al. (2011)). These models incorporated the effect of ambipolar diffusion into magnetically subcritical regions.

In massive star-forming regions, the turbulent core model by McKee and Tan (2002) proposes that supersonic micro-turbulence as the major role in star-forming process rather than a strong magnetic field. A number of observations toward high-mass star-forming regions reported supersonic non-thermal velocity dispersion (Caselli and Myers, 1995; Pirogov et al., 2003; Shirley et al., 2003; Wang et al., 2008; Vasyunina et al., 2011; Sanhueza et al., 2012) ; meanwhile, the more recent, higher angular resolution observations (Beuther et al., 2018; Hacar et al., 2018; Monsch et al., 2018; Sokolov et al., 2018; Li et al., 2020) revealed subsonic non-thermal internal motions in massive star-forming molecular clouds on small spatial scales. Whether turbulence contribute significantly to the stability of the massive star-forming regions remains a question that requires further investigation.

On the other hand, dust polarization studies (Zhang et al., 2014) toward massive star-forming clumps suggested that the magnetic field is dynamically important during the collapse and fragmentation of parsec-scale clumps and the formation of dense cores. The inferred magnetic field morphology and the field strengths up to few milliGauss in the massive star-forming cores based on more polarization analysis also suggested the magnetic field to be dynamically important (Frau et al., 2014; Qiu et al., 2014; Li et al., 2015; Pillai et al., 2016).

Whether magnetic field or turbulence, or a hybrid mode of both, governs the star-forming process remains unclear. Mapping the magnetic field strength and morphology through observations in the molecular clouds remains one of the key probes to further constrain this issue.

1.3 Methods of Measuring Magnetic Fields (Technique)

Inferences about interstellar magnetic fields are often made through either dust continuum observations that allow the plane-of-sky morphology to be inferred (Lazarian, 2007; Hoang and Lazarian, 2008), direct observation of the Zeeman splitting (Crutcher and Kemball, 2019; Crutcher, 2012; Goldreich et al., 1973; Elitzur, 1996), or observations of the Goldreich-Kylafis (G-K) effect (Goldreich and Kylafis, 1981, 1982; Kylafis, 1983b; Deguchi and Watson, 1984; Lis et al., 1988; Cortes et al., 2005).

1.3.1 Dust Polarization

Dust polarization observations allow the magnetic field morphology to be inferred in the plane of the sky (Lazarian, 2007). This technique relies on the fact that the observed linear polarization of thermal continuum emission from dust at millimeter and sub-millimeter wavelengths arises either from extinction by or emission from dust grains aligned due to the local magnetic field; this causes the measured electric vector position angle (EVPA) of the linearly-polarized dust emission to be either parallel or perpendicular to the local projected field lines (Lazarian, 2007). It is worth noting that the dust polarization may also arise from Rayleigh scattering if the grain sizes are smaller than the observing wavelength (e.g. Kataoka et al. (2015)). Continuum dust polarization observations therefore yield information on the orientation of the magnetic field on the plane of sky. However such observations do not provide field magnitude directly as the predicted degree of dust continuum linear polarization is only weakly dependent on the magnetic field strength (Crutcher, 2012). The field strength information can possibly be inferred from the Davis-Chandrasekhar-Fermi (DCF) technique (Davis, 1951; Chandrasekhar and Fermi, 1953), which is based on the assumption that turbulence-induced Alfvén waves will distort B-field orientations.

1.3.2 Zeeman Effect

The Zeeman effect occurs when degenerate magnetic sublevels are split by the presence of magnetic field; such observations are the primary technique for measuring magnetic field strength directly, as discussed in the reviews by Crutcher and Kemball (2019) and Crutcher (2012). The Zeeman effect can be measured in both thermal and maser line emission and is of a higher magnitude in transitions of paramagnetic atoms or molecules. Given the intrinsic compactness and brightness of maser components, at high angular resolution they act as vital probes at small spatial scales, including shock-enhanced and higher density regions in the CSE (Reid and Moran, 1981; Gray, 2012). Due to the high mass-loss rates and resulting obscuration, maser

polarization observations at radio and millimeter wavelengths have played an important role in providing information regarding the magnetic field in the extended envelopes of late-type evolved stars (Moran et al., 1979; Elitzur, 1980; Miyoshi et al., 1994; Diamond et al., 1994). Specific molecular species observed in such maser polarization studies include SiO (Kemball and Diamond, 1997; Diamond and Kemball, 2003; Kemball et al., 2009), H_2O (Fiebig and Guesten, 1989; Vlemmings et al., 2006), and OH (Kemball and Diamond, 1993). Maser polarization observations of the full set of Stokes parameters, coupled with a radiative transport model for polarized maser emission, allow the inference of both the projected magnetic field direction and magnitude. However there remain theoretical uncertainties concerning polarized maser radiation transport that introduce ambiguities into this inference process (Watson, 2009; Gray, 2012).

1.3.3 Goldreich-Kylafis (G-K) Effect

The G-K effect produces linear polarization in thermal line emission and is induced by anisotropic velocity gradients that produce an anisotropic radiation field or an intrinsic radiation anisotropy in the presence of a magnetic field of sufficient magnitude (Goldreich and Kylafis, 1981). As also noted above in regard to Zeeman splitting, a magnetic field removes the degeneracy between magnetic sublevels and transitions between these sublevels have polarizations either predominantly parallel or perpendicular to the magnetic field (Crutcher, 2012). Unequal magnetic sublevel populations result in net linear polarization. Under the large velocity gradient approximation (LVG or Sobolev approximation) (Sobolev, 1960) a velocity gradient produces a gradient in optical depth. This yields a net linear polarization in the line emission that can be either parallel or perpendicular to the local magnetic field, depending on the transition properties and the relative alignment between the magnetic field and the velocity gradient anisotropy. This field morphology ambiguity can be resolved through detailed source modeling of the G-K effect (Goldreich and Kylafis, 1981; Cortes et al., 2005; Yang and Lai, 2010). G-K observational studies have been undertaken toward molecular clouds (Lai et al., 2003; Cortes et al., 2005; Li and Henning, 2011), associated structures in star-forming regions such as the outflows and jets (Ching et al., 2016; Lee et al., 2018), AGB stars (Wannier et al., 1983; Glenn et al., 1997a; Vlemmings et al., 2012; Girart et al., 2012), red supergiant (RSG) stars (Vlemmings et al., 2017), and pre-planetary nebulae (Sabin et al., 2014).

The principal advantage of using the G-K effect to study magnetic fields is its potential to probe field geometry in depth; the effect is weakly dependent on the field strength as long as it exceeds $\sim 1\mu$G (Kylafis, 1983a). The CSE contains a range of molecular species with various chemical stratification and excitation profiles over the envelope. The G-K polarization signal also arises from underlying physics that is distinct from the generating mechanisms of continuum dust polarization and the spectral line Zeeman effect; therefore it is a unique and valuable complementary probe of magnetic field morphology subject to different systematic errors in both observation and theory.

It was first proposed by Goldreich and Kylafis (1981, 1982); Kylafis (1983b) that spectral-line polarization

provides a way to measure the magnetic field line orientation. The sublevels of rotational lines are split by the Zeeman effect. The associated transitions have polarization directions either parallel or perpendicular to the magnetic field. The large velocity gradient (LVG) approximation provides a preferred direction for radiation where the resulting optical depths in the two orthogonal directions (parallel or perpendicular to the velocity gradient in the 1-D sense) are different. This velocity gradient in the end causes a net polarization in accordance with the preferred direction decided by the velocity gradient geometry.

The two main sets of equations involved are: (1) the radiative transfer equation, and (2) the rate equation of rotational states. The radiative transfer equations for specific source intensity with polarization either perpendicular or parallel to the magnetic field (Goldreich and Kylafis, 1981, 1982; Kylafis, 1983b):

$$\frac{dI^q_{JJ'}}{d\tau^q_{JJ'}} = -\phi(\nu)(I^q_{JJ'} - S^q_{JJ'}), \qquad q = \perp \; or \; \parallel \tag{1.1}$$

where $\phi(\nu)$ is the line profile. And the rate equation specifying the rate of change for number density of particles populating at state $i = (J, M)$, through radiative and collisional transitions from and to state $j = (J', M')$ (Deguchi and Watson, 1984):

$$0 = \frac{dn_i}{dt} = \left[-\sum_{J>J'} P_{ij} + \sum_{J<J'} P_{ji} \right] + \sum_j (C_{ji} n_j - C_{ij} n_i) \tag{1.2}$$

The radiative transition rate P_{ij} involves spontaneous emission, absorption, and stimulated emission.

$$P_{ij} = A_{ij} \left[n_i + R^{\Delta M}_{JJ'} (n_i - n_j) \right] \tag{1.3}$$

The term $R^{\Delta M}_{JJ'}$ is as follows:

$$R^0_{JJ'} = \frac{3c^2}{2h\nu^3} \int \frac{d\Omega}{4\pi} \int d\nu \phi(\nu - \nu_{JJ'}) \sin^2\theta I^{\parallel}_{JJ'}(\Omega) \tag{1.4a}$$

$$R^1_{JJ'} = \frac{3c^2}{4h\nu^3} \int \frac{d\Omega}{4\pi} \int d\nu \phi(\nu - \nu_{JJ'}) \left[I^{\perp}_{JJ'}(\Omega) + \cos^2(\theta) I^{\parallel}_{JJ'}(\Omega) \right] \tag{1.4b}$$

where θ is the angle between the propagation direction and the z axis (the direction of B field). In terms of absorption and stimulated emission, this means the rate equation is also dependent on the radiation intensity, $I^q_{JJ'}$. [2] In this integration, the large velocity gradient (LVG) approximation gives the optical depth that is dependent on the geometry and thus yields a way for simplifying the equation and the solution. By LVG

[2] Specifically the integral of the intensity over frequency and solid angle.

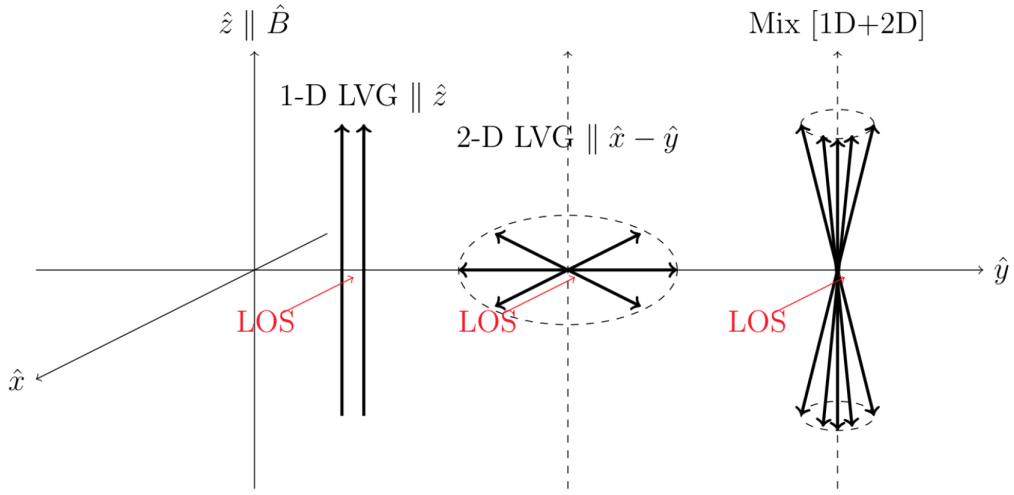

Figure 1.1: The schematic plot for three types of velocity gradient geometry as implemented in our existing G-K model (from left to right): i) 1-D velocity anisotropy parallel the magnetic field; ii) a 2-D velocity gradient along the 2-D plane perpendicular to the magnetic field; and, iii) a mixed model of (i) and (ii), yielding a cone-shaped velocity gradient lobe. This schematic plot is adapted from Yang and Lai (2010). The "LOS" label in red denotes the line-of-sight direction. The magnetic field orientation $\hat{B}$ is set to be aligned with the z-axis, i.e. $\hat{z} \parallel \hat{B}$. And the black arrows in the plot point in the direction of the velocity gradient field. In our model we have adopted the mixed LVG velocity gradient geometry on the basis that of the three velocity gradient geometries, this model is closest to the modest axisymmetry that could reasonably be expected in the late AGB phase.

approximation, the equation 1.4 is simplified as:

$$\int I^q_{JJ'} \phi(\nu - \nu_{JJ'}) d\nu = S^q_{JJ,}(1 - \beta^q_{JJ,}) + \frac{B}{2}\beta^q_{JJ,} \tag{1.5}$$

and $\beta^q_{JJ,}$ is the LVG escape probability involving the optical depth

$$\beta^q_{JJ,} = \left[1 - \exp(-\tau^q_{JJ,})\right] / \tau^q_{JJ,} \tag{1.6}$$

The LVG optical depth $\tau^q_{JJ,}$ is dependent on the LVG geometry. The associated scaling relations according to different geometries (illustrated in Figure 1.1) are listed in Table 1.1.

Under the LVG approximation, the simplified radiative transfer equation is

$$I^q_{JJ,} = \left(S^q_{JJ,} - \frac{B}{2}\right)\left[1 - \exp(-\tau^q_{JJ,})\right] \tag{1.7}$$

Table 1.1: The optical depth geometry dependence on the LVG geometry.

	1-D	2-D	mix (1-D + 2-D)
optical depth	$\tau^q_{JJ'}(\theta) \propto \frac{k^q_{JJ'}(\theta)}{\cos^2\theta}$	$\tau^q_{JJ'}(\theta) \propto \frac{k^q_{JJ'}(\theta)}{\sin^2\theta}$	$\tau^q_{JJ'}(\theta) \propto \frac{k^q_{JJ'}(\theta)}{(\alpha\sin^2\theta + \cos^2\theta)}$

The combination of the radiative transfer equation and the rate equation constitutes a nonlinear system. We need n_i, accounting for source function $S^q_{JJ'}$, thus for calculating the radiation intensity $I^q_{JJ'}$, in turns we also need $I^q_{JJ'}$ in the rate equation for calculating n_i. In general we need to solve the equations through numerical iteration.

With the final calculated intensity, the conventional polarization is defined as:

$$P = \frac{I_\perp - I_\parallel}{I_\perp + I_\parallel} \tag{1.8}$$

where $I_\perp$ and $I_\parallel$ are the emergent specific intensity perpendicular and parallel to the magnetic fields on the plane of sky (POS), and B is the cosmic background blackbody radiation. For the predicted polarization signal not only the magnitude matters, the sign of the modeled polarization is also important in determining whether the EVPA is perpendicular or parallel to the inferred magnetic field line. In the definition given by equation 1.8, a positive sign indicates the predicted EVPA to be aligned with $I_\perp$, otherwise the EVPA is aligned with $I_\parallel$. In this, the observed EVPA along with G-K modeling will lend us an insight into the magnetic field line direction (with 180° ambiguity.) The modeling work in the literature (Goldreich and Kylafis, 1981, 1982; Kylafis, 1983b; Deguchi and Watson, 1984; Cortes et al., 2005; Yang and Lai, 2010) has been extended from 1-D to a 3-D mixing model, and higher transition levels are taken into account. The predicted linear polarization strength varies depending on these parameters as well as the direction along the line of sight with respect to the configuration of the magnetic field and the velocity gradient.

The principal advantage of using the G-K effect to study the magnetic field surrounding AGB stars is that different molecular transitions probe different depths of the circumstellar environment, and we can use this to study the profile of the plane-of-sky magnetic field with depth into the CSE and constrain the full 3-D magnetic field. This is because the molecular abundances are dependent on radius from the star. Also the transitions are sensitive to temperature and collisional-partner density, which are differentiated by distance from the star. The combination of these features brings a rich source of diagnostic tools. As mentioned earlier, the information provided by the G-K effect is weakly dependent on the field strength. Also, given that the source mechanism for the G-K polarization signal is different from the other two approaches, dust continuum emission and the Zeeman effect, the G-K effect is considered a valuable, independent probe for the magnetic field morphology.

Chapter 2

Radio Interferometry and Data Model

Dual-polarization receivers on radio telescope enable us to characterize the full polarization state of the incident radio waves from the space (Thompson et al., 2017; Robishaw and Heiles, 2018).

Polarization can be induced by physical processes that are either associated with magnetic fields (e.g. the Zeeman effect, dust polarization, the Goldreich-Kylafis effect, and synchrotron radiation), independent of magnetic fields (e.g. scattering, gravitational wave) (Robishaw and Heiles, 2018), or can be induced spuriously by instrumental effects. To allow proper inference of physical properties such as the interstellar magnetic field, the observed polarization signals need to be carefully calibrated before scientific analysis. The calibration requires a data model that takes into account all propagation and instrumental effects in the signal path from the frame of astronomical source to the correlator output (Hamaker et al., 1996; Thompson et al., 2017; Kemball and Richter, 2011).

Here we first briefly review the basic description of polarized radiation and the Stokes parameters (section 2.1). Following that, the description and details of the data model will be reviewed (section 2.2).

2.1 Polarized Radiation and Stokes Parameters

Electromagnetic (EM) waves are the traveling wave solutions based on the Maxwell Equations for the electromagnetic field (Jackson, 1998). The EM waves are transverse, which means the associated electric and magnetic field are perpendicular to the direction of wave propagation $\hat{k}$. Furthermore, the electric and magnetic field are in phase and mutually perpendicular. We can therefore characterize an incoming quasi-monochromatic EM signal solely with the electric fields oscillating on the plane that is perpendicular to the wave propagation vector (Rybicki and Lightman, 1979), and the associated description of the magnetic field can be written in the form of electric field.

The electric field associated with an incident EM signal can be written as:

$$\vec{E} = E_1\vec{e_1} + E_2\vec{e_2} \tag{2.1}$$

The $\vec{e}_1$ and $\vec{e}_2$ can be any orthogonal basis pair that is perpendicular to the wave propagation vector $\hat{k}$ (assuming $\vec{k} \parallel \vec{z}$), for example, $(\vec{e}_x, \vec{e}_y)$ in X-Y basis or $(\vec{e}_R, \vec{e}_L)$ in R-L basis. E_1 and E_2 are pure scalar

components. Both E_1 and E_2 are scalar complex numbers and are functions of frequency and time.

The Stokes parameters were developed to completely quantify the polarization properties of the propagating EM waves (Stokes, 1851; Jackson, 1998). The Stokes parameters, in a circular (R-L) or linear (X-Y) basis, takes the form:

$$I = \langle E^R E^{R*} \rangle + \langle E^L E^{L*} \rangle = \langle E^X E^{X*} \rangle + \langle E^Y E^{Y*} \rangle \tag{2.2}$$

$$Q = \langle E^R E^{L*} \rangle + \langle E^L E^{R*} \rangle = \langle E^X E^{X*} \rangle - \langle E^Y E^{Y*} \rangle \tag{2.3}$$

$$U = \tfrac{1}{j} \cdot [\langle E^R E^{L*} \rangle - \langle E^L E^{R*} \rangle] = \langle E^X_m E^{Y*}_n \rangle + \langle E^Y E^{X*} \rangle \tag{2.4}$$

$$V = \langle E^R E^{R*} \rangle - \langle E^L E^{L*} \rangle = \tfrac{1}{j} \cdot [\langle E^X E^{Y*} \rangle - \langle E^Y E^{X*} \rangle] \tag{2.5}$$

The bracket $\langle\rangle$ denotes the quantity is averaged over time. The four Stokes parameters are all real scalar quantities and describe the total intensity (I), two orthogonal linear polarization components (Q, U), and a circular polarization component (V). The following relation holds in general, as waves may be fully or partially polarized:

$$I^2 \geq (Q^2 + U^2 + V^2) \tag{2.6}$$

The equality holds only for fully polarized radiation.

As mentioned earlier, Q and U are two orthogonal linear polarization components, which can be expressed as:

$$Q = \sqrt{Q^2 + U^2} \cos 2\chi \tag{2.7}$$

$$U = \sqrt{Q^2 + U^2} \sin 2\chi \tag{2.8}$$

where the χ is the electric vector position angle (EVPA). The EVPA can be therefore expressed in terms of Stokes parameters as:

$$\chi = \frac{1}{2} \tan^{-1} \left[\frac{U}{Q} \right], \qquad 0 < \chi < \pi \tag{2.9}$$

The fractional linear polarization is expressed as:

$$m_l = \frac{\sqrt{Q^2 + U^2}}{I}, \tag{2.10}$$

and the fractional circular polarization :

$$m_c = \frac{V}{I} \tag{2.11}$$

The form Stokes parameters may be represented as a 1×4 matrix known as the Stokes vector (e.g.

Robishaw (2008)):

$$\vec{e}^S = \begin{bmatrix} I \\ Q \\ U \\ V \end{bmatrix} \tag{2.12}$$

2.2 Data Model in the Signal Path

To consider both the propagation and instrumental effects in our model, we describe the data reduction using the general interferometric data model developed by Hamaker et al. (1996) and Sault et al. (1996), which presented a novel matrix formalism of radio interferometric polarimetry.

We will start with a general review of the data model and the detailed representations for both circular and linear systems will be presented in Sections 2.2.2 and 2.2.3 separately. In practice, the choice of basis will influence the observation patterns and the calibration heuristics (Moellenbrock, 2017).

2.2.1 Signal Path, Jones Matrices, and Mueller Matrices

Consider a general linear operation, represented as a 2×2 Jones matrix $\mathbf{J}$, that converts one signal vector $\vec{E}_{in}$ to another $\vec{E}_{out}$ in the Jones matrix formalism:

$$\vec{E}^{out} = \mathbf{J}\vec{E}^{in} \tag{2.13}$$

The Jones formalism was initially introduced in optics (Jones 1941). It describes the process as electromagnetic waves pass through an optical element which results in the changed polarization for the emerging beam (Born and Wolf, 1959). The original vector $\vec{E}$ is expressed as a 1×2 matrix, which is known as a Jones vector.

Along the full signal path, all the net effects can be viewed as a series of linear operations ($\mathbf{J_i}$) that alter the intrinsic signal. The observed signal ($\vec{E}^{obs}$) then can be expressed in the form of the true signal $\vec{E}^{true}$ as:

$$\vec{E}^{obs} = (\mathbf{J_1 J_2} \cdots \mathbf{J_n})\vec{E}^{true} \tag{2.14}$$

The true signal $\vec{E}^{true}$ is defined as the incident electric field at the top of the atmosphere.

For an interferometric system, we consider the following processes in constructing our data model for individual antenna, m, following Hamaker et al. (1996):

1. Propagation effects from the atmosphere ($\mathbf{T}_m$)
2. Phase shift from varying parallactic angle ($\mathbf{P}_m$)
3. D-terms ($\mathbf{D}_m$)
4. Cross-hand delay ($\mathbf{K^{crs}}_m$)

5. Gain response ($\mathbf{G}_m$)
6. Bandpass effect ($\mathbf{B}_m$)

A schematic of the signal path adapted from Hamaker et al. (1996) is provided in Figure 2.1. Note that in this schematic plot, we aggregated the terms coming from different parts of the signal path to guide the discussion. In practice, some of the terms are coupled or mathematically degenerate, which means that they are not perfectly separable as individual components in calibration or optically isolated to one part of the signal path. For example, the cross-hand delay ($\mathbf{K^{crs}}_m$) is the accumulated time delay from the feed to the end of the signal path, and is coupled with terms such as gain ($\mathbf{G}_m$) and bandpass ($\mathbf{B}_m$). In an other example we consider gain ($\mathbf{G}_m$) and bandpass ($\mathbf{B}_m$) . In reality, the instrumental response is a composite term that is a function of both time t and angular frequency ω, say $\mathbf{C}_m(\omega, t)$. In solving for this instrumental response, we factor this term as:

$$\mathbf{C}_m(\omega, t) = \mathbf{B}_m(\omega) \cdot \mathbf{G}_m(t) \tag{2.15}$$

with the assumption that the frequency- and time-dependent constitutes are separable.

Propagation effects ($\mathbf{T}_m$) The propagation effects from the atmosphere includes the effects from the ionosphere and troposphere (Kemball et al., 1995). The propagation through the ionosphere will add extra phase rotation into the signal due to ionospheric Faraday rotation. This ionospheric delay term has strong frequency dependence: $\gamma_m^{R-L} \propto \frac{1}{\nu^2}$ (Thompson et al., 2017; Kemball et al., 1995); thus this term is negligible at mm-wavelength. For propagation through the **troposphere**, **water vapor** dominates the propagation effect at mm-wavelength.

Parallactic angle ($\mathbf{P}_m$) The parallactic angle α_m is defined as the angle between the local source meridian and the great circle through source and zenith. As the tracking antenna rotates with respect to the given source direction, the angle α_m varies with time as well; this projected coordinate rotation thus incorporates an equivalent phase rotation over time into the signal. For example, the altitude-azimuth mounts, which are adopted by CARMA, VLA, and ALMA, the sources intrinsic polarization appears to be varying in the frame of receivers as the parallactic angle varies with time.

Polarization leakage ($\mathbf{D}_m$) The polarization leakage, also known as feed contamination, is the cross-coupling between signals from nominally orthogonal polarization receptors. For example in the R receptor[1], the leakage response (from the L receptor) contaminates the E_m^R as $(E_m^R + D_m^R E_m^L)$, where the coefficient D_m^R characterizes the small amount of contamination leaked to the R receptor from the other channel (i.e. L). Here R is defined as Right-hand Circular Polarization (RCP), and L as Left-hand Circular Polarization (LCP). The same concept applies to a linear (X-Y) system.

Cross-hand Delay ($\mathbf{K}_m^{crs}$) When the signals are split by the polarizer, the analog signal electrical paths are slightly different for each polarization receptor. This introduces a small time delay in the signal

[1] A receptor is a nominally orthogonal polarization measured by the feed.

that needs to be corrected. This is known as the cross-hand delay.

Gain ($\mathbf{G}_m$) The instrumental response includes an amplitude gains and a change in phase. As described in Equation 2.15, we attribute the time-dependent instrumental response to this Gain term, and write as: $G_m^p = g_m^p(t)e^{j\phi_m^p(t)}, p \in [R, L]$ or $[X, Y]$.

Bandpass ($\mathbf{B}_m$) The bandpass effects are the instrumental response that has frequency dependence as described in Equation 2.15.

In sum, the observed signal takes the form:

$$\vec{E}_m^{obs} = \mathbf{J}_m \cdot \vec{E}_m^{true} = (\mathbf{B}_m\mathbf{G}_m\mathbf{K}_m^{crs}\mathbf{D}_m\mathbf{P}_m\mathbf{T}_m) \cdot \vec{E}_m^{true} \tag{2.16}$$

Mueller Formalism

In practice, the correlator outputs from a set of baseline pairs (antennas m and n) are the interferometric data products, which can be expressed as $\vec{V}_{mn}^{obs} = \langle \vec{E}_m^{obs} \otimes \vec{E}_n^{obs*} \rangle$. More generally the correlator product $\vec{V}_{mn}$ can be written as (in a circular basis, for example):

$$\vec{V}_{mn} = \langle \vec{E}_{mn} \otimes \vec{E}_{mn}^{*} \rangle = \begin{bmatrix} \langle E_m^R E_n^{R*} \rangle \\ \langle E_m^R E_n^{L*} \rangle \\ \langle E_m^L E_n^{R*} \rangle \\ \langle E_m^L E_n^{L*} \rangle \end{bmatrix} \tag{2.17}$$

The bracket $\langle\rangle$ denotes the quantity averaged over time.

For two matrices $\mathbf{A}$ ($l_1 \times l_2$) and $\mathbf{B}$ ($n_1 \times n_2$) the outer product (which is known as the direct or tensor product or Kronecker product) is defined as $\mathbf{A} \otimes \mathbf{B}$ (Arfken and Weber, 2005). The form of $\mathbf{A} \otimes \mathbf{B}$ is the $l_1 n_1 \times l_2 n_2$ block matrix, where every element a_{ij} in $\mathbf{A}$ is replaced by $a_{ij}\mathbf{B}$. For a 2×2 matrix $\mathbf{A}$ and a 2×2 matrix $\mathbf{B}$ as examples, the elements of the outer product matrix takes the form:

$$\mathbf{A} \otimes \mathbf{B} = \begin{bmatrix} a_{11} \begin{bmatrix} b_{11} & b_{12} \\ b_{21} & b_{22} \end{bmatrix} & a_{12} \begin{bmatrix} b_{11} & b_{12} \\ b_{21} & b_{22} \end{bmatrix} \\ a_{21} \begin{bmatrix} b_{11} & b_{12} \\ b_{21} & b_{22} \end{bmatrix} & a_{22} \begin{bmatrix} b_{11} & b_{12} \\ b_{21} & b_{22} \end{bmatrix} \end{bmatrix} = \begin{bmatrix} a_{11}b_{11} & a_{11}b_{12} & a_{12}b_{11} & a_{12}b_{12} \\ a_{11}b_{21} & a_{11}b_{22} & a_{12}b_{21} & a_{12}b_{22} \\ a_{21}b_{11} & a_{21}b_{12} & a_{22}b_{11} & a_{22}b_{12} \\ a_{21}b_{21} & a_{21}b_{22} & a_{22}b_{21} & a_{22}b_{22} \end{bmatrix} \tag{2.18}$$

The Kronecker product has the mixed-product property (Arfken and Weber, 2005):

$$(\mathbf{A}_1 \otimes \mathbf{A}_2)(\mathbf{B}_1 \otimes \mathbf{B}_2) = (\mathbf{A}_1\mathbf{B}_1) \otimes (\mathbf{A}_2\mathbf{B}_2) \tag{2.19}$$

For the correlator output, we have:

$$\vec{V}_{mn}^{obs} = \langle (\mathbf{J}_m \vec{E}) \otimes (\mathbf{J}_n^* \vec{E}^*) \rangle = \langle (\mathbf{J}_m \otimes \mathbf{J}_n^*)(\vec{E} \otimes \vec{E}^*) \rangle = \langle (\mathbf{J}_m \otimes \mathbf{J}_n^*) \vec{V}_{mn}^{true} \tag{2.20}$$

where:

$$\begin{aligned} \mathbf{J}_m \otimes \mathbf{J}_n^* &= (\mathbf{B}_m \mathbf{G}_m \mathbf{K}_m^{crs} \mathbf{D}_m \mathbf{P}_m \mathbf{T}_m) \otimes (\mathbf{B}_n^* \mathbf{G}_n^* \mathbf{K}_n^{crs,*} \mathbf{D}_n^* \mathbf{P}_n^* \mathbf{T}_n^*) \\ &= (\mathbf{B}_m \mathbf{G}_m \mathbf{T}_m \mathbf{K}_m^{crs} \mathbf{D}_m \mathbf{P}_m) \otimes (\mathbf{B}_n^* \mathbf{G}_n^* \mathbf{T}_n^* \mathbf{K}_n^{crs,*} \mathbf{D}_n^* \mathbf{P}_n^*) \\ &= (\mathbf{B}_m \otimes \mathbf{B}_n^*)(\mathbf{G}_m \otimes \mathbf{G}_n^*)(\mathbf{T}_m \otimes \mathbf{T}_n^*)(\mathbf{K}_m^{crs} \otimes \mathbf{K}_n^{crs,*})(\mathbf{D}_m \otimes \mathbf{D}_n^*)(\mathbf{P}_m \otimes \mathbf{P}_n^*) \\ &\equiv [\mathbf{M_B M_G M_T M_{K^{crs}} M_D M_P}]_{mn} \end{aligned} \tag{2.21}$$

and $\vec{V}_{mn}^{true}$ is the intrinsic correlator output in an ideal case without propagation and instrumental effects.

The correlator product $\vec{V}_{mn}$ can be converted into a Stokes vector via transformation matrix $\mathbf{T}$ or $\mathbf{S}$ as (Hamaker et al., 1996):

$$\vec{e}^S = \begin{bmatrix} I \\ Q \\ U \\ V \end{bmatrix} = \mathbf{T} \cdot \vec{V} \equiv \mathbf{S}^{-1} \cdot \vec{V} \tag{2.22}$$

The quantities in the Stokes vector are independent of choice of basis (R-L or X-Y), while the correlator products are not. Therefore the transformation matrices $\mathbf{T}$ and $\mathbf{S}$ vary by the choice of basis.

In the circular basis (Hamaker et al., 1996),

$$\mathbf{S}^{-1}|_{RL} = \begin{bmatrix} 1 & 0 & 0 & 1 \\ 0 & 1 & 1 & 0 \\ 0 & -j & j & 0 \\ 1 & 0 & 0 & -1 \end{bmatrix} \tag{2.23}$$

In linear basis (Hamaker et al., 1996),

$$\mathbf{S}^{-1}|_{XY} = \begin{bmatrix} 1 & 0 & 0 & 1 \\ 1 & 0 & 0 & -1 \\ 0 & 1 & 1 & 0 \\ 0 & -j & j & 0 \end{bmatrix} \tag{2.24}$$

The Mueller formalism is the system of Matrix Optics (Parke, 1948) that was developed to characterize the properties of radiation and its interaction with optical instruments by linear transformations of vectors (Soleillet, 1929; Perrin, 1942; Mueller, 1948; Parke, 1948). This formalism characterizes the optical instrument by a 4×4 matrix, the radiation by a 1×4 Stokes vector, and the interaction between the radiation

and the optical elements via linear transformation(s) (Mueller, 1948):

$$\vec{e}^{S}_{obs} = \mathbf{M} \cdot \vec{e}^{S}_{true} = \mathbf{M} \cdot \mathbf{S}^{-1} \vec{V^{true}} = \mathbf{S}^{-1} \vec{V^{obs}} \tag{2.25}$$

In essence, the relation between the Mueller and Jones formalism is as:

$$\mathbf{J}_m \otimes \mathbf{J}^*_n = \mathbf{S} \cdot \mathbf{M} \cdot \mathbf{S}^{-1} \tag{2.26}$$

This expression applies to describe partially polarized waves and the superposition of waves that are either coherent, incoherent, or partially coherent (Mueller, 1948).

In the final representation of the intrinsic and the output signals for an interferometric baseline (m, n) derives from Equation 2.21, 2.22, and 2.25:

$$\vec{e}^{S}_{obs}|_{mn} = \left[\mathbf{T}\left[\mathbf{M_B M_G M_T M_{K^{crs}} M_D M_P}\right]_{mn} \mathbf{T}^{-1}\right] \cdot \vec{e}^{S}_{true} \tag{2.27}$$

It was pointed out by Robishaw (2008) that the Mueller and Jones calculi are equivalent for systems that do not depolarize, which means systems transforming incoming 100% polarized light into outgoing 100% polarized light. In practice, generally the incoming astronomical radiation is partially polarized. Hence, we need to follow the Mueller formalism, which reveals the features of partial polarization in the most general sense (Robishaw, 2008).

2.2.2 Data Model for a Circular Basis (CARMA, VLA)

For circular response system, the electric field signal arriving above the atmosphere at antenna m takes the form:

$$\vec{E}_{in,m} = \begin{bmatrix} E_R \\ E_L \end{bmatrix}_{in,m} \tag{2.28}$$

As mentioned earlier, the Jones matrix $\mathbf{J}$ can be any linear response that transforms the signal from $\vec{E}_{in,m}$ to $\vec{E}_{out,m}$. For example, if the signal is amplified by factor λ, which results in $\begin{bmatrix} E_R \\ E_L \end{bmatrix}_{out} = \begin{bmatrix} \lambda E_{R,in} \\ \lambda E_{L,in} \end{bmatrix}$. Then corresponding matrix to this linear response is $\mathbf{J} = \begin{bmatrix} \lambda & 0 \\ 0 & \lambda \end{bmatrix}$.
For all the terms associated with antenna m considered in Section 2.2.1, we have written those in explicit form for a circular system below:

Propagation Effects, $\mathbf{T}_m$: For a structured water vapor layer, since the refraction index varies differently along different signal paths, the accumulated phase delay η_m will be different for each antenna over time. This phase delay is assumed independent of polarization since the water vapor layer in general

is neutral. Therefore $\eta_m^R = \eta_m^L = \eta_m$ is adopted. Also, we consider this phase delay should be constant across a frequency range $\Delta\nu \approx 15$ GHz (which covers our observing bandwidth) and any fixed point of time. Therefore the 2×2 matrix for tropospheric delay takes the form[2]:

$$\mathbf{T}_m = \begin{bmatrix} e^{j\eta_m} & 0 \\ 0 & e^{j\eta_m} \end{bmatrix} \tag{2.29}$$

Parallactic Angle, $\mathbf{P}_m$: The absolute value of phase delay introduced by this geometric effect should be the same for R- and L-hand polarizations (i.e. $|\alpha_m^R| = |\alpha_m^L| \equiv |\alpha_m|$); only the signs are the opposite for two polarizations. This is a coordinate rotation relative to the sky frame; thus a positive angle $(+\alpha)$ will be toward R-polarization direction,and correspondingly for L-polarization. For a relatively compact array, we often assume $\alpha_m = \alpha_n = \psi$; thus the parallactic term takes the form:

$$\mathbf{P}_m = \begin{bmatrix} e^{j\psi} & 0 \\ 0 & e^{-j\psi} \end{bmatrix} \tag{2.30}$$

Polarization Leakage, $\mathbf{D}_m$: The leakage term (feed contamination between the two receptors) takes the form:

$$\mathbf{D}_m = \begin{bmatrix} 1 & D_m^R \\ D_m^L & 1 \end{bmatrix} \tag{2.31}$$

Cross-hand Delay, $\mathbf{K}_m^{crs}$: The time delayed between the two senses of polarization takes the form [3]:

$$\mathbf{K}_m^{crs} = \begin{bmatrix} e^{2\pi j\nu\tau_m^R} & 0 \\ 0 & e^{2\pi j\nu\tau_m^L} \end{bmatrix} \tag{2.32}$$

Gain, $\mathbf{G}_m$: The time-dependent gain takes the form:

$$\mathbf{G}_m = \begin{bmatrix} G_m^R & 0 \\ 0 & G_m^L \end{bmatrix} = \begin{bmatrix} g_m^R(t)e^{j\phi_m^R(t)} & 0 \\ 0 & g_m^L(t)e^{j\phi_m^L(t)} \end{bmatrix} \tag{2.33}$$

Bandpass The frequency dependent gain takes the form:

$$\mathbf{B}_m = \begin{bmatrix} B_m^R & 0 \\ 0 & B_m^L \end{bmatrix} = \begin{bmatrix} B_m^R(\omega) & 0 \\ 0 & B_m^L(\omega) \end{bmatrix} \tag{2.34}$$

[2]From 16th Synthesis Imaging Workshop (https://science.nrao.edu/science/meetings/2018/16th-synthesis-imaging-workshop/home), Lecture *Calibration* by George Moellenbrock.

[3]From 16th Synthesis Imaging Workshop (https://science.nrao.edu/science/meetings/2018/16th-synthesis-imaging-workshop/home), Lecture *Polarization* by Frank Schinzel.

In Equation 2.16, given matrices $\mathbf{B}_m$, $\mathbf{G}_m$, and $\mathbf{K}_m^{crs}$ are all diagonal and therefore commute, i.e. $(\mathbf{K}_m^{crs}\mathbf{B}_m\mathbf{G}_m) = (\mathbf{B}_m\mathbf{G}_m\mathbf{K}_m^{crs})$, etc. Also note that $\mathbf{T}_m$ is a scalar matrix, so it commutes with any matrix. Following Equation 2.17, the correlator product in a circular basis can be denoted as:

$$\vec{V}_{mn}^{obs} = \langle \vec{E}_m^{'} \otimes \vec{E}_n^{'*} \rangle = \begin{bmatrix} \langle E_m^{R'} E_n^{R'*} \rangle \\ \langle E_m^{R'} E_n^{L'*} \rangle \\ \langle E_m^{L'} E_n^{R'*} \rangle \\ \langle E_m^{L'} E_n^{L'*} \rangle \end{bmatrix} \equiv \begin{bmatrix} r_{mn}^{RR} \\ r_{mn}^{RL} \\ r_{mn}^{LR} \\ r_{mn}^{LL} \end{bmatrix} \tag{2.35}$$

From Equation 2.21, the data model is expanded as:

$$\vec{V}_{mn}^{obs} = \mathbf{M_B}\mathbf{M_G}\mathbf{M_T}\mathbf{M_{K^{crs}}}\mathbf{M_D}\mathbf{M_P} \cdot \vec{V}^{true} \tag{2.36}$$

$$\mathbf{M_B}|_{m,n} = \mathbf{B}_m \otimes \mathbf{B}_n^* = \begin{bmatrix} B_m^R B_n^{R*} & 0 & 0 & 0 \\ 0 & B_m^R B_n^{L*} & 0 & 0 \\ 0 & 0 & B_m^L B_n^{R*} & 0 \\ 0 & 0 & 0 & B_m^L B_n^{L*} \end{bmatrix} \tag{2.37}$$

$$\mathbf{M_G}|_{m,n} = \mathbf{G}_m \otimes \mathbf{G}_n^* = \begin{bmatrix} G_m^R G_n^{R*} & 0 & 0 & 0 \\ 0 & G_m^R G_n^{L*} & 0 & 0 \\ 0 & 0 & G_m^L G_n^{R*} & 0 \\ 0 & 0 & 0 & G_m^L G_n^{L*} \end{bmatrix} \tag{2.38}$$

$$\mathbf{M_{K^{crs}}}|_{m,n} = \mathbf{K}_m^{crs} \otimes \mathbf{K}_n^{crs,*} = \begin{bmatrix} e^{j2\pi\nu(\tau_m^R - \tau_n^R)} & 0 & 0 & 0 \\ 0 & e^{j2\pi\nu(\tau_m^R - \tau_n^L)} & 0 & 0 \\ 0 & 0 & e^{j2\pi\nu(\tau_m^L - \tau_n^R)} & 0 \\ 0 & 0 & 0 & e^{j2\pi\nu(\tau_m^L - \tau_n^L)} \end{bmatrix} \tag{2.39}$$

$$\mathbf{M_D}|_{m,n} = \mathbf{D}_m \otimes \mathbf{D}_n^* = \begin{bmatrix} 1 & D_n^{R*} & D_m^R & D_m^R D_n^{R*} \\ D_n^{L*} & 1 & D_m^R D_n^{L*} & D_m^R \\ D_m^L & D_m^L D_n^{R*} & 1 & D_n^{R*} \\ D_m^L D_n^{L*} & D_m^L & D_n^{L*} & 1 \end{bmatrix} \tag{2.40}$$

$$\mathbf{M_P}|_{m,n} = \mathbf{P}_m \otimes \mathbf{P}_n^* = \begin{bmatrix} e^{j(\alpha_m - \alpha_n)} & 0 & 0 & 0 \\ 0 & e^{j(\alpha_m + \alpha_n)} & 0 & 0 \\ 0 & 0 & e^{-j(\alpha_m + \alpha_n)} & 0 \\ 0 & 0 & 0 & e^{-j(\alpha_m - \alpha_n)} \end{bmatrix} = \begin{bmatrix} 1 & 0 & 0 & 0 \\ 0 & e^{j2\psi} & 0 & 0 \\ 0 & 0 & e^{-j2\psi} & 0 \\ 0 & 0 & 0 & 1 \end{bmatrix} \tag{2.41}$$

$$\mathbf{M_T}|_{m,n} = \mathbf{T}_m \otimes \mathbf{T}_n^* = \begin{bmatrix} e^{j(\eta_m - \eta_n)} & 0 & 0 & 0 \\ 0 & e^{j(\eta_m - \eta_n)} & 0 & 0 \\ 0 & 0 & e^{j(\eta_m - \eta_n)} & 0 \\ 0 & 0 & 0 & e^{j(\eta_m - \eta_n)} \end{bmatrix} \tag{2.42}$$

Given the measured $\vec{V}_{mn}^{obs}$, the calibration of the data is the process of solving sequentially or in iterative sense for all the matrices to estimate true incoming, scientific signal $\vec{V}_{mn}^{true} = \begin{bmatrix} S^{RR} \\ S^{RL} \\ S^{LR} \\ S^{LL} \end{bmatrix} = \begin{bmatrix} \langle E_m^R E_n^{R*} \rangle \\ \langle E_m^R E_n^{L*} \rangle \\ \langle E_m^L E_n^{R*} \rangle \\ \langle E_m^L E_n^{L*} \rangle \end{bmatrix}$.

Combining the first four diagonal matrices and factoring out $\mathbf{D}_m\mathbf{P}_m$ in Equation 2.36 we obtain:

$$\vec{V}_{mn}^{obs} = [[\mathbf{M_B}\mathbf{M_G}\mathbf{M_T}\mathbf{M_{K^{crs}}}]\,\mathbf{M_D}\mathbf{M_P}]_{mn} \cdot \vec{V}^{true} \equiv [\mathbf{N} \cdot \mathbf{M_D}\mathbf{M_P}]_{mn} \cdot \vec{V}^{true} \tag{2.43}$$

where

$$\mathbf{N}_{mn} \equiv [\mathbf{M_B}\mathbf{M_G}\mathbf{M_T}\mathbf{M_{K^{crs}}}]_{mn} = \begin{bmatrix} N_{RR} & 0 & 0 & 0 \\ 0 & N_{RL} & 0 & 0 \\ 0 & 0 & N_{LR} & 0 \\ 0 & 0 & 0 & N_{LL} \end{bmatrix}_{mn} \tag{2.44}$$

Each element in the matrix $\mathbf{N}$ is a complex number involving amplitude and phase and with both time and frequency dependence. Here we will use an example to illustrate the data reduction process. For antenna pair $(m,n) = (1,2)$, the data model takes the form:

$$r_{12}^{RR} = N_{RR,12}[S^{RR}e^{j\Delta\alpha} + S^{RL}D_2^{R*}e^{j\Sigma\alpha} + S^{LR}D_1^R e^{-j\Sigma\alpha} + S^{LL}D_1^R D_2^{R*}e^{-j\Delta\alpha}]$$

$$r_{12}^{RL} = N_{RL,12}[S^{RR}D_2^{L*}e^{j\Delta\alpha} + S^{RL}e^{j\Sigma\alpha} + S^{LR}D_1^R D_2^{L*}e^{-j\Sigma\alpha} + S^{LL}D_1^R e^{-j\Delta\alpha}]$$

$$r_{12}^{LR} = N_{LR,12}[S^{RR}D_1^L e^{j\Delta\alpha} + S^{RL}D_1^L D_2^{R*}e^{j\Sigma\alpha} + S^{LR}e^{-j\Sigma\alpha} + S^{LL}D_2^{R*}e^{-j\Delta\alpha}]$$

$$r_{12}^{LL} = N_{LL,12}[S^{RR}D_1^L D_2^{L*}e^{j\Delta\alpha} + S^{RL}D_1^L e^{j\Sigma\alpha} + S^{LR}D_2^{L*}e^{-j\Sigma\alpha} + S^{LL}e^{-j\Delta\alpha}]$$

where $\Delta\alpha = (\alpha_1 - \alpha_2)$, and $\Sigma\alpha = (\alpha_1 + \alpha_2)$.

R-L Phase Calibration

Consider a simple array consisting of 3 antennae. For each baseline with an expansion for the parallel-hand RR phase $\varphi_{mn}^{obs,RR}$:

$$\varphi_{12}^{obs,RR} = \varphi^{true,RR}(u,v) + \varepsilon_2^R - \varepsilon_1^R \tag{2.45}$$

$$\varphi_{13}^{obs,RR} = \varphi^{true,RR}(u,v) + \varepsilon_3^R - \varepsilon_1^R \tag{2.46}$$

$$\varphi_{23}^{obs,RR} = \varphi^{true,RR}(u,v) + \varepsilon_3^R - \varepsilon_2^R \tag{2.47}$$

where the ε_m^R is the phase excess at each antenna m. From this equation set, there is one degree of freedom left from the four unknown variables $\varepsilon_i^R, i \in (1,2,3)$ and $\varphi^{true,RR}(u,v)$. We choose to set $\varepsilon_1^R = 0$, which means in practice that we treat antenna 1 as the reference antenna. The equation set does not constrain the phase at the reference antenna.

Similarly for parallel-hand LL phase:

$$\varphi_{12}^{obs,LL} = \varphi^{true,LL}(u,v) + \varepsilon_2^L - \varepsilon_1^L \tag{2.48}$$

$$\varphi_{13}^{obs,LL} = \varphi^{true,LL}(u,v) + \varepsilon_3^L - \varepsilon_1^L \tag{2.49}$$

$$\varphi_{23}^{obs,LL} = \varphi^{true,LL}(u,v) + \varepsilon_3^L - \varepsilon_2^L \tag{2.50}$$

After self-calibration separately in RR and LL, the difference $\varepsilon_1^L - \varepsilon_1^R$ remains undetermined (the $\mathbf{X^r}$ in Moellenbrock (2017)).

The cross-polarization phase $\varphi_{12}^{obs,RL}$ can be expressed as :

$$\varphi_{12}^{obs,RL} = \varphi^{true,RL}(u,v) + \varepsilon_2^L - \varepsilon_1^R \tag{2.51}$$

Parallel-hand self-calibration for $\varepsilon_i^R, i \in (1,2,3)$ and $\varepsilon_i^L, i \in (1,2,3)$ assuming $\varepsilon_1^R = 0$ and $\varepsilon_1^L = 0$. Applying these corrections to the cross-polarized data:

$$\varphi_{12}^{obs,RL} = \varphi^{true,RL}(u,v) + (\varepsilon_2^L - \varepsilon_1^L) - (\varepsilon_1^R - \varepsilon_1^L) \tag{2.52}$$

Thus $(\varepsilon_1^R - \varepsilon_1^L)$ is the only remaining unknown that we need to solve for (R-L phase term).

This term $(\varepsilon_1^L - \varepsilon_1^R)$ is known as cross-hand phase (Moellenbrock, 2017) and needs to be calibrated as part of the data reduction. Inadequate cross-hand phase calibration will contaminate the leakage calibration and propagates error that further reduces the Q and U signal detection quality.

D-term Calibration

After incremental and sequential calibrations for other terms such as $\mathbf{M_G}$ and $\mathbf{M_B}$, the remaining major term is the polarization leakage, $\mathbf{M_D}$. By neglecting the 2nd-order terms (D^2), the data model at this stage can be written as (Kemball et al., 1995):

$$r'^{RR}_{mn}(u,v,w) = S^{RR} \tag{2.53}$$

$$r'^{LL}_{mn}(u,v,w) = S^{LL} \tag{2.54}$$

$$r'^{RL}_{mn}(u,v,w) = S^{RL} + D^{L*}_{n}(S^{RR}) + D^{R}_{m}(S^{LL}) \tag{2.55}$$

$$r'^{LR}_{mn}(u,v,w) = S^{LR} + D^{L*}_{m}(S^{RR}) + D^{R}_{n}(S^{LL}) \tag{2.56}$$

2.2.3 Data Model for a Linear Basis (ALMA)

With an X-Y receptor basis, the electric field can be written as $\vec{E} = E_X\vec{e}_X + E_Y\vec{e}_Y$ and the correlator output is the outer product of the signals from the two antennae on each baseline, $\vec{V}_{mn} = \langle\vec{E}'_m \otimes \vec{E}'^{*}_n\rangle$. Following Equation 2.17 $\vec{V}_{mn}$ takes the form:

$$\vec{V}_{mn}|_{XY} = \langle\vec{E}_m \otimes \vec{E}^{*}_n\rangle|_{XY} = \begin{bmatrix} \langle E^X_m E^{X*}_n\rangle \\ \langle E^X_m E^{Y*}_n\rangle \\ \langle E^Y_m E^{X*}_n\rangle \\ \langle E^Y_m E^{Y*}_n\rangle \end{bmatrix} \equiv \begin{bmatrix} r^{XX}_{mn} \\ r^{XY}_{mn} \\ r^{YX}_{mn} \\ r^{YY}_{mn} \end{bmatrix} \tag{2.57}$$

The true Stokes parameters for the baseline pair (m,n), $\vec{e^S}_{mn}$ can be written as:

$$\vec{e}^S_{mn} = \begin{bmatrix} I_{mn} \\ Q_{mn} \\ U_{mn} \\ V_{mn} \end{bmatrix} \tag{2.58}$$

with each element written with X-Y basis are (Equation 2.2- 2.5):

$$I_{mn} = \langle E^X_m E^{X*}_n\rangle + \langle E^Y_m E^{Y*}_n\rangle$$

$$Q_{mn} = \langle E^X_m E^{X*}_n\rangle - \langle E^Y_m E^{Y*}_n\rangle$$

$$U_{mn} = \langle E^X_m E^{Y*}_n\rangle + \langle E^Y_m E^{X*}_n\rangle$$

$$V_{mn} = \frac{1}{j}[\langle E^X_m E^{Y*}_n\rangle - \langle E^Y_m E'^{*}_n\rangle]$$

For all the terms associated with antenna m considered in Section 2.2.1, we consider them here in explicit form for a linearly-polarized receptor basis:

Propagation effects, $\mathbf{T}_m$: Properties of atmospheric propagation considered for a circular basis carry forward here. ALMA uses water vapor radiometer (WVR) to monitor the atmospheric water vapour line at 183 GHz along the line of sight above each antenna to correct for phase delays introduced by the wet component of the troposphere (Maud et al., 2017). Note that it is assumed this term is

un-polarized. The 2×2 matrix for tropospheric delay takes the form [4]:

$$\mathbf{T}_m = \begin{bmatrix} e^{j\eta_m} & 0 \\ 0 & e^{j\eta_m} \end{bmatrix} \tag{2.59}$$

Parallactic angle, $\mathbf{P}_m$: In a relatively compact array we assume parallactic angle $\alpha_m = \alpha_n = \psi$. Following Hamaker et al. (1996); Sault et al. (1996), the linear transformation in an X-Y basis is written for this rotation from the sky frame as:

$$\mathbf{P}_m = \begin{bmatrix} \cos\psi & \sin\psi \\ -\sin\psi & \cos\psi \end{bmatrix} \tag{2.60}$$

Polarization leakage, $\mathbf{D}_m$: The polarization leakage in an X-Y basis takes the for :

$$\mathbf{D}_m = \begin{bmatrix} 1 & D_m^X \\ D_m^Y & 1 \end{bmatrix} \tag{2.61}$$

Cross-hand Delay, $\mathbf{K}_m^{crs}$: The cross-polarized delay effect in an X-Y basis can be expanded as [5]:

$$\mathbf{K}_m^{crs} = \begin{bmatrix} e^{2\pi j\nu\tau_m^X} & 0 \\ 0 & e^{2\pi j\nu\tau_m^Y} \end{bmatrix} \tag{2.62}$$

Gain, $\mathbf{G}_m$: The time-dependent instrumental response in an X-Y basis is written as:

$$\mathbf{G}_m = \begin{bmatrix} G_m^X & 0 \\ 0 & G_m^Y \end{bmatrix} = \begin{bmatrix} g_m^X(t)e^{j\phi_m^X(t)} & 0 \\ 0 & g_m^Y(t)e^{j\phi_m^Y(t)} \end{bmatrix} \tag{2.63}$$

Bandpass, $\mathbf{B}_m$: The net bandpass effect,equivalently the frequency-dependent instrumental gain can be written as:

$$\mathbf{B}_m = \begin{bmatrix} B_m^X & 0 \\ 0 & B_m^Y \end{bmatrix} = \begin{bmatrix} B_m^X(\omega) & 0 \\ 0 & B_m^Y(\omega) \end{bmatrix} \tag{2.64}$$

The final output correlated signals $\vec{R}_{mn}$ in an X-Y basis can be expanded as:

$$\vec{V}_{mn}^{obs} = \langle(\mathbf{J}_m\vec{E}) \otimes (\mathbf{J}_n^*\vec{E}^*)\rangle|_{X-Y} = \langle(\mathbf{J}_m \otimes \mathbf{J}_n^*)(\vec{E} \otimes \vec{E}^*)\rangle|_{X-Y} = \mathbf{M}_{mn}|_{X-Y} \cdot \vec{V}^{true} \tag{2.65}$$

[4]From 16th Synthesis Imaging Workshop (https://science.nrao.edu/science/meetings/2018/16th-synthesis-imaging-workshop/home), Lecture *Calibration* by George Moellenbrock.

[5]From 16th Synthesis Imaging Workshop (https://science.nrao.edu/science/meetings/2018/16th-synthesis-imaging-workshop/home), Lecture *Polarization* by Frank Schinzel.

where

$$
\begin{aligned}
[\mathbf{M}_{mn} = \mathbf{J}_m \otimes \mathbf{J}_n^*]\,|_{X-Y} \quad &= [(\mathbf{B}_m \otimes \mathbf{B}_n^*)(\mathbf{G}_m \otimes \mathbf{G}_n^*)(\mathbf{T}_m \otimes \mathbf{T}_n^*)(\mathbf{K}_m^{crs} \otimes \mathbf{K}_n^{crs,*})(\mathbf{D}_m \otimes \mathbf{D}_n^*)(\mathbf{P}_m \otimes \mathbf{P}_n^*)]\,|_{X-Y} \\
&\equiv [\mathbf{M_B M_G M_{K^{crs}} M_D M_P}]\,|_{mn,X-Y} \\
&= [\mathbf{M_B^r M_G^r X^r M_{K^{crs}} M_D M_P}]\,|_{mn,X-Y}
\end{aligned}
\tag{2.66}
$$

In the last line of Equation 2.66, the transformation $\mathbf{M_B M_G}$ is re-written as $\mathbf{M_B^r M_G^r X^r}$ (Moellenbrock, 2017). This is to reflect that in the reduction process, we actually measure the $\mathbf{M_B^r}$ and $\mathbf{M_G^r}$ relative to an assumed zero reference antenna phase as discussed in relation to Section 2.2.2 above. This undetermined X-Y phase difference at the reference antenna takes the form:

$$
\mathbf{X^r}|_{m,n} = \begin{bmatrix} e^{j\epsilon_{X0}} & 0 \\ 0 & e^{j\epsilon_{Y0}} \end{bmatrix} \otimes \begin{bmatrix} e^{-j\epsilon_{X0}} & 0 \\ 0 & e^{-j\epsilon_{Y0}} \end{bmatrix} = \begin{bmatrix} 1 & 0 & 0 & 0 \\ 0 & e^{j\rho} & 0 & 0 \\ 0 & 0 & e^{-j\rho} & 0 \\ 0 & 0 & 0 & 1 \end{bmatrix}
\tag{2.67}
$$

where $\rho \equiv (\epsilon_{X0} - \epsilon_{Y0})$.

Following Moellenbrock (2017), we re-write the data model in terms of the measured correlator products ($\vec{V}_{mn}^{obs}|_{XY}$) and the intrinsic Stokes vector ($\vec{e}_{true,mn}^{S}$). Based on Equation 2.66 and the transformation between the Stokes vector and the correlator product, we have:

$$
\begin{aligned}
\vec{V}_{mn}^{obs}|_{XY} = \mathbf{T}^{-1} \cdot \vec{e}_{obs,mn}^{S} \quad &= [\mathbf{M_B M_G M_T M_{K^{crs}} M_D M_P}]\,\mathbf{T}^{-1}\mathbf{T} \cdot \vec{V}_{mn}^{true}|_{XY} \\
&= [\mathbf{M_B M_G M_T M_{K^{crs}} M_D M_P}]\,\mathbf{T}^{-1} \cdot \vec{e}_{true,mn}^{S}
\end{aligned}
\tag{2.68}
$$

For all other matrices:

$$
\mathbf{M_B}|_{m,n} = \mathbf{B}_m \otimes \mathbf{B}_n^* = \begin{bmatrix} B_m^X B_n^{X*} & 0 & 0 & 0 \\ 0 & B_m^X B_n^{Y*} & 0 & 0 \\ 0 & 0 & B_m^Y B_n^{X*} & 0 \\ 0 & 0 & 0 & B_m^Y B_n^{Y*} \end{bmatrix}
\tag{2.69}
$$

$$
\mathbf{M_G}|_{m,n} = \mathbf{G}_m \otimes \mathbf{G}_n^* = \begin{bmatrix} G_m^X G_n^{X*} & 0 & 0 & 0 \\ 0 & G_m^X G_n^{Y*} & 0 & 0 \\ 0 & 0 & G_m^Y G_n^{X*} & 0 \\ 0 & 0 & 0 & G_m^Y G_n^{Y*} \end{bmatrix}
\tag{2.70}
$$

$$\mathbf{M}_{\mathbf{K^{crs}}}|_{m,n} = \mathbf{K}_m^{crs} \otimes \mathbf{K}_n^{crs,*} = \begin{bmatrix} e^{j2\pi\nu(\tau_m-\tau_n)} & 0 & 0 & 0 \\ 0 & e^{j2\pi\nu(\tau_m-\tau_n)} & 0 & 0 \\ 0 & 0 & e^{j2\pi\nu(\tau_m-\tau_n)} & 0 \\ 0 & 0 & 0 & e^{j2\pi\nu(\tau_m-\tau_n)} \end{bmatrix} \tag{2.71}$$

$$\mathbf{M}_{\mathbf{D}}|_{m,n} = \mathbf{D}_m \otimes \mathbf{D}_n^* = \begin{bmatrix} 1 & D_n^{X*} & D_m^X & D_m^X D_n^{X*} \\ D_n^{Y*} & 1 & D_m^X D_n^{Y*} & D_m^X \\ D_m^Y & D_m^Y D_n^{X*} & 1 & D_n^{X*} \\ D_m^Y D_n^{Y*} & D_m^Y & D_n^{Y*} & 1 \end{bmatrix} \tag{2.72}$$

$$\mathbf{M}_{\mathbf{P}}|_{m,n} \cdot \mathbf{T}^{-1} = [\mathbf{P}_m \otimes \mathbf{P}_n^*] \cdot \mathbf{T}^{-1} = \begin{bmatrix} 1 & \cos 2\psi & \sin 2\psi & 0 \\ 0 & -\sin 2\psi & \cos 2\psi & j \\ 0 & -\sin 2\psi & \cos 2\psi & -j \\ 0 & -\cos 2\psi & -\sin 2\psi & 0 \end{bmatrix} \tag{2.73}$$

$$\mathbf{M}_{\mathbf{T}}|_{m,n} = \mathbf{T}_m \otimes \mathbf{T}_n^* = \begin{bmatrix} e^{j(\eta_m-\eta_n)} & 0 & 0 & 0 \\ 0 & e^{j(\eta_m-\eta_n)} & 0 & 0 \\ 0 & 0 & e^{j(\eta_m-\eta_n)} & 0 \\ 0 & 0 & 0 & e^{j(\eta_m-\eta_n)} \end{bmatrix} \tag{2.74}$$

The we group the terms that are purely diagonal ($\mathbf{M_B M_G M_T M_{K^{crs}}} \equiv \mathbf{N}$) and move these to the left-hand side of the Equation:

$$\mathbf{N}^{-1} \cdot \vec{V}_{mn}^{obs}|_{XY} = \left[\mathbf{M_D M_P T}^{-1}\right] \cdot \vec{e}_{true,mn}^{S} \tag{2.75}$$

where $\mathbf{N}$ is:

$$\mathbf{N} = \mathbf{M_B M_G M_T M_{K^{crs}}} = \begin{bmatrix} N_1 & 0 & 0 & 0 \\ 0 & N_2 & 0 & 0 \\ 0 & 0 & N_3 & 0 \\ 0 & 0 & 0 & N_4 \end{bmatrix} \tag{2.76}$$

For baseline (m, n):

$$r_{mn}^{XX'}/N_1 = (I + Q_\psi) + D_m^x(U_\psi - jV) + (U_\psi + jV)D_n^{x*} + D_m^x(I - Q_\psi)D_n^{x*} \tag{2.77}$$

$$r_{mn}^{YY'}/N_4 = (I - Q_\psi) + D_m^y(U_\psi - jV) + (U_\psi - jV)D_n^{y*} + D_m^y(I + Q_\psi)D_n^{y*} \tag{2.78}$$

$$r_{mn}^{XY'}/N_2 = (U_\psi + jV) + D_m^x(I - Q_\psi) + (I + Q_\psi)D_n^{y*} + D_m^x(U_\psi - jV)D_n^{y*} \tag{2.79}$$

$$r_{mn}^{YX'}/N_3 = (U_\psi - jV) + D_m^y(I + Q_\psi) + (I - Q_\psi)D_n^{x*} + D_m^y(U_\psi + jV)D_n^{x*} \tag{2.80}$$

in which we have abbreviated the Q, U, ψ term as Q_ψ and U_ψ following the expression shown below (Moel-

lenbrock, 2017):

$$Q_\psi = Q \cdot \cos 2\psi + U \cdot \sin 2\psi \tag{2.81}$$

$$U_\psi = -Q \cdot \sin 2\psi + U \cdot \cos 2\psi \tag{2.82}$$

We note that the parallactic angle ψ part is known and that the D-terms can then be solved via the modulated Q_ψ and U_ψ over a good parallactic angle coverage throughout the observation.

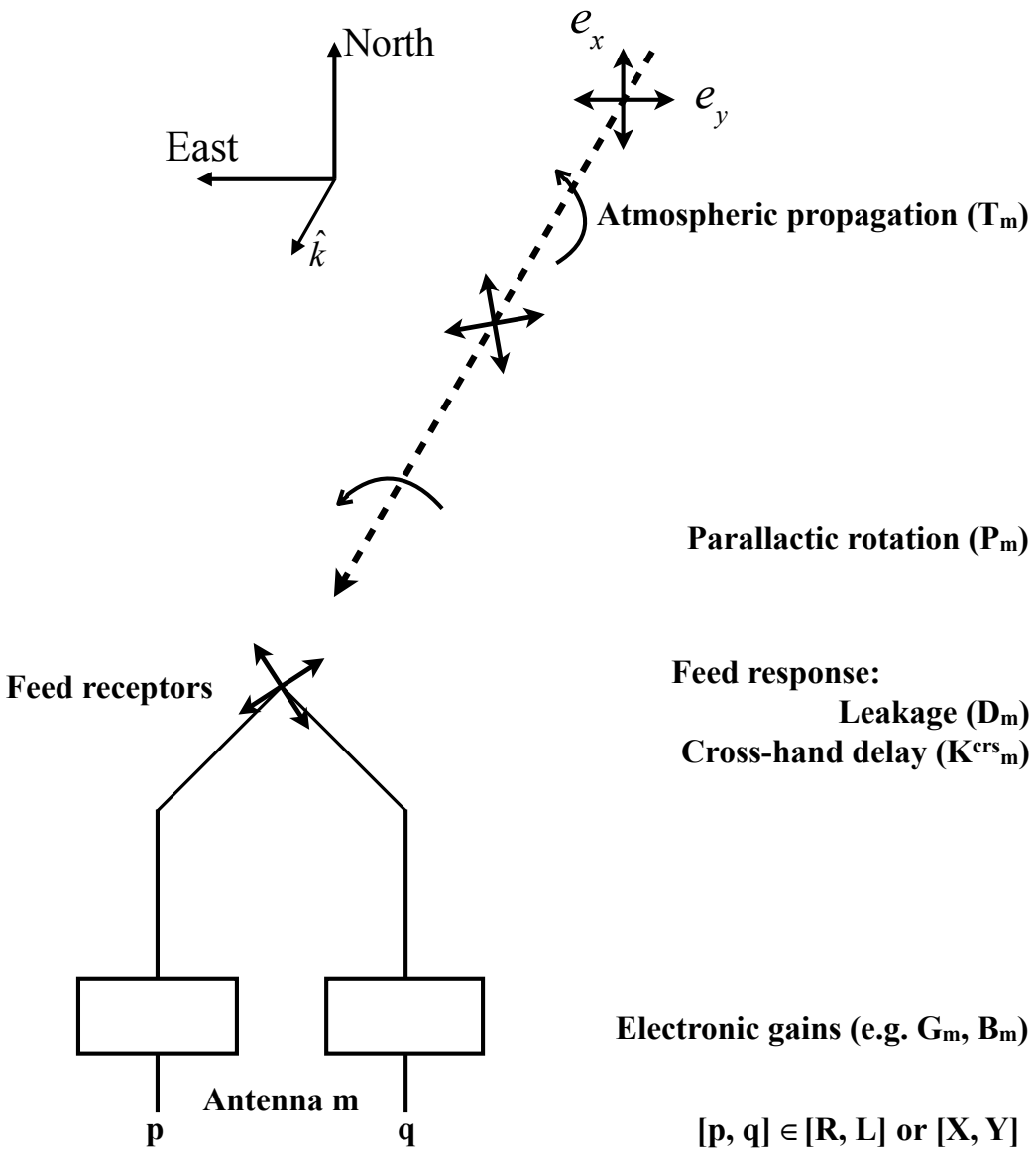

Figure 2.1: Schematic of the signal path of an incoming astronomical radiation that reaches to an antenna. The plot is adapted from (Hamaker et al., 1996). Note that in this schematic plot, we aggregated the terms coming from different part of the signal path to guide the discussion. In practice, some of the terms are coupled or mathematically degenerate, which means they are not perfectly separable as individual components in calibration or optically isolated to one part of the signal path. See detailed discussion in Section 2.2.1

Chapter 3

Mapping Circumstellar Magnetic Fields of AGB stars with CARMA

Mapping magnetic fields is the key to resolving what remains an unclear physical picture of circumstellar magnetic fields in late-type evolved stars as described in Chapter 1. Observations of linearly polarized emission from thermal molecular line transitions due to the Goldreich-Kylafis (G-K) effect provides valuable insight into the magnetic field geometry in these sources that is complementary to other key studies. This Chapter derives substantially from a published paper: "Huang et al. (2020)"[1]. In addition to the published results (Huang et al., 2020), more detailed diagnostics concerning the calibration quality assurance are also included here.

In this Chapter, we present the detection of spectral-line polarization from both the thermal $J = 2 - 1$ CO line and the $v = 1, J = 5 - 4$ SiO maser line toward two Thermal-Pulsing (TP-) AGB stars, R Crt and R Leo, with the Combined Array for Research in Millimeter-wave Astronomy (CARMA[2]) at 1.3 mm wavelength. The observed fractional linear polarization due to the G-K effect in the CO emission is measured as $m_l \sim 3.1\%$ and $m_l \sim 9.7\%$ for R Crt and R Leo respectively. A circumstellar envelope (CSE) model profile and the associated parameters are estimated (Section 3.5.1) and used as input to a more detailed modeling of the predicted linear polarization from the G-K effect (Section 3.5.2). The observed thermal line polarization level is consistent with the predicted results from the G-K model for R Crt; additional effects need to be considered for R Leo.

Pertinent information about the sources is displayed below in Table 3.1. This Table includes the right ascension and declination (J2000), chemical classification, variability type or sub-type, pulsation period P (days), and distance (pc) for each star.

R Crt is a semiregular (SRb) AGB star at a parallax distance 236 pc (Gaia Collaboration et al., 2018; Luri et al., 2018) with a pulsation period of 160 days (Samus' et al., 2017) and a mass-loss rate $\dot{M} \sim 8 \times 10^{-7}\,[M_\odot/\mathrm{yr}]$ (Paladini et al., 2017). It has been found that the Gaia parallax results for the extended, pulsating, and bright AGB stars are often unreliable (van Langevelde et al., 2018; Xu et al., 2019; Ramstedt et al., 2020). As discussed in (Ramstedt et al., 2020), this is even true for stars with that appear to have good astrometric solutions, such as R Crt. However, since R Crt is an SRb variable star, this could also imply significant uncertainties when using a Period-Luminosity (P-L) distance (Feast et al., 1989); accordingly we

[1] This chapter is published in The Astrophysical Journal as Huang et al. 2020, ApJ, 899, 152

[2] https://www.mmarray.org/

adopt the Gaia distance for R Crt. Adopted distances in Table 3.1 are used only in establishing figure length scales in this Chapter. The inferred magnetic field strength from single-dish SiO maser Zeeman observations ranges from $B \sim 0.0 - 3.7$ G over spectral components (Herpin et al., 2006). R Crt has been identified with a companion star (Proust et al., 1981; Cox et al., 2012) and is believed to harbor an outflow structure (Ishitsuka et al., 2001; Kim et al., 2018) possibly aligned with the magnetic field direction inferred from OH maser observations (Szymczak et al., 1999).

R Leo is a nearby, typical M-type AGB star with a P-L distance of 95 pc (Matthews et al., 2018) derived using P-L relation from (Feast et al., 1989) and data from (Haniff et al., 1995). R Leo has been intensively studied in several molecular lines including: SiO lines (e.g. Cotton et al. (2009); de Vicente et al. (2016); Herpin et al. (2006)), H_2O masers (e.g. Menten and Melnick (1991); Yates et al. (1995)), OH masers (e.g. Fish et al. (2006); Etoka and Le Squeren (1997)), CO thermal lines (e.g. Ramstedt and Olofsson (2014); De Beck et al. (2010); Teyssier et al. (2006)), and HCN thermal lines (e.g. Schöier et al. (2013)). The dust shell properties have been observed in infrared and radio continuum (Wittkowski et al., 2016; Ireland et al., 2004; Schöier et al., 2013); R Leo shows statistically-significant deviations from sphericity in its radio photosphere (Matthews et al., 2018; Reid and Menten, 2007) and its dusty environment (Paladini et al., 2017). The pulsation period of R Leo is 310 days (Whitelock and Feast, 2000; Samus' et al., 2017) and the mass-loss rate estimate is $\dot{M} \sim 1.1 \times 10^{-7}\,[M_\odot/\mathrm{yr}]$ (Danilovich et al., 2015). The magnetic field strength in the near CSE of R Leo is estimated from single-dish SiO maser Zeeman observations to be: $B \sim 4.2 - 4.6$G (Herpin et al., 2006). R Leo has also been suggested as hosting a Jovian planet remnant (Wiesemeyer et al., 2009). Recent ALMA observations of R Leo (Vlemmings et al., 2019) provide important insight into the extended atmosphere region $R \sim 1 - 2R_*$ and measure an asymmetric expansion with a mean velocity of 10.6 ± 1.4 km/s.

Table 3.1: Source information

Name	RA (J2000)	Dec (J2000)	Chem. class	Variability	P (days)	Distance (pc)
R Crt	11:00:33.85	-18:19:29.85	O-rich[a]	SRb[a]	160[a]	236[b]
R Leo	09:47:33.49	+11:25:43.67	O-rich[a]	Mira[a]	309.95[a]	95[c]

a. Chemical classification, variability type, and pulsation period P are from (Samus' et al., 2017).
b. Parallax distance estimate is from Gaia DR2 (Gaia Collaboration et al., 2018; Luri et al., 2018).
c. P-L distance estimate is from (Matthews et al., 2018).

In the current work, our aim is to extract morphological information regarding the circumstellar magnetic fields surrounding the two target TP-AGB stars, R Leo and R Crt, using CARMA continuum and molecular line observations. More broadly, we seek to gain insights into the magnetic field geometry and its connection to the more general picture concerning CSE evolution towards the post-AGB and PNe phases, as discussed previously in Section 1.1.2. The observing strategy includes continuum and molecular line observations to study different emission mechanisms that provide complementary insights into the magnetic field in the CSE. These include maser lines in order to study the Zeeman effect, thermal molecular lines targeting the

G-K effect, and continuum observations in order to study dust polarization. Dust polarization observations constrain magnetic field morphology and orientation; the Zeeman observations offer an estimate of the magnetic field strength and, with theoretical inference, the possible magnetic field alignment; and the G-K effect, which is a physically-independent probe, offers insight in the magnetic field morphology at more extended radial distances in the stellar envelope. The overarching goal of the current work is to use the joint and mutual constraints offered by these three approaches to form a more comprehensive picture of the magnetic field morphology in the CSE toward these late-type evolved stars.

We believe that these are the only G-K imaging results obtained by CARMA toward late-type evolved stars at $\lambda = 1.3$mm in full polarization. We do successfully detect the G-K linear polarization signal in the CO thermal emission at the level $m_l \sim 3-9\%$; detailed modeling results for these observations are presented later in this Chapter.

3.1 Observation

The observations of R Crt and R Leo were performed in the E-configuration ($8.5-66$ m baseline lengths) of the CARMA array, in full Stokes mode. Two observing runs were performed, on November 16, 2014 and November 11, 2014 respectively, with each run of total duration 3.7 hours. The correlator was configured in full Stokes mode to observe the SiO $v = 1, J = 5-4$ line in the lower sideband (LSB) and the CO $J = 2-1$ line in the upper sideband (USB), with adopted transition rest frequencies of 215.596 GHz and 230.538 GHz respectively (Lovas et al., 2009). Both lines were observed in narrow-band (line) spectral windows of bandwidth $\triangle\nu = 62.2$ MHz each sampled over 191 frequency channels with corresponding nominal velocity resolutions of 0.453 km/s and 0.423 km/s respectively. In addition, two wide-band (continuum) spectral windows each of bandwidth $\triangle\nu = 489.6$ MHz and sampled over 47 frequency channels each were centered on the spectral lines both for calibration transfer and in order to observe the continuum emission.

3.2 Data Reduction

In describing the data reduction we use the general interferometric data model described by Hamaker et al. (1996); Sault et al. (1996). For a detailed discussion of the data model adopted, see Chapter 2. In this formalism, in a circularly-polarized basis, the detected electric field at antenna m in the array can be expressed as:

$$\mathbf{E}'_m = \begin{bmatrix} E'^R_m \\ E'^L_m \end{bmatrix} = \mathbf{J}_m \mathbf{E}_m = (\mathbf{G}_m \mathbf{B}_m \mathbf{D}_m \cdots) \begin{bmatrix} E^R_m \\ E^L_m \end{bmatrix} \tag{3.1}$$

where $\mathbf{E}_m$ represents the intrinsic incident electromagnetic signal and $\mathbf{E}'_m$ the measured signal, both in a circularly-polarized basis (R,L) as used by CARMA. As previously defined, Jones matrices $\mathbf{J}_m$ are 2×2 matrices representing all the linear operations along the signal path, including both instrumental and

propagation effects. These include the frequency-independent gain $\mathbf{G}_m$, net frequency-dependent passband $\mathbf{B}_m$, and instrumental polarization leakage $\mathbf{D}_m$ amongst others.

The radio interferometric cross correlation of the signals at antennas (m and n) takes the form:

$$\begin{aligned}\mathbf{R}'_{mn} = \langle \mathbf{E}'_m \otimes \mathbf{E}'^{*}_n \rangle = (\mathbf{J}_m \otimes \mathbf{J}^*_n)\, \mathbf{R}_{mn} \\ = [(\mathbf{G}_m \mathbf{B}_m \mathbf{D}_m \cdots) \otimes (\mathbf{G}^*_n \mathbf{B}^*_n \mathbf{D}^*_n \cdots)]\, \mathbf{R}_{mn}\end{aligned} \tag{3.2}$$

where $\otimes$ denotes the outer matrix product. The overall goal of calibration is to infer the intrinsic $\mathbf{R}_{mn}$ from the measured $\mathbf{R}'_{mn}$. The calibration and imaging of CARMA polarization continuum data is described by Hull and Plambeck (2015). Polarization calibration for a pre-cursor connected-element millimeter-wavelength array, the Owens Valley Radio Observatory (OVRO), is described by Akeson (1997).

3.2.1 Calibration

The parallel-hand (RR, LL) data calibration was performed using the CArma Data REduction pipeline, `CADRE` (Friedel, 2013), which in turn uses the Multichannel Image Reconstruction, Image Analysis and Display data analysis package (`MIRIAD`) (Sault et al., 1995). The parallel-hand data reduction allows solution and correction of the antenna-based passband ($\mathbf{B}_m$) and gain ($\mathbf{G}_m$) calibration terms. The passband correction removes the net frequency-dependent instrumental response, while gain calibration corrects time-dependent amplitude and phase errors induced along the signal path. The existing `CADRE` pipeline reduction did not support full-polarization reduction and was modified accordingly. This included the appropriate use of full Stokes data (RR, LL, RL, LR) in the automated flagging phase and the support of dual-polarization in the regular gain and bandpass calibration stages.

For R Crt, 3C279 was used as the bandpass, gain, and leakage calibrator. In the case of R Leo, 3C84 was used as the bandpass calibrator, and OJ287 as the gain and leakage calibrator. The flux density values of the gain calibrators (3C279 in R Crt, and OJ287 in R Leo) were obtained from the ALMA band 6 ($211-275$ GHz) calibrator catalogue[3] with observing dates closest to ours and with adequate gain and flux calibration. The resulting absolute flux densities used for the calibrators are 8.38 ± 0.39 Jy (3C279) and 3.04 ± 0.17 Jy (OJ287)[4]. The antenna-based R and L gains $(G^R_m, G^L_m) = (g^R_m e^{i\phi^R_m}, g^L_m e^{i\phi^L_m})$ were solved separately over time using the parallel-hand data (RR,LL) respectively, where $\mathbf{G}_m = \mathrm{diag}(G^R_m, G^L_m)$. Solutions showing high time-variability or outlier behavior in the differential polarization amplitude gain ratio $g^{R/L}_m$ were detected and the underlying data flagged.

[3] https://almascience.nrao.edu/alma-data/calibrator-catalogue
[4] https://almascience.nrao.edu/alma-data/calibrator-catalogue

3.2.2 Polarization Calibration

In addition to the standard parallel-hand data reduction described above, the calibration process for full polarization data requires: i) R-L phase ($\phi_{RL,m}$) calibration and ii) polarization leakage (D-term, $\mathbf{D}_m$) calibration (Thompson et al., 2017; Hull and Plambeck, 2015). The R-L phase describes the residual phase difference between R and L channels: $\phi_{RL,m} = \phi_m^R - \phi_m^L$. In the mm-wavelength regime this is mainly attributable to the instrumental response as the atmosphere is predominantly non-dispersive (e.g. Kemball and Richter (2011)).

R-L phase calibration is needed to allow accurate absolute electric vector polarization angle (EVPA) measurement and also for correct polarization leakage calibration. The CARMA 10-m telescopes allow instrumental calibration of the R-L phase by injecting an artificial linearly polarized noise signal as a source of linear polarization with a known polarization position angle into the 10-m telescope system (Hull, 2014; Hull and Plambeck, 2015). The `MIRIAD` task `xyauto` solves for the R-L phase corrections for all the 10-m antennas based on these injected signals (Hull, 2014; Hull and Plambeck, 2015). The R-L solution from a reference 10-m antenna was then bootstrapped and applied to the 6-m antennas to correct their R-L phases using `MIRIAD` task `mfcal`.

The instrumental polarization leakage term $\mathbf{D}_m$ describes the cross-coupling between the signals from the nominally orthogonal receptor polarizations (R,L) (Thompson et al., 2017). This calibration term can be solved for from the cross-polarized data (RL and LR) obtained on a bright calibrator source after parallel-hand calibration and correction for the residual R-L phase difference, modulated by observation over a sufficient range of parallactic angle coverage. An adequate parallactic angle range $\Delta\alpha > 60^\circ$ has been estimated as required for a robust leakage solution with CARMA (Hull and Plambeck, 2015). The instrumental polarization leakage terms were solved for using the `MIRIAD` task `gpcal` with `options` = `qusolve`.

The IQUV images were formed from the fully calibrated visibilities by `MIRIAD` task `invert` using natural visibility gridding weighting. At 230 GHz, the beam size is $5.73'' \times 4.21''$ (at PA = 29.7°) for the calibrated R Crt data and $5.07'' \times 3.58''$ (at PA = 80.1°) for the calibrated R Leo data. The synthesized maps of linearly polarized intensity P were de-biased (Wardle and Kronberg, 1974) using `MIRIAD` task `impol` and were masked below 5σ in Stokes I and 4σ in P. The spectral channels were averaged over 1 km s^{-1} in both the CO and SiO channel maps. The final calibrated continuum maps of the gain calibrators, 3C279 and OJ287, are shown in Figure 3.1 and Figure 3.2. The calculated theoretical noise level in the spectral-line image cubes for a 1.0 km s^{-1} channel width and with these observing parameters is between 29.6 mJy/beam (good weather) $\sim$ 56.8 mJy/beam (typical weather). This is calculated using the CARMA sensitivity calculator [5]. The measured median of the off-source noise over frequency from the spectral-line, total intensity data cubes is between 50.1 $\sim$ 274.1 mJy/beam, over the separate transitions.

[5] http://bima.astro.umd.edu/carma/observing/tools/rms.html

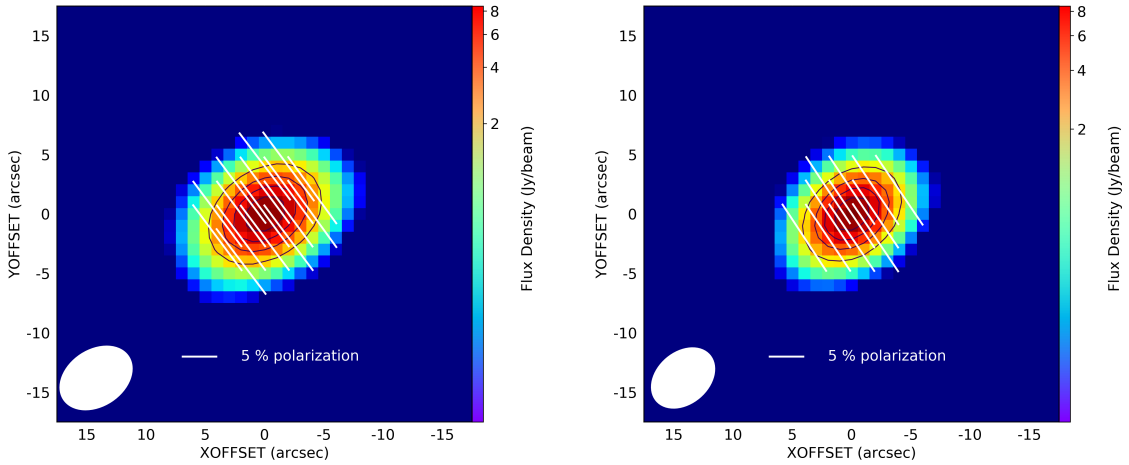

(a) Polarization map of 3C279, LSB

(b) Polarization map of 3C279, USB

Figure 3.1: Linear polarization maps of 3C279 in both LSB and USB. The color map shows the total intensity; the peak total intensity is 8.361 Jy/beam in LSB and 8.363 Jy/beam in USB. The contour levels as the linear polarization intensity from 20%, 40%, 60%, and 80% of the maximum linear polarization intensity, which is 0.968 Jy/beam in LSB, and 0.967 Jy/beam in USB respectively. The synthesized beam is shown at lower left.

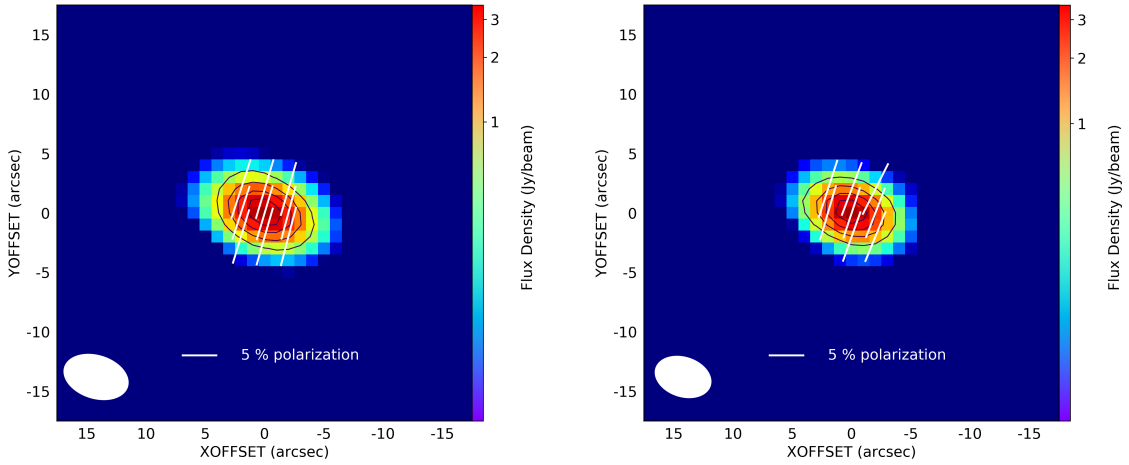

(a) Polarization map of OJ287, LSB

(b) Polarization map of OJ287, USB

Figure 3.2: Linear polarization maps of OJ287 in both LSB and USB. The color map shows the total intensity; the peak total intensity is 3.034 Jy/beam in LSB and 3.029 Jy/beam in USB. The contour levels as the linear polarization intensity from 20%, 40%, 60%, and 80% of the maximum linear polarization intensity, which is 0.244 Jy/beam in LSB, and 0.230 Jy/beam in USB respectively.The synthesized beam is shown at lower left.

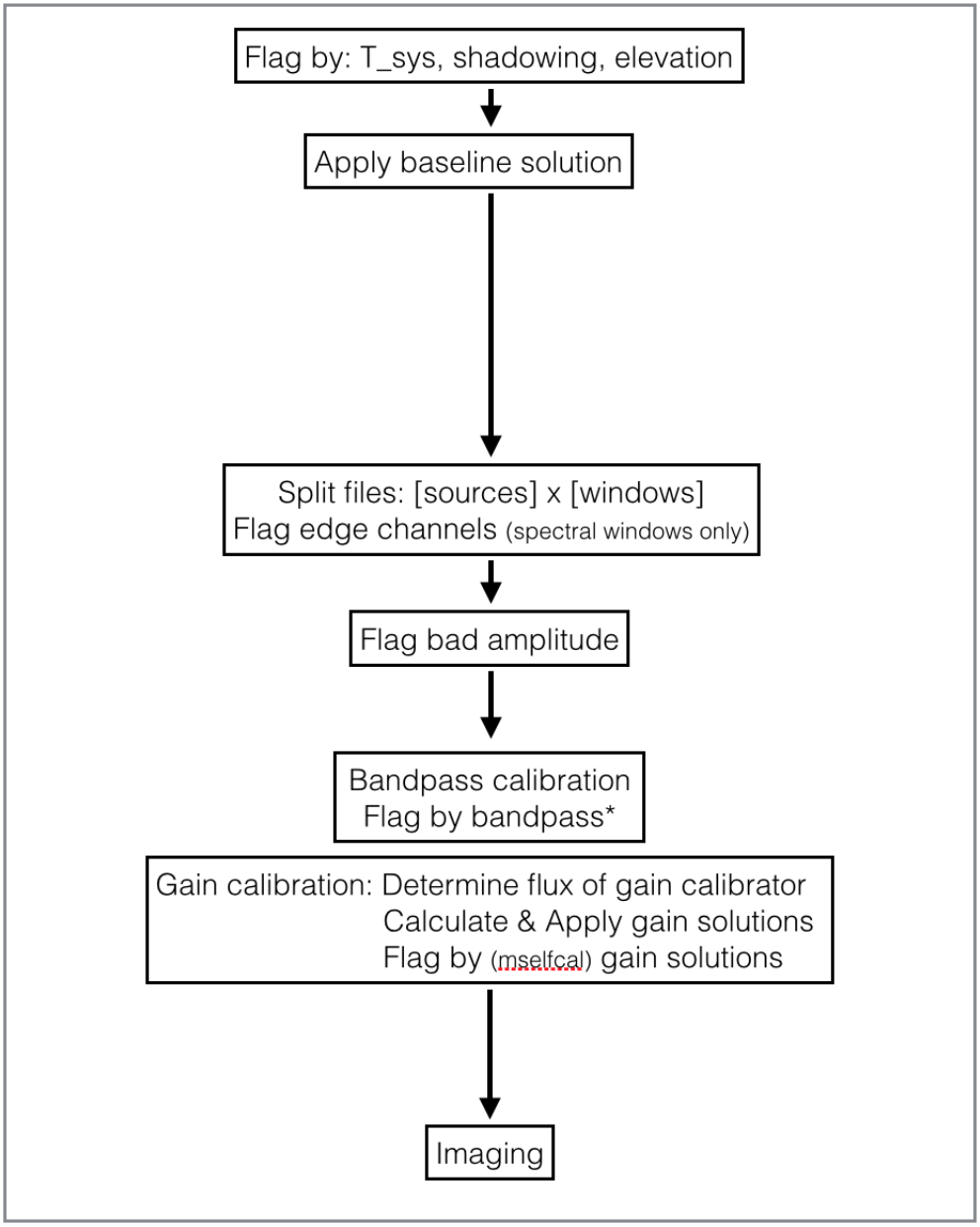

Figure 3.3: The flowchart of reduction script generated by the CADRE pipeline (Friedel, 2013) before modification.

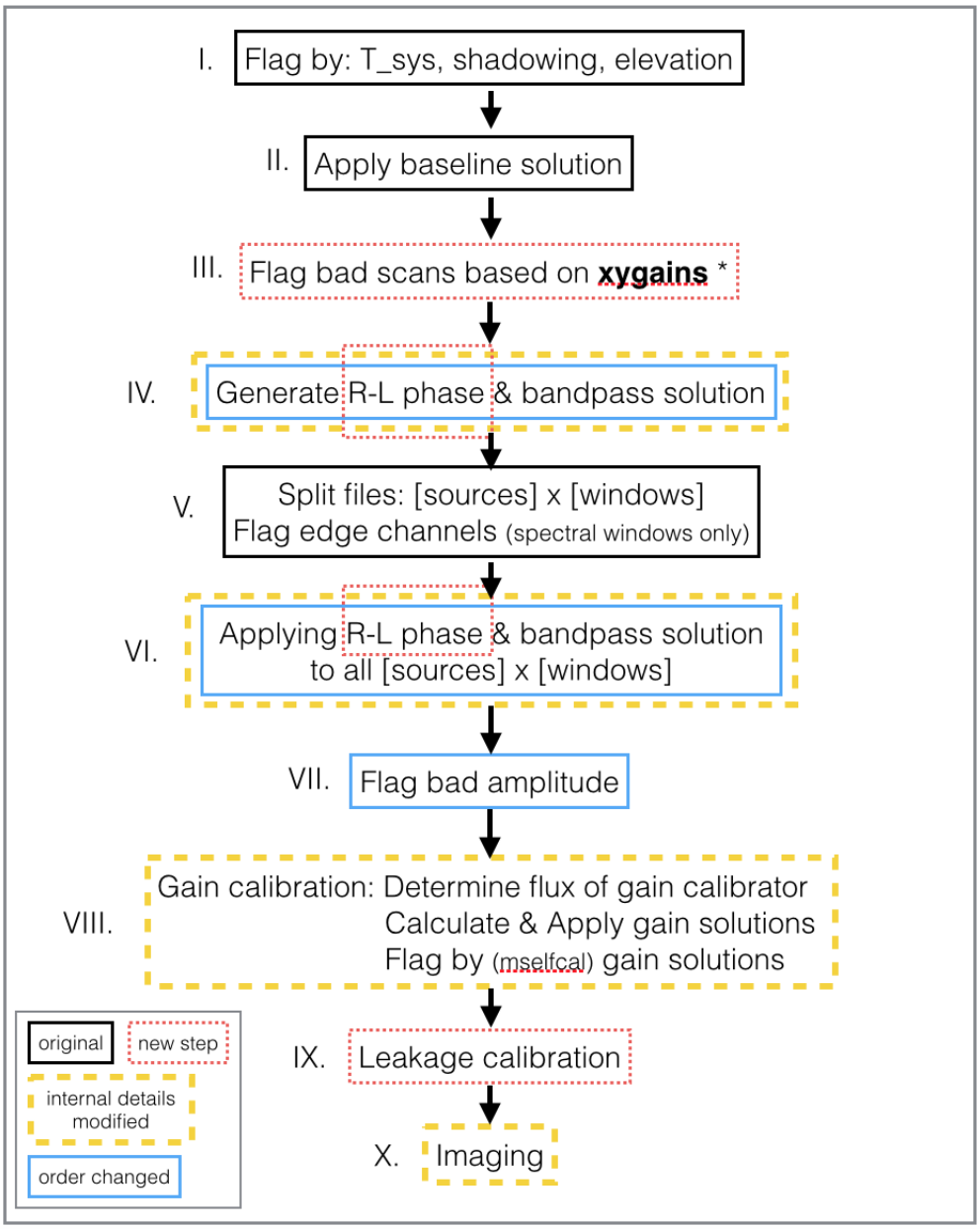

Figure 3.4: The flowchart for the modified reduction process for CARMA full-Stokes spectral-line data. The red dotted line outlines the parts where the new steps were added; yellow dashed lines mark fine tuning of the original process, and the blue solid lines mark a change in order from the original flow.

3.2.3 The Final Flowchart of the Modified Data Reduction Process

In Figure 3.3 a brief flowchart of the reduction script generated by the CADRE pipeline (Friedel, 2013) before our modification is outlined, and in Figure 3.4 the flowchart for the modified data reduction process is presented. This final version of calibration procedure is a hybrid product of both the script generated by CADRE (Friedel, 2013) and the modifications based on consideration described in Section 3.2.1 and 3.2.2. In the following, the details at each step are illustrated in accordance with the Roman number labeling in Figure 3.4.

I. Preliminary flagging: A preliminary round of flagging is executed. Data with system temperatures above the assigned threshold will be flagged. The cutoff value is set to be 5000K. Besides, if one antenna is shadowed by the other antenna, the data from the shadowed antenna are flagged. CADRE also flags data with high elevations ($> 85°$) as the tracking at these high elevations has insufficient accuracy.

II. Apply baseline solution: This calibrates for antenna position errors. The resulting baseline solution[6] is applied to data.

III. Flag bad scans based on cross-polarized gains: In general, this R/L gain solution ratio is expected to be slowly varying about a unity level throughout the observations. Any drastic drop or rise from the global trend signals a change in data quality; this is typically reflected in higher scattering of the data. We inspected the R/L ratio of the gain solutions obtained from the output of MIRIAD task `gpplt` with `options` = `xygains` and exclude these source scans associated with discrepant R/L solution ratios. Figure 3.5 shows example LSB data indicating this flagging process for data from the R Crt observing run.

IV. & VI. R-L phase and bandpass calibration: The R-L phase calibration is determined during bandpass calibration process as noted above. The bandpass calibration corrects the frequency-dependent artifacts introduced along the signal path, indicating both the atmosphere and instrumental components. For the amplitude response over frequency, we increased the pre-averaging over channel number to enhance the solution quality.

As discussed in Section 2.2.2, there remains uncertainty in the R-L phase difference of the reference antenna itself, equivalently absolute R-L phase difference. This absolute R-L phase difference will in turn cause a net rotation of the EVPA of all the targets observed if not corrected. This calibration is performed using scientific measurements from other facilities. Details for the absolute EVPA alignment are discussed later in Section 3.3.

V. Split the data into files for each source and spectral window: The data are split into subsets sorted by targets and spectral window. Three edge channels on each side of the spectral-line win-

[6]CADRE can also searches for the most recent system baseline solution if available (Friedel, 2013).

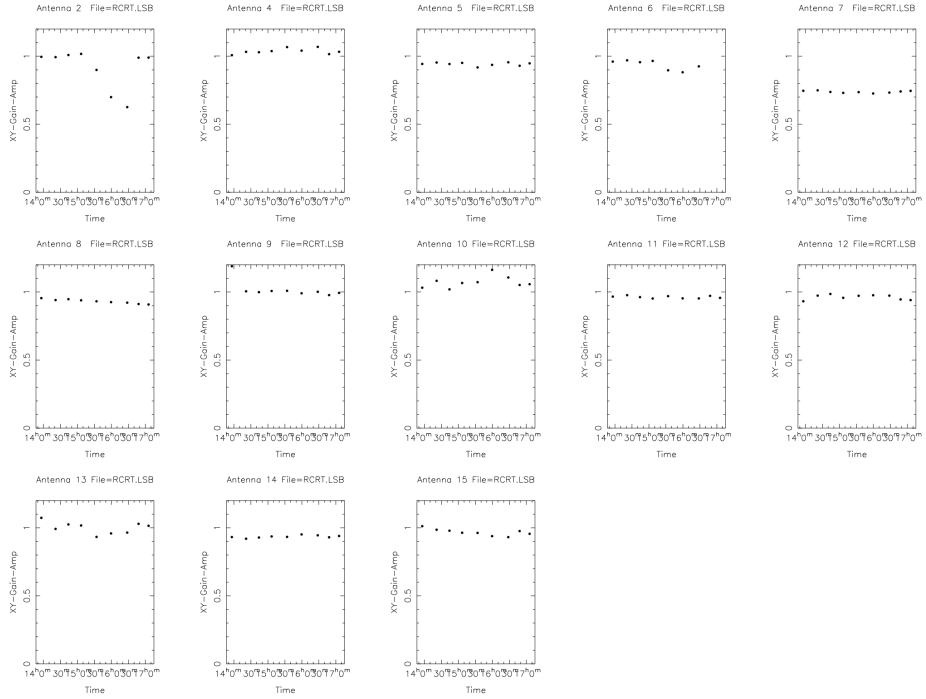

(a) The RR and LL gain solution ratio of all antennae indicating outliers before flagging.

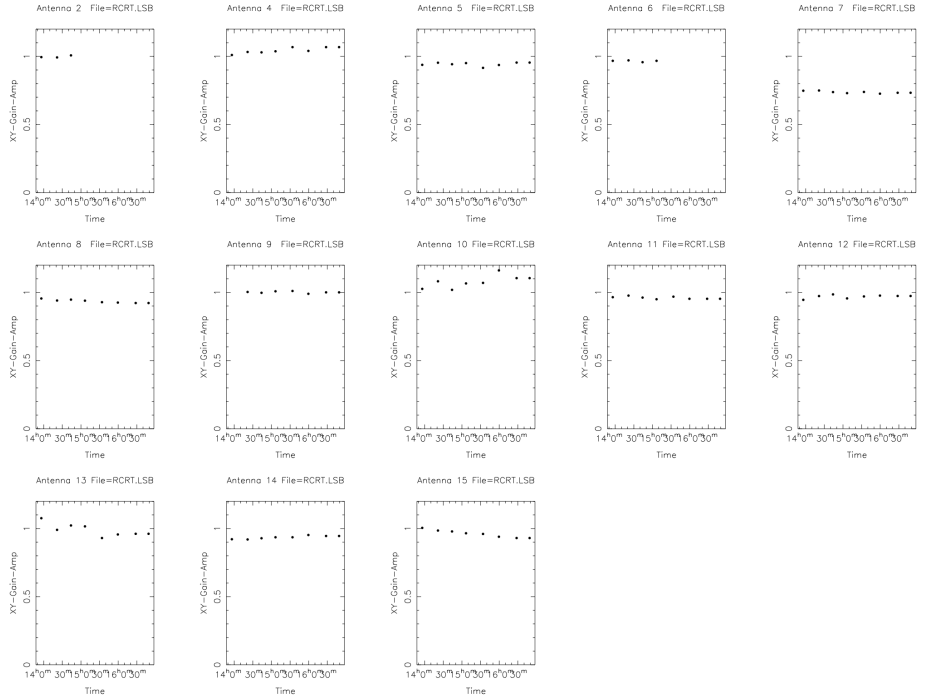

(b) The RR and LL gain solution ratio of all antennae after flagging outlier scans.

Figure 3.5: The example from the R Crt LSB data of flagging by R/L gain solution ratio.

dows are then flagged on each side of the spectral-line windows as those low-amplitude edge channels are often noisier.

VII. Flag bad amplitude: CADRE obtains the statistical information characterizing the data using the MIRIAD task `uvlist` with `options = stat`; this is used to identify and flag amplitude anomalies in the data. The data can be represented at this stage as:

$$V_{ij}^{obs} = G_i(t)G_j^*(t)V_{ij}^{true} + N_{thermal}(\sigma) + \epsilon_{systematic} \tag{3.3}$$

where the $N_{thermal}(\sigma)$ is the thermal noise with a standard deviation σ, and $\epsilon_{systematic}$ is the systematic error. We modified[7] the CADRE pipeline to calculate the amplitude running average ($\overline{V}_{ij}^{obs}(t)$) and the associated standard deviation $\sigma_{ij}(t)$ over time. Outliers deviating from the running average $\overline{V}_{ij}^{obs}(t)$ by greater than $3 \times \sigma_{ij}(t)$ for each scan are flagged. The data were also flagged for their deviation from the global average. In practice this process takes place before the gain calibration, meaning the slowly time-varying, instrumental response is not removed from the signal yet.

VIII. Gain calibration: Gain calibration is performed to correct the time-dependent amplitude and phase response. In general, the instrumental gain response in R and L receptors are different. For the full-Stokes mode data, we switch to MIRIAD task `mfcal` instead of `mselfcal` for solving RR and LL gain response individually[8].

IX. Leakage calibration: The cross-coupling of RCP and LCP channels is corrected by polarization leakage calibration. Because the CARMA uses altitude-azimuth mounts, the RL and LR cross correlation amplitude is modulated in a predictable way (Hull and Plambeck, 2015). As noted above, an adequate parallactic angle range[9] $\Delta\alpha > 60^\circ$ has been estimated as required for a robust leakage solution with CARMA (Hull and Plambeck, 2015).

X. Imaging and De-biasing: The basic imaging process involves inverting the $u-v$ data into dirty maps, cleaning and restoring the maps (Thompson et al., 2017). This yields maps of the Stokes I, Q, U, and V emission separately. The Stokes Q and U components were used to calculate the linear polarization intensity as: $P = \sqrt{Q^2 + U^2} \equiv R'$.

Consider both Q and U are quantities of random Gaussian noise with a variance σ^2 centering at peak Q_0 and U_0 respectively. The quantity P can be viewed as the magnitude of the superposed vector $\vec{P} = (Q \cdot \vec{e_Q} + U \cdot \vec{e_U})$ from $Q\vec{e_Q}$ and $U\vec{e_U}$, where $\vec{e_Q}$ and $\vec{e_U}$ are an orthogonal basis. This is plotted in Figure 3.6. The uncertainty of the magnitude P of this vector deviates from the Gaussian distribution, and the measured peak (R') deviates from the intrinsic value $\sqrt{Q_0^2 + U_0^2} \equiv R$. The goal

[7] Original CADRE process was using the all-time amplitude average as the flagging benchmark.

[8] This also provides R/L gain amplitude ratio for inspection and flagging.

[9] To achieve such good coverage of parallactic angle, a duration for the polarization observation exceeding 3 hours across transit is usually required with the CARMA array.

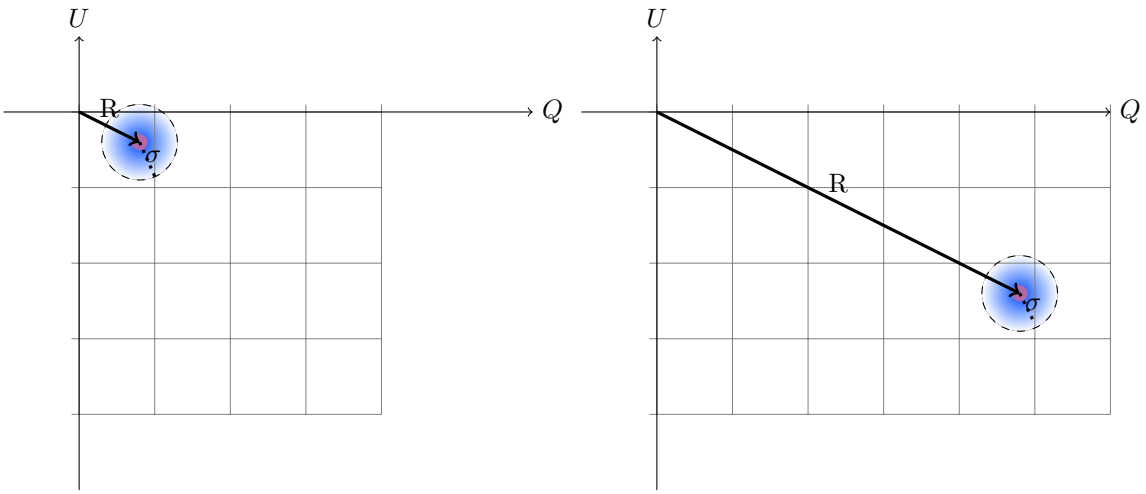

Figure 3.6: The schematic for two extreme cases of $\frac{R}{\sigma} < 1$ (left panel) and $\frac{R}{\sigma} \gg 1$ (right panel).

of the de-biasing process is to restore R from the measured peak and variance (Wardle and Kronberg, 1974).

Following the analysis of Vinokur (1965) and Wardle and Kronberg (1974), the derived probability distribution for the polarized intensity R' follows a Rice distribution:

$$f(R') = \frac{R'}{\sigma^2} I_0(\frac{RR'}{\sigma^2}) \exp(-\frac{R^2 + R'^2}{2\sigma^2}) \tag{3.4}$$

where I_0 is the 0-th order of the modified Bessel function. The following are two asymptotic cases (Wardle and Kronberg, 1974):
(I.) $\frac{R}{\sigma} \leq 1$: the $f(R')$ distribution approaches the Rayleigh distribution with a variance $(2 - \pi/2)\sigma^2$ (see also Figure 3.7 (a)) :

$$f(R')|_\sigma = (\frac{R'}{\sigma^2}) \cdot e^{-(\frac{R'^2}{2\sigma^2})} \tag{3.5}$$

(II.) $\frac{R}{\sigma} \gg 1$: the probability distribution approaches a Gaussian with variance σ^2, centered on $R' = R$ (Figure 3.7 (b)):

$$f(R')|_\sigma = \frac{1}{\sqrt{2\pi\sigma^2}} \cdot e^{-\frac{(R'-R)^2}{2\sigma^2}} \tag{3.6}$$

The MIRIAD task `impol` synthesizes Q and U maps into a de-biased linearly polarized map using specified parameters `sigma` $=\sigma_{Q,U}, \sigma_I$ specified. The value σ_I is the standard deviation of the Stokes I image, and $\sigma_{Q,U}$ is the mean standard deviation of the noise in the Q and U images. In practice, the noise in the Q and U images are comparable with each other, thus $\sigma_{Q,U}$ is comparable to σ in Equation 3.4. An approximation that holds for $\frac{R}{\sigma} > 0.5$ was given by Wardle and Kronberg (1974)

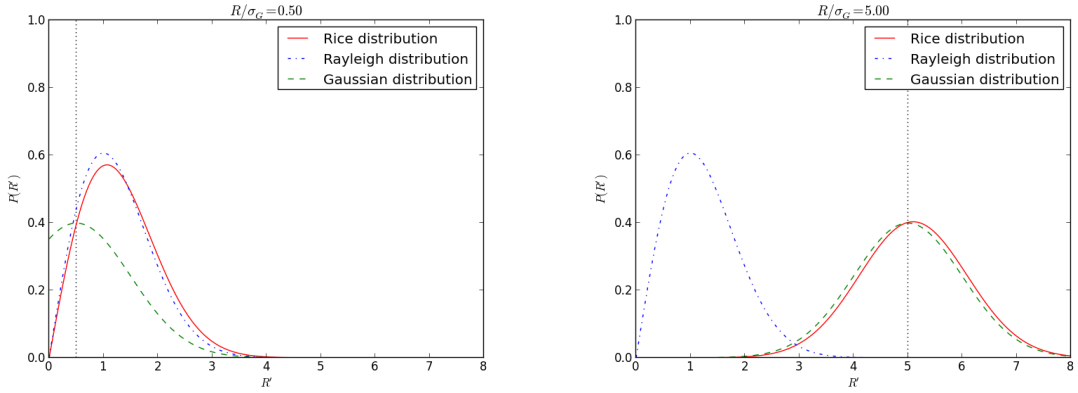

(a) When $\frac{R}{\sigma} \leq 1$ (b) $\frac{R}{\sigma} \gg 1$

Figure 3.7: Schematic plots of Rice distribution at two asymptotic cases: $\frac{R}{\sigma} \leq 1$ and $\frac{R}{\sigma} \gg 1$.

(their Equation A3):

$$R \sim R'_M \left[1 - (\frac{\sigma'}{R'_M})^2\right]^{1/2} \tag{3.7}$$

Using this relation, the measured $\sigma_{Q,U} \sim \sigma'$ can be used to estimate the intrinsic linear polarization signal strength R in Equation 3.7.

Caution is also needed in estimating the noise level of the linear polarization intensity map from its off-source region before de-biasing process. The distribution of the off-source regions in the linear polarization intensity map before de-biasing is expected to follow the Rayleigh distribution as we expect low-to-none signal in those regions. The measured variance should be therefore corrected as $(2 - \pi/2)\sigma'^2$ to obtain σ'^2.

3.3 Calibration Quality Assurance

The polarization observations with CARMA were extremely limited; hence we need to run through the quality assurance of the solutions and calibrated data.

In inspecting the calibration quality, several indicators are often examined, including the calibration solution behavior, the corrected data behavior (e.g. over time and frequency), and the imaging products from data at different calibration stages. In this section, we highlight the key quality assurance products from the calibrator source 3C279 taken as an example. 3C279 is the bandpass, gain, and leakage calibrator for the R Crt observing run.

3.3.1 Parallel-hand Calibration Quality

As noted above, the parallel-hand (RR, LL) calibration allows correction of the antenna-based passband ($\mathbf{B}_m$) and gain ($\mathbf{G}_m$) calibration terms. After parallel-hand calibration, we generally expect flattened RR and

LL data dependence over both frequency and time. Figure 3.8 shows the change in amplitude dependence over frequency of the 3C279 USB data for baseline $(4-15)$, before and after the parallel-hand calibration. Figure 3.9 shows the analogous change in phase for this baseline before and after the parallel-hand calibration. Figure 3.10 and 3.11 shows comparable plots over time for baseline $(10-15)$. show such contrast before and after parallel-hand calibration, in data behavior over time. The flattened dependence of both RR and LL correlation data is apparent.

3.3.2 Polarization Calibration Quality

Several quality assurance tests were applied to assess the quality of the fully calibrated data specifically including the polarization calibration.

The amplitude of the derived polarization leakage terms, across all spectral windows and both observing runs, ranged from few percent to a maximum of $\sim 20\%$. Prior continuum polarimetry with CARMA showed a comparable range in values (Hull and Plambeck, 2015). We also compared our solved D-term amplitude with a separately reduced CARMA archival data set[10] from a continuum polarimetry survey of extragalactic active galactic nuclei (Bower (2014), hereinafter the TADPOL data). This comparison is displayed in Figure 3.12 and 3.13. In this Figure, TADPOL denotes the CARMA archival data (Bower, 2014), R Crt denotes the D-term derived from the associated USB calibrator (OJ287) in the current work, and R Leo denotes the D-term derived from the 3C279 USB data in the current work. In all cases, D_R denotes the D-term from R receptors, and D_L the D-term from L receptors. The antenna-based D-term values are not expected to be precisely constant with time and independent of frequency within the band; however, a moderate level of instrumental stability is expected. We therefore examined the rank correlation of the antenna-based D-term amplitudes against those obtained from the referenced CARMA archival data set[11] (Bower, 2014). The rank correlation measures the ordinal association of two data sets (Zwillinger and Kokoska, 1999). In this test we computed: Spearman's rank-order correlation (Zwillinger and Kokoska, 1999) with scipy using `SciPy.stats.spearmanr`[12], Kendall's tau (Knight, 1966) using `SciPy.stats.kendalltau`, and the Pearson correlation coefficient (Pearson, 1895) using `SciPy.stats.pearsonr`. Correlations of -1.0 or $+1.0$ imply an exact monotonic relationship, and zero implies no correlation. All three correlation coefficients were computed for both the R Crt (3C279) and R Leo (OJ287) data, across all spectral windows, for both $|D_m^R|$ and $|D_m^L|$ against the corresponding reference TADPOL values. The maximum number of antennas in our data was 15 and the rank-order correlation coefficients fell within the range $r \in [0.1 \sim 0.6]$ with a median value $r \sim 0.4$; this indicates moderate correlation, consistent with our physical expectation.

The quality of the polarization calibration was also assessed by examining the scatter of the calibrator cross-polarized visibility data in complex plane before and after polarization calibration, as shown for 3C279

[10] CARMA project ID: c1217; Observing Block ID: c1217.2D_2303c279.2
[11] CARMA project ID: c1217; Observing Block ID: c1217.2D_2303c279.2
[12] http://www.scipy.org

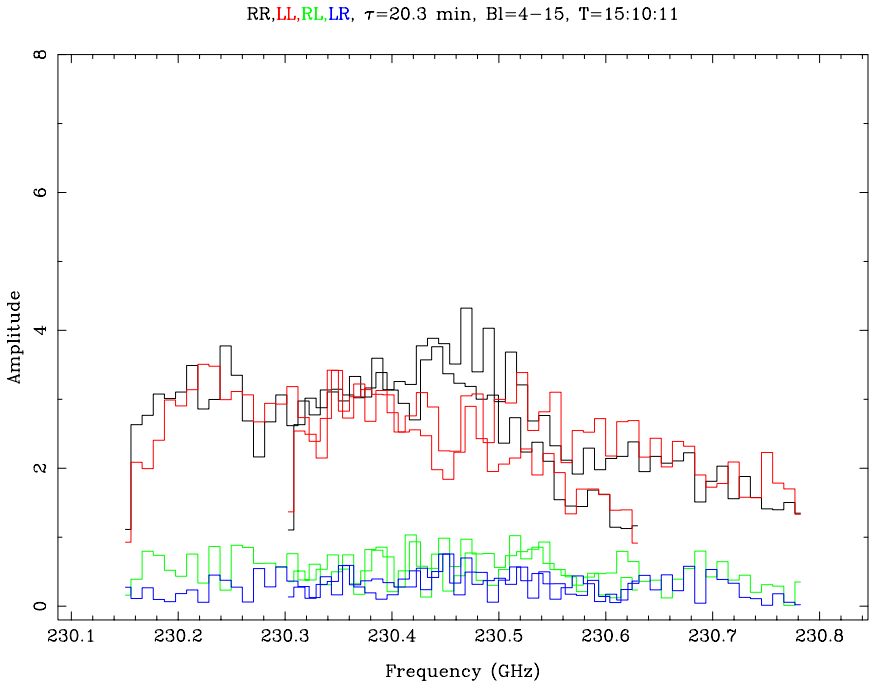

(a) Plot of 3C279 USB data amplitude over frequency before BP calibration.

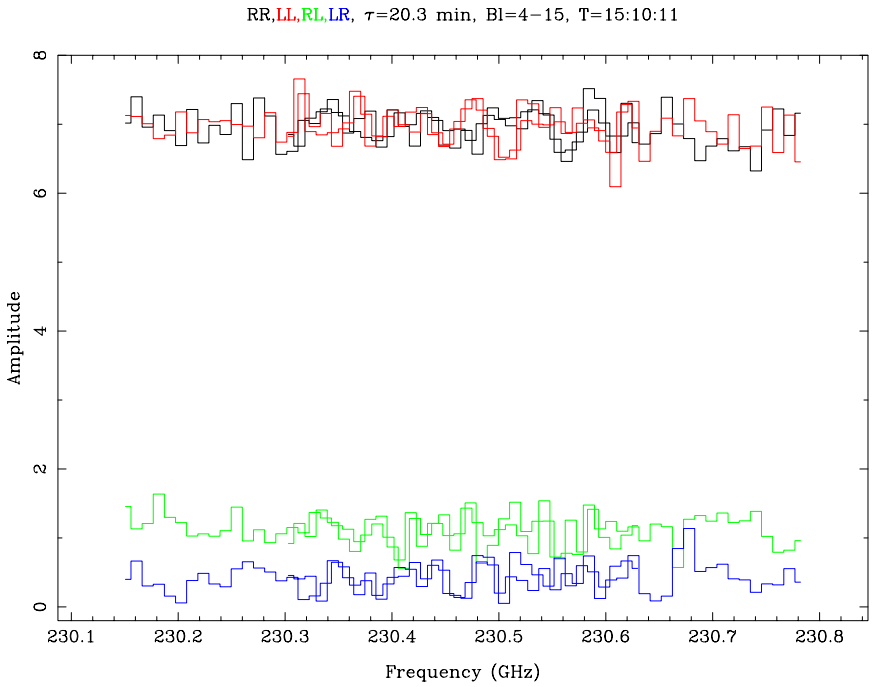

(b) Plot of 3C279 USB data amplitude over frequency after BP calibration.

Figure 3.8: The C279 USB data for baseline pair $(4-15)$. This shows amplitude over frequency (a) before and (b) after parallel-hand calibration.

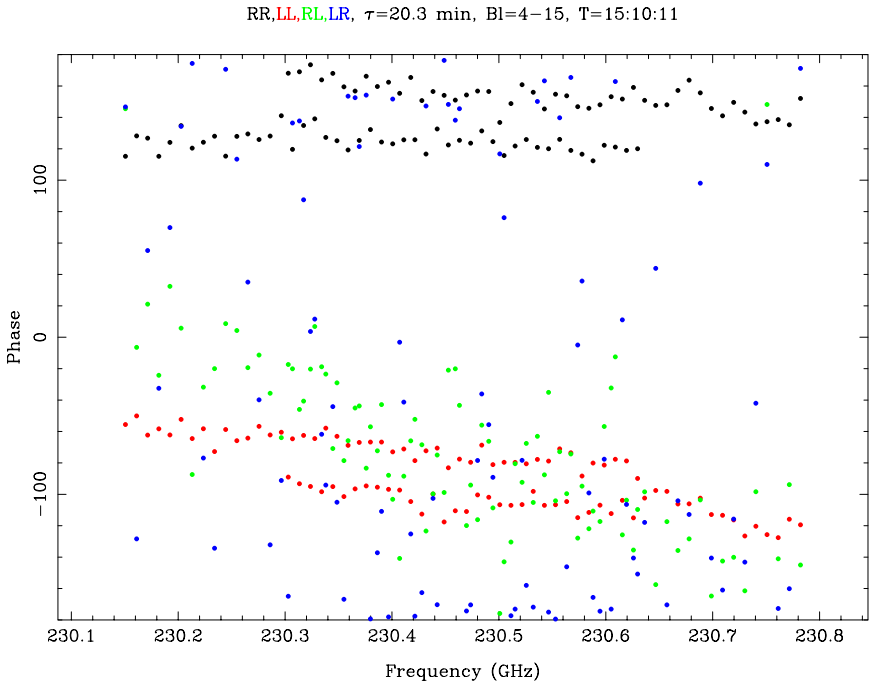

(a) 3C279 USB data phase over frequency before bandpass calibration.

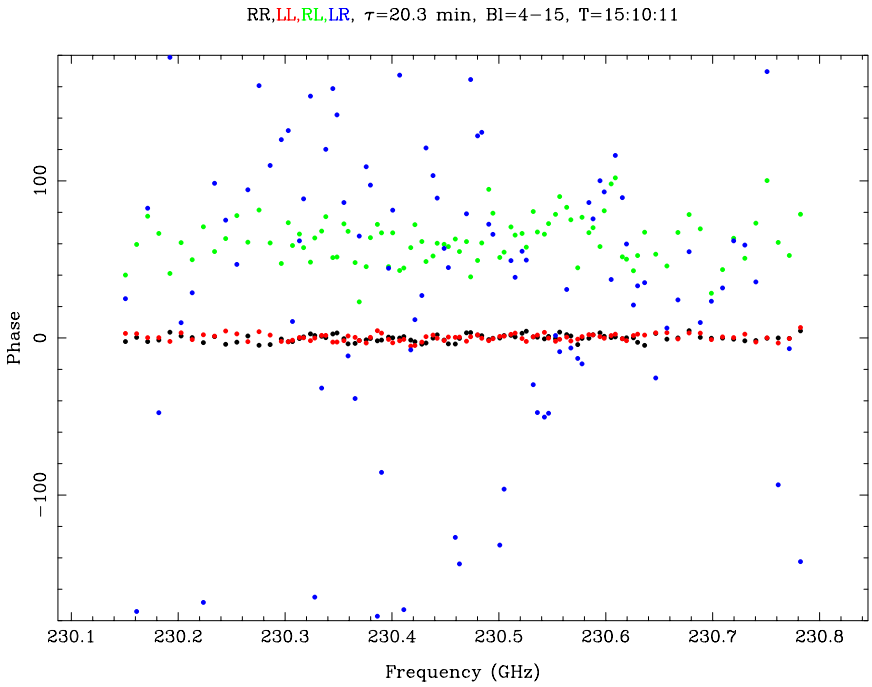

(b) 3C279 USB data phase over frequency after bandpass calibration.

Figure 3.9: The C279 USB data for baseline pair $(4-15)$. This shows phase over frequency (a) before and (b) after parallel-hand calibration.

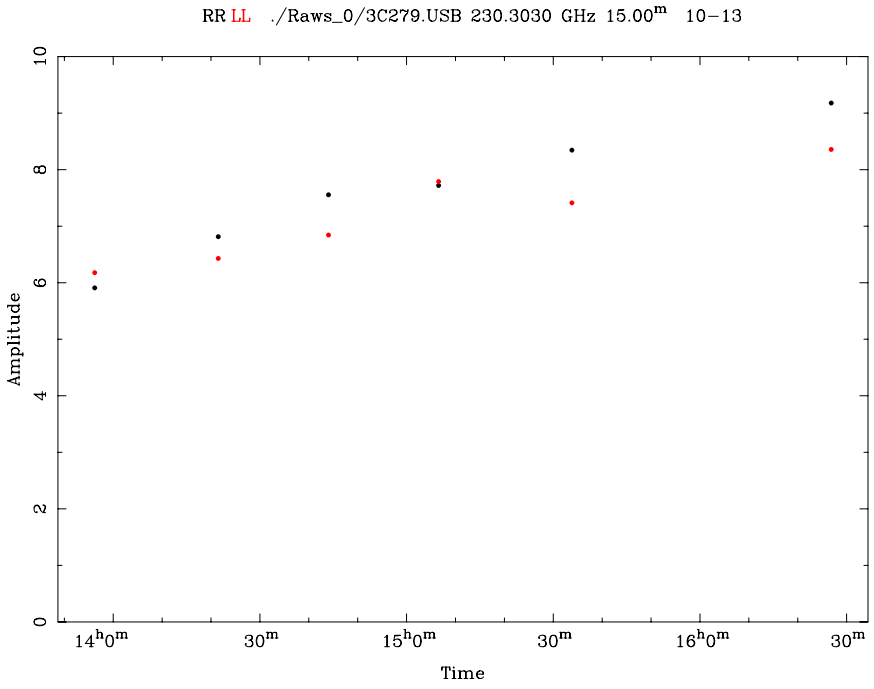

(a) 3C279 USB data amplitude over time before gain calibration.

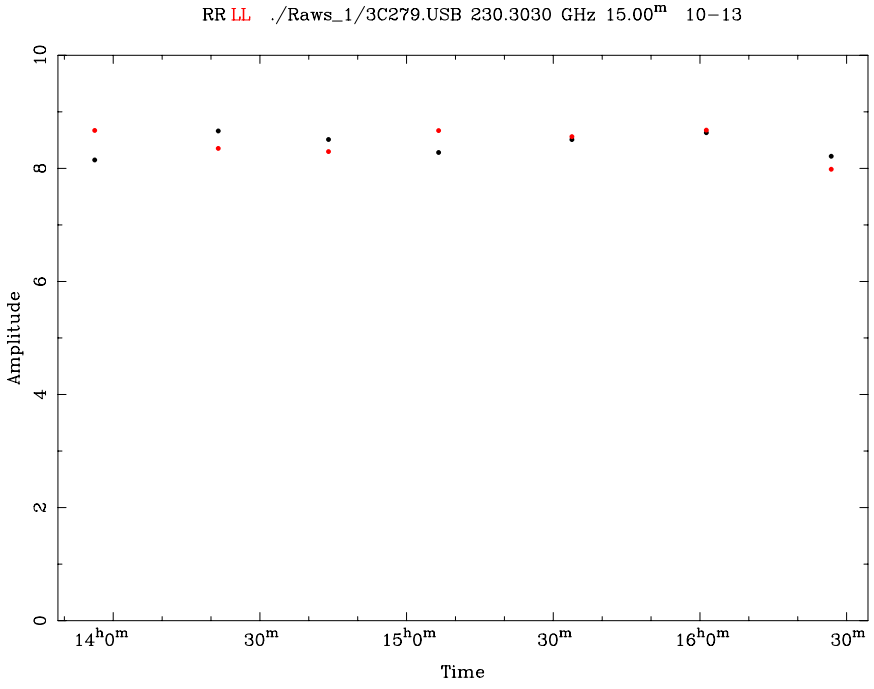

(b) 3C279 USB data amplitude over time after gain calibration.

Figure 3.10: The 3C279 USB data for baseline pair $(10-13)$. This show amplitude over time (a) before and (b) after parallel-hand calibration.

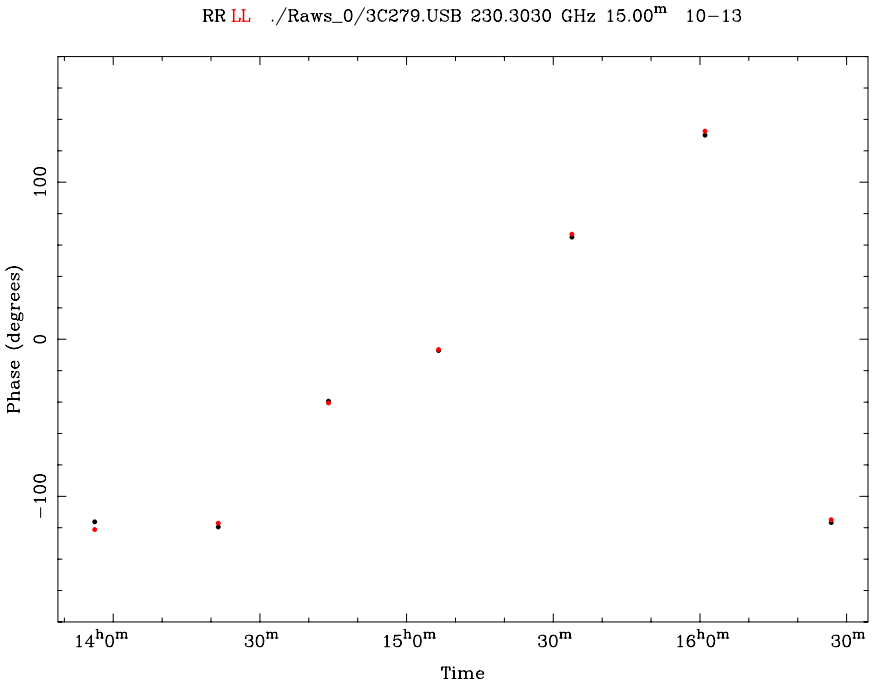

(a) 3C279 USB data phase over time, before gain calibration.

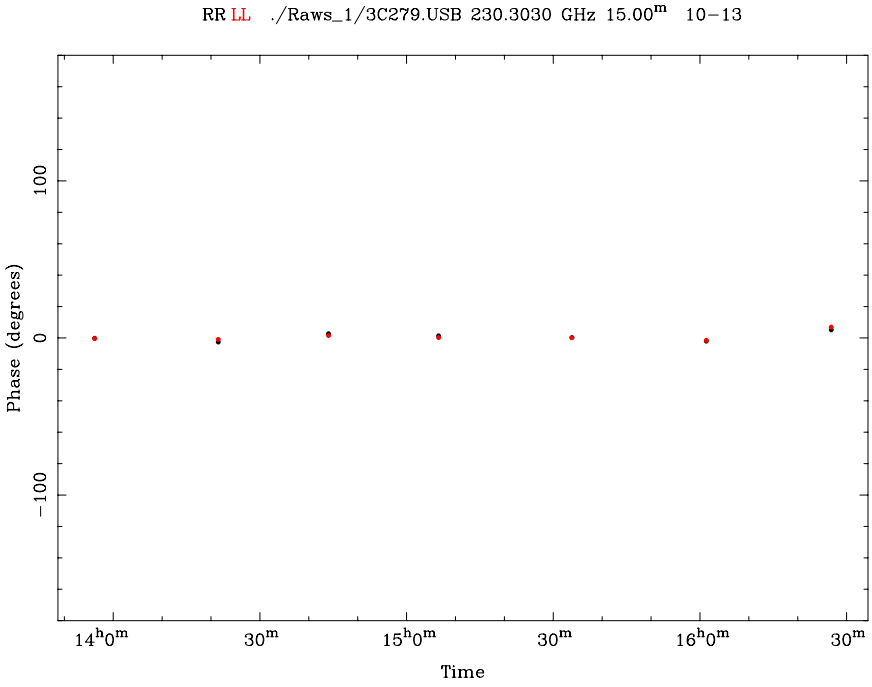

(b) 3C279 USB data phase over time, after gain calibration.

Figure 3.11: The 3C279 USB data for baseline pair $(10 - 13)$. This show phase over time (a) before, and (b) after parallel-hand calibration.

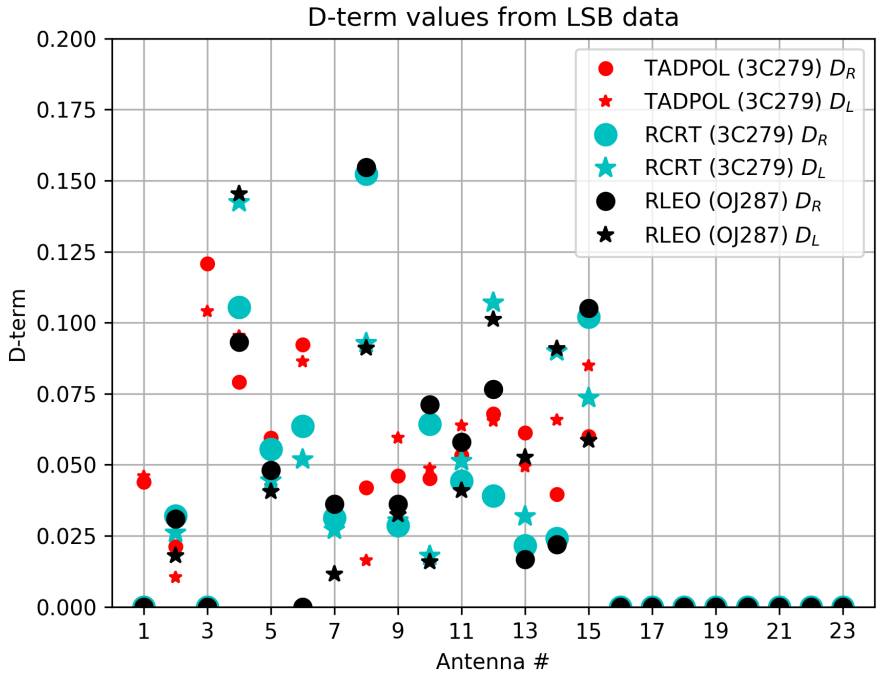

Figure 3.12: The compiled D-term results from all LSB data. The antennas associated with zero-values are the antennas either not available during the observation or flagged later in the data reduction. In this Figure, TADPOL denotes the CARMA archival data (Bower, 2014), R Crt denotes the D-term derived from the associated USB calibrator (OJ287) in the current work, and R Leo denotes the D-term derived from the 3C279 USB data in the current work. In all cases, D_R denotes the D-term from R receptors, and D_L the D-term from L receptors.

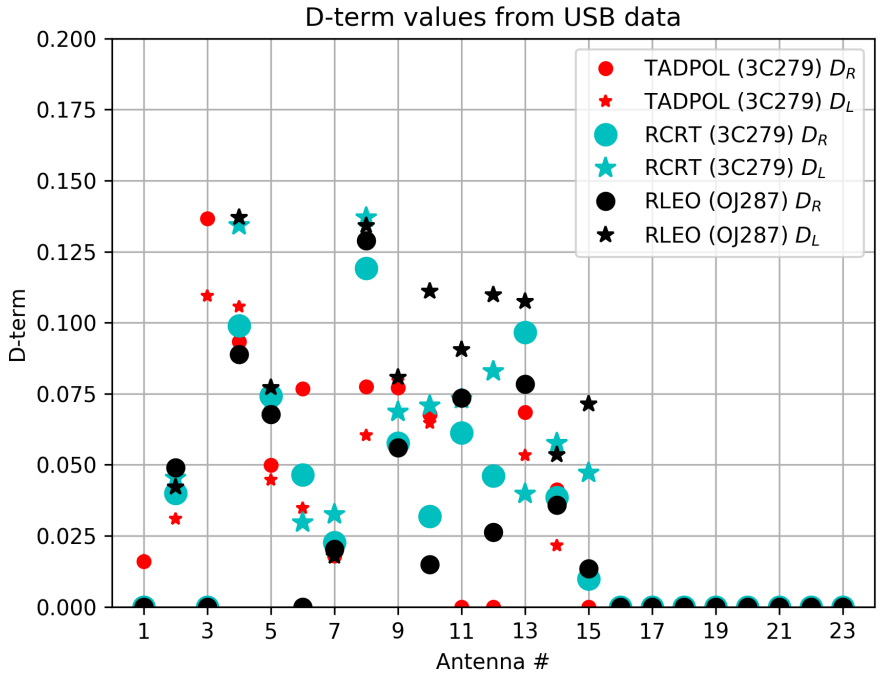

Figure 3.13: The compiled D-term results from all USB data. The antennas associated with zero-values are the antennas either not available during the observation or flagged later in the data reduction. In this Figure, TADPOL denotes the CARMA archival data (Bower, 2014), R Crt denotes the D-term derived from the associated USB calibrator (OJ287) in the current work, and R Leo denotes the D-term derived from the 3C279 USB data in the current work. In all cases, D_R denotes the D-term from R receptors, and D_L the D-term from L receptors.

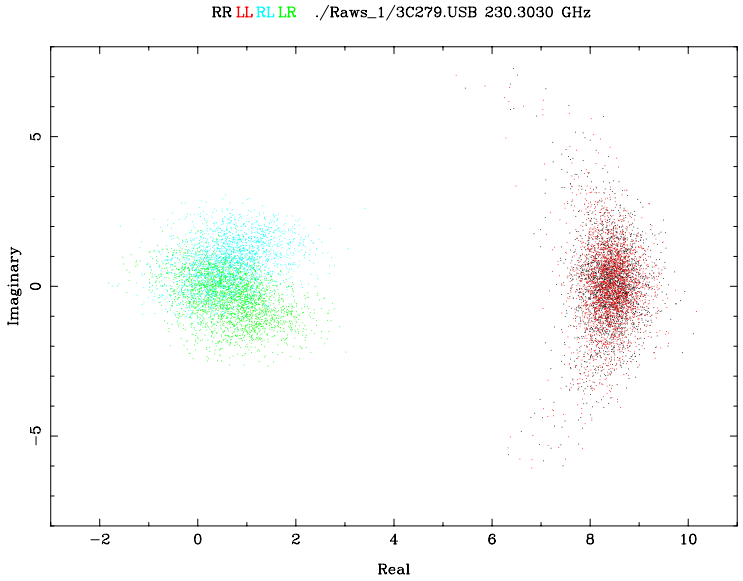

Figure 3.14: Plot of 3C279 D-term scattering in the complex plane before calibration.

USB data in Figure 3.14 and 3.15 separately. Polarization calibration was found to improve the scatter significantly, especially the RL and LR correlation distribution in the complex plane was more compact after the polarization calibration, as expected.

The statistical distribution of the R-L phase difference derived from the visibility data was also narrower after R-L phase calibration and polarization leakage calibration. This is illustrated in Figure 3.16 which shows the histogram of phase differences of the cross-hand correlation signals (RL and LR) under 3 cases: (a) the data calibrated only with the parallel-hand calibrations, (b) data calibrated with the parallel-hand and R-L phase calibrations (i.e. no leakage calibration yet), and (c) the fully-calibrated data set. Figure 3.17 and 3.18 show this comparison for R-L phase difference from only 6.1-m and 10.4-m antennas respectively. To interpret these plots, we examined the phase of the RL and LR visibility data for baseline pair (m, n):

$$\begin{aligned} \phi^{RL}_{mn} &\equiv \phi^{R}_{m} - \phi^{L}_{n} + \psi^{RL}_{mn} \\ \phi^{LR}_{mn} &\equiv \phi^{L}_{m} - \phi^{R}_{n} + \psi^{LR}_{mn} \end{aligned} \tag{3.8}$$

where $\phi^{R,L}_{m}$ is the calibration phase at antenna m in the indicated receptor polarizations and ϕ^{RL}_{mn} the source structure phase in the indicated correlation pair. The visibility phase difference between the RL and LR

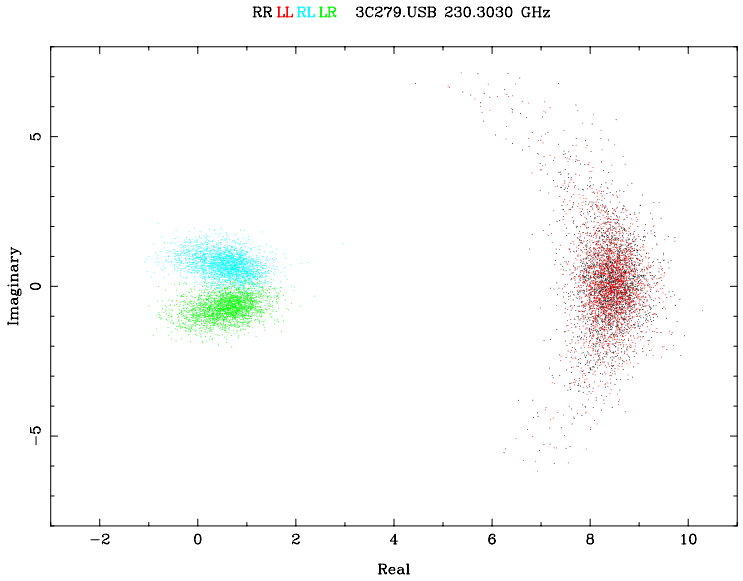

Figure 3.15: Plot of 3C279 D-term scattering in the complex plane after calibration.

correlation is therefore:

$$\begin{aligned}\Delta\phi_{mn} \equiv (\phi_{RL} - \phi_{LR})_{mn} &= (\phi_m^R - \phi_n^L) - (\phi_m^L - \phi_n^R) + \psi_{mn}^{RL} - \psi_{mn}^{LR} \\ &= (\phi_m^R - \phi_m^L) + (\phi_n^R - \phi_n^L) + \psi_{mn}^{RL} - \psi_{mn}^{LR}\end{aligned}$$

For point-like sources such as 3C279 in these observations, $\psi_{mn}^{RL} - \psi_{mn}^{LR} \sim constant$ and independent of baseline length. Denoting $\delta\phi_m^{RL} = (\phi_m^R - \phi_m^L)$, the equation above therefor secures: $\Delta\phi_{mn} = \delta\phi_m^{RL} + \delta\phi_n^{RL} = constant$. The ultimate goal of R-L phase calibration is to correct the extra R-L phase difference introduced along the signal path, $(\delta\phi_{R-L})$. A good R-L phase calibration is expected to minimize the description of the compound quantity $(\delta\phi_{R-L}, m + \delta\phi_{R-L}, n)$ The diagnostic plots Figure 3.16 provides a quality assurance on this association. As expected, the distribution of $(\phi_{RL} - \phi_{LR})$ is more compact when the full version of calibration is carried out. The rms variation $(\sigma_{\delta\phi})$ of the R-L phase difference is shown in right panel of Figure 3.16. The variation $\sigma_{\delta\phi}$ of the R-L phase difference is reduced after full polarization calibration. Note the plotted R-L phase difference data were all wrapped around 360° to confine all points within [−180°, 180°].

The dynamic range of the polarization calibrator polarization intensity maps was also shown to be improved from $\sim$ 30 to $\sim$ 150 by polarization calibration. Figure 3.19 shows the IQUV maps before and after the full calibration including the leakage calibration.

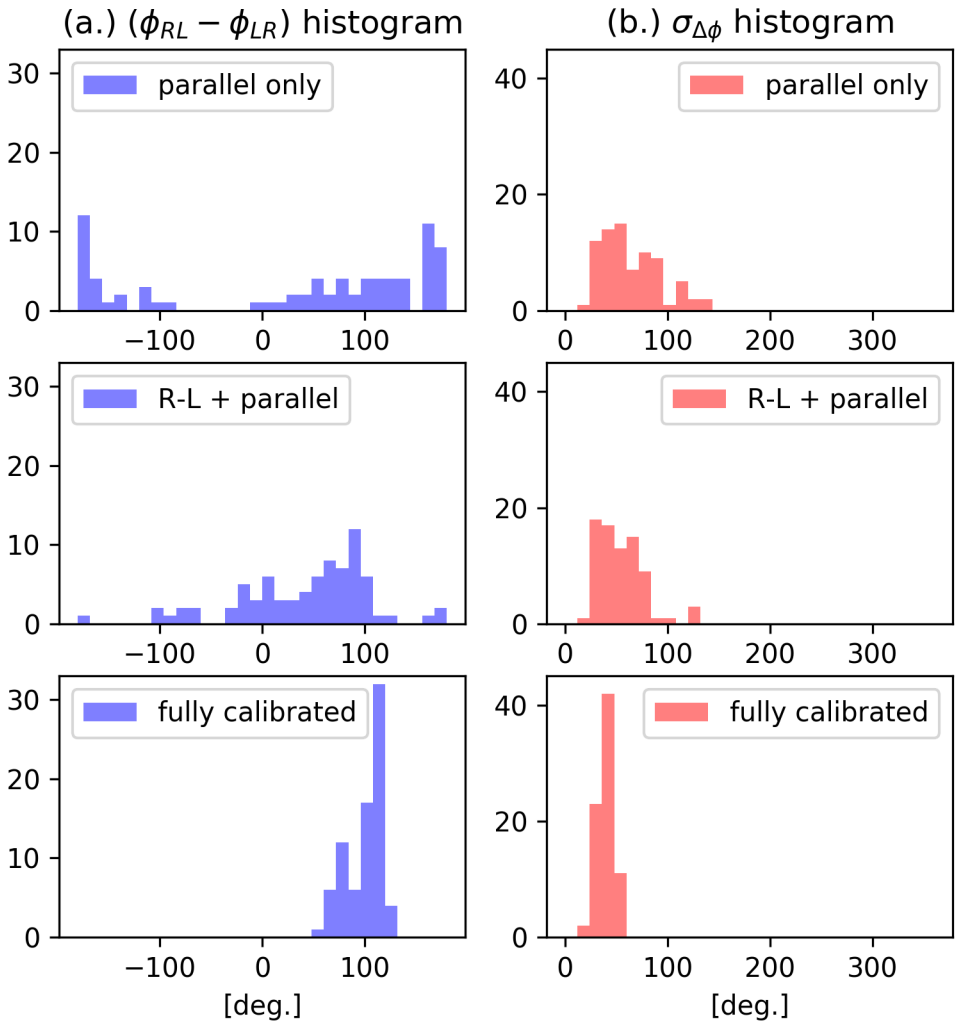

Figure 3.16: Histogram of 3C279 USB: (a)the cross-polarized phase difference ($\phi_{RL} - \phi_{LR}$) and (b) their rms $\sigma_{\Delta\phi}$. The top, middle, and the bottom panels are for different levels of applied calibrations. This plot includes data from all available baselines.

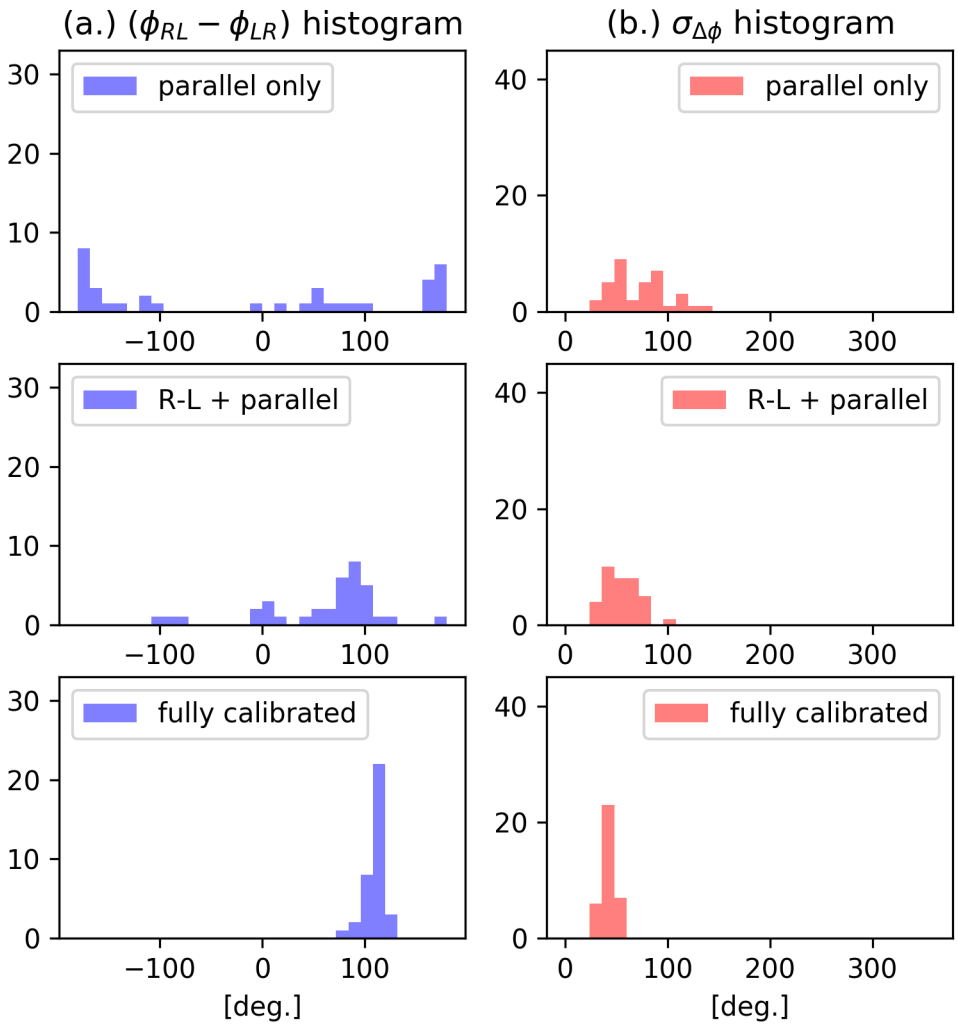

Figure 3.17: Histogram of 3C279 USB: (a)the cross-polarized phase difference ($\phi_{RL} - \phi_{LR}$) and (b) their rms $\sigma_{\Delta\phi}$. The top, middle, and the bottom panels are for different levels of applied calibrations. This plot includes data from all available baselines with only 6.1-m antennas

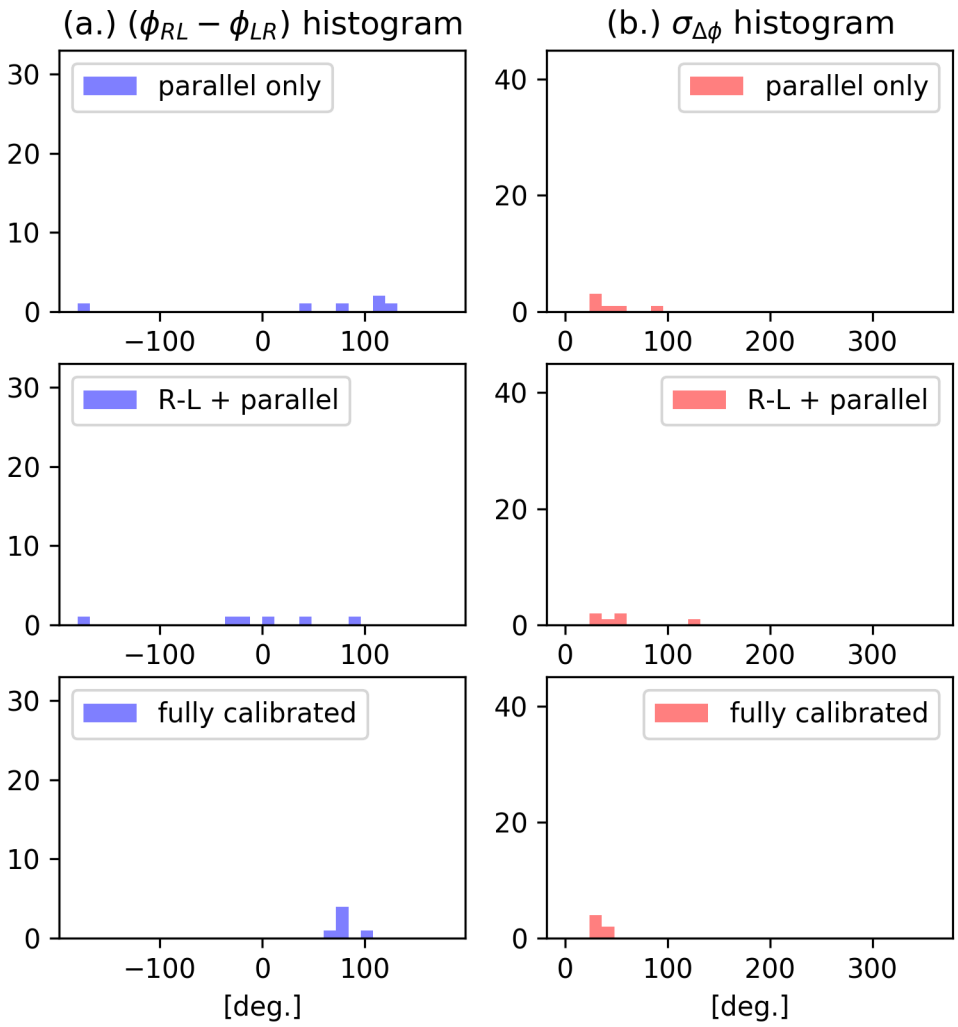

Figure 3.18: Histogram of 3C279 USB: (a)the cross-polarized phase difference ($\phi_{RL} - \phi_{LR}$) and (b) their rms $\sigma_{\Delta\phi}$. The top, middle, and the bottom panels are for different levels of applied calibrations. This plot includes data from all available baselines with only 10.4-m antennas

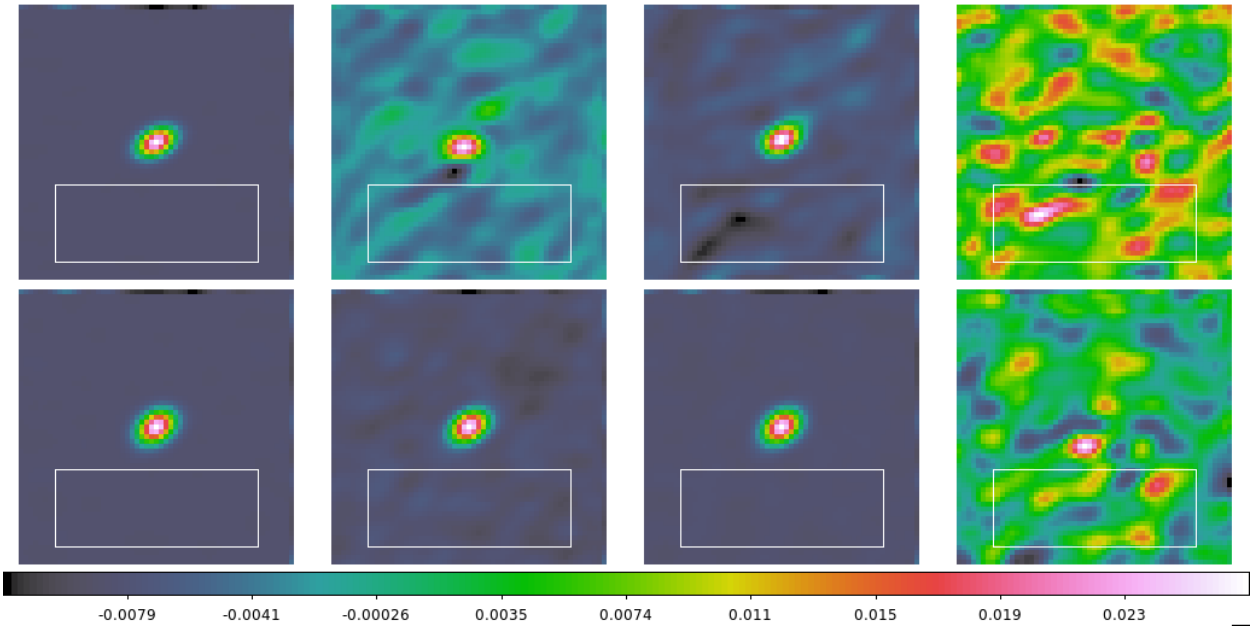

(a) 3C379 LSB IQUV maps before (top panel) and after (bottom panel) the full calibration.

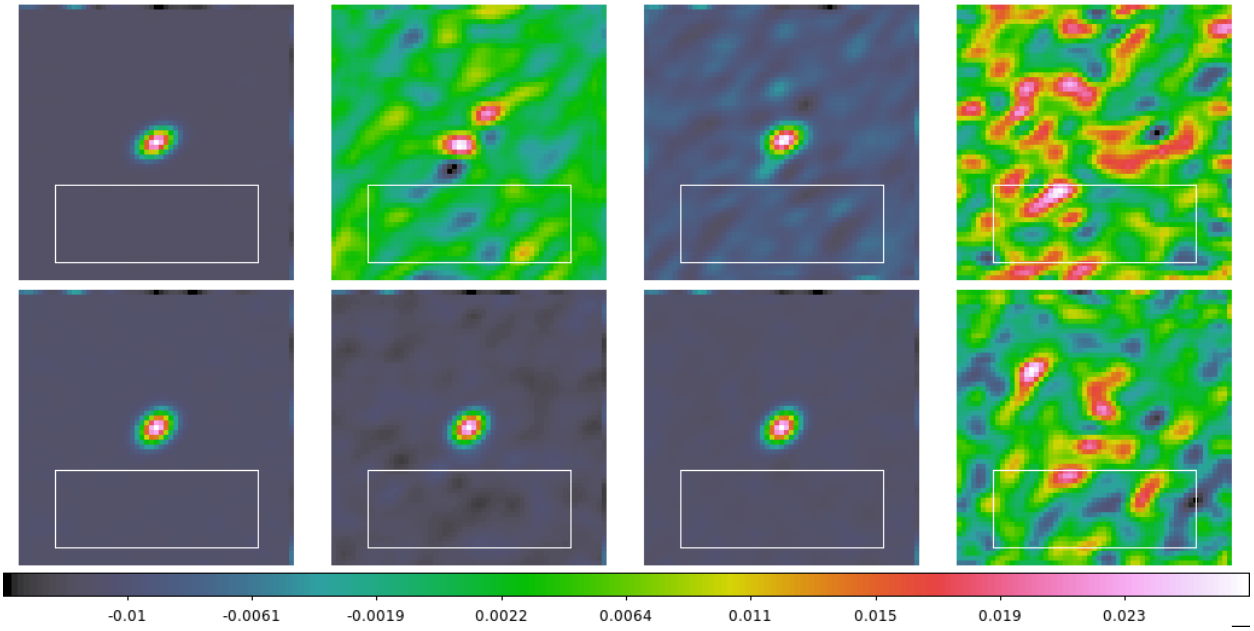

(b) 3C379 USB IQUV maps before (top panel) and after (bottom panel) the full calibration.

Figure 3.19: Map comparison of dynamic range before and after leakage calibration with (a) LSB, and (b) USB data of the calibrator 3C279. The displayed white rectangles are the selected region for calculating the off-source noise.

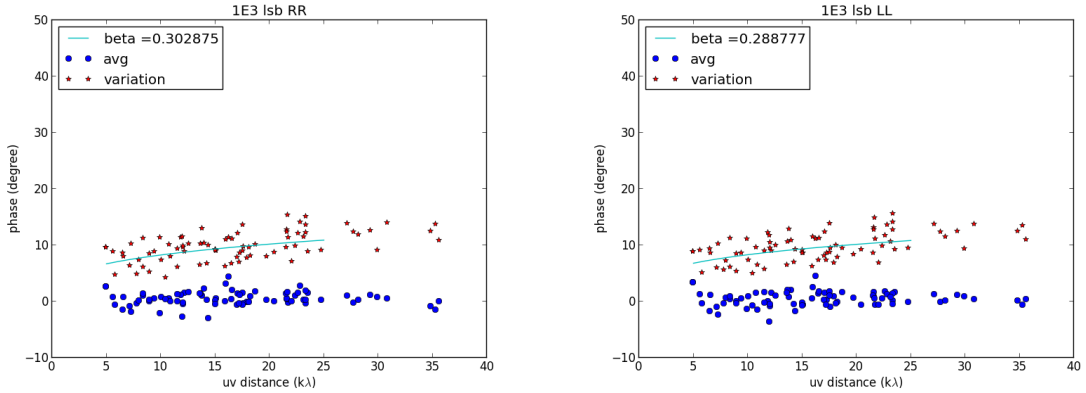

(a) RR (b) LL

Figure 3.20: Phase structure of 3C279 LSB data in RR and LL components. The red asterisks plotted is the rms defined in Equation 3.10. We also fitted the rms with the form: $\sigma_{\phi_{mn}} = \frac{2\pi a d^{\beta}}{\lambda}$ following the Thompson et al. (2017) in characterizing the atmospheric fluctuations (their Equation 13.78a).

The phase structure function of the fully calibrated parallel-hand data of the calibrators in the continuum windows (averaged over frequency) was inspected as well. The fluctuation of the atmosphere can be characterized by the structure function of phase ($\mathcal{D}_{\phi}(d)$) (Thompson et al., 2017):

$$\mathcal{D}_{\phi_{mn}}(d) = \langle[\Phi_{m,t}(x) - \Phi_{n,t}(x-d)]^2\rangle_t \equiv \langle|\Delta\phi_{mn,t}(d)|^2\rangle_t \tag{3.9}$$

where d refers to baseline length, and the $\Phi_{m,t}(x)$ refers to the phase at arbitraty point x. And the rms deviation is:

$$\sigma_{\phi_{mn}} = \sqrt{\mathcal{D}_{\phi_{mn}}(d)} = \sqrt{\langle|\Delta\phi_{mn,t}(d)|^2\rangle_t} \tag{3.10}$$

For 3C279 (calibrator in R Crt observation), after the calibration the residual phase rms σ_{ϕ} is approximately 9.8° and for OJ287 (calibrator in R Leo observation) $\sigma_{\phi} \sim 17.0°$. Both phase structure functions also showed a slow increase of $\sim 10°$ over a uv distance from 5.0 kλ to 40.0 kλ. The compactness of the residual phase distribution is evidence of sufficiently robust phase calibration. In Figure 3.20 and 3.21, the phase structure function and the rms of the function are plotted for 3C279 LSB and USB data.

Hull and Plambeck (2015) list the following sources of systematic error in polarization observations with CARMA: i) the need to de-bias linear polarization measurements (Wardle and Kronberg, 1974), as noted above we correct all linear polarization intensity maps after imaging; ii) limitations due to polarization leakage uncertainties; iii) absolute EVPA angle accuracy; and, iv) direction-dependent polarization across the primary-beam (beam squint and beam squash).

Concerning polarization leakage calibration uncertainties, (Hull and Plambeck, 2015) note that for weakly linearly polarized sources ($m_l \leq 0.5\%$) caution needs to be used regarding the EVPA interpretation. In the current data, the linear polarization level is typically a few percent, which is above this threshold. To verify

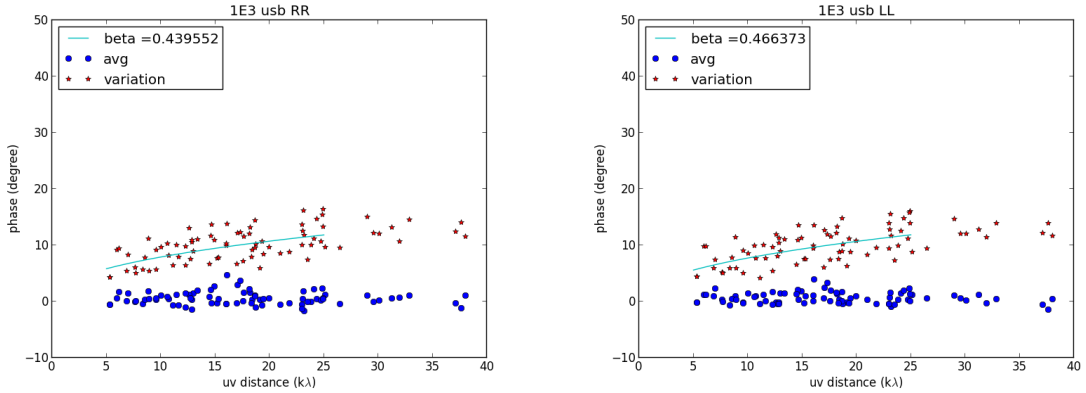

(a) RR (b) LL

Figure 3.21: Phase structure of 3C279 USB data in RR and LL components. The red asterisks plotted is the rms defined in Equation 3.10. We also fitted the rms with the form: $\sigma_{\phi_{mn}} = \frac{2\pi a d^{\beta}}{\lambda}$ following the Thompson et al. (2017) in characterizing the atmospheric fluctuations (their Equation 13.78a).

the accuracy of the absolute EVPA alignment, equivalent to any residual uncorrected R-L phase difference at the reference antenna, we compared the measured EVPA values of the quasar calibrators (3C279, OJ287) in our data against surveys or other observations that are available near our observing dates. Our current data yielded an error-weighted average EVPA measurement for 3C279 of $36.6° \pm 0.07°$ and $33.9° \pm 0.08°$, and for OJ287 of $-16.5° \pm 0.33°$ and $-19.0° \pm 0.40°$, for the LSB and USB continuum spectral windows respectively. As noted above these 500 MHz spectral windows are centered on $\sim$ 215 GHz and $\sim$ 230 GHz respectively. Applicable external EVPA values were obtained from the MOJAVE project (Lister et al. (2009), private communication), the VLBA-BU-BLAZAR program ((Jorstad and Marscher, 2016; Jorstad et al., 2017), private communication), and the POLAMI project[13] (Agudo et al., 2018a,b). We selected external measurements falling within $\pm$14 days from our observations. Available observations were limited, and we considered data within a frequency range of $43.0 \sim 230.5$ GHz. The resulting 14-day averaged EVPA for 3C279 thus obtained is $42.88° \pm 10.83°$, and for OJ287 is $159.85° \pm 11.58°$. As a global reference, we note that when averaging over 1000 days the EVPA value obtained for 3C279 is $135.4° \pm 18.3°$ (MOJAVE) and $151.4° \pm 26.0°$ (VLBA-BU-BLAZAR); for OJ287 this global average over 1000 days is $21.5° \pm 4.4°$ (MOJAVE) and $29.3° \pm 17.7°$ (VLBA-BU-BLAZAR). In summary, our measured EVPA of both OJ287 and 3279 were found to be consistent with the external contemporaneous EVPA measurements in broadly comparable frequency bands. For the primary beam polarization noted in (iv) above, when the source is not on-axis, additional distortions will be introduced across the primary beams of the telescopes (Hull and Plambeck, 2015). Such distortions are characterized by beam squint and beam squash in general. Beam squint is embodied in a double-lobed pattern in Stokes V maps, while beam squash is evident as a cloverleaf pattern in the Stokes Q and U maps (Hull and Plambeck, 2015). Our sources are less than 10" in angular

[13] http://polami.iaa.es

Table 3.2: Summary of the detected molecular lines of R Crt and R Leo in CARMA observation.

Source	Line	ν_0 [GHz]	F_ℓ [Jy beam^{-1} km s^{-1}]	F_I [Jy beam^{-1} km s^{-1}]
R Crt	CO (J = 2-1)	230.538	3.6027	433.88
	SiO (J=5-4, v=1)	215.596	1.3099	27.913
R Leo	CO (J = 2-1)	230.538	2.6156	297.93
	SiO (J=5-4, v=1)	215.596	89.873	492.34

Note: The listed are the rest frequency (ν_0) of the detected molecular lines, the integrated brightness over velocity channels of the linearly polarized intensity (F_ℓ) and total intensity (F_I) in each observation

extent and centered on the optical axis. At $\lambda \sim 1.3$mm wavelength, the FWHM of the primary beam for the CARMA 10-m antennas is ~ 30", and for the 6-m antennas it is ~ 56" (Hull and Plambeck, 2015). Our $10''$ source extent is therefore well within the inner primary beam and we therefore do not expect strong primary beam polarization effects. We find no evidence of a quadrupolar squash pattern in the Stokes Q or U images in the current data. We expect our quasar calibrators to have negligible intrinsic circular polarization (Rybicki and Lightman, 1979). This internal astrophysical consistency check yields a residual Stokes V signal in our calibrators of $m_c \sim 0.32\%$ for 3C279 (in the R Crt observing run), and $m_c \sim 0.77\%$ for OJ287 (in the R Leo observing run) after full calibration. These values define the limits on our intrinsic polarization accuracy but also similarly limit the magnitude of the beam squint effect.

3.4 Results

In Table 3.2, the rest frequency ν_0, integrated brightness over velocity channels of the linear polarization (F_ℓ) and the total intensity (F_I) of the detected molecular lines are listed for both R Crt and R Leo. The integrated spectra of the emission from the $J = 2 - 1$ CO and $v = 1, J = 5 - 4$ SiO transitions are shown in Figure 3.22. These spectra were obtained by summing all total intensity points above 3σ in each image plane per velocity channel of the interferometric image cubes using `MIRIAD` task `imspec`.

We detect continuum emission toward R Crt of 14.9 ± 2.4 mJy/beam in the LSB continuum spectral window and 18.3 ± 2.9 mJy/beam in the counterpart USB window. The provided uncertainties are statistical errors from the off-source image region and do not include any systematic errors in the absolute flux density calibration. These values are measured at the peak-brightness pixel and the error is the off-source rms noise. In the same spectral windows, continuum emission is detected toward R Leo of 118.2 ± 3.2 mJy/beam in LSB and 123.0 ± 3.4 mJy/beam in USB using the same measurement methodology. No continuum polarization was detected toward either R Crt or R Leo, likely due to sensitivity limitations and the expected weakness of the dust continuum emission relative to the underlying stellar continuum. By comparison with the stellar continuum flux densities reported by Vlemmings et al. (2019) for R Leo, the dust contribution does not exceed $\sim 20\%$; a comparable result is expected for R Crt.

The maximum detected linear polarization intensity ($\mathrm{P_p}$), the peak total intensity at the associated pixel and velocity channel ($\mathrm{I_p}$) in molecular lines, and the derived peak fractional linear polarization ($\mathrm{m_{\ell,p}}$) and the error-weighted polarization angle (χ_{wav}, or $\bar{\chi}$) are summarized in Table 3.3 for both sources. This table also enumerates the detection of linearly-polarized $v = 1,\ J = 5 - 4$ SiO maser emission toward R Leo and R Crt, and circularly-polarized SiO maser emission toward R Leo. The observed linearly polarized intensity maps for the $J = 2 - 1$ CO emission toward both sources are displayed as contours in Figure 3.23 overlaid on color plots of the total intensity in the molecular line emission. Analogous maps of the linearly-polarized and total intensity emission in the $v = 1, J = 5 - 4$ SiO molecular line are shown in Figure 3.24.

The measured EVPA for R Crt in the $J = 2 - 1$ CO maps ranges from 38.0° to -19.8° over the angular and frequency extent of the source with an error-weighted average $\chi_{wav} = 7.6^\circ$, as cited in Table 3.3 as the representative value for the field; in the $v = 1, J = 5 - 4$ SiO maps the EVPA ranges from 49.5° to -34.2° with $\chi_{wav} = -15.4^\circ$. For R Leo in the $J = 2 - 1$ CO emission the EVPA ranges from -65.4° to -86.6° with $\chi_{wav} = -77.7^\circ$; in the $v = 1,\ J = 5 - 4$ SiO maps the EVPA ranges from 89.7° to -88.6° with $\chi_{wav} = -1.1^\circ$. These average values are taken from point detections with statistical significance exceeding 4σ, and the samples generally cover a velocity width $\Delta v = 2.0 \sim 4.0$ km/s and extend over physical scales of ~ 10 arcseconds on the plane of the sky.

We estimated both the random error (σ_{wav}) and the systematic error (σ_{sys}) in the measured EVPA values. Each measured EVPA is assigned a statistical uncertainty as follows (Wardle and Kronberg, 1974):

$$\sigma_\chi \simeq \frac{1}{2} \times (\frac{\sigma_P}{P}) \times \frac{180^\circ}{\pi} \tag{3.11}$$

and this error is propagated through error-weighted averaging as (Taylor, 1996):

$$\sigma_{wav} = \frac{1}{\sqrt{\sum_i \left(\frac{1}{\sigma^2_{\chi_i}}\right)}} \tag{3.12}$$

This is based on the assumption that each EVPA χ_i is randomly sampled from a normal distribution with standard deviation σ_{χ_i}. The estimated random errors after error-weighted averaging for R Crt are $\sigma_{wav} = 1.0^\circ$ in the $J = 2 - 1$ CO maps and $\sigma_{wav} = 0.7^\circ$ in the $J = 5 - 4, v = 1$ SiO maps. For R Leo $\sigma_{wav} = 1.7^\circ$ in the $J = 2 - 1$ CO maps and $\sigma_{wav} = 0.03^\circ$ in the $v = 1, J = 5 - 4$ SiO maps. We adopted the uncertainty from the absolute EVPA alignment (see Section 3.3) of the quasar calibrators against external measurements as a conservative estimate of the systematic error (σ_{sys}). Based on the alignment for 3C279, the systematic error of EVPA for R Crt is estimated as 10.8°; from OJ287 alignment the systematic error of EVPA for R Leo is estimated as 11.6°. The statistical and systematic errors in EVPA are included in Table 3.3.

Table 3.4 lists the peak-pixel circularly-polarized intensity V_p in the $v = 1, J = 5 - 4$ SiO spectral-line image cube (Figure 3.24) and associated LSR velocity v_{LSR}, point total intensity I_p and resulting degree of

fractional circular polarization $m_{c,p}$ at V_p; circular polarization is only detected toward R Leo.

Table 3.3: Polarization properties at the position of peak linearly-polarized intensity in the spectral-line image cubes.

Source	Line	v_{LSR} [km s^{-1}]	P_p [Jy beam^{-1}]	I_p [Jy beam^{-1}]	$m_{\ell,p}$ [%]	$\bar{\chi}$ [°]
R Crt	SiO (J=5-4, v=1)	12.0	0.778	4.52	17.2 (17.3 σ)	-15.4
	σ		0.045	0.05	–	$\pm 0.7 \pm 10.8$
	CO (J = 2-1)	20.0	0.361	11.44	3.13 (7.2 σ)	7.6
	σ		0.050	0.27	–	$\pm 1.0 \pm 10.8$
R Leo	SiO (J=5-4, v=1)	-4.0	18.67	53.98	34.6 (317 σ)	-1.1
	σ		0.06	0.17	–	$\pm 0.03 \pm 11.6$
	CO (J = 2-1)	4.0	0.375	3.86	9.71 (6.1σ)	-77.7
	σ		0.062	0.14	–	$\pm 1.7 \pm 11.6$

Table 3.4: Polarization properties at the position of peak circularly-polarized intensity in the spectral-line image cubes.

Source	Line	v_{LSR} [km s^{-1}]	V_p [Jy beam^{-1}]	I_p [Jy beam^{-1}]	$m_{c,p}$ [%]
R Crt	SiO (J=5-4, v=1)	–	–	–	–
	σ	–	–	–	–
R Leo	SiO (J=5-4, v=1)	-3.0	2.95	51.34	5.7 (40.3 σ)
	σ		0.07	0.17	–

The final part of this Section will consider comparisons between the G-K signal, SiO maser polarization, and further source properties in the literature.

3.5 G-K Modeling Analysis and Discussion

3.5.1 CSE Modeling

Previously it was highlighted that the principal advantage of using the G-K effect to study the magnetic field surrounding AGB stars is based on the different depths sampled by different molecular transitions in the CSE; this is the result of both chemical abundance stratification for these molecules and radiative excitation effects. The CO molecule is generally expected to be found from radii near the stellar surface ($\sim 1R_*$) to the outer edge of the circumstellar envelope ($\gtrsim 10^4 R_*$) (Höfner and Olofsson, 2018). Its fractional abundance $X_{CO} = \left(\frac{n_{CO}}{n_{H_2}}\right)$ through the entire circumstellar envelope is thought to remain roughly constant (Duari et al., 1999; Decin et al., 2010) until it reaches the photo-dissociation radius. The CO envelope therefore covers a very extended CSE region and accordingly a diverse set of physical and chemical environments. In contrast, SiO is prone to depletion in the inner CSE including due to adsorption onto dust grains (Teyssier et al., 2006; Decin et al., 2010; Gail and Sedlmayr, 2013a; Gobrecht et al., 2016). SiO density declines within $\sim 10^2 R_*$ and has an outer photodissociation radius well within CO (Decin et al., 2010; Khouri et al., 2014). CO and

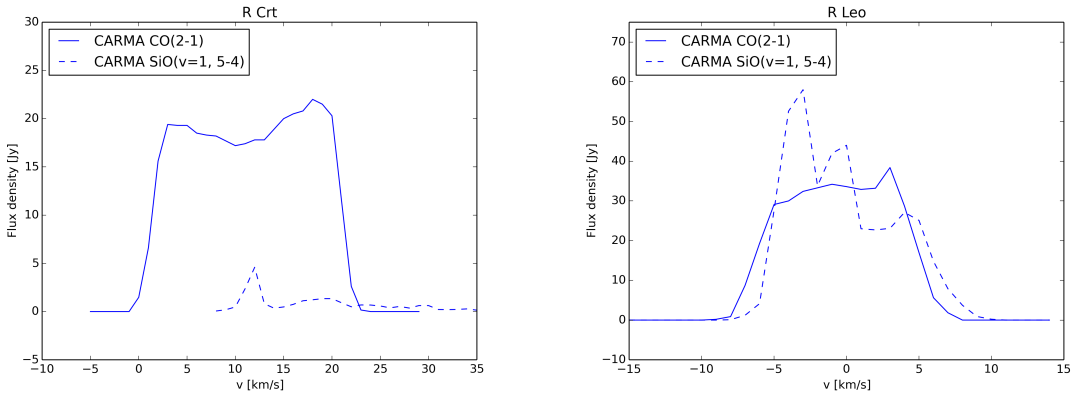

(a) R Crt (b) R Leo

Figure 3.22: Integrated spectra for both (a) R Crt and (b) R Leo. The spectra were obtained by summing the total intensity at all points above 3σ in each image plane of the interferometric image cube using `MIRIAD` task `imspec`. The spectra are binned at a $\triangle v = 1$km/s interval.

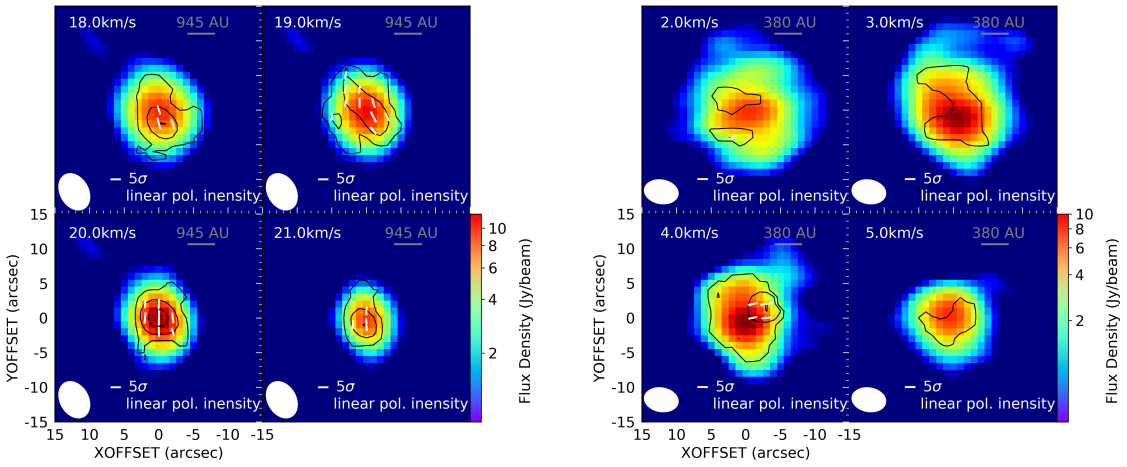

(a) R Crt (b) R Leo

Figure 3.23: CO(2-1) spectral-line polarization maps of (a) R Crt, and (b) R Leo. The channels are averaged over interval of 1 km s^{-1}. The color map shows the spectral-line emission total intensity in log scale, and the contour levels of the linear polarization intensity are 4, 5, 6, and 7 times σ where σ is the noise level of each source. The white segments indicates the polarization angle and the scaled length represents the strength of linear polarization. Beam size is also displayed at the lower-left corner in each map.

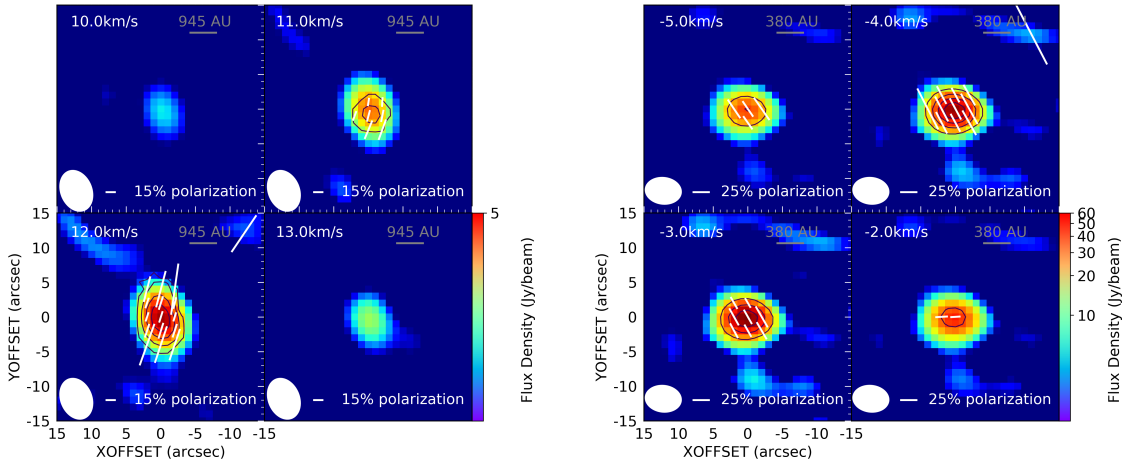

(a) R Crt

(b) R Leo

Figure 3.24: SiO(5-4, v=1) spectral-line polarization maps of (a) R Crt, and (b) R Leo. Again the channels are averaged over 1 km s^{-1} interval. The color corresponds to total intensity of the emission in log scale, contour levels as the linear polarization intensity from 20%, 40%, 60%, and 80% of the maximum, and white segments as the polarization angle with the scaled length as display of the linear polarization strength.

SiO are thus sensitive to different scales in the CSE.

Our G-K model requires as input radial CSE profiles in temperature $T(r)$ and density $n(r)$ in addition to a characterization of radiation anisotropy and velocity gradient structure. Detailed modeling of the kinematics, dynamics, and chemical structure in the CSE requires numerical approaches (Bowen, 1988; Humphreys et al., 1996; Ireland et al., 2008, 2011) given the inherent complexity of pulsation shock structure and mass loss in this region, amongst other fine-scale physical processes. However, the input temperature, density, and velocity profiles required for our G-K modeling can be adequately derived using a semi-analytic model for the CSE as described below, and we adopt that approach here. Our specific target is to model the G-K effect in CO emission, as observed in the current work.

Temperature profile

Power-law temperature profile Following (Bowen, 1988) as cited by Cherchneff et al. (1992), the kinetic temperature dependence on radius is approximated as a power-law:

$$\frac{T(r)}{T(R_*)} = \left(\frac{r}{R_*}\right)^{-\alpha} \tag{3.13}$$

where the exponent index, α, is often adopted to be 0.6 (Cherchneff et al., 1992; Decin et al., 2010; Gobrecht et al., 2016). The functional form of this relation can be derived from the assumption of a gray stellar atmosphere (Bowen, 1988). For R Leo, the effective stellar blackbody equilibrium temperature T_* is esti-

mated from modeling of the spectral energy distribution (SED) to be $T_* = 1.8 \times 10^3 K$ (Schöier et al., 2013; Danilovich et al., 2015). We adopt an inner dust condensation radius $R_c \sim 1.6 \times 10^{14}$ cm from SED modeling (Danilovich et al., 2015). These parameters predict a thermal temperature at the dust-condensation radius $T(R_c) \sim 5.3 \times 10^2 K$.

Density profile

Semi-analytic CSE solutions exist for the approximate conditions applicable within broad radial zones in the CSE. For this reason we consider the CSE to consist of an inner region, extending from the photosphere to the dust formation radius R_c, and an intermediate-outer CSE region extending beyond R_c to the outer edge of the photodissociation zone. Both regions are modeled here to establish continuity in the density relation.

I. Inner CSE The inner CSE includes the shock formation radius R_0 (Hill and Willson, 1979). (Cherchneff et al., 1992) have derived a radial density profile $n(r)$ in the shock-extended region by considering averaged physical quantities in the momentum equation, including average flow velocity $v = \gamma v_{esc}$ and average dynamical scale height $H(r)$ (Willson and Bowen, 1986), in conjunction with the radial temperature profile in Equation 3.13. Here v_{esc} is the escape velocity and $\gamma = \frac{\triangle v}{v_{esc}}$, where $\triangle v$ is the shock amplitude (Cherchneff et al., 1992). The resulting density profile of the inner CSE is (Cherchneff et al., 1992):

$$\frac{n(r)}{n(R_0)} = e^{\left\{ \frac{-R_0(1-\gamma^2)}{H_0(R_0)(1-\alpha)} \left[1 - \left(\frac{r}{R_0} \right)^{\alpha - 1} \right] \right\}} \quad , \qquad R_0 \leq r \leq R_c. \tag{3.14}$$

where $H_0(R_0)$ is the static scale height in the stellar photosphere. (Cherchneff et al., 1992) fit a power law to the numerical CSE model results for $\gamma = \frac{\triangle v}{v_{esc}} = f(P, M_*, R_*, r)$ presented by Willson and Bowen (1986) where P is the pulsation period (days), M_* is the stellar mass, and R_* is the photospheric radius. This allows the derivation of an approximate expression for the shock formation radius R_0 in the form (Cherchneff et al., 1992):

$$R_0 = R_* \left[\frac{8.24 P^{0.82}}{(\Delta v / v_{esc})} \left(\frac{M_*}{M_\odot} \right)^{0.41} \left(\frac{R_\odot}{R_*} \right)^{1.23} \right]^{0.81} \tag{3.15}$$

The radius R_0 is expected to be of the same order as one stellar radius. For R Leo, $R_0 \simeq \left[0.75 \times \left(\frac{\triangle v}{v_{esc}} \right)^{-0.81} \right] \times R_*$, therefore $R_0 \sim R_*$.

II. Intermediate-outer CSE In this region, the velocity is often fitted by the classical β-law (Lamers and Cassinelli, 1999b; Danilovich et al., 2015):

$$v_\beta(r) = v_c + (v_\infty - v_c) \times \left[1 - (\frac{R_c}{r}) \right]^\beta \tag{3.16}$$

We use this relation combined with mass continuity to derive a density profile for the intermediate-outer CSE region. From Equation 3.16:

$$\frac{dv_\beta}{dr} = \frac{\beta}{r}\left[v_c + (v_\infty - v_c)\left(1 - \frac{R_c}{r}\right)^{\beta-1} - v_c - (v_\infty - v_c)\left(1 - \frac{R_c}{r}\right)^{\beta}\right] \equiv \frac{\beta}{r}[v_{\beta-1} - v_\beta] \tag{3.17}$$

where R_c is the dust condensation radius defined above and v_c is the expansion velocity at R_c. Typically $v_c \sim 3$ km/s based on the approximate sound speed at this radius (Danilovich et al., 2015). The terminal expansion velocity v_∞ can be assumed constant for individual stars, e.g. $v_\infty \sim 8.5$ km/s for R Leo and $v_\infty \sim 12.0$ km/s for R Crt in CO emission (Danilovich et al., 2015). Exponent $\beta \geq 0$ is the profile index; we adopt a range $\beta = 0 \sim 5$ (Danilovich et al., 2015). Note that $\beta = 0$ is equivalent to a constant and isotropic outflow.

By continuity in the equation of mass,

$$\frac{\partial \rho}{\partial t} + (\vec{v} \cdot \vec{\nabla})\rho + \rho \vec{\nabla} \cdot \vec{v} = 0 \tag{3.18}$$

which yields,

$$\frac{d\rho}{dr} + \frac{\rho}{r}\left[(2 - \beta) + \beta \cdot \frac{v_{\beta-1}}{v_\beta}\right] = 0 \tag{3.19}$$

with the quasi-static state and zeroth-order approximation $\vec{v} = v\hat{r}$ assumed.

We used the SciPy[14] package `odeint` to solve the differential equation in Equation 3.19 applying a boundary condition of continuity across the inner-region boundary $r = R_c$ to derive the density profile $n(r)$ in this region. We model the CSE of R Leo in this manner, adopting parameters: $R_* = 1.4$ AU (De Beck et al., 2010), $T_* = 1800$ K, (Schöier et al., 2013), $R_c = 10.7$ AU (Danilovich et al., 2015), $v_\infty = 8.5$ km/s (Danilovich et al., 2015), and $\dot{M} = 1.1 \times 10^{-7} M_\odot$/yr (Danilovich et al., 2015). Photospheric temperature estimates in the literature fall in the ranges $T_* \sim 1800 - 2100$ K (Schöier et al., 2013; Ramstedt and Olofsson, 2014; González Delgado et al., 2003) and $T_* \sim 2850 - 2890$ K (De Beck et al., 2010; Vlemmings et al., 2019).

The continuity condition across the boundary was enforced by estimating the number density at the dust condensation radius as $n(R_c) = \frac{\dot{M}}{4\pi R_c^2 v_c}$ and assuming a photospheric density 10^{14} cm^{-3} (Gobrecht et al., 2016). This is a re-parametrization that avoids computing uncertain parameters in Equation 3.14.

As described above, the scientific goal of the semi-analytic CSE models is to produce temperature and density as input to the G-K modeling. The semi-analytic CSE models do not include modeling of spectral line excitation or emission. The derived profiles in velocity, density, and temperature are displayed in Figure 3.25. The derived CSE parameter sets (temperature T(r) and H_2 number density n(r) profiles) solved for here and used as input to the G-K model are summarized in Table 3.5. For the G-K modeling, we assume that we lie within the CO photodissociation radius. In the G-K modeling, the general H_2 density defines

[14] https://www.scipy.org

the collisional partner for CO but we are not highly sensitive to the exact CO abundance ratio assumed.

As noted above, the semi-analytic CSE models do not include spectral line excitation or emission. However, an important coupling exists between the adopted mass-loss rate and CO outflow kinematics and the predicted CO emission intensity. To test this consistency we examine recent modeling initiatives of the CO emission intensity toward R Leo, as listed in Table 3.6, where each model was previously used in the literature to estimate the mass-loss rate $\dot{M}$. Each model in this Table is described by the outflow velocity v_c at the dust condensation radius, the terminal CO expansion velocity v_∞, the β velocity exponent in Equation 3.16, and the estimated mass-loss rate $\dot{M}$. We have used our numerical CSE model to derive density profiles $n_k(r)$ for each set k of CO emission model parameters in Table 3.6. The resultant minima and maxima in the density profiles $n_k(r)$ at the radii sampled in Table 3.5 and across the CO emission model sets k are summarized in Table 3.7. These density ranges are consistent with the range in densities produced by our semi-analytic CSE model for R Leo in Table 3.5 under the input parameters described earlier. We therefore consider the densities produced by our model to be conservative but reasonable estimates within the uncertainty that exists regarding the mass-loss rate.

Table 3.5: The radial profiles in temperature $T(r)$, density $n(r)$, and velocity (as represented by parameter β in Equation 3.16), generated from the CSE analytic models. Note: (a) The density $n(r)$ is shown as a minimum and maximum range across the set of integer values of $\beta \in \{0, 1, .., 5\}$ enumerated.

Source	r	T	n(r)^a	β
	$[R_*]$	[K]	[cm^{-3}]	
R Leo	567.1	40	$[1.38 \times 10^3, 3.88 \times 10^3]$	$\{0, 1, .., 5\}$
	392.9	50	$[2.90 \times 10^3, 8.11 \times 10^3]$	$\{0, 1, .., 5\}$
	289.0	60	$[5.39 \times 10^3, 1.50 \times 10^4]$	$\{0, 1, .., 5\}$
	123.2	100	$[2.99 \times 10^4, 8.13 \times 10^4]$	$\{0, 1, .., 5\}$
	19.9	300	$[1.50 \times 10^6, 3.19 \times 10^6]$	$\{0, 1, .., 5\}$

Table 3.6: CO emission models for R Leo.

v_c	v_∞	β	$\dot{M}$	Reference
[km/s]	[km/s]		[$10^{-7} M_\odot$/yr]	
3.0	8.5	5.0	1.1	(Danilovich et al., 2015)
-	5.0	0	1.8	(Schöier et al., 2013)
-	6.0	0	1.0	(Ramstedt and Olofsson, 2014)
-	6.0	0	2.0	(González Delgado et al., 2003)
-	6.0	0	1.2	(Teyssier et al., 2006)
-	9.0	0	0.92	(De Beck et al., 2010)

3.5.2 G-K modeling

As shown in Table 3.3, the peak fractional linear polarizations for the $J = 2 - 1$ CO line emission are $m_l = 3.13\%$ and $m_l = 9.7\%$ for R Crt and R Leo respectively. Detailed modeling is necessary in order to determine if this linear polarization in the thermal $J = 2 - 1$ CO emission arises from the G-K effect and the

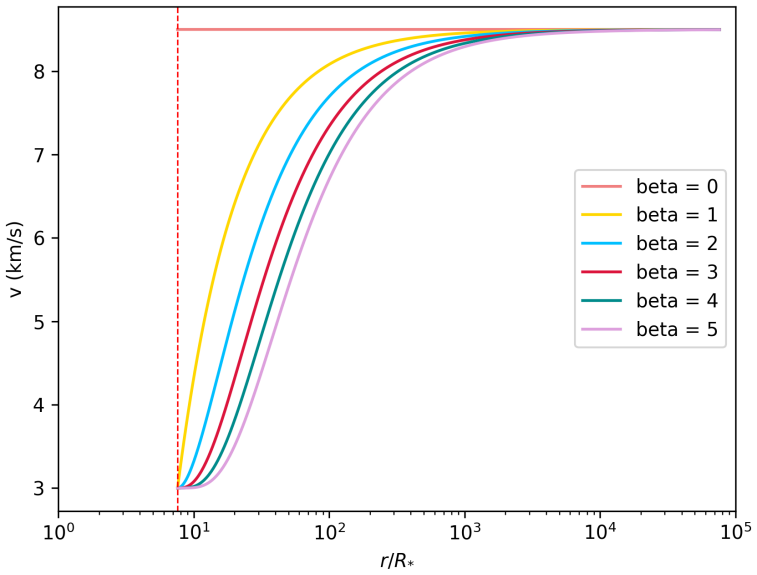

(a) Velocity profile for the range $\beta = 0 \sim 5$ and based on the adopted physical parameters of R Leo.

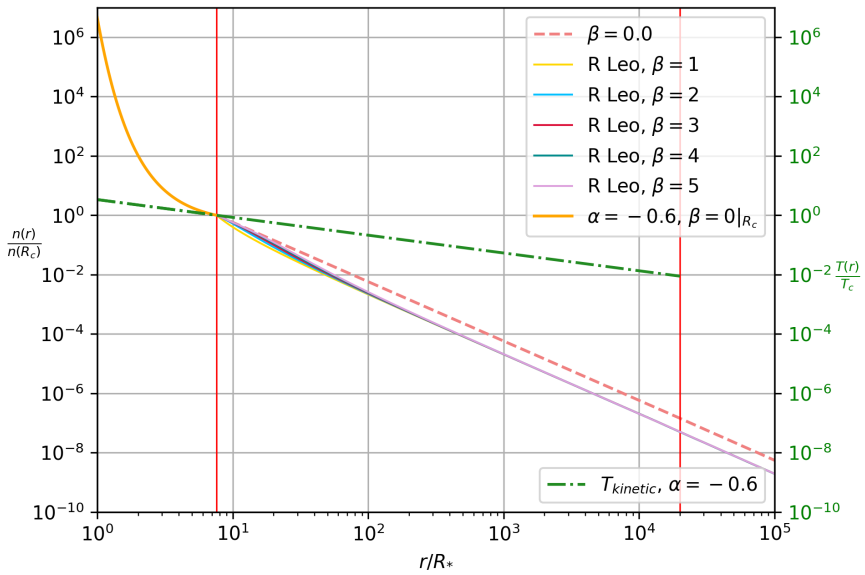

(b) Density and temperature profiles based on the listed physical parameters of R Leo. The left vertical axis labels the normalized number density, $\frac{n(r)}{n(R_c)}$. The vertical axis on the right marks the scale for the normalized temperature profile $\frac{T(r)}{T_c}$. The green dash-dotted line portrays the calculated temperature profile. The red dashed line is the density profile for a model with $\beta = 0$ and $v_\infty = 3.0$ km/s. The remaining density profile lines overlap significantly at larger $\frac{r}{R_*}$ and include models with $\beta \neq 0, v_c = 3.0$ km/s, $v_\infty = 8.5$ km/s.

Figure 3.25: CSE parameters as G-K modeling input.

Table 3.7: Minima and maxima in the radial density profiles $n_k(r)$ across the CO emission models tabulated in Table 3.6 sampled at or very near the radii listed in Table 3.5.

Source	r $[R_*]$	T [K]	$n_{\min}(r)$ $[\mathrm{cm}^{-3}]$	$n_{\max}(r)$ $[\mathrm{cm}^{-3}]$
R Leo	567.1	40	1.75×10^3	3.82×10^3
	392.9	50	3.72×10^3	7.95×10^3
	289.0	60	6.74×10^3	1.47×10^4
	123.2	100	3.71×10^4	8.09×10^4
	19.9	300	1.45×10^6	3.11×10^6

associated underlying magnetic field geometry, which has been shown in Section 3.5.1. The detailed G-K modeling will be described, and modeled results will be presented.

Framework

We use the G-K modeling framework developed independently by Yang and Lai (2010). The differences between the numerical code and prior approaches is described briefly here. Original work by Goldreich and Kylafis (1981, 1982) and Kylafis (1983a) considered 1-D and 2-D LVG geometries, a $J = 1 - 0$ transition, and a collisional rate C to Einstein coefficient $A_{a,b}$ ratio of $\frac{C}{A_{a,b}} = 0.212$. Deguchi and Watson (1984) extended these calculations to multi-level transitions in CO, CS, and SiO using molecular data from Green and Chapman (1978) and Robinson and van Blerkom (1981). Cortes et al. (2005) moved further to include the influence of anisotropic radiation, a mixture of 1-D and 2-D LVG geometries, and updated molecular data from Flower (2001). The G-K numerical work by Cortes et al. (2005) was motivated by their observational results of polarized emission in the CO $J = 1 - 0$ line taken jointly with observations of polarized CO $J = 2 - 1$ emission by Lai et al. (2003). In combination these observations indicated orthogonal linearly-polarized CO emission electric vector position angles in different rotational (J) transitions. Yang and Lai (2010) developed an independent G-K numerical model incorporating these prior physical approaches, but excluding anisotropic radiation, and similarly focused on star formation. The code uses updated molecular data from the Leiden Atomic and Molecular Database (LAMDA) Schöier et al. (2005). Results from the Yang and Lai (2010) code have been checked qualitatively for consistency against published results by Goldreich and Kylafis (1981), Deguchi and Watson (1984), and Cortes et al. (2005) over a range of physical conditions and LVG geometries.

In the current work the (Yang and Lai, 2010) G-K code was applied in a CSE environment and a source of radiative anisotropy was introduced to model emission from the central AGB star. Representative densities and temperatures for the CSE, as tabulated in Table 3.5, differ from those in star-forming regions described above.

The model used here considers a uniform magnetic field and uniform velocity gradient through the slab of material with constant thickness and density, as a first-order approximation. As noted above, we allow for anisotropic radiation from the central star; this effect is not dominant however and is discussed further

at the end of Section 3.5.2.

As mentioned in Section 1.3.3, the two main sets of equations involved in the G-K model are: i) the radiative transfer equation; and, ii) the population rate equation of rotational states. The radiative transfer equation for the specific intensity of a source with polarization either perpendicular or parallel to the magnetic field, following (Goldreich and Kylafis, 1981; Cortes et al., 2005; Yang and Lai, 2010) is given by:

$$\frac{dI^q_{JJ'}}{d\tau^q_{JJ'}} = -\phi(\nu)(I^q_{JJ'} - S^q_{JJ'}), \qquad q = \perp \; or \; \parallel$$

where I is the line intensity, S is the source function, τ is the optical depth, and $\phi(\nu)$ is the line profile. The labeling $q = \perp \; or \; \parallel$ denotes the source with polarization either perpendicular or parallel to the magnetic field. The labeling JJ' refers to the transition from state J to J'. The rate equation specifying the rate of change of the number density of particles populating state $i = (J, M)$, through radiative and collisional population exchange with state $j = (J', M')$, following (Deguchi and Watson, 1984; Cortes et al., 2005; Yang and Lai, 2010) is given by:

$$0 = \frac{dn_i}{dt} = -\sum_{J>J'} P_{ij} + \sum_{J<J'} P_{ji} + \sum_j (C_{ji} n_j - C_{ij} n_i)$$

n_i is the population density at state i. The radiative transition rate P_{ij} includes spontaneous emission, absorption, and stimulated emission, and C_{ij} denotes the collision rate. Note that steady state is assumed, thus $\frac{dn_i}{dt} = 0$ (Deguchi and Watson, 1984; Cortes et al., 2005; Yang and Lai, 2010). In terms of absorption and stimulated emission, this means the rate equation is dependent on the radiation intensity, $I^q_{JJ'}$, specifically the integral of the intensity over frequency and over solid angle. The combination of the radiative transfer equation and the rate equation constitutes a coupled nonlinear system that we need to solve through numerical iteration.

The large velocity gradient (LVG) approximation (Sobolev, 1960) was used to simplify the equations and their solution. In our G-K model, the following three types of velocity gradient geometry are implemented: i) 1-D velocity anisotropy parallel to the magnetic field; ii) a 2-D velocity gradient along the 2-D plane perpendicular to the magnetic field; and, iii) a mixed model of (i) and (ii), yielding a cone-shaped velocity gradient lobe. We used model (iii) to model bipolar outflows. A repeated schematic plot (first shown in Chapter 1) of the velocity gradient geometries is provided in Figure 3.26.

Adapted for the nomenclature used in this paper, the final calculated fractional polarization is written as (Deguchi and Watson, 1984; Cortes et al., 2005; Yang and Lai, 2010):

$$m_\ell = \frac{I_\perp - I_\parallel}{I_\perp + I_\parallel}$$

where $I_\perp$ and $I_\parallel$ are the emergent specific intensity perpendicular and parallel to the magnetic fields.

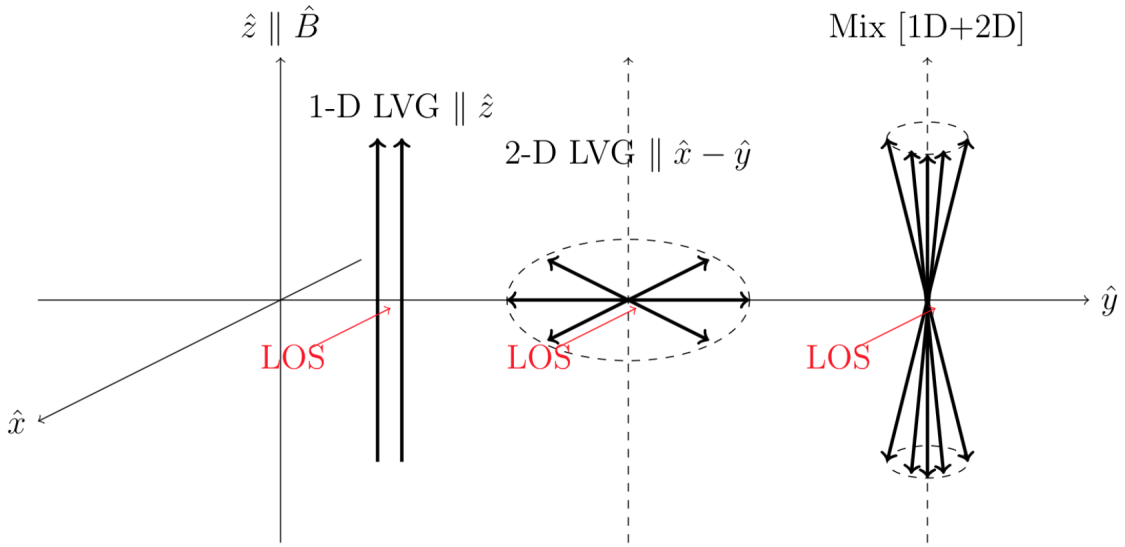

Figure 3.26: The schematic plot for three types of velocity gradient geometry as implemented in our existing G-K model (from left to right): i) 1-D velocity anisotropy parallel the magnetic field; ii) a 2-D velocity gradient along the 2-D plane perpendicular to the magnetic field; and, iii) a mixed model of (i) and (ii), yielding a cone-shaped velocity gradient lobe. This schematic plot is adapted from Yang and Lai (2010). The "LOS" label in red denotes the line-of-sight direction. The magnetic field orientation $\hat{B}$ is set to be aligned with the z-axis, i.e. $\hat{z} \parallel \hat{B}$. And the black arrows in the plot point in the direction of the velocity gradient field. In our model we have adopted the mixed LVG velocity gradient geometry on the basis that of the three velocity gradient geometries, this model is closest to the modest axisymmetry that could reasonably be expected in the late AGB phase. This is a repeated plot as we have shown it earlier in Chapter 1.

Observed linear polarization and the G-K model predictions

For the CSE parameters listed in Table 3.5, the predicted fractional linear polarization generated by the G-K model levels are shown as a function of optical depth, temperature, and density in Figure 3.27. The primary independent variable in this Figure is optical depth; different temperatures and densities are plotted representing various effective distances from the central stars. The two styles of lines denote the conditions derived from the lower and upper bound of the density profile from the exponent range $\beta \in [0, 5]$. In the model, the sign of the predicted fractional linear polarization refers to the direction of the EVPA relative to the magnetic field. This includes the case that the EVPA is perpendicular (positive sign) or parallel (negative sign) to the magnetic field lines. The inferred EVPA from our G-K model is therefore parallel to the local magnetic field. Accordingly, the displayed EVPA in Figure 3.23 must therefore be aligned with the local magnetic field. In our model, we have adopted the mixed LVG velocity gradient geometry (as shown in Figure 3.26) on the basis that of the three velocity gradient geometries, this model is closest to the modest axisymmetry that could reasonably be expected in the late AGB phase. A comparative study of the effect on the G-K profile of changing velocity gradient geometry at a fixed representative temperature and density is shown in Figure 3.28.

The predicted fractional linear polarization for the G-K effect is at $\sim 3\%$ level, which is consistent with our observational results for R Crt. On the other hand the detected fractional linear polarization for R Leo is at the $\sim 9.7\%$ level, and is larger than expected from our modeling results.

We note however that if the CO total intensity emission is missing flux density due to spatial filtering by the interferometer and if the polarized emission originates from a region of smaller spatial extent than the Stokes I emission, then the measured linear polarization m_l may be over-estimated.

It was pointed out by Morris et al. (1985) that the presence of an anisotropic radiation field from the central star or the circumstellar dust regions can possibly provide a preferred axis for the alignment of molecules and thus for linear polarization in the absence of either LVG conditions or a non-radial magnetic field profile. (Morris et al., 1985) lists the predicted linear polarization levels for several molecular species due to an anisotropic radiation field, but CO lines were not included. The expected fractional linear polarization can exceed 10%. In the presence of modest magnetic field ($B \geq 1\mu G$), however, the alignment due to this anisotropic radiation field will be greatly diminished, and the remaining alignment is governed by the magnetic field. Further computations regarding anisotropic radiation sources in the G-K effect were performed by Cortes et al. (2005). Their predicted fractional linear polarization levels for the $J = 2 - 1$ CO line were no greater than 5%. Concerning this, we also implemented an anisotropic radiation source in our G-K model. In the case of the CSE surrounding an AGB star, the possible brightest radio source of anisotropy is the star itself. We considered the relative brightness in radio of the star and a dust clump at the dust-forming radius. Typical values adopted were a stellar source temperature of several thousand Kelvin

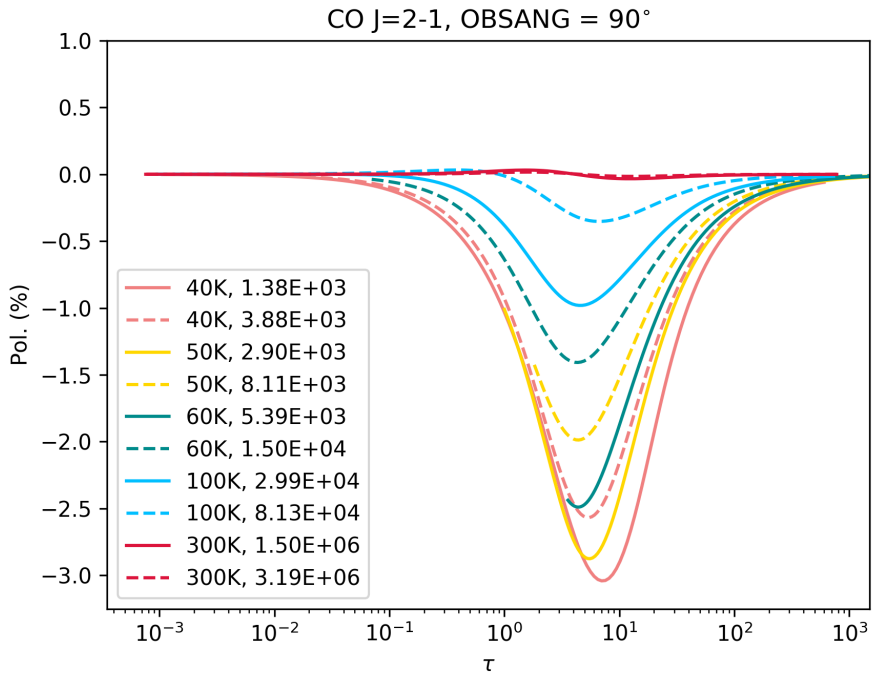

Figure 3.27: The predicted polarization signal level from our G-K modeling using mix model (corresponding to $\alpha = 0.1$ as discussed in (Cortes et al., 2005)), density and temperature profile calculated based on R Leo case as listed in Table 3.5. The colors denote the temperature from low to high. The styles denote the lower bound (solid) and the upper bound (dashed) of the density profile listed in Table 3.5.

and an angle of ~ 0.01 rad subtended by the central star in the CO region of the CSE at $\sim 200R_*$. Using these parameters the G-K polarization peaked at the same optical depth but the stellar radiation anisotropy produced a negligible change in the measured linear polarization m_l. We expanded the radiation anisotropy parameter region over a range of physical, and even unphysical conditions, but conclude from these tests that fractional linear polarization greater than 5% cannot readily be generated by this mechanism with our existing G-K model.

Lastly we note that uncertainty in T_* noted earlier translates to uncertainty in the CSE temperature following Equation 3.13 but does not have a significant effect on our inferred G-K linear polarization magnitude.

3.5.3 SiO maser polarization

As indicated in Table 3.4 we detect linear polarization in the $v = 1,\ J = 5 - 4$ SiO maser emission toward R Crt at $m_l \sim 17.2\%$ and R Leo at $m_l \sim 34.6\%$. At the closest corresponding velocities in the $v = 1,\ J = 2 - 1$ SiO maser spectra presented by Herpin et al. (2006) the associated fractional linear polarization is $m_l \sim 15\%$ for R Crt and $m_l \sim 26\%$ for R Leo. In the same $v = 1,\ J = 2 - 1$ SiO maser

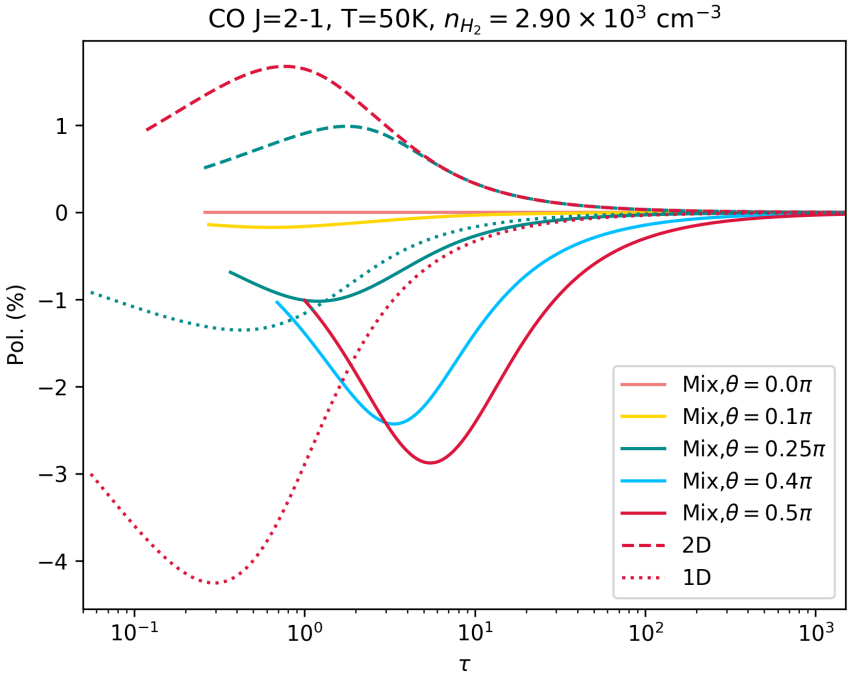

Figure 3.28: A comparison of the predicted G-K polarization profiles for the $J = 2-1$ CO line under various choices of velocity gradient geometries (Figure 3.26) and the line-of-sight (LOS) viewing angles. The angle θ (see color legend) refers to the angle between the LOS direction and the presumed magnetic field direction. Line style indicates the 1-D, 2-D, and Mix LVG geometry models. The CSE parameters used here are: T = 50K, n(r) = 2.9×10^3cm^{-3}.

transition, (Wiesemeyer et al., 2009) report a fractional linear polarization toward R Leo of $m_l \sim 24-26\%$. We note however that these are different SiO rotational transitions at different spatial resolution and that SiO maser emission is highly time-variable (Pardo et al., 2004). Nonetheless these results are broadly consistent with the current work. Linear polarization in the current $v = 1,\ J = 5-4$ SiO maser transition has been observed toward other target sources including VY CMa at $m_l \sim 10-60\%$ (Shinnaga et al., 2004) and VX Sgr at $< m_l >= 26 \pm 16\%$ (Vlemmings et al., 2011). Watson (2009) argues that the high fractional linear polarization in circumstellar SiO maser emission (approaching $\sim 50\%$) would require an unphysical degree of maser saturation; higher values of m_l are more readily explained by anisotropic pumping. High fractional linear polarization in high$-J$ SiO maser transitions strengthens the case for anisotropic pumping (Lankhaar and Vlemmings, 2019).

We detect peak fractional circular polarization $m_c \sim 5.7\%$ in the $v = 1, J = 5-4$ SiO maser line toward R Leo as indicated in Table 3.3, but do not detect statistically significant circular polarization in this transition toward R Crt perhaps due to sensitivity. For reference, (Herpin et al., 2006) report $m_c \sim 9-10\%$ toward R Leo in the $v = 1, J = 2-1$ SiO maser transition.

3.5.4 Comparison with other intrinsic alignments

In this Section, we consider the relation between the magnetic field orientation measured in the current work for R Crt and R Leo and other intrinsic alignments published for these sources in the literature. The compiled results are listed in Table 3.8, and illustrated in Figure 3.29. For R Crt as observed in the current work, the inferred magnetic field orientation of the $J = 2-1$ CO envelope from the G-K effect is $7.6^\circ \pm 1.0^\circ \pm 10.8^\circ$, while the measured EVPA of the $v = 1, J = 5-4$ SiO maser polarization is $-15.4^\circ \pm 0.7^\circ \pm 10.8^\circ$. The format of the inferred/measured angles from our work are as: [error-weighted value] $\pm\sigma_{wav}$[statistical error] $\pm\,\sigma_{sys}$[(systematic error] . We compare our EVPA and magnetic field measurements with results from the literature, specifically: i) $v = 1, J = 2-1$ SiO maser linear polarization EVPA $\chi = 120^\circ$ (Herpin et al., 2006); ii) H_2O maser observations indicating an inferred bipolar outflow with PA= 136° (Ishitsuka et al., 2001); iii) 1667-MHz OH maser observations with an inferred magnetic field orientation of -30° (Szymczak et al., 1999); iv) the fitted inclination angle of the elongated star $\phi_{incl} = 157^\circ$ (Paladini et al., 2017); and, v) the visible light scattered by dust grains observed using SPHERE/ZIMPOL on the VLT reveals a biconical outflow extending over a region up to at least 500 mas from the central star (Khouri et al., 2020). The position angle of this structure ($\sim 160^\circ$) is consistent with those measured for the magnetic field and the elongation of the star in the mid-infrared (Khouri et al., 2020).

From the current observations of R Leo, the inferred magnetic field orientation of the $J = 2-1$ CO envelope obtained from the G-K effect is $-77.7^\circ \pm 1.7^\circ \pm 11.6^\circ$, while the measured EVPA of the $v = 1, J = 5-4$ SiO maser polarization is $-1.1^\circ \pm 0.03^\circ \pm 11.6^\circ$. We compare our measurements with results from the literature, specifically: i) $v = 1, J = 2-1$ SiO maser linear polarization EVPA $\chi = 80^\circ$ (Herpin et al., 2006);

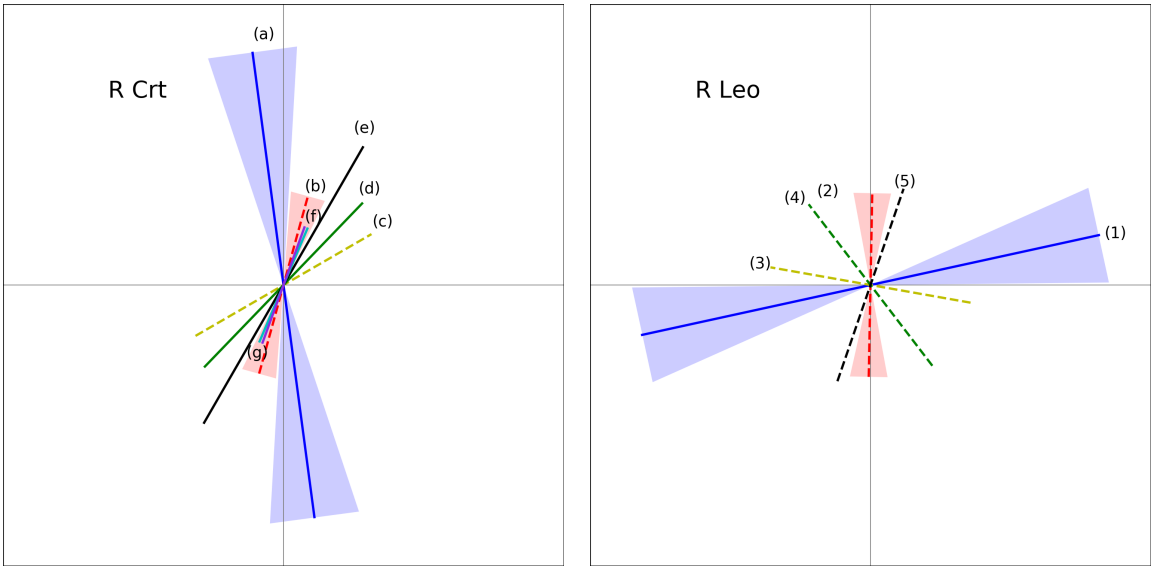

(a) R Crt (b) R Leo

Figure 3.29: Schematic plot from the compiled results. The labeling refers to the literature cited in Table 3.8

ii) $v = 1, J = 2 - 1$ SiO maser linear polarization EVPA $\chi = [-40°, -35°]$ (Wiesemeyer et al., 2009); and, iii) $v = 1, J = 2 - 1$ SiO maser linear polarization EVPA $\chi = -19° \pm 65°$ (Glenn et al., 2003).

Several caveats apply when interpreting these alignment and orientation data. The measured SiO maser EVPA has a 90° ambiguity ($\parallel, \perp$) with respect to the magnetic field, depending on the angle between the line of sight and the magnetic field line in relation to the Van Vleck angle $\theta_F \sim 55°$ (Goldreich et al., 1973). The physical conditions and associated radial distances sampled by the SiO, H_2O, OH, and CO molecules differ significantly as noted earlier. Similarly, different transitions from same molecule, such as the $v = 1, J = 5-4$ and $v = 1, J = 2 - 1$ SiO maser transitions sample different physical conditions (Humphreys et al., 2002; Gray et al., 2009; Soria-Ruiz et al., 2004; Yoon et al., 2018). In Figure 3.29, we plot the compiled results in schematic form, where the opening angle of the shaded area indicates the uncertainty in the orientation if this is available. Note that the uncertainties plotted for the current work are the combination of the statistical and the systematic error as $\sigma_{tot} \sim \sqrt{\sigma_{wav}^2 + \sigma_{sys}^2}$. In Figure 3.29, the EVPA from the SiO maser polarization EVPA are plotted with dashed lines, to stress the 90° ambiguity relative to the magnetic field orientation, as described above. The length of each line is monotonically proportional to the distance scales traced by each transition, but not drawn strictly to scale for clarity of presentation. Figure 3.29 shows that for R Crt, the measured angles are confined to within a more limited range compared to the case of R Leo.

3.6 Conclusions

We have successfully detected the G-K effect in thermal $J = 2-1$ CO line emission from the CSE of the TP-AGB stars R Leo and R Crt in λ1.3 mm full-Stokes observations with CARMA. The fractional linear

polarization measured in the $J = 2 - 1$ CO line for R Crt ($m_l \sim 3.1\%$) is consistent with the predicted signal strength from detailed G-K modeling, while for R Leo the measured fractional linear polarizaion ($m_l \sim 9.7\%$) is higher than expected. Our G-K modeling is able to resolve the directional degeneracy, placing the measured EVPA parallel to the magnetic field lines. We also have detected linear polarization in the $v = 1, J = 5 - 4$ SiO maser line toward the CSE of R Crt and R Leo with values in the range $m_l \sim 17 - 34\%$. We detect circular polarization in this maser line toward R Leo but not toward R Crt, the latter possibly due to sensitivity limitations. We detect continuum emission toward R Crt and R Leo in the wide-band spectral windows. However, no successful detection of polarized continuum emission is achieved likely due to sensitivity limitations and the relative weakness of dust emission to the stellar continuum. These results with CARMA from both observation and modeling demonstrate that the G-K effect is a viable means of extracting information concerning magnetic field morphology in the CSE around late-type evolved stars at various depths in the envelope. These observations are profoundly sensitivity-limited compared to modern telescopes such as ALMA but are the first such observations with CARMA and confirm the scientific importance of observations of this nature (Vlemmings et al., 2012). At greater sensitivity, future in-depth morphological mapping of the circumstellar magnetic field around late-type stars is possible using a range of molecular species and the associated transitions. In addition, these G-K observations are complemented by associated Zeeman and continuum observations.

Table 3.8: Intrinsic position angles and alignments measured for R Crt and R Leo.

Source	Position angle	Emission	Telescope or Instrument	Reference	Label
R Crt	$\phi_B = 7.6^\circ \pm 1.0^\circ \pm 10.8^\circ$	CO ($J = 2-1$)	CARMA	This work	(a)
	$\chi = -15.4^\circ \pm 0.7^\circ \pm 10.8^\circ$	SiO ($J = 5-4, v = 1$)	CARMA	This work	(b)
	$\chi = 120^\circ / -60^\circ$	SiO ($J = 2-1, v = 1$)	IRAM 30 m	(Herpin et al., 2006)	(c)
	$\phi_{outflow} = 136^\circ / -44^\circ$	H2O maser	Japanese VLBI Network	(Ishitsuka et al., 2001)	(d)
	$\phi_B = -30^\circ$	OH 1667-MHz maser	MERLIN array	(Szymczak et al., 1999)	(e)
	$\phi_{star} = 157^\circ$	Mid-IR [i]	VLTI/MIDI	(Paladini et al., 2017)	(f)
	$\phi_{outflow} = 160^\circ$	Visible [ii]	VLT/SPHERE/ZIMPOL	(Khouri et al., 2020)	(g)
R Leo	$\phi_B = -77.7^\circ \pm 1.7^\circ \pm 11.6^\circ$	CO ($J = 2-1$)	CARMA	This work	(1)
	$\chi = -1.1^\circ \pm 0.03^\circ \pm 11.6^\circ$	SiO ($J = 5-4, v = 1$)	CARMA	This work	(2)
	$\chi = 80^\circ$	SiO ($J = 2-1, v = 1$)	IRAM 30 m	(Herpin et al., 2006)	(3)
	$\chi = [-40^\circ, -35^\circ]$ [iii]	SiO ($J = 2-1, v = 1$)	IRAM 30 m	(Wiesemeyer et al., 2009)	(4)
	$\chi = -19^\circ \pm 65^\circ$	SiO ($J = 2-1, v = 1$)	NRAO 12 m Telescope	(Glenn et al., 2003)	(5)

In this table, χ denotes an SiO emission EVPA, ϕ_B an inferred G-K magnetic field direction, $\phi_{outflow}$ an outflow direction, and ϕ_{star} the position angle of a stellar elongation.

Note: [(i)] Stellar elongation. [(ii)] Dust scattering. [(iii)] The listed EVPA range is extracted from their Figure 2; the geometric mean of this range is plotted in Figure 3.29.

Chapter 4

Mapping Circumstellar Magnetic Fields of AGB stars with VLA

As described in Chapter 3, the magnetic field around late-type evolved stars is not yet fully understood, including the role of the magnetic field interacting with the star(s) in the stellar system and the origin of the field. The Goldreich-Kylafis (G-K) effect provides valuable insight in the three-dimensional magnetic field morphology via observations in multiple molecular lines. As describe in Chapter 3, the linear polarization signal from the G-K effect has been successfully detected in the CO line in our observations of two Thermal-Pulsating (T-P) AGB stars: R Crt and R Leo, using CARMA at 1.3-mm wavelength. In a follow-up project, we have also observed these two AGB stars with the Karl G. Jansky Very Large Array (VLA)[1] in the $v = 0, J = 1-0$ SiO and $v = 0, J = 1-0$ CS transitions as prospective tracers of the magnetic field through the G-K effect and the $v = 1, 2; J = 1-0$ SiO maser lines as tracers of the Zeeman effect; all transitions fall in the λ7mm VLA Q band.

SiO line emission is often found in evolved stars (de Vicente et al., 2016). The vibrational excited ($v \geq 1$ low-J transitions in AGB stars, especially in O-rich Mira variables, show intense maser features with some narrow spikes each over only several km/s spectral width (e.g. Buhl et al. (1974); Bujarrabal et al. (1987); Jewell et al. (1991)). The SiO $v = 0$ $J = 1 - 0$ emission from late-type evolved stars are less frequently explored partially due to their weak strength compared to $v > 0$ components (de Vicente et al., 2016). The measured SiO $v = 0, J = 1 - 0$ emission is found to show a composite profile involving a broad parabolic or flat-topped component and a central spiked component that is thought to arise from maser emission (Jewell et al., 1991; Boboltz and Claussen, 2004; de Vicente et al., 2016). A wide single-dish survey of SiO $v = 0, J = 1-0$ emission over more than 20 AGB stars found such a composite profile presents systematically in O-rich and S-type AGB stars (de Vicente et al., 2016). The reported SiO $v = 0, J = 1 - 0$ flux density of R Crt and R Leo are 0.95 Jy and 5.9 Jy in this study.

In general, carbon monosulfide (CS) molecules are favored in a carbon-rich (C-rich) environment, where oxygen coexists with other species but is less abundant than carbon. This is because of the high binding energy of carbon monoxide (CO). In oxygen-rich (O-rich) star, for example, most carbon will be locked in CO molecules, and we mostly detect oxides rather than carbon-bearing species (Gail and Sedlmayr, 2013b) though some observations also suggested that C-bearing molecules can still be produced in O-rich shells by

[1]The National Radio Astronomy Observatory is a facility of the National Science Foundation operated under cooperative agreement by Associated Universities, Inc.

a combination of photospheric shocks and photochemistry (Ziurys et al., 2009). Thus, in the C-rich stars, there is spare carbon to form more molecular species other than CO. Strong CS rotational lines have been found in C-rich AGB stars and proto-planetary nebulae (PPNe), while weak CS lines were found in some O-rich planetary nebulae (Edwards et al., 2014; Zhang, 2017). For our two targets, there is no report of detecting CS transitions thus far. But out hope was that these could be detected with the sensitivity of the upgraded VLA.

4.1 VLA Observation

The observations of R Crt and R Leo were performed in the C-configuration of the Karl G. Jansky Very Large Array (VLA) in high-frequency (Q band; $\lambda 7$ mm), full Stokes mode. Two observing runs were performed, on November 26, 2018 and November 21, 2018, respectively with each run of total duration 3.7 hours. The correlator was configured in full Stokes mode to observe the SiO $v = 0, 1, 2; J = 1 - 0$ line in the lower sideband (LSB) and the CS $v = 0, 1; J = 1 - 0$ line in the upper sideband (USB). The adopted transition rest frequencies are: 43.424 GHz ($v = 0, J = 1-0$ SiO), 43.122 GHz ($v = 1, J = 1-0$ SiO), 42.820 GHz ($v = 2, J = 1-0$ SiO), 48.991 GHz ($v = 0, J = 1-0$ CS), and 48.636 GHz ($v = 1, J = 1-0$ CS). These 5 transitions were observed in narrow-band (line) spectral windows. These spectral windows are of bandwidth $\triangle\nu = 16.0$ MHz, each sampled over 256 frequency channels with corresponding nominal velocity resolutions of 0.438 km/s, 0.435 km/s, 0.432 km/s, 0.382 km/s, and 0.385 km/s respectively. In addition, 11 wide-band (continuum) spectral windows each of bandwidth $\triangle\nu = 128.0$ MHz and sampled over 64 frequency channels each were used to observe the continuum emission. Five out of these 11 continuum windows are placed over each target spectral line, for potential solution transfer. The remaining seven continuum windows were placed in the line-free frequency region; two were placed in the 43-GHz band, and 5 were placed in 49-GHz band.

For both the R Crt and R Leo observing runs with the VLA, J1331+3030 was used as the flux density calibrator and absolute EVPA calibrator, and J0854+2006 as the bandpass calibrator and leakage-term calibrator. For R Crt, J1002+1216 was used as the phase gain calibrator. For R Leo, J1048-1909 was used as the gain calibrator and as a secondary leakage-term calibrator.

4.2 Data Reduction

The VLA observes with circular polarization receptors at Q band. This VLA observation therefore has a similar polarization data model to that described for CARMA in Chapter 2. The R Crt and R Leo observations were reduced and calibrated based on the scripts generated by the VLA standard pipeline with CASA version 5.1.2. The final version of the scripts were modified to allow optimization for spectral-line polarization data. The flowchart for the final version of the scripts is provided in Figure 4.1. The key

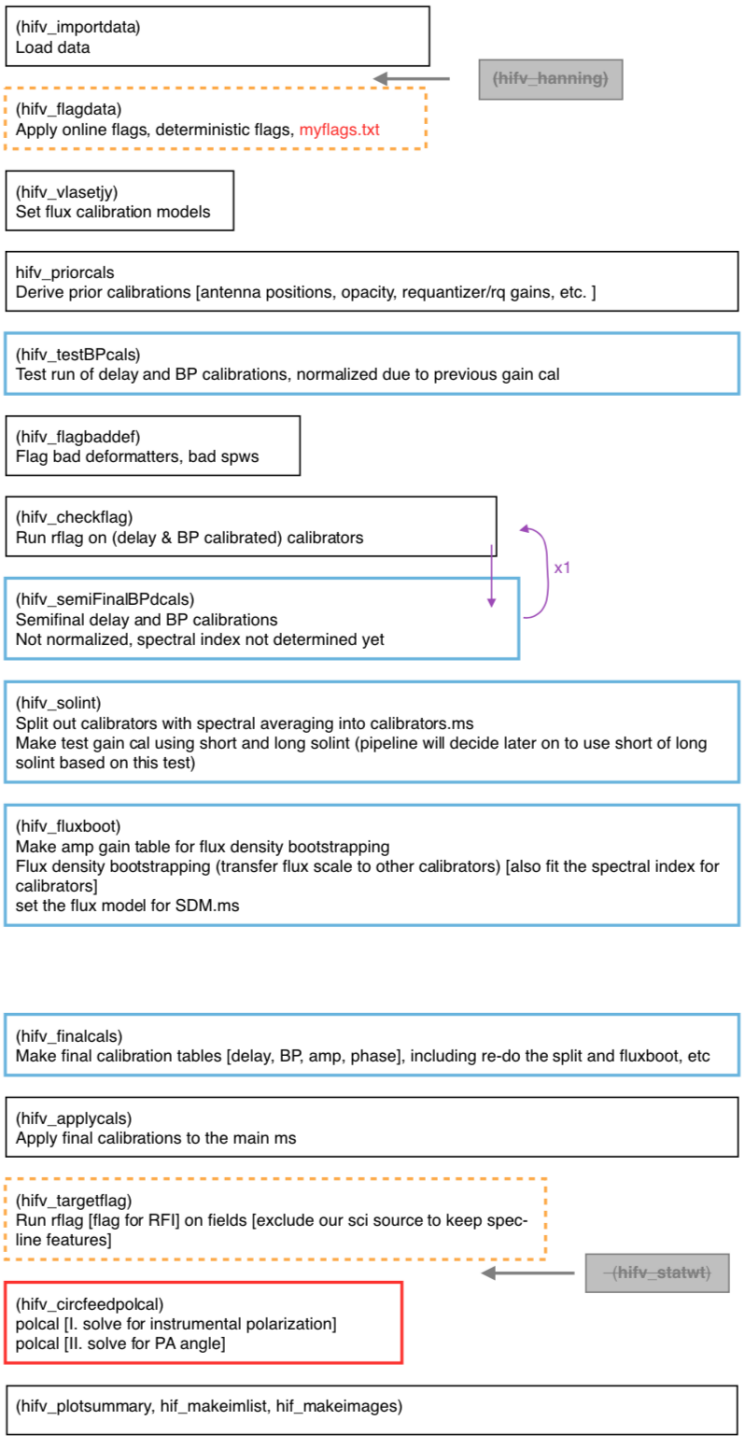

Figure 4.1: The flowchart of the final scripts after modification for generating our science results of R Crt and R Leo. The section outlined with orange dashed lines are steps with modification to the original set up. The section outlined with red solid lines are the newly included step in the original scrip.

modifications are summarized below:

Modification to the default mode pipeline: In the default reduction scripts generated automatically by the CASA VLA pipeline, there are several steps that need to be modified for spectral-line data. Specifically this includes the removal of two commands: **hifv_hanning** and **hifv_statwt**, and tuning the parameters for **hifv_targetflag**.

The **hifv_hanning** steps employ Hanning smoothing to lessen the Gibbs ringing from strong spectral features such as strong and narrow RFI, or maser lines. This will interfere with our analysis of spectral-line data including maser lines. Preliminary inspection does not indicate the presence of RFI signals. We thus remove this step from the script. In the **hifv_statwt** step, the visibility data are weighted by the inverse square of their RMS noise, i.e. σ^{-2}. Strong spectral lines will increase the RMS and will therefore be down-weighted. Accordingly, we therefore remove this step as well. For the **hifv_targetflag** step, either RFI or strong spectral line signals in our science targets could inadvertently trigger flagging. We therefore need to confine the flagging to continuum calibrators only by specifying the parameter *intents='*CALIBRATE*'*.

Modification for Polarization Data Calibration: Polarization calibration includes calibration of polarization angle, R-L phase, leakage (D-term), and absolute EVPA. To achieve this, the pipeline command `hifv_circfeedpolcal` was added to the script after `hifv_finalcals`.

Additional Flagging: Additional flagging was added based on discrepant values of the R/L gain solution ratio over time and based on the switched power gains quality.

Self-Calibration: The maser emission in the AGB CSE is expected to be compact; and at our resolution, the SiO masing region is expected to be unresolved. Accordingly, we performed phase self-calibration using the brightest maser transition SiO (J=1−0; v=1) in both observations to enhance the phase calibration quality. The adopted solution interval was 60 seconds; this choice was confirmed empirically.

4.3 Results

In Table 4.1 the rest frequency ν_0, integrated brightness over velocity channel of the linear polarization (F_ℓ), and integrated brightness of total intensity (F_I) of the detected molecular lines are listed for both R Crt and R Leo. For R Crt, the velocity range of the brightness integration is $\sim -1 - 25$ km/s, and for R Leo the velocity ranges is $\sim -13 - 17$ km/s.

We detect continuum emission toward R Crt of 4.13 ± 0.06 mJy/beam in the 43-GHz group of continuum windows and 5.31 ± 0.06 mJy/beam in the 49-GHz group of continuum windows. No continuum polarization was detected toward either R Crt or R Leo, likely due to sensitivity limitations and the expected weakness of

Table 4.1: Summary of the detected molecular lines of R Crt and R Leo in the VLA observation.

Source	Line	ν_0 [GHz]	F_ℓ [Jy beam^{-1} km s^{-1}]	F_I [Jy beam^{-1} km s^{-1}]
R Crt	SiO (J = 1-0, v=0)	43.424	19.93	209.71
	SiO (J = 1-0, v=1)	43.122	139.029	945.35
	SiO (J = 1-0, v=2)	42.820	19.16	197.88
R Leo	SiO (J = 1-0, v=0)	43.424	37.43	117.23
	SiO (J = 1-0, v=1)	43.122	4798.89	27248.44
	SiO (J = 1-0, v=2)	42.820	1698.92	15722.07

Note: Column includes the rest frequency (ν_0) of the detected molecular lines, the integrated brightness over velocities of the linearly polarized intensity (F_ℓ) and total intensity (F_I).

the dust continuum emission relative to the underlying stellar continuum emission. We report no detection for the $v = 0, 1; J = 1 - 0$ CS transitions in either target.

The emission channel maps for the $v = 0, 1, 2; J = 1 - 0$ SiO transitions for both sources are shown in Fig. 4.2 - 4.7. Contours depict linearly-polarized intensity P with associated vectors indicating EVPA χ; both are overlaid on color plots of total intensity. The peak-pixel linearly-polarized intensity P across these spectral-line image cubes is tabulated in Table 4.2 for each source and transition. We denote this as P_p. This table includes the associated LSR velocity v_{LSR}, point total intensity I_p and resulting fractional linear polarization $m_{l,p}$ at P_p. The EVPA χ_p associated with the peak-pixel linearly-polarized intensity P is also listed in Table 4.2. Table 4.3 lists the peak-pixel circularly-polarized intensity V_p in the $v = 0, 1, 2; J = 1 - 0$ SiO spectral-line image cube and associated LSR velocity v_{LSR}, point total intensity I_p and resulting degree of fractional circular polarization $m_{c,p}$ at V_p; circular polarization is only detected toward R Leo. At 43 GHz, the beam size is $0.76'' \times 0.42''$ for the calibrated R Crt data and $0.48'' \times 0.44''$ for the calibrated R Leo data.

4.4 Analysis and Discussion

In Table 4.2, the peak fractional linear polarizations for the $v = 0, J = 1 - 0$ SiO line emission are $m_l = 29.4\%$ and $m_l = 60.5\%$ for R Crt and R Leo respectively. These detected fractional linear polarization levels are not atypical for SiO maser emission (e.g. Herpin et al. (2006)). Detailed modeling is therefore necessary in order to determine if this linear polarization in the $v = 0, J = 1 - 0$ SiO emission arises from the G-K effect in thermal emission or if other effects need to be considered.

4.4.1 G-K Analysis

We used the modeled CSE parameters by Huang et al. (2020), as described in Section 3.5.1, as the input to our G-K modeling of the $v = 0, J = 1 - 0$ SiO transition. Our G-K model predicts peak linear polarization for the $v = 0, J = 1 - 0$ SiO transition of $m_l \sim -0.2\%$ (Fig. 4.8). This level is much lower than our observed

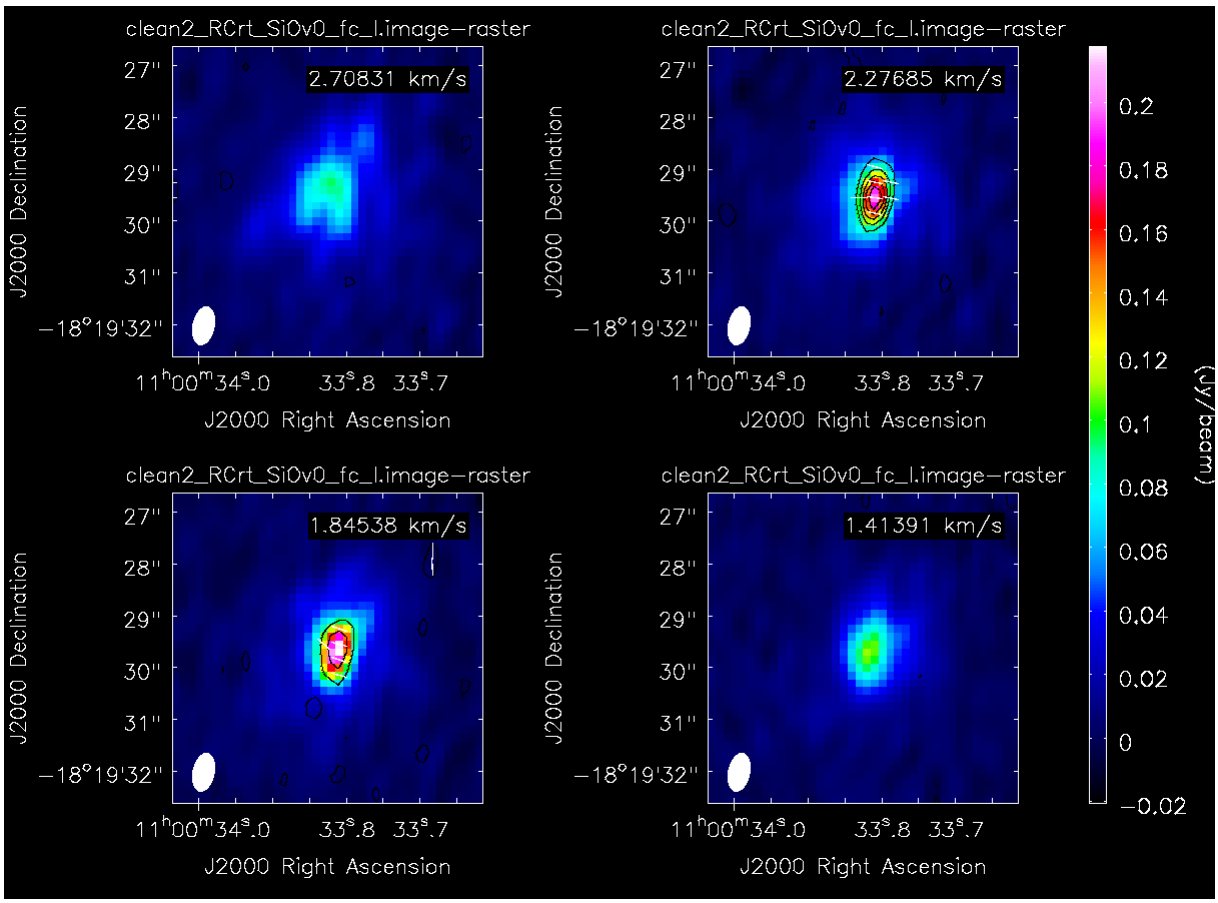

Figure 4.2: SiO (J=1-0,v=0) spectral-line polarization maps of R Crt. The channel width is $\sim$ 0.4 km s^{-1}. The color map shows the spectral-line emission total intensity, and the contour levels are the linear polarization intensity as 2, 4, 6, 8, and 10 times σ where σ is the off-source noise level of each source. The white segments indicates orientation of the EVPA. The synthesized beam size is displayed in the lower-left corner in each map. The plotted EVPA threshold is $5\sigma_{polI}$ with σ_{polI} is the rms quiet region noise after de-bias.

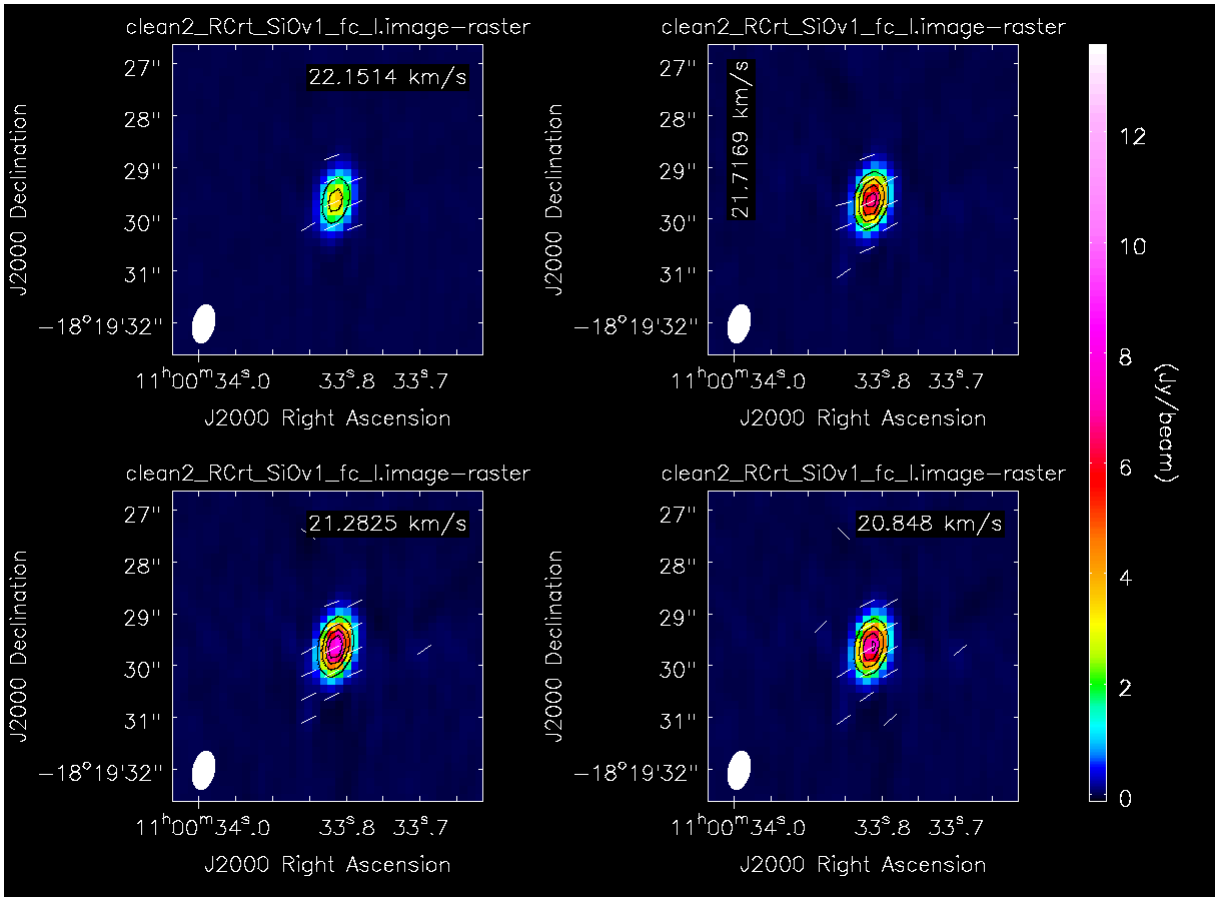

Figure 4.3: SiO(J=1-0,v=1) spectral-line polarization maps of R Crt. The channel widths are $\sim$ 0.4 km s^{-1}. The color images correspond to total intensity, and contour levels are the linear polarization intensity from 20%, 40%, 60%, and 80% of the maximum value. White segments indicate the EVPA orientation. The plotted EVPA threshold is $5\sigma_{polI}$ with σ_{polI} is the rms quiet region noise after de-bias.

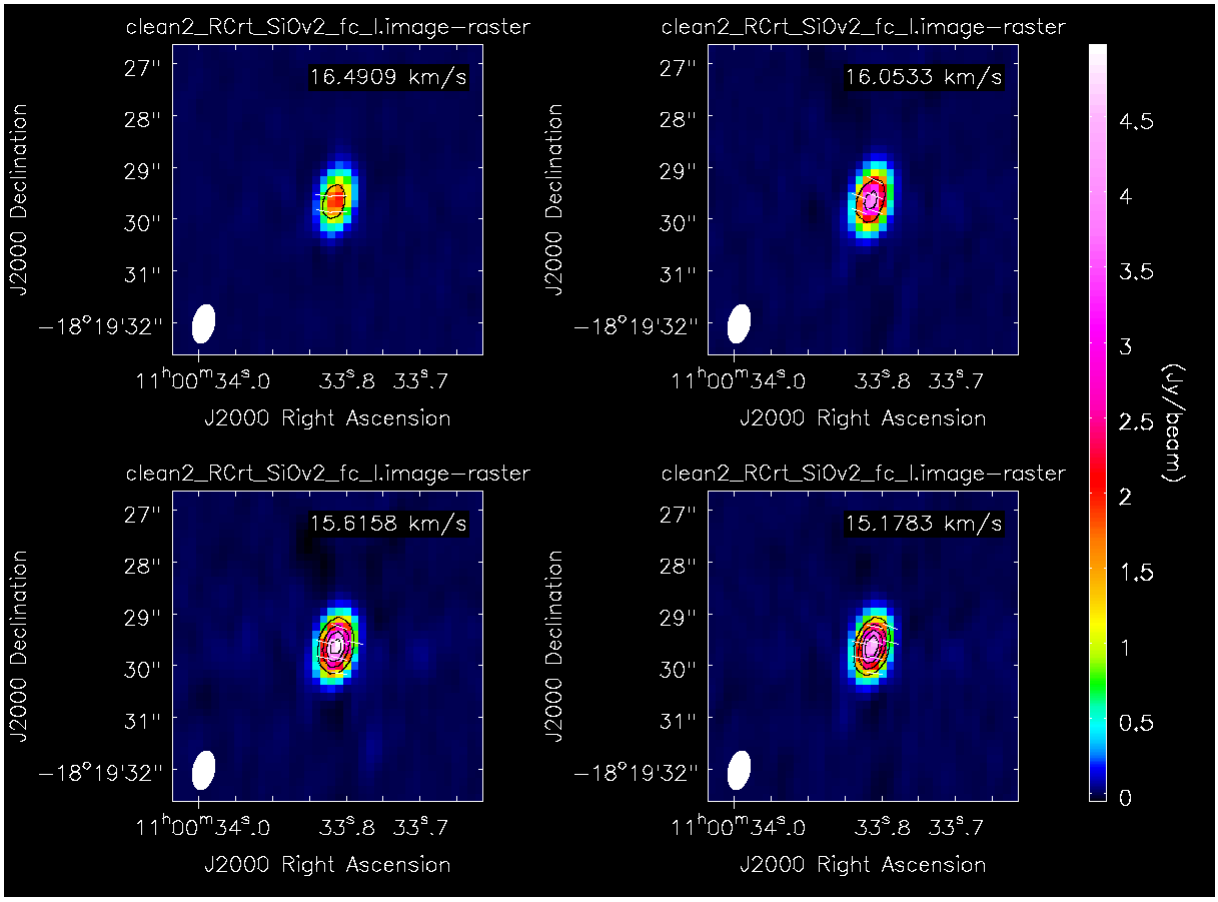

Figure 4.4: SiO(J=1-0,v=2) spectral-line polarization maps of R Crt. The channel widths are $\sim$ 0.4 km s^{-1}. The color images correspond to total intensity, and contour levels are the linear polarization intensity from 20%, 40%, 60%, and 80% of the maximum value. White segments indicate the EVPA orientation. The plotted EVPA threshold is $5\sigma_{polI}$ with σ_{polI} is the rms quiet region noise after de-bias.

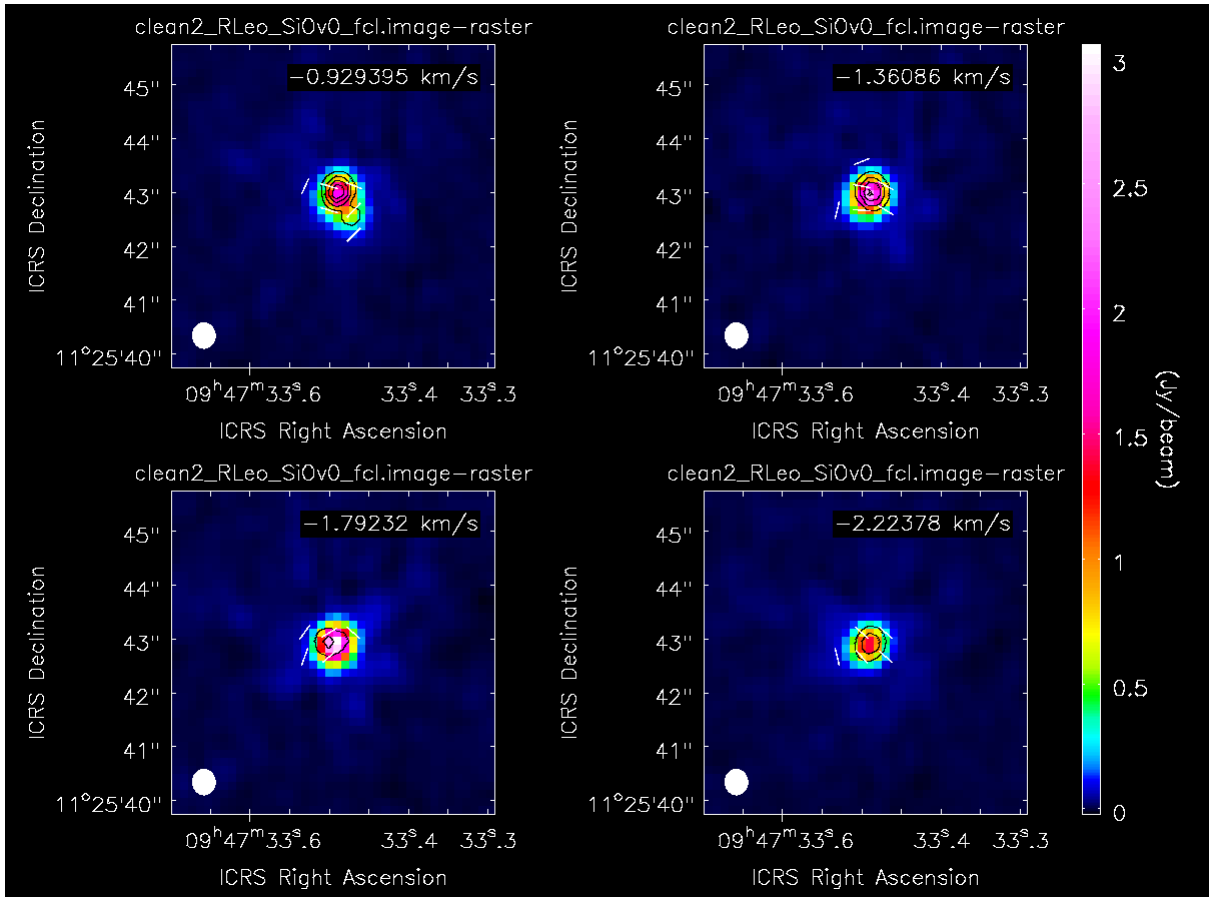

Figure 4.5: SiO(J=1-0,v=0) spectral-line polarization maps of R Leo. The channel widths are $\sim$ 0.4 km s^{-1}. The color images correspond to total intensity, and contour levels are the linear polarization intensity from 20%, 40%, 60%, and 80% of the maximum value. White segments indicate the EVPA orientation. The plotted EVPA threshold is $5\sigma_{polI}$ and $20\sigma_I$, with σ_I is the off-source rms of the total intensity map and σ_{polI} is the off-source rms of the linearly polarized intensity map after de-bias.

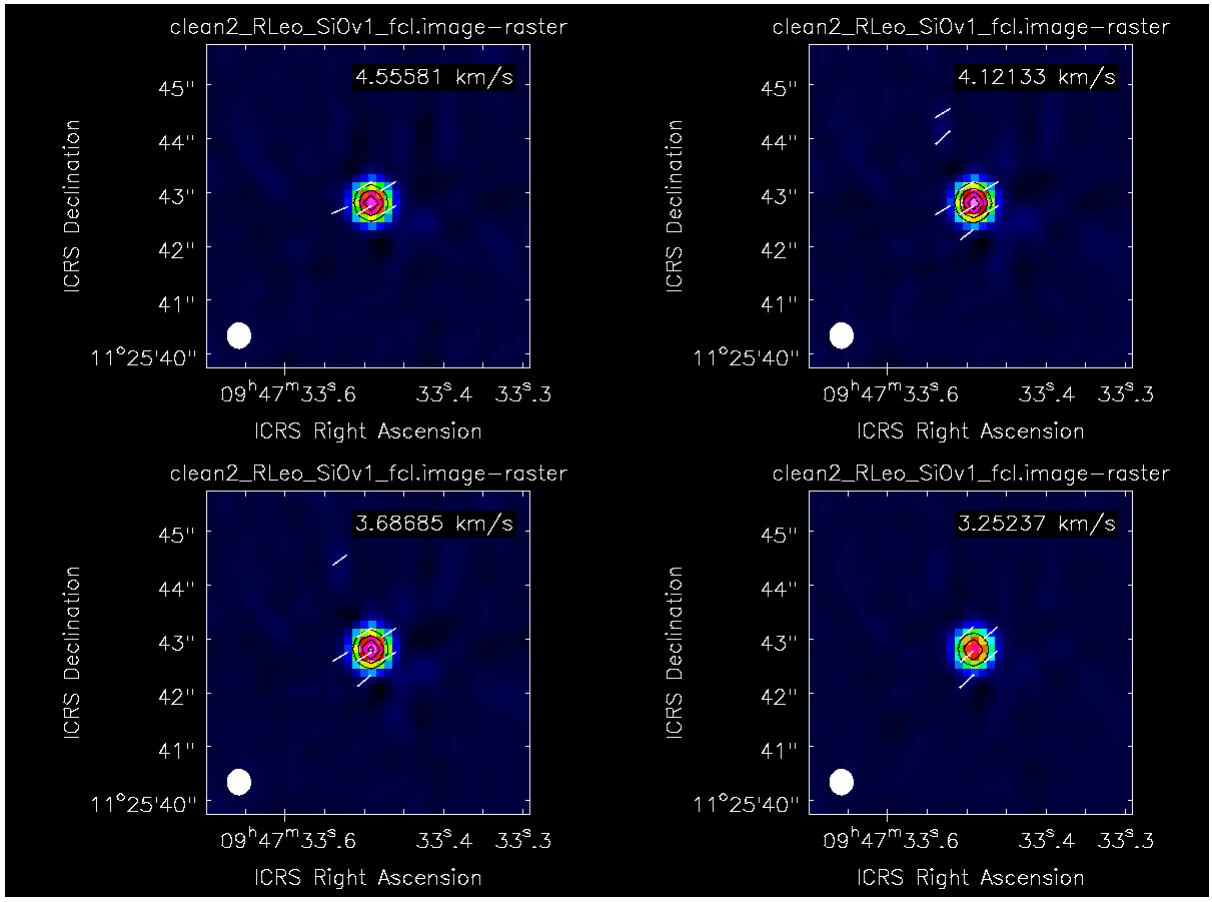

Figure 4.6: SiO(J=1-0,v=1) spectral-line polarization maps of R Leo. The channel widths are $\sim$ 0.4 km s^{-1}. The color images correspond to total intensity, and contour levels are the linear polarization intensity from 20%, 40%, 60%, and 80% of the maximum value. White segments indicate the EVPA orientation. The plotted EVPA threshold is $5\sigma_{polI}$ and $20\sigma_I$, with σ_I is the off-source rms of the total intensity map and σ_{polI} is the off-source rms of the linearly polarized intensity map after de-bias.

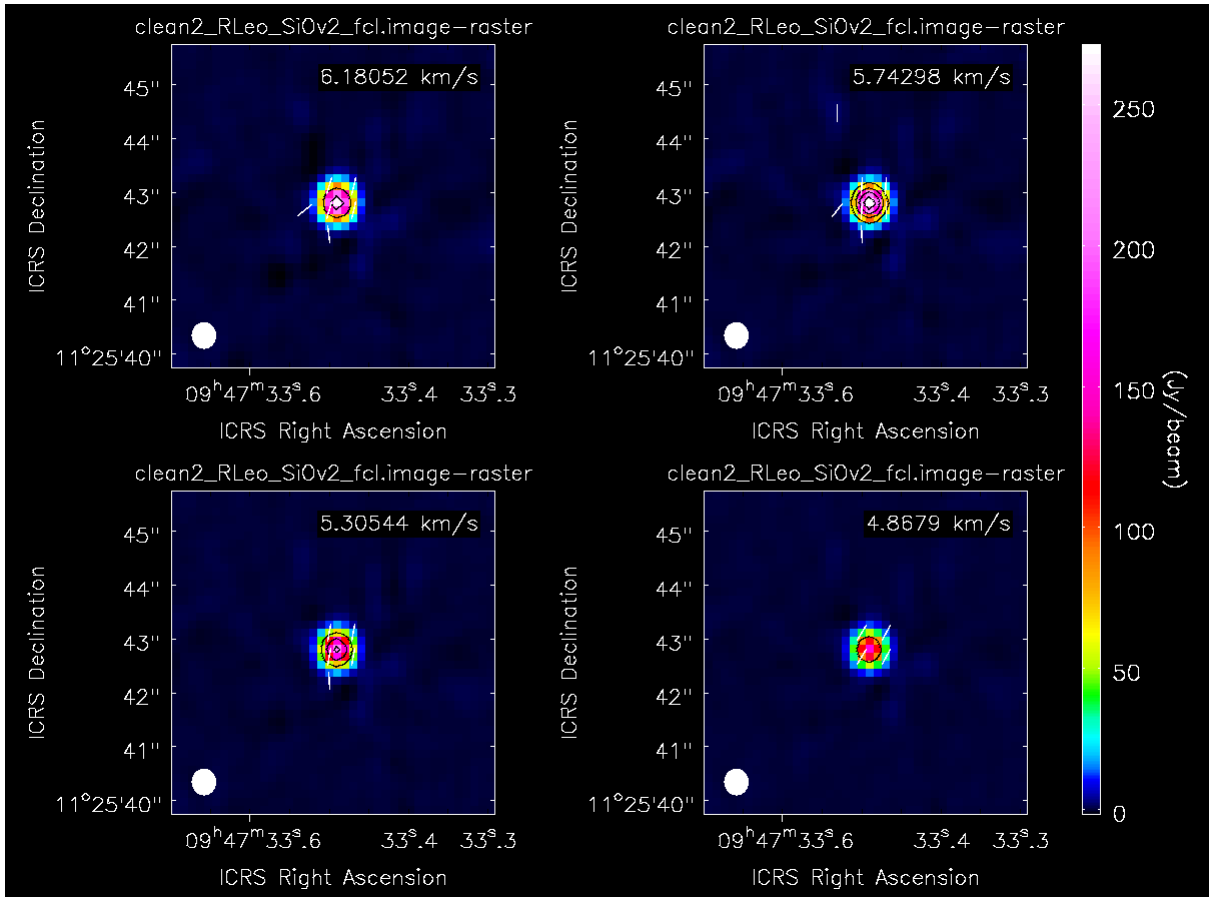

Figure 4.7: SiO(J=1-0,v=2) spectral-line polarization maps of R Leo. The channel widths are $\sim$ 0.4 km s^{-1}. The color images correspond to total intensity, and contour levels are the linear polarization intensity from 20%, 40%, 60%, and 80% of the maximum value. White segments indicate the EVPA orientation. The plotted EVPA threshold is $5\sigma_{polI}$ and $20\sigma_I$, with σ_I is the off-source rms of the total intensity map and σ_{polI} is the off-source rms of the linearly polarized intensity map after de-bias.

Table 4.2: Polarization properties at the position of peak linearly-polarized intensity in the spectral-line image cubes.

Source	Line	v_{LSR} [km s^{-1}]	P_p [Jy beam^{-1}]	I_p [Jy beam^{-1}]	$m_{\ell,p}$ [%]	χ_p [°]
R Crt	SiO (J=1-0, v=0)	2.277	0.0585	0.1991	29.4% (12.6 σ)	29.68
	σ	–	0.0046	0.0032	–	0.32
	SiO (J = 1-0, v=1)	21.283	2.831	8.605	32.9% (598 σ)	-61.8
	σ	–	0.0047	0.0040	–	0.01
	SiO (J = 1-0, v=2)	15.178	0.134	4.523	2.952 (30.7 σ)	58.5
	σ	–	0.0044	0.0030	–	0.19
R Leo	SiO (J=1-0, v=0)	-0.929	1.245	1.90	60.5% (329 σ)	38.31
	σ	–	0.0038	0.0027	–	0.02
	SiO (J = 1-0, v=1)	4.121	121.6	397.5	30.6% (1136 σ)	-47.55
	σ	–	0.11	0.11	–	0.0002
	SiO (J = 1-0, v=2)	5.743	44.05	271.9	16.2% (1024 σ)	-10.97
	σ	–	0.043	0.062	–	0.0006

Note: Column includes the velocity associated with the listed peak linear polarization, the peak linear polarization, the associated total intensity, the derived peak fractional linear polarization, and the error-weighted polarization angles.

Table 4.3: Polarization properties at the position of peak circularly-polarized intensity in the spectral-line image cubes.

Source	Line	v_{LSR} [km s^{-1}]	V_p [Jy beam^{-1}]	I_p [Jy beam^{-1}]	$m_{c,p}$ [%]
R Crt	SiO (J=1-0, v=0)	–	–	–	–
	σ	–	–	–	–
	SiO (J=1-0, v=1)	16.503	-0.445	10.51	-4.23% (148 σ)
	σ	–	0.00301	0.00395	–
	SiO (J=1-0, v=2)	15.178	-0.0556	4.523	-1.23% (19.4 σ)
	σ	–	0.00286	0.00297	–
R Leo	SiO (J=1-0, v=0)	-1.361	0.746	2.632	28.3% (283 σ)
	σ	–	0.00264	0.00268	–
	SiO (J=1-0, v=1)	3.687	10.57	379.9	2.78% (190 σ)
	σ	–	0.0557	0.110	–
	SiO (J=1-0, v=2)	6.181	4.614	265.0	1.74% (168 σ)
	σ	–	0.0274	0.0618	–

Note: Column includes the velocity associated with the listed peak circular polarization, the peak circular polarization, the associated total intensity, and the derived peak fractional circular polarization.

results for both R Crt ($m_{\ell,p} \sim 29.4\%$) and R Leo ($m_{\ell,p} \sim 60.5\%$).

It is noted in the literature (Jewell et al., 1991; Boboltz and Claussen, 2004; de Vicente et al., 2016) that the measured $v = 0, J = 1 - 0$ SiO profile in some AGB stars may contain maser components. Later in Section 4.4.2, two analyses are presented in order to further characterize the measured $v = 0, J = 1 - 0$ SiO transition profile in this context.

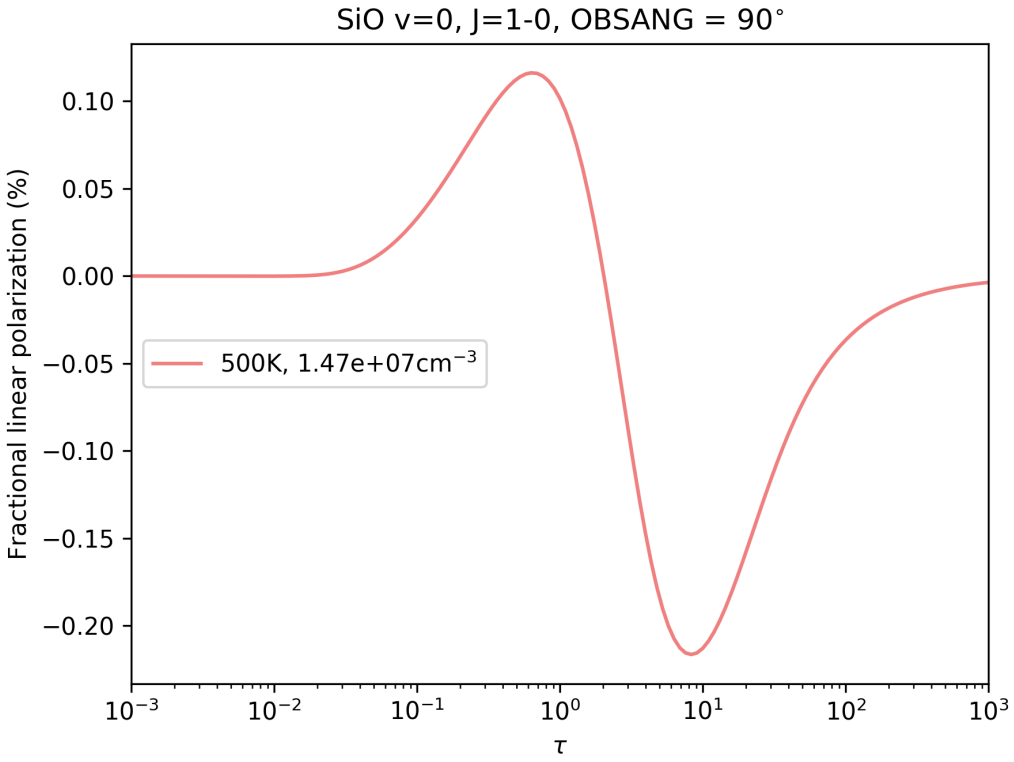

Figure 4.8: The predicted polarization signal level from our G-K modeling for $J = 1 - 0, v = 0$ SiO transition using the mix model (corresponding to = 0.1 as discussed in Cortes et al. (2005)), with density and temperature profiles calculated based on the R Leo case as listed in Table 3.5.

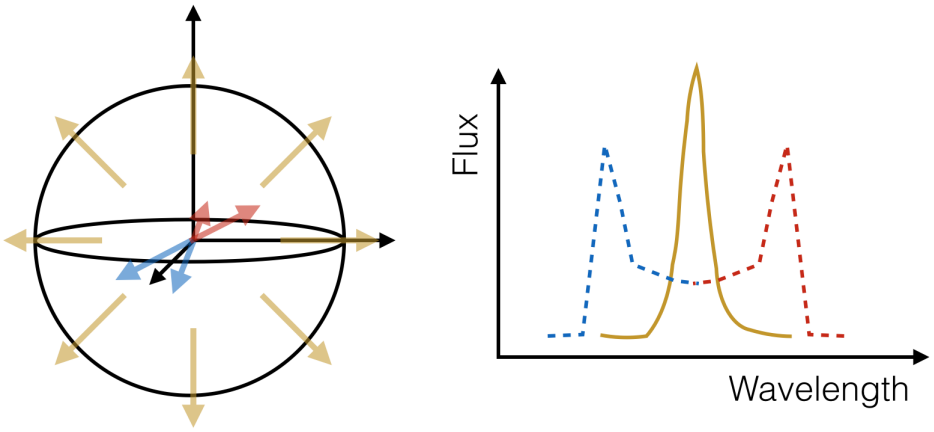

Figure 4.9: A schematic plot illustrating the spatial and spectral profile of an idealized spherical CSE with spherical mass outflow. For a spherical-symmetric radial outflow the practical spectrum is shown in blue and red. A tangentially amplified spectrum is shown in yellow.

4.4.2 Maser Analysis

As discussed in Section 4.4.1, there may be maser features blended into the observed J=1−0; v=0 SiO line profiles of R Crt and R Leo. High-resolution very long baseline interferometry (VLBI) images of the SiO masers are found frequently in a broken ring structure (Diamond et al., 1994; Greenhill et al., 1995; Boboltz et al., 1997). As indicated by Gray (2012), such an observed ring pattern suggests predominantly tangential amplification paths for SiO masers, confined in a restricted range of radii within the CSE. The SiO masers typically exhibit such ring-like structures on shell sizes of a few tens of mas (Boboltz and Claussen, 2004). A schematic shown in Figure 4.9 illustrates the spatial and spectral location of features for both tangential and radial amplification. Note in practice, the masing clumps can be radially accelerated by shocks in the inner CSE, and the distribution often deviates from the idealized spherical symmetry (Gray, 2012).

Boboltz and Claussen (2004) performed a simultaneous observation of the $v = 0, J = 1 - 0$ SiO and the $v = 1, J = 1 - 0$ SiO transitions towards six O-rich evolved stars. They pointed out the observed $v = 0, J = 1 - 0$ SiO transitions are generally weaker and have different spectral morphology than the first vibrationally excited-state components. It was found that the derived brightness temperature in the detected $v = 0, J = 1 - 0$ SiO transition is above 10^4K, and four out of the six sources exhibited spectral features with multiple maser peaks. They also analyzed the spatial distribution and the brightness of the emission components over frequency. Qualitatively they found that the vibrational ground-state SiO appears to spatially distribute over larger regions in the CSE than the $v = 1$ counterpart (Boboltz and Claussen, 2004). Following Boboltz and Claussen (2004), we examined the brightness temperature of the emission

components in order to determine whether the observed J=1−0; v=1 SiO line profile is likely to contain maser components (Section 4.4.2). We also follow a further analysis in Boboltz and Claussen (2004) and fit the peaks in each spectral frame by two-dimensional profiles in order to further characterize the spatial distribution of the potential masing components (Section 4.4.2).

Brightness Temperature of the Emission Components

The fitted component flux densities are converted to equivalent brightness temperature using (Boboltz and Claussen, 2004):

$$T_b = \frac{S_\nu \lambda^2}{2k\Omega_s} \sim 936 \frac{S_\nu}{\theta_s^2} \tag{4.1}$$

where the S_ν is flux density in Jy, and θ_s is the geometric mean of the fitted source size in arcseconds. For our two objects, the derived brightness temperature from our observations are $T_b = 894.8$K and $T_b = 8.96 \times 10^4$K, for R Crt and R Leo respectively.

We then compare T_b with the kinetic temperature (T_k) of the gas in the CSE as considered by Boboltz and Claussen (2004). We estimate the gas kinetic temperature T_k using our modeled CSE profiles in Section 3.5.1. Using R Leo as a standard example, the angular extent of the $v = 0, J = 1 - 0$ SiO emission from R Leo is about $\sim$ 1 arcsecond (see Section 4.4.2, Figure 4.13), which corresponds to $\sim$ 80 R_*. The estimated kinetic temperature at this angular extent is $\sim$ 130K. In Boboltz and Claussen (2004), they used the estimated kinetic temperature of $v = 1$ maser transition $T_{k,v1} = 1500$K as a conservative estimate of the kinetic temperature of the $v = 0$ transition. The true value should be in between these two values.

For R Leo, the brightness temperature is far higher than even the most conservative estimate of kinetic temperature. This clearly indicates that masing is a significant component. The brightness temperature of $v = 0, J = 1 - 0$ SiO emission in R Crt is in the kinetic temperature range. It can be either that this transition in R Crt is close to thermal emission and we need other sources to take account for high linear polarization in SiO (see relevant discussion in Section 3.5.2); or it still is a maser feature, but its intrinsic weakness makes the estimate of the morphology in the line profile less accurate.

Two-Dimensional Spatial Fitting of the Emission Components

We performed image-plane component fitting of the $v = 0, 1, 2; J = 1 - 0$ SiO maps in each velocity channel for both R Crt and R Leo with two-dimensional Gaussian profiles following the method of Boboltz and Claussen (2004). Boboltz and Claussen (2004) performed this analysis on the $v = 0, 1; J = 1 - 0$ SiO maps of multiple evolved stars and as noted above, found that the fitted $v = 0$ components tend to be spatially more extended than the $v = 1$ counterparts. Our goal here is to characterize the spatial and spectral distribution of each emission component by this image-plane analysis, and determine if our results comply with this prior finding. We would also like to determine whether there is the spectral-spatial association in each transition provided by the schematic shown in Figure 4.9. This may produce a correlation between

the line center and the outer regions of the spatial distribution for maser features, and between the thermal expansion wings and the center of the spatial distribution. We are observing in the same frequency band and at a similar angular resolution (VLA C configuration) as in the work by Boboltz and Claussen (2004). Our two TP-AGB stars (R Crt and R Leo) were not observed by Boboltz and Claussen (2004) however. We also consider additional analysis from the $v = 2, J = 1 - 0$ SiO emission that was not covered in the work by Boboltz and Claussen (2004).

We note that the image-plane component analysis here needs to deblend component near or below the VLA resolution. It is difficult to determine the position of image components that are heavily overlapping spatially (Plambeck et al., 2009). However, one can still fit the isolated image components to an accuracy of $\sim 0.5 \times \frac{\theta_{FWHM}}{SNR}$ (Reid et al., 1988), so this analysis is possible in a high SNR regime. The image-plane analysis also shares difficulties with uv-fitting, in that there is no prior knowledge of the number of image components. Compared to fitting in the visibility domain, image-plane fitting has the advantage of localizing the imaging components spatially; in the visibility domain all sources within the telescope primary beam contribute to the fit (Plambeck and Wright, 2016). Within these caveats, we interpret our image-plane component analysis only in a qualitative sense concerning the spatial distribution. A mode quantitative constraint on the spatial distribution of these transitions will require higher-resolution interferometric observations.

As the number of emission components in each image plane could vary over velocity channel, the two-dimensional Gaussian fitting was carried out per channel with the associated interactive 2D fitting tool in the CASA image viewer [2]. In the initial analysis, a single 2-D Gaussian fit was performed for most channels; while for those image planes that present double or multiple peaks visible by eyes, we performed multiple Gaussian fits over specified sub-regions. We set the fit cut-off to be 10-σ where σ is the off-source rms-noise, and we exclude pixels below 10-σ from the fitting process. Each 2D Gaussian fit provides output parameters including the integrated and peak brightness, the image component size (convolved and deconvolved by the beam), and the position of the source component. The fitted peak brightness and the fitted component position (relative to the phase center) are presented in Figure 4.10 - 4.15.

For R Crt, the reported formal position errors from CASA range from 5 mas up to 70 mas in $v = 0$ fits, and from less than 1 mas up to 20 mas in $v \geq 1$ counterpart fits. For R Leo, the reported position errors from CASA range from 2 mas up to 105 mas in $v = 0$ fits, and from less than 1 mas up to 1.5 mas in $v \geq 1$ counterpart fits. The typical rms residual from the fits for R Crt are 13 mJy/beam, 10 mJy/beam, and 5 mJy/beam for the $v = 0, 1, 2$ SiO components respectively. The rms residual from the fits to the peak total intensity channel for R Crt are 14 mJy/beam, 27 mJy/beam, and 13 mJy/beam for the $v = 0, 1, 2$ SiO components respectively. The typical rms residual from the fits are 13 mJy/beam, 0.5 Jy/beam, and 0.3 Jy/beam for the case of R Leo, for the $v = 0, 1, 2$ SiO components respectively. The rms residual from the fits to the peak total intensity channel are 19 mJy/beam, 1.0 Jy/beam, and 0.5 Jy/beam for the case

[2]This 2D fitting tool reaches to the same top level interface "ImageFitter" for fitting image source components as the CASA task `imfit`

of R Leo, for the $v = 0, 1, 2$ SiO components respectively. The typical rms values correspond to 6.5%, 0.1%, and 0.1% of the peak total intensity in R Crt, and 0.7%, 0.3%, and 0.2% of the peak total intensity in R Leo, for the $v = 0, 1, 2$ SiO components respectively. We considered sources of position uncertainty due to phase uncertainty from the bandpass calibration and the phase self calibration. At the SNR of our bandpass calibrators we believe our bandpass calibration is of sufficient accuracy, and not to have erroneous phase slopes. The phase self-calibration solution transferred from the $v = 1, J = 1 - 0$ SiO data was shown to enhance the final results compared to the phase solution transferred from the phase calibrator only.

For both cases of R Crt and R Leo, we note that the $v = 0$ profiles are qualitatively more extended spatially than their $v \geq 1$ counterparts by a factor of several. As pointed out by Boboltz and Claussen (2004), the observed more extended spatial distribution of $v = 0$ emission supports the idea that the $v = 0$ SiO maser occurs at distance larger than the $v \geq 1$ shells, and they may not be excited in the same gas layers (Boboltz and Claussen, 2004).

Comparison with SiO maser observation in the literature

We compare the detected $v = 0, J = 1 - 0$ SiO line emission in R Crt and R Leo with the results presented by de Vicente et al. (2016). For R Leo, our detected total intensity is consistent within the range in the spectra presented over stellar phases reported by de Vicente et al. (2016). The observed R Crt total intensity of this transition is lower but of a same order of magnitude to that reported by de Vicente et al. (2016) over two epochs. We note that the estimated stellar variation period of R Crt is given as 160 days (see Table 3.1), but it is a semiregular (SRb) AGB star. The duration between the two epochs presented by de Vicente et al. (2016) is 214 days, which slightly exceeds one stellar period. It is possible that our R Crt observation is at a different stellar phase from the two presented by de Vicente et al. (2016).

For the $v = 1$ polarization results, we compared against observations presented by Herpin et al. (2006) and by Wiesemeyer et al. (2009). As indicated in Table 4.2, the detected linear polarization ($m_{\ell,p}$) in the $v = 1, J = 1 - 0$ SiO transition is 32.9% and 30.6% for R Crt and R Leo respectively. Herpin et al. (2006) reported fractional linear polarization at the closest corresponding velocities of $m_l \sim 15\%$ for R Crt and $m_l \sim 36\%$ for R Leo. The observed fractional circular polarization in this work is -4.23% and 2.78% for R Crt and R Leo respectively. Their reported fractional circular polarization at associated velocity channels is -8% for R Crt and -9% for R Leo. Wiesemeyer et al. (2009) also reported a fractional linear polarization toward R Leo of $m_l \sim 24 - 26\%$, along with fractional circular polarization $m_l \sim 1 - 3\%$. We note that these are different SiO rotational transitions at differing spatial resolution and that SiO maser emission is highly time-variable (Pardo et al., 2004). Given this, the linear polarization results in the literature are broadly consistent with our results.

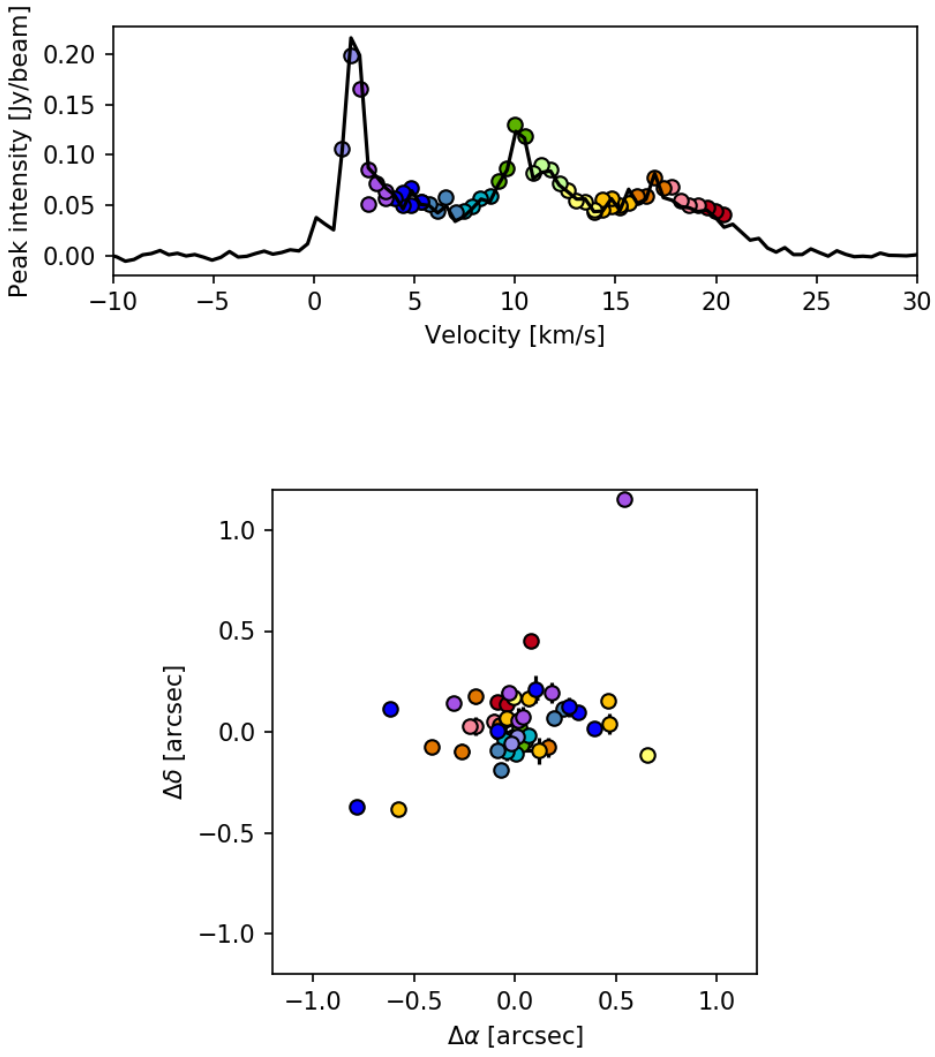

Figure 4.10: The observed $v = 0, J = 1 - 0$ SiO line emission toward R Crt. The upper panel shows the total intensity interferometric spectrum. The colored dots indicates channels in which component fits were performed; the color code indicates velocity. The fitted component positions in right ascension $\Delta\alpha$ and declination $\Delta\delta$ offset relative to the field center are shown in the lower panel; line segments indicate position errors.

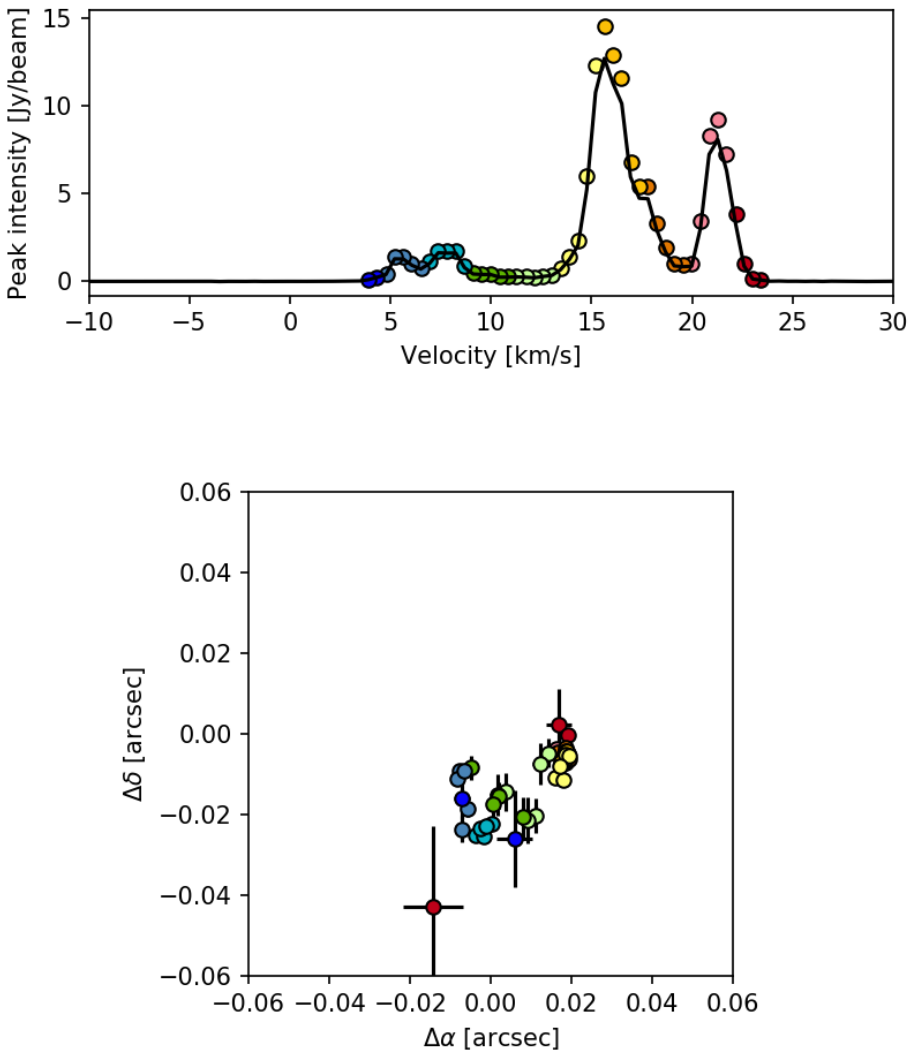

Figure 4.11: The observed $v = 1, J = 1 - 0$ SiO line emission toward R Crt. The upper panel shows the total intensity interferometric spectrum. The colored dots indicates channels in which component fits were performed; the color code indicates velocity. The fitted component positions in right ascension $\Delta\alpha$ and declination $\Delta\delta$ offset relative to the field center are shown in the lower panel; line segments indicate position errors.

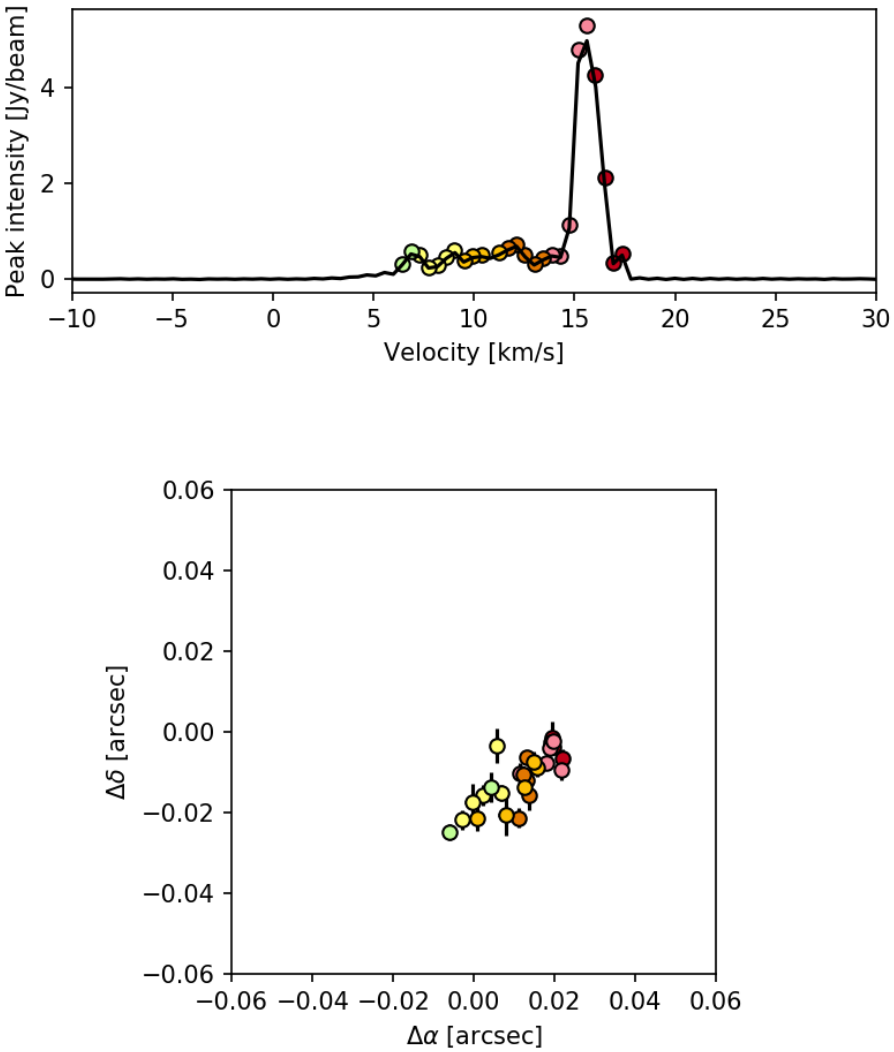

Figure 4.12: The observed $v = 2, J = 1 - 0$ SiO line emission toward R Crt. The upper panel shows the total intensity interferometric spectrum. The colored dots indicates channels in which component fits were performed; the color code indicates velocity. The fitted component positions in right ascension $\Delta\alpha$ and declination $\Delta\delta$ offset relative to the field center are shown in the lower panel; line segments indicate position errors.

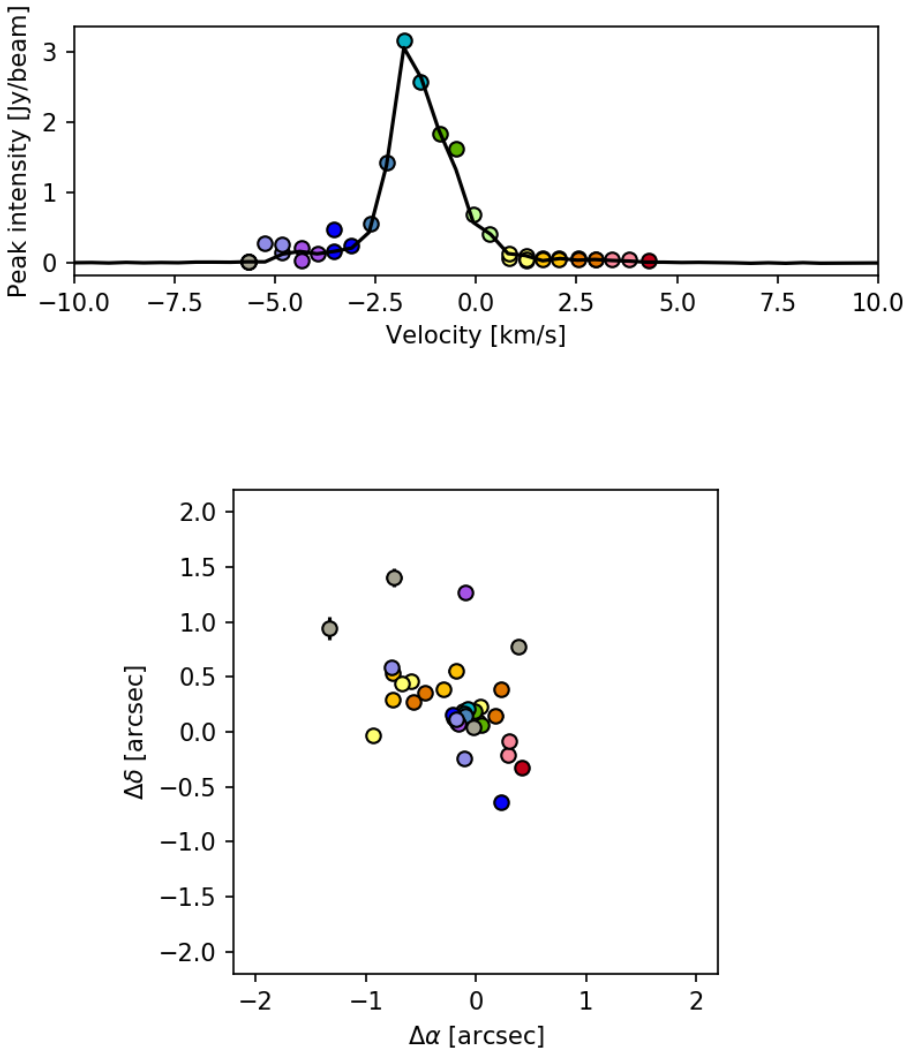

Figure 4.13: The observed $v = 0, J = 1 - 0$ SiO line emission toward R Leo. The upper panel shows the total intensity interferometric spectrum. The colored dots indicates channels in which component fits were performed; the color code indicates velocity. The fitted component positions in right ascension $\Delta\alpha$ and declination $\Delta\delta$ offset relative to the field center are shown in the lower panel; line segments indicate position errors.

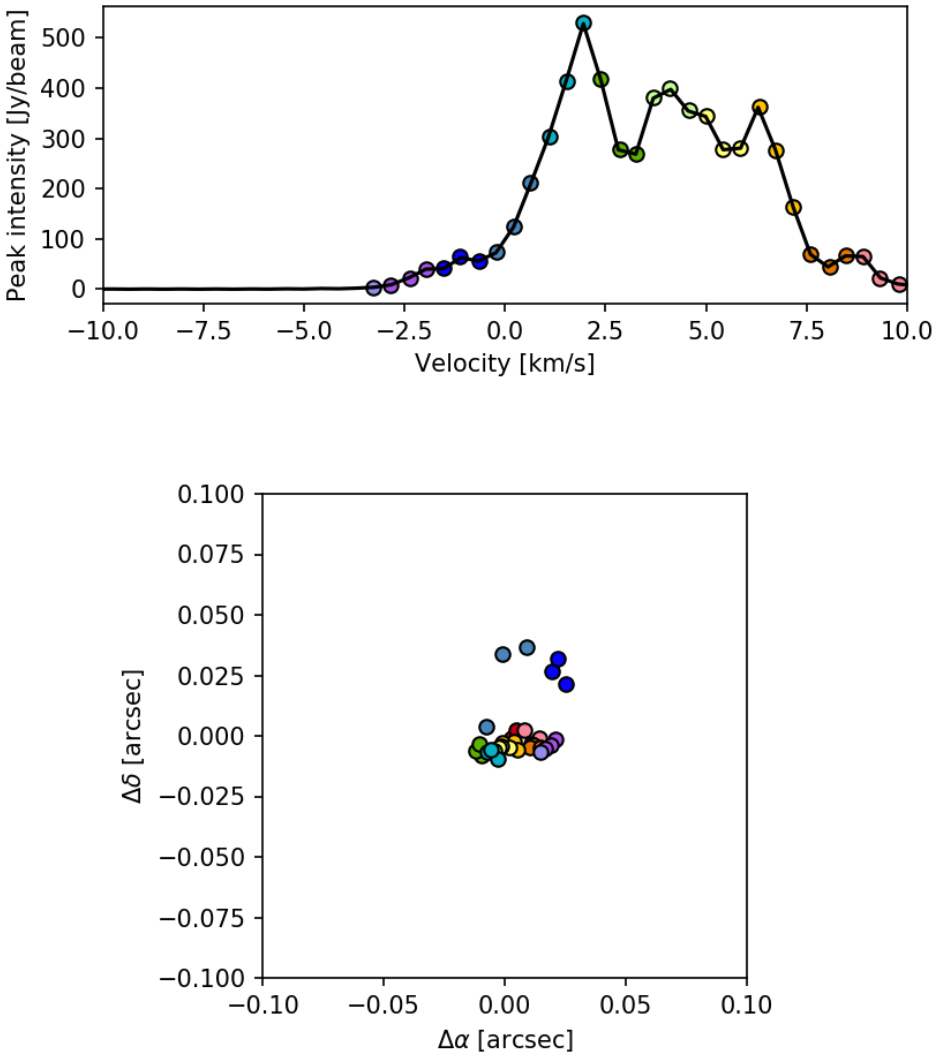

Figure 4.14: The observed $v = 1, J = 1 - 0$ SiO line emission toward R Leo. The upper panel shows the total intensity interferometric spectrum. The colored dots indicates channels in which component fits were performed; the color code indicates velocity. The fitted component positions in right ascension $\Delta\alpha$ and declination $\Delta\delta$ offset relative to the field center are shown in the lower panel; line segments indicate position errors.

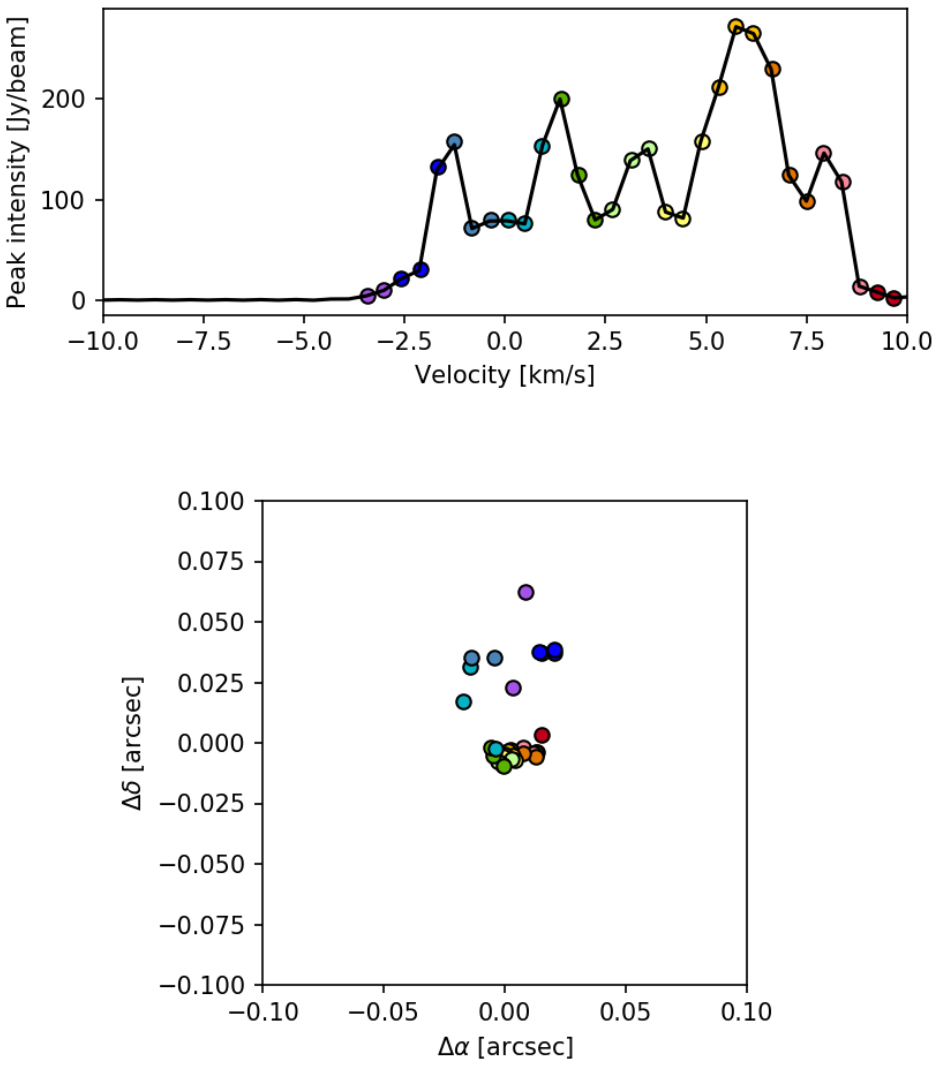

Figure 4.15: The observed $v = 2, J = 1 - 0$ SiO line emission toward R Leo. The upper panel shows the total intensity interferometric spectrum. The colored dots indicates channels in which component fits were performed; the color code indicates velocity. The fitted component positions in right ascension $\Delta\alpha$ and declination $\Delta\delta$ offset relative to the field center are shown in the lower panel; line segments indicate position errors.

4.5 Conclusion

We have observed with the VLA the $v = 0, J = 1 - 0$ SiO and $v = 0, J = 1 - 0$ CS transitions as tracers of the magnetic field through the G-K effect, and the $v = 1, 2; J = 1 - 0$ SiO maser lines as tracers for Zeeman effect in Q band observations toward the sources R Crt and R Leo. We have detected the SiO $v = 0, 1, 2; J = 1 - 0$ transitions and their associated polarization properties. The detected high linear polarization fractions in the SiO $v = 0, J = 1 - 0$ transition for both R Crt and R Leo suggests that this transition in both targets may include maser features. We analyzed the detected brightness temperature T_b in comparison to the gas kinetic temperature T_b estimated in the region of the SiO $v = 0, J = 1 - 0$ emission. The estimated values satisfy $T_b \gtrsim T_k$, suggesting at least the observation in this transition for R Leo presents maser emission. We also analyzed the spatial distribution of each spectral components for both targets for all three $v = 0, 1, 2$ transitions to seek the possible correlations between spectral component at the line center and spatial distribution. At our spatial resolution, we do not confirm such a spectral-spatial association. However, we note that the $v = 0$ components tend to be more extended spatially compared to other $v \geq 1$ counterparts. We report no detection in the CS $v = 0, 1; J = 1 - 0$ transition in both targets with the most sensitive results after self-calibration. We also report no detection in continuum polarization, possibly because of the sensitivity limitation and the expected dust component.

Chapter 5

Mapping magnetic fields in star-forming regions with ALMA

Massive stars ($M \gtrsim 8M_{\odot}$) have short Kelvin-Helmholtz timescales compared to other relevant evolutionary timescale (such as accretion time), thus they are expected to influence their environment soon after a proto-stellar core has formed (Garay and Lizano, 1999). At their earliest evolutionary stage, the mass accretion from the surrounding dense molecular gas in the proto-stellar envelope continues even after the ignition of hydrogen burning (Kahn, 1974; Garay and Lizano, 1999). The newly formed massive stars also produce energetic, ionizing photons that later creates an ultracompact (UC) HII region [1]. In other words, the UC HII regions are manifestations of newly formed massive stars that are still embedded in their natal molecular clouds (Churchwell, 2002). The UC HII regions are small ($\lesssim 0.1$ pc), very dense (typically $\gtrsim 10^4$ cm^{-3}), and bright (with emission measures $\gtrsim 10^7$ pc cm^{-6}) (Churchwell, 2002; Hoare et al., 2007) The copious UV radiation and the radiation-induced strong stellar wind from the massive stars interact with the interstellar medium that these objects are shrouded in (Hoare et al., 2007).

The UC HII region complex G10.6-0.4 is a well studied OB-cluster star-forming region (Caswell et al., 1975; Ho and Haschick, 1981; Ho et al., 1983, 1986, 1994; Keto et al., 1987, 1988, 2008; Guilloteau et al., 1988; Keto, 1990, 2002; Omodaka et al., 1992; Sollins et al., 2005; Sollins and Ho, 2005; Keto and Wood, 2006; Klaassen et al., 2009) at distance $\sim 4.95 - 6$ kpc (Caswell et al., 1975; Downes et al., 1980; Sanna et al., 2014). The detected high bolometric luminosity ($\sim 10^6 L_{\odot}$) and bright free-free continuum emission in this molecular cloud suggest that a cluster of O-type stars has formed (Ho and Haschick, 1981). In previous high angular resolution observations with molecular lines and dust continuum, a ~ 10 pc scale organized structure has been revealed, with filamentary geometry at ~ 5 pc scale and lower that might link to the central $\lesssim 1$ pc scale flattened rotating accretion flow (Keto et al., 1987; Liu et al., 2010, 2011, 2012).

G10.6-0.4 is one of the most luminous HII regions with embedded OB stars and thus is a good template for investigating the massive star formation processes (Wong and An, 2018), which surely includes the influence of the magnetic field. In this project, we studied the molecular cloud G10.6-0.4 in continuum, CO, and CN linear polarization observations with ALMA to explore the magnetic field in this high-mass star forming region, and to understand the role of magnetic fields in the high-mass star-formation process. These data comprised ALMA project with proposal ID: 2016.1.00187.S (PI: Richard Crutcher, CoI: Athol Kemball).

[1] The term was coined by Israel et al. (1973). And the UC HII regions were first distinguished from merely compact HII regions, and came to be defined observationally (Wood and Churchwell, 1989; Hoare et al., 2007)

5.1 Observation

The observations of G10.6-0.4 were performed with the Atacama Large Millimeter Array (ALMA) in Band 3 and in full Stokes mode in C43-3 configuration, with resolution achieved $\sim 1.7''$. The observing run was executed on April 13th, 2018, with total duration ~ 5 hours. The observation was split into five execution blocks (EBs). The correlator was configured in full Stokes mode to observe the polarization properties of the CN $N = 1 - 0$ hyperfine lines and the CO $J = 1 - 0$ line. The adopted transition rest frequencies were: 113.1442 GHz ($J = 1/2-1/2, F = 1/2-3/2$ CN), 113.1705 GHz ($J = 1/2-1/2, F = 3/2-1/2$ CN), 113.1913 GHz ($J = 1/2 - 1/2, F = 3/2 - 3/2$ CN), 113.4881 GHz ($J = 3/2 - 1/2, F = 3/2 - 1/2$ CN), 113.4910 GHz ($J = 3/2 - 1/2, F = 5/2 - 3/2$ CN), 113.4996 GHz ($J = 3/2 - 1/2, F = 1/2 - 1/2$ CN), 113.5089 GHz ($J = 3/2 - 1/2, F = 3/2 - 3/2$ CN) (Crutcher et al., 1996; Crutcher and Kemball, 2019); and 115.271 GHz ($J = 1-0$ CO) (Lovas et al., 2009). These transitions were observed in narrow-band (line) spectral windows. The CN spectral window covers the $N = 1 - 0$ hyperfine transitions and is of bandwidth $\triangle\nu = 468.75$ MHz sampled over 1920 frequency channels with a corresponding nominal velocity resolutions of ~ 0.646 km/s. The CO spectral window covers the CO $J = 1 - 0$ transition and is of bandwidth $\triangle\nu = 234.375$ MHz sampled over 1920 frequency channels with a corresponding nominal velocity resolutions of ~ 0.317 km/s. In addition, two wide-band (continuum) spectral windows were observed each of bandwidth $\triangle\nu = 2.0$ GHz and sampled over 64 frequency channels.

In this observation, J1924-2914 was used as the bandpass calibrator, Ganymede was used as the flux calibrator, J1832-2039 as the gain (phase and amplitude) calibrator, and J1733-1304 (NRAO 530) was used as the polarization calibrator.

5.2 Data Reduction

The data reduction process is derived from the automated scripts provided along with the data delivery from the observatory. The calibration was performed with the scripts in the Common Astronomy Software Applications package (CASA; version 5.1.1). In the default mode of reduction (see Figure 5.1), each execution block (EB) data has its own parallel-hand calibration script module. The 5 parallel-hand calibrated EBs were concatenated, then the polarization calibration and imaging process was then performed in this default track.

To optimize the calibration solution quality, we proceed with a merged calibration script solving for bandpass and gain calibration that applies to the full concatenated data (see Figure 5.2). After preliminary calibration (e.g. for antenna position errors) and before solving for the bandpass and gain solution, the line and continuum spectral windows are split by spectral resolution (see Figure 5.2), as the sensitivity and solution quality will vary by channel width. This choice improves the consistency in the flagging and calibration process. The polarization calibration and the imaging process were performed after the parallel-

hand calibration for bandpass and gain. In addition to these changes in data reduction workflow, we also performed further flagging based on the calibration solution and data quality.

5.2.1 Calibration

The reduction process generally follows the standard on-axis reduction for ALMA polarization data (Nagai et al., 2016; Hull et al., 2020). The bandpass solution was determined using bandpass calibrator J1924-2914 with a preliminary phase-gain solution applied on-the-fly. The amplitude and phase gain calibration followed, assuming an unpolarized source model for the calibrators. All calibrators were self-calibrated, while the gain solution from the gain calibrator J1832-1304 was transferred to our science target G10.6-0.4. The phase and amplitude gain were solved for X and Y polarization receptors independently (*gaintyp='G'*). A simplified flowchart is listed in the upper half of Figure 5.3.

5.2.2 Polarization Calibration

A condensed flowchart for the polarization calibration is listed in the lower half of Figure 5.3. All solutions in the polarization calibration process are derived using the polarization calibrator J1733-1304 (NRAO 530), the cross-hand delay ($\mathbf{K_{crs}}$) and the XY phase offset at the reference antenna (**XY0**). A final source model ((I, Q, U) model) of J1733-1304 is determined during the process of resolving the ambiguity in XY0 phase using the task `xyamb` from `almapolhelpers.py`. This J1733-1304 source model including an estimated Q and U components is then applied in a further gain calibration (**Gpol2**) to remove the residual polarization response from the gain amplitude (Hull et al., 2020). Finally, the leakage terms (D-terms, **Df0gen**) were derived, using the final source model and accumulated calibration solutions. A final gain offset (**Gxyamp**) was derived using the final source model and accumulated calibration solutions (including **Df0gen**) applied on-the-fly. The final calibration solutions were applied collectively at the end of the polarization calibration process.

5.2.3 Imaging and De-bias Process

After completing the full data calibration process, we performed imaging in I, Q, U, V components using the standard imaging task `tclean`. The primary beam correction was applied to all images using CASA task `impbcor`.

The statistical information was derived from the Q and U images for use in the debiasing calibration (Wardle and Kronberg, 1974) using CASA task `immath`. After de-biasing, the polarization intensity and EVPA maps were produced.

5.3 Quality Assurance

We review the three major diagnostics in verifying the calibration quality in general. These diagnostics include: the calibration solution behavior, the corrected data properties, and the full Stokes images of the calibrator(s). In this section the key results from these diagnostics are presented.

A. SOLUTION BEHAVIOR

All the solutions applied to our data are presented for four selected antennas: DA46, DA50, DV14, DV22. The bandpass solution are plotted over frequency in Figure 5.4. The gain solutions (**G** are plotted over time in Figure 5.5.

B. DATA BEHAVIOR

It is also informative to review the calibration quality by inspecting the data behavior before and after the calibration is applied. We present data at three calibration stages: only with preliminarily processing, after the parallel-hand calibration, and with full calibration. Figure 5.6 reveals the data quality being improved in both the amplitude and phase behavior over frequency. Both the data scattering and the instrumental response over frequency has been greatly reduced after the parallel-hand calibration. Figure 5.7 shows the data quality being enhanced in both the amplitude and phase behavior over time. Both the data scattering and the instrumental response over time has been greatly reduced after the parallel-hand calibration. Figure 5.8 shows the data quality being enhanced by the reduced scattering on the complex plane, especially noticeable in the case for the calibrator J1733-1304.

C. STOKES MAPS of CALIBRATED DATA

The dynamic range of the calibrator J1733-1304 polarization intensity maps was shown to be improved from ~ 30 to ~ 60 by polarization calibration. Figure 5.9 shows the IQU maps for J1733-1304 before and after the polarization calibration with. This comparison of the map product reveals that the polarization calibration did improve the data as anticipated.

5.4 Results

Here we discuss the dust continuum and CO line polarization results based on the initial calibration described above (Section 5.2). The full results will be expanded upon in future publications.

The linear polarization results for the continuum emission are summarized in Table 5.1. We detect continuum emission toward G10.6-0.4 of 2.10 ± 0.0031 Jy/beam. These values are measured at the peak-brightness pixel and the uncertainty is statistical error from the off-source image region and do not include any systematic errors in the absolute flux density calibration.

The maximum detected CO linear polarization intensity (P_p), the peak total intensity at the associated pixel and velocity channel (I_p) in the molecular line, and the derived peak fractional linear polarization ($m_{\ell,p}$) and the error-weighted polarization angle (χ_{wav}, or $\bar{\chi}$) are also summarized in Table 5.1. The measured EVPA for G10.6-0.4 in the dust continuum maps ranges from 20.7° to −1.56° over the angular extent of the source with an error-weighted average $\chi_{wav} = 7.1°$ as cited in Table 5.1 as the representative value for the field. The measured EVPA for G10.6-0.4 in the $J = 1 - 0$ CO maps ranges from 90.0° to −90° over the angular and frequency extent of the source with an error-weighted average $\chi_{wav} = -9.4°$ as cited in Table 5.1 as the representative value for the field. These average values are taken from point detections with statistical significance exceeding 3σ in polarization intensity and 10σ in total intensity, and the samples generally cover a velocity width $\Delta v = -14.7.0 \sim 48.5$ km/s, and extend over physical scales of ~ 30 arcseconds on the plane of the sky. This physical extent is approximately ~ 0.7 pc if we estimate assuming a distance of 4.95 kpc (Sanna et al., 2014).

We estimated both a random error (σ_{wav}) and a systematic error (σ_{sys}) in the measured EVPA values. Each measured EVPA is assigned a statistical uncertainty following Wardle and Kronberg (1974). We estimated the systematic error by inspecting the observation from the external survey Analytic Matrix for ALMA POLArimetry (AMAPOLA)[2] with the most adjacent observing time. J1733-1304 was observed in 97.5-GHz band by AMAPOLA on Apr. 13, 2018 obtaining a total intensity 2.972 ± 0.052 Jy, linear polarization intensity 0.029 Jy, and EVPA $-47.9 \pm 11.2°$. We observed J1733-1304 to have a total intensity of 2.87 Jy, linear polarization intensity of 0.018 Jy, and EVPA of −68.7°. We give the estimate of the systematic EVPA error using the difference of the measured EVPA in this two, which is 20.8°. The systematic EVPA error is dominated by the rapid intrinsic fluctuation of the quasar calibrators used in this analysis. These estimated errors are listed in Table 5.1.

Table 5.1: Polarization properties at the position of peak linearly-polarized intensity in the spectral-line image cube and the dust continuum result.

Source	Emission	v_{LSR} [km s^{-1}]	P_p [Jy beam^{-1}]	I_p [Jy beam^{-1}]	$m_{\ell,p}$ [%]	$\bar{\chi}$ [°]
G10.6-0.4	Dust continuum	–	0.032	2.10	1.52 (64.0σ)	7.1
	σ	–	0.00050	0.0031	–	$\pm 2.7 \pm 20.8$
	CO (J=1-0)	4.30	0.048	2.11	2.28 (11 σ)	-9.4
	σ	–	0.0044	0.064	–	$\pm 0.016 \pm 20.8$

5.5 Analysis and Discussion

Based on the results presented, several analyses were performed. We inspected both the total intensity line profile from the CO ($J = 1 - 0$) (Section 5.5.1) and the detected dust continuum polarization (Section

[2]http://www.alma.cl/ skameno/AMAPOLA/

5.5.2). We also investigated the CO linear polarization results using further modeling of the G-K effect (Section 5.5.3).

5.5.1 Total Intensity Line Profile

The CO channel maps after continuum subtraction show significant optical and spectral structure. The channel maps reveal both emission and absorption features at various spatial locations. To systematically characterize this property, we examined grid spectra over the area of interest, and plotted the color-coded, pixel-base spectra in Figure 5.13.

In Figure 5.13, there seems to be a correlation between the spatial and spectral location, where we see more emission in the outer region, and absorption at the center of the region. In the analysis by Keto et al. (1987), they performed an opacity mapping derived from a comparison of the main-line versus satellite-line brightness of the NH_3 transitions. They also derived another opacity estimate based on the comparison of the line versus background continuum emission. The observed absorption features, coming from the gas in the line-of-sight to the HII region, have velocities that are always redshifted with respect to the velocities seen in emission that occur spatially away from the HII region implying an infall velocity of 5 ± 1.7 km s^{-1} (Keto et al., 1987). Their analysis of opacity distribution, along with the temperature and density distribution show strong velocity gradient with rotational motion across the HII region (Keto et al., 1987). The estimated velocity gradients from $0.7 \sim 3.0$ pc were found to be consistent with Keplerian rotation; while within the inner 0.1 pc, the gas appears to be infalling toward the HII region, instead of being rotationally supported.

In our observation, the total intensity absorption feature does occur in the reshifted wing (see Figure 5.13). It will be important to continue a systematic analysis such following Keto et al. (1987) for this part of the data, including analyzing Stokes QUV profiles on top of the Stokes I profile.

5.5.2 Dust Continuum Polarization

Liu et al. (2012) pointed out that, based on their no-detection of the dust continuum polarization with SMA, the linear polarization level of dust continuum of G10.6-0.4 at 0.87mm-wavelength was constrained to be lower than 2.8%. This is consistent with our results as 1.52% at 2.6mm after extrapolating their estimate to our observing frequency.

5.5.3 G-K Modeling of CO and Comparison with Observation

G-K Observations in the Literature

The G-K effect has been detected in several molecular species in a number of molecular clouds and their associated structures: CO (Greaves et al., 1999; Girart et al., 1999; Greaves et al., 2001; Lai et al., 2003; Cortes et al., 2005; Cortes and Crutcher, 2006; Cortes et al., 2006, 2008; Beuther et al., 2010; Li and Henning, 2011; Houde et al., 2013; Ching et al., 2016), CS (Forbrich et al., 2008), HCO+ (Glenn et al., 1997b), and

SiO (Lee et al., 2014). The reported peak (best SNR) CO linear polarization levels are often at ~ 0.5 to a few percent level (Greaves et al., 1999; Girart et al., 1999; Greaves et al., 2001; Lai et al., 2003; Cortes et al., 2005; Cortes and Crutcher, 2006; Cortes et al., 2006; Beuther et al., 2010; Houde et al., 2013; Ching et al., 2016). Our results as presented in Table 5.1 are consistent with this range.

Analysis with G-K Modeling of This Work

Detailed modeling is necessary in order to determine if this linear polarization in the thermal $J = 1 - 0$ CO emission in the current data (as presented in Section 5.4) arises from the G-K effect and the associated underlying magnetic field geometry. For the relevant discussion concerning the alternative sources of CO polarization, see Section 3.5.2. Here we describe the detailed G-K modeling and the associated modeled results.

We adopted estimated physical parameters for G10.6-0.4 including cloud temperature and density from Keto (1990). In their Table 2, the estimated parameters are given at various physical scales. The two main observation scales from our observations are: 0.05 pc (from ~ 2 arcsec with our beam size of 2.17×1.67 arcsec), and 0.7 pc (physical scale of our region of interest). Based on these data, we currently choose a parameter space for G-K investigation as: $T \in [20, 40]$K, and $n \in [20, 2.0 \times 10^4]$ cm^{-3}.

In Figure 5.15 and 5.14, we show the G-K model results derived for 20K and 40K respectively. The model results show that our detection of linear polarization in the thermal $J = 1 - 0$ CO emission is broadly consistent.

5.6 Conclusion and Outlook

We have successfully detected dust continuum polarization and CO $J = 1 - 0$ linear polarization with ALMA in Band 3 toward a massive star-forming region G10.6-0.4. Significant properties has been shown with initial analysis. The detected dust continuum polarization is at 1.52% with a fairly concentrated spatial structure, and with error-weighted PA $\sim 7.1°$. The peak fractional linear polarization measured in the $J = 1 - 0$ CO line ($m_{\ell,p} \sim 2.28\%$) is consistent with the predicted signal strength from detailed G-K modeling. An interesting total intensity CO line profile has also been revealed, which demands further investigation in future work. The CN data included in this observation will be analyzed in future work as well.

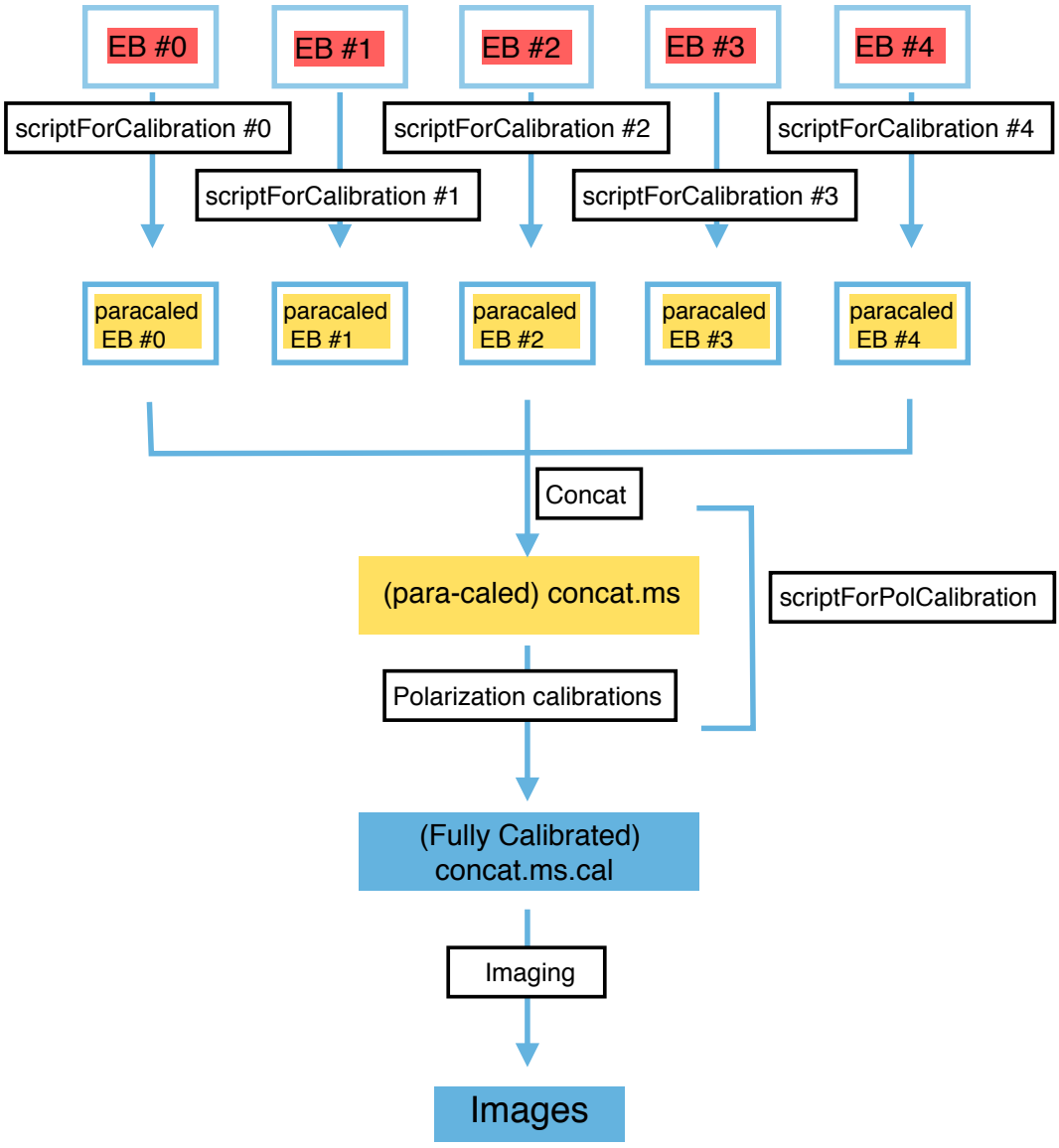

Figure 5.1: The flowchart of the default calibration process for ALMA spectral-line polarization data. The data from each execution block (EB) has its own parallel-hand calibration script module, and are merged before polarization calibration and imaging process.

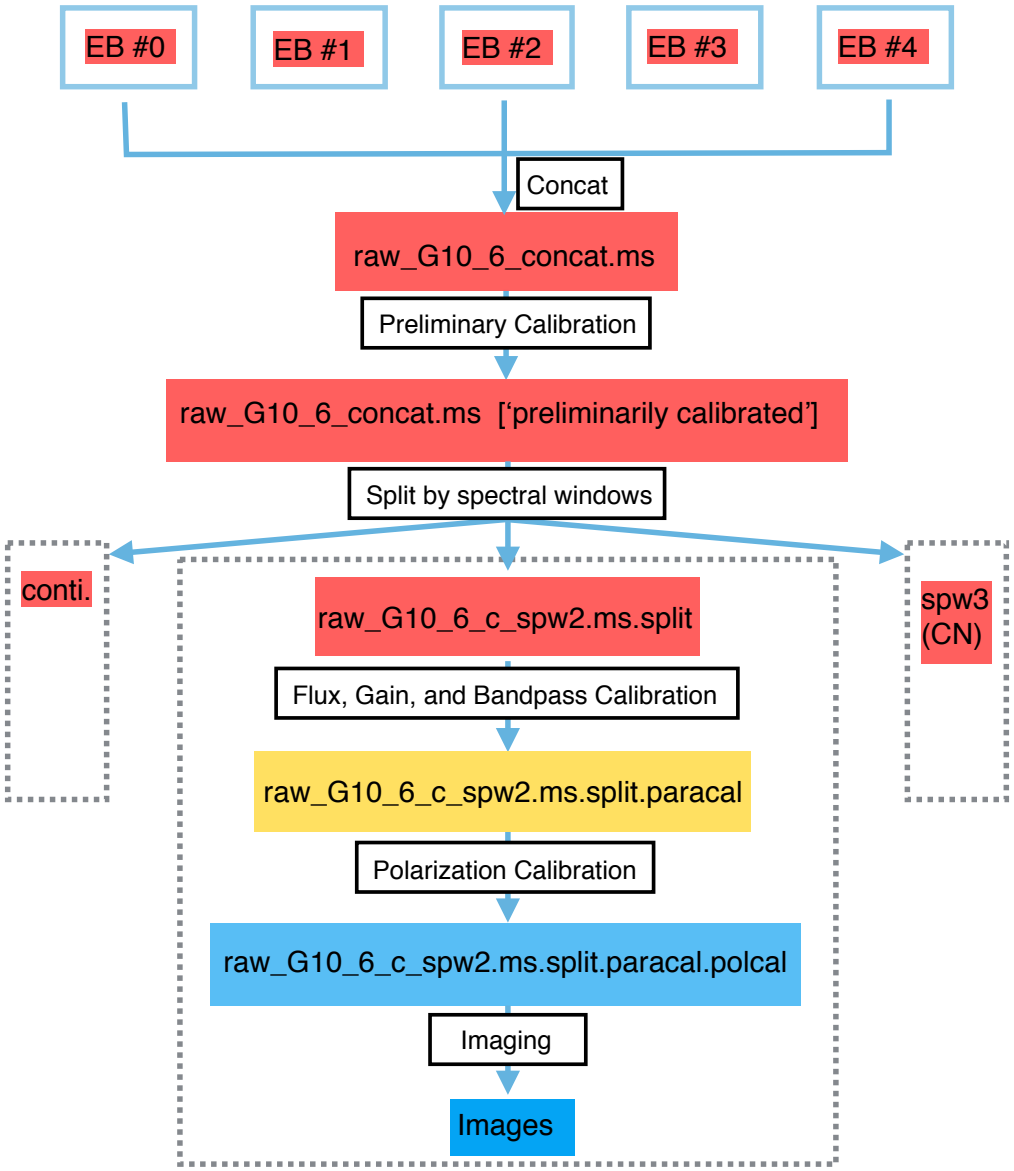

Figure 5.2: The flowchart of the modified calibration process for ALMA spectral-line polarization data for this work. This is a merged calibration workflow solving for bandpass and gain calibration that applies to the full concatenated data. The concatenated raw data comprises observations from execution block (EB) 0 to 4. After preliminary calibration, and before solving for the bandpass and gain solution, the line and continuum spectral windows are split by spectral resolution.

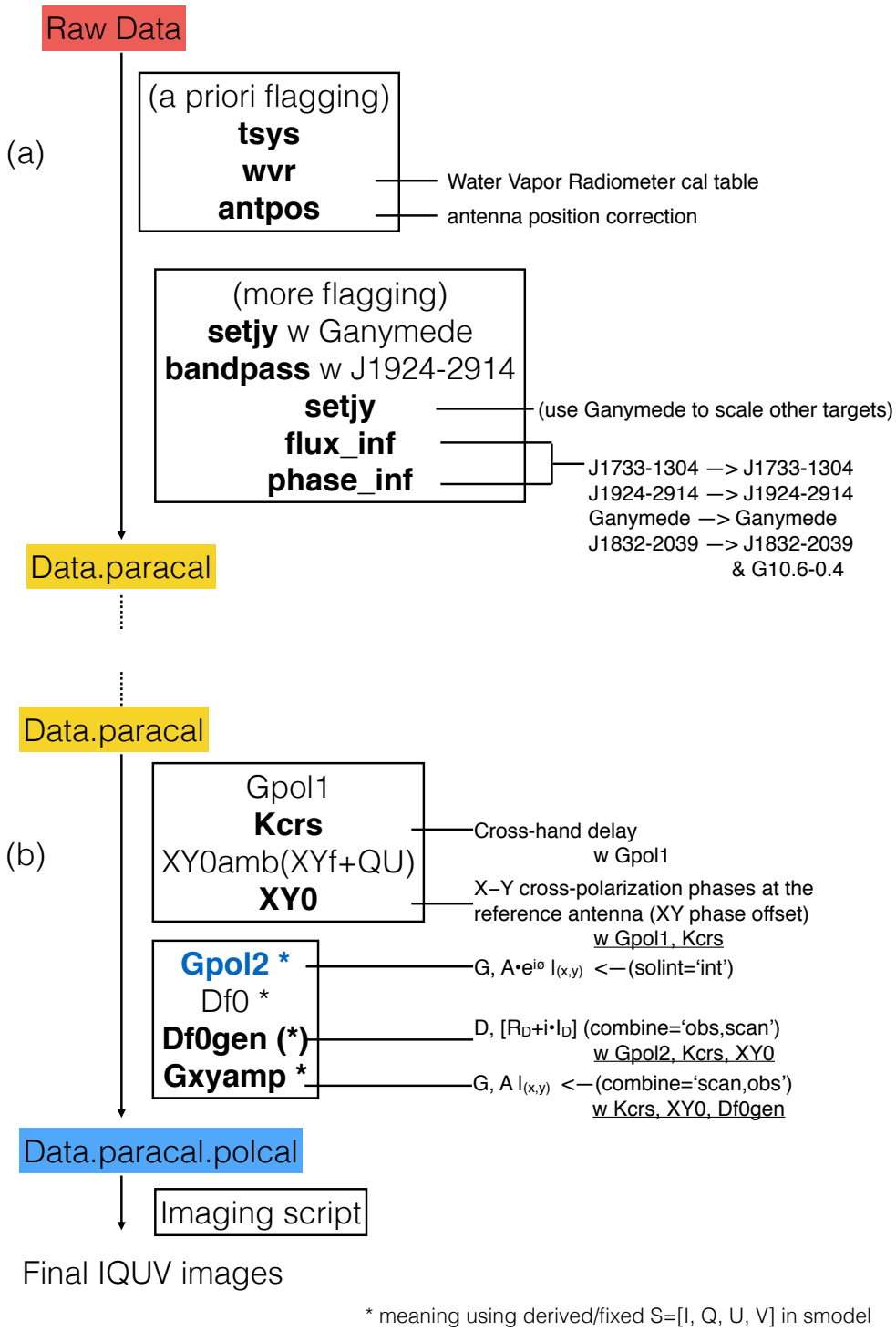

Figure 5.3: (a) An expansion of the box "Flux, Gain, and Bandpass Calibration" in Figure 5.2; (b) and expansion of the box "Polarization Calibration" in Figure 5.2 above.

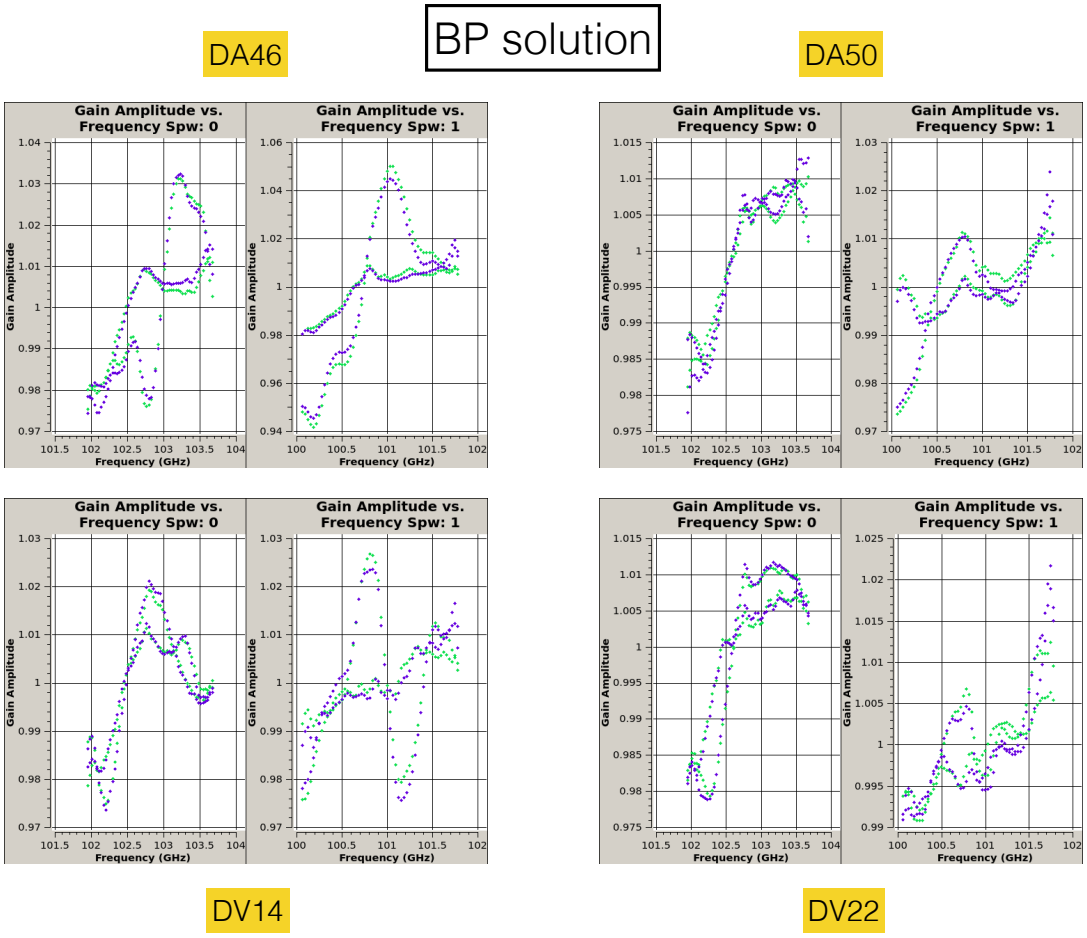

Figure 5.4: The derived bandpass solution for ALMA antennas DA46, DA50, DV14, and DV22 as labeled. The shown solutions are from the two continuum windows of observation, as labeled spw0 and spw1. The two colors marks the solution from two polarization receptors.

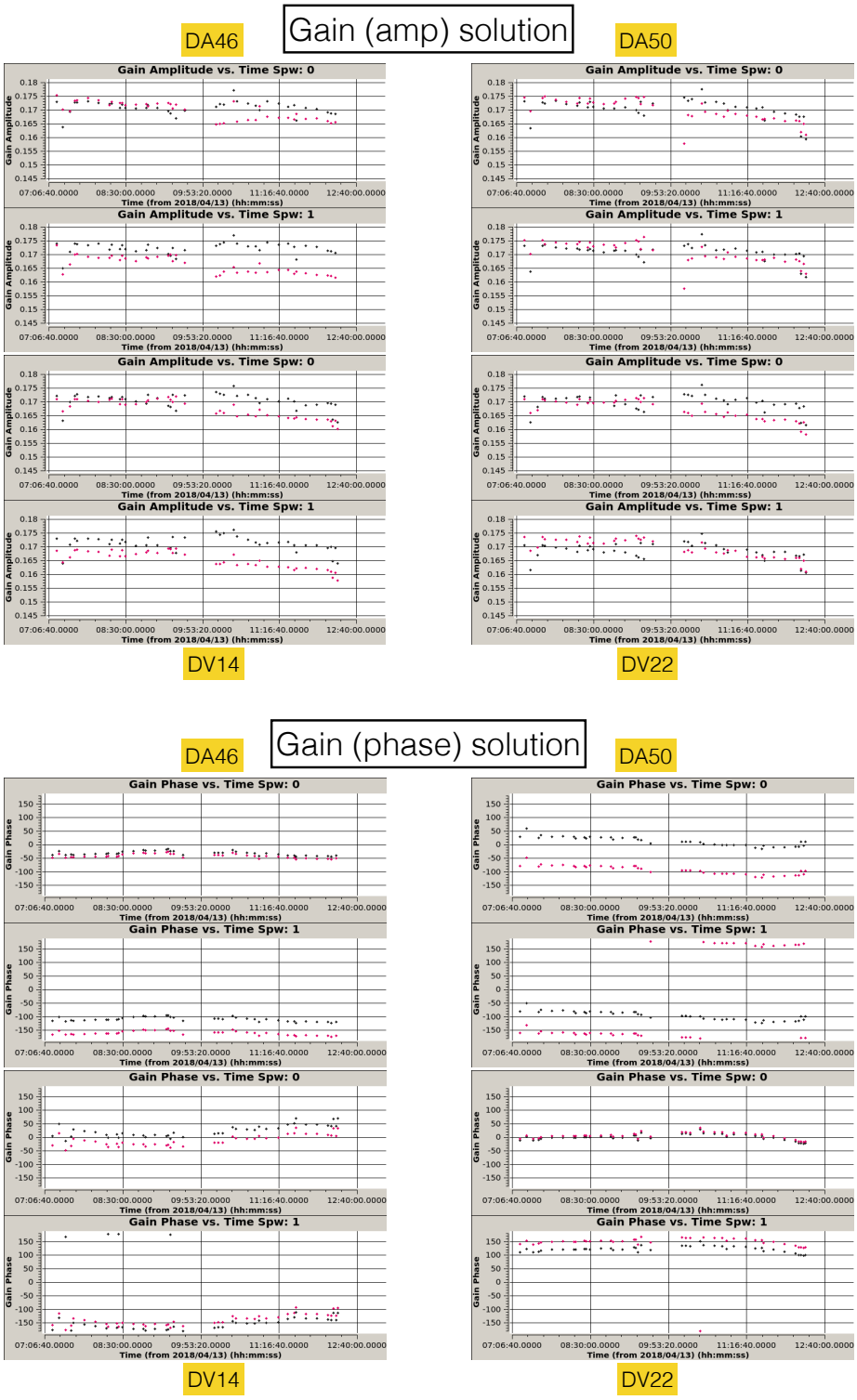

Figure 5.5: The derived gain solution (amplitude and phase) for ALMA antennas DA46, DA50, DV14, and DV22 as labeled. The shown two rows of solution in each antenna are from the two continuum windows of observation, as labeled spw0 and spw1. The two colors marks the solution from two polarization receptors.

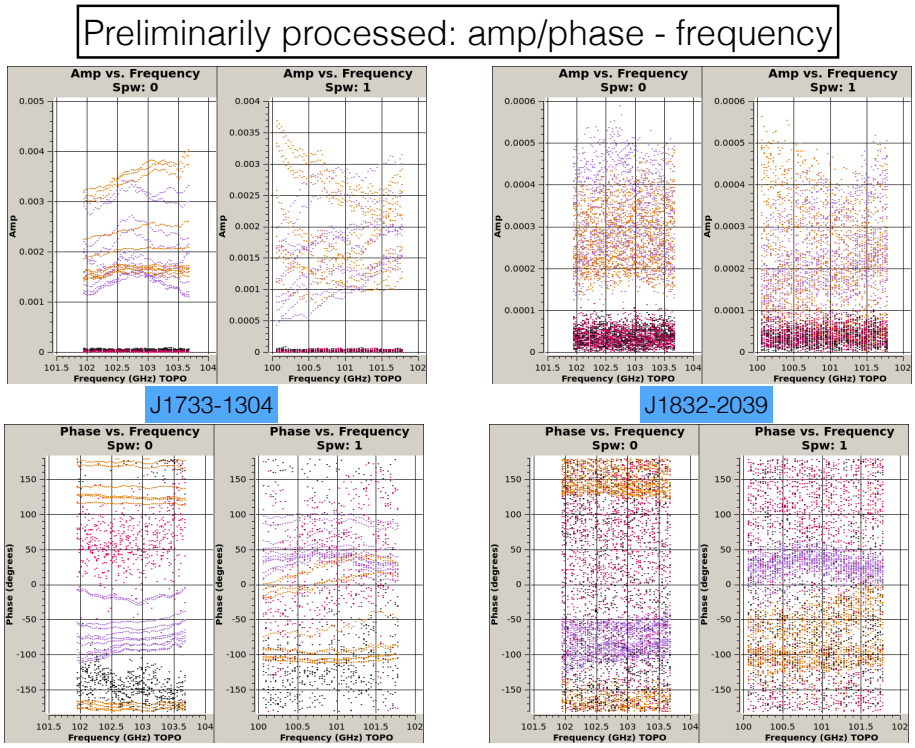

(a) The data behavior over frequency before the gain and bandpass calibration.

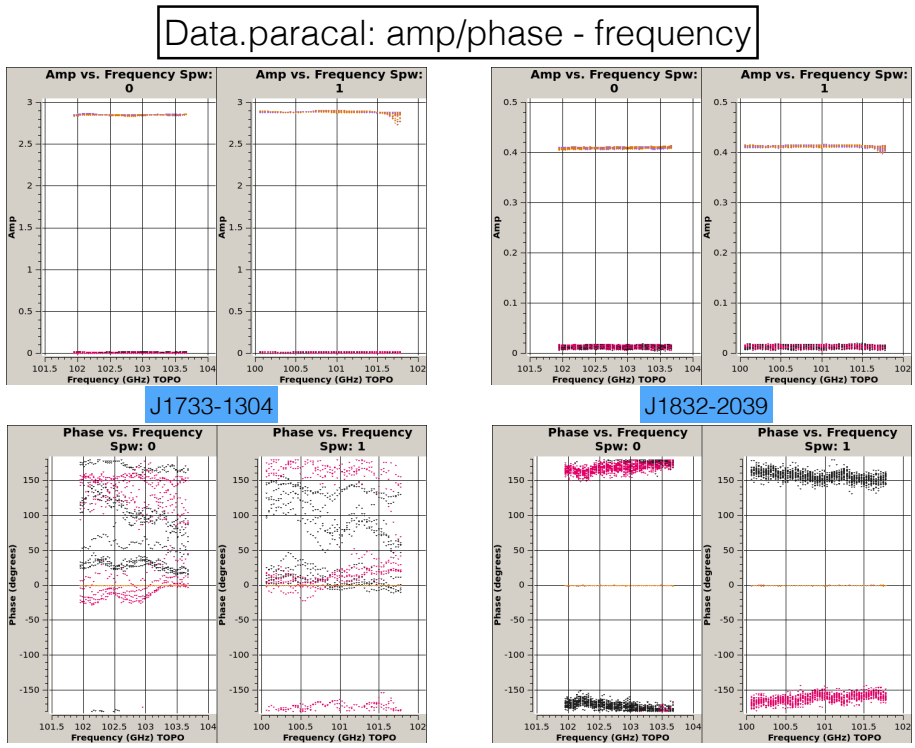

(b) The data behavior over frequency after the gain and bandpass calibration.

Figure 5.6: Data behavior over frequency of the calibrators J1733-1304 and J1832-2039 before and after the gain and bandpass calibration. The four colors mark the four correlator products: XX (purple), YY (orange), XY (magenta), and YX (black).

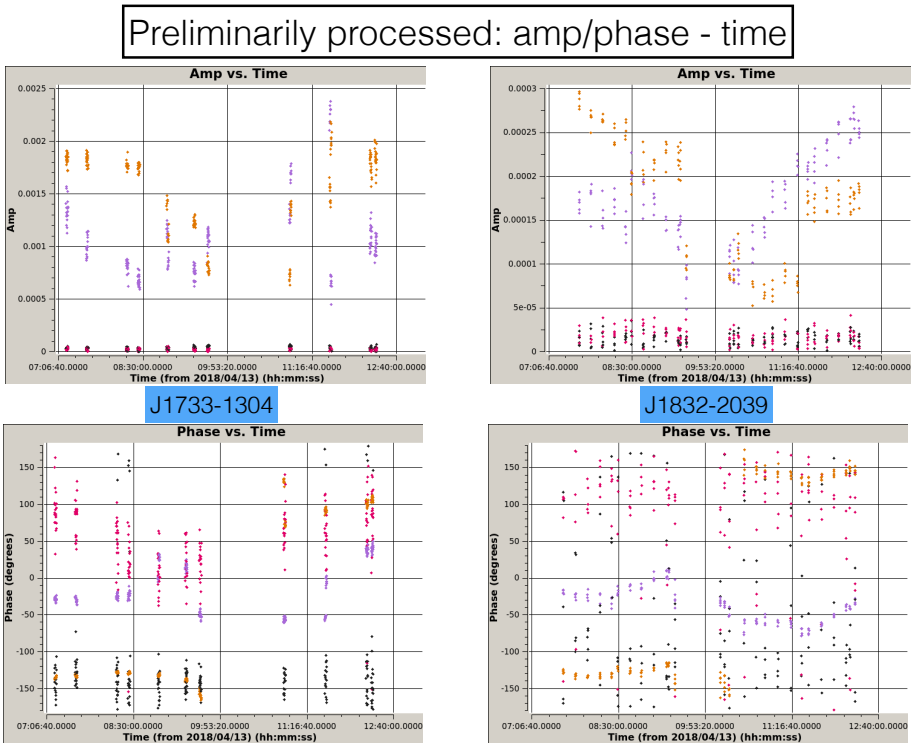

(a) The data behavior over time before the gain and bandpass calibration.

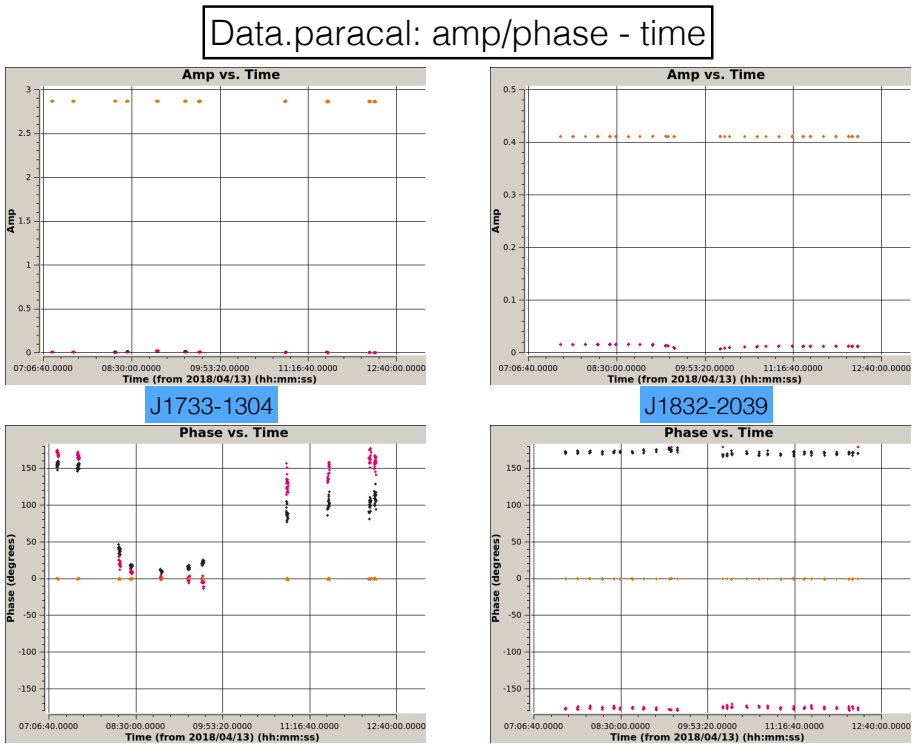

(b) The data behavior over time after the gain and bandpass calibration.

Figure 5.7: Data behavior over time of the calibrators J1733-1304 and J1832-2039 before and after the gain and bandpass calibration. The four colors mark the four correlator products: XX (purple), YY (orange), XY (magenta), and YX (black).

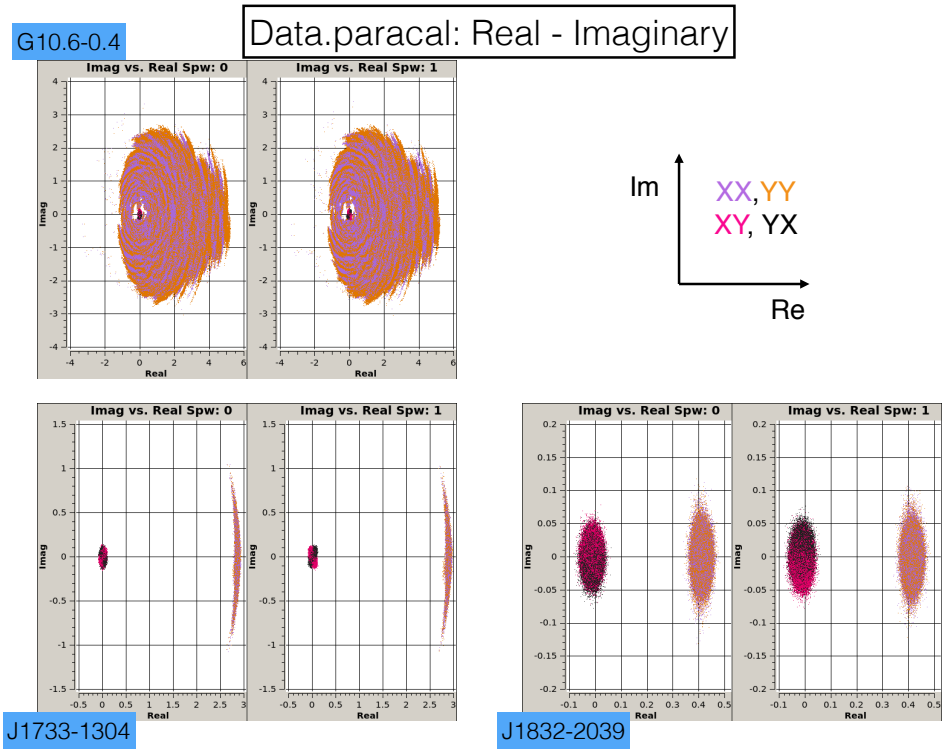

(a) The data behavior in the real-imaginary plane, before polarization calibration.

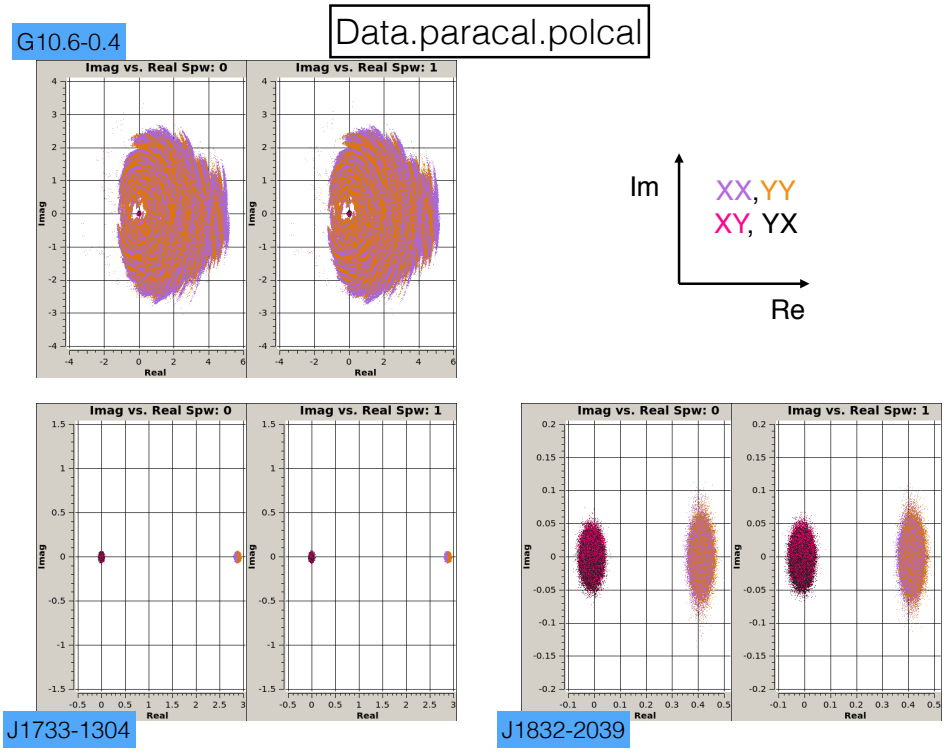

(b) The data behavior in the real-imaginary plane, after the polarization calibration.

Figure 5.8: Data behavior in the complex plane for the calibrators J1733-1304 and J1832-2039 before and after the polarization calibration. The four colors mark the four correlator products: XX (purple), YY (orange), XY (magenta), and YX (black).

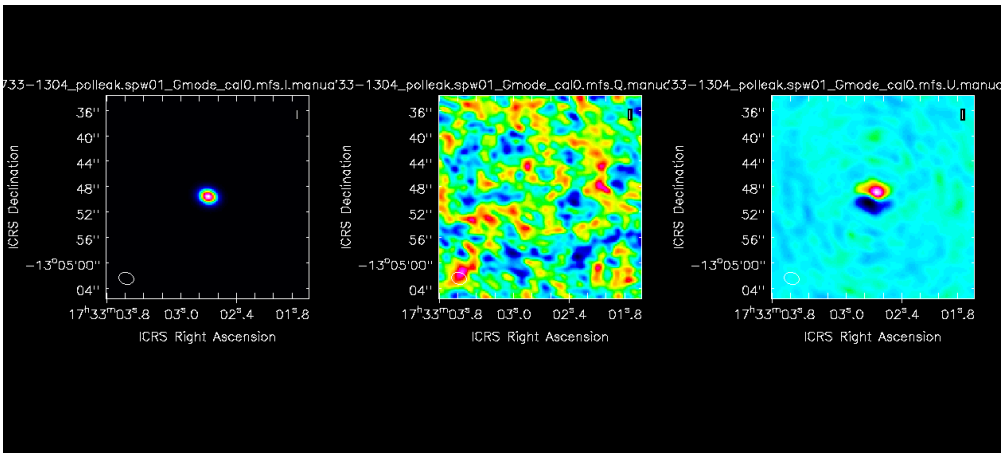

(a) The [I, Q, U] maps before the polarization calibration.

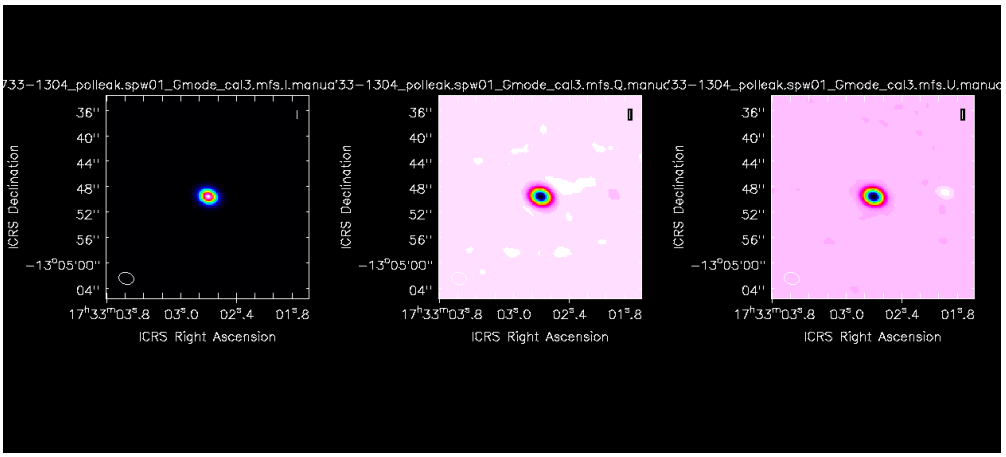

(b) The [I, Q, U] maps after the polarization calibration.

Figure 5.9: The [I, Q, U] maps for the calibrator J1733-1304: (a) before, and (b) after the polarization calibration. The left column shows the Stokes I images, the middle column shows the Stokes Q images, and on the right column the Stokes U images are shown. The color map shows the intensity of each Stokes component.

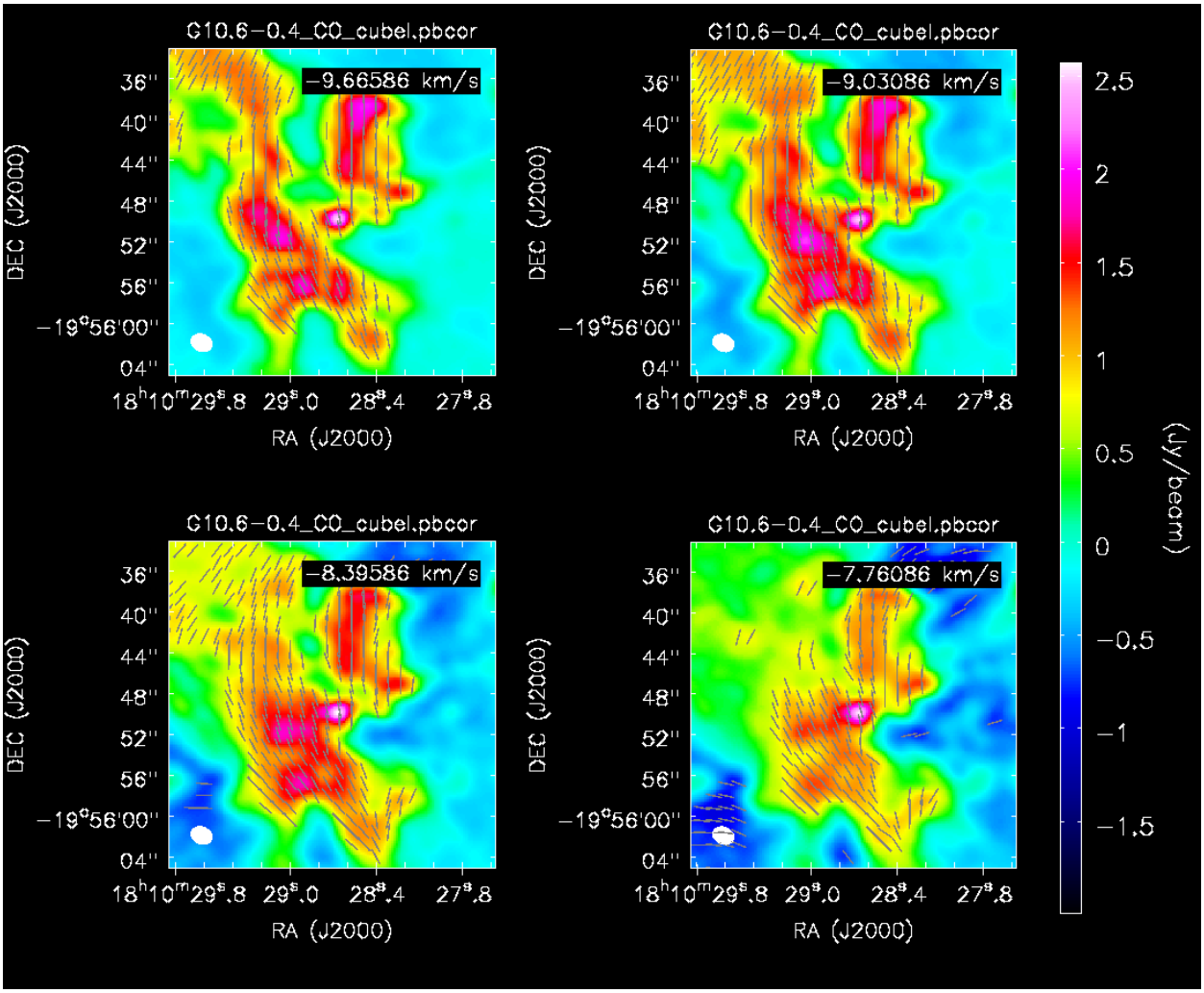

Figure 5.10: ALMA CO linear polarization channel maps part I: CO maps from velocity channel $v = -9.7$ km/s to -7.8 km/s. The CO total intensity is displayed in false colors, and the grey line segments indicate the EVPA orientation. EVPA vectors are not drawn for pixels with total intensity below $10\sigma_I$ or linear polarization intensity below $3\sigma_p$.

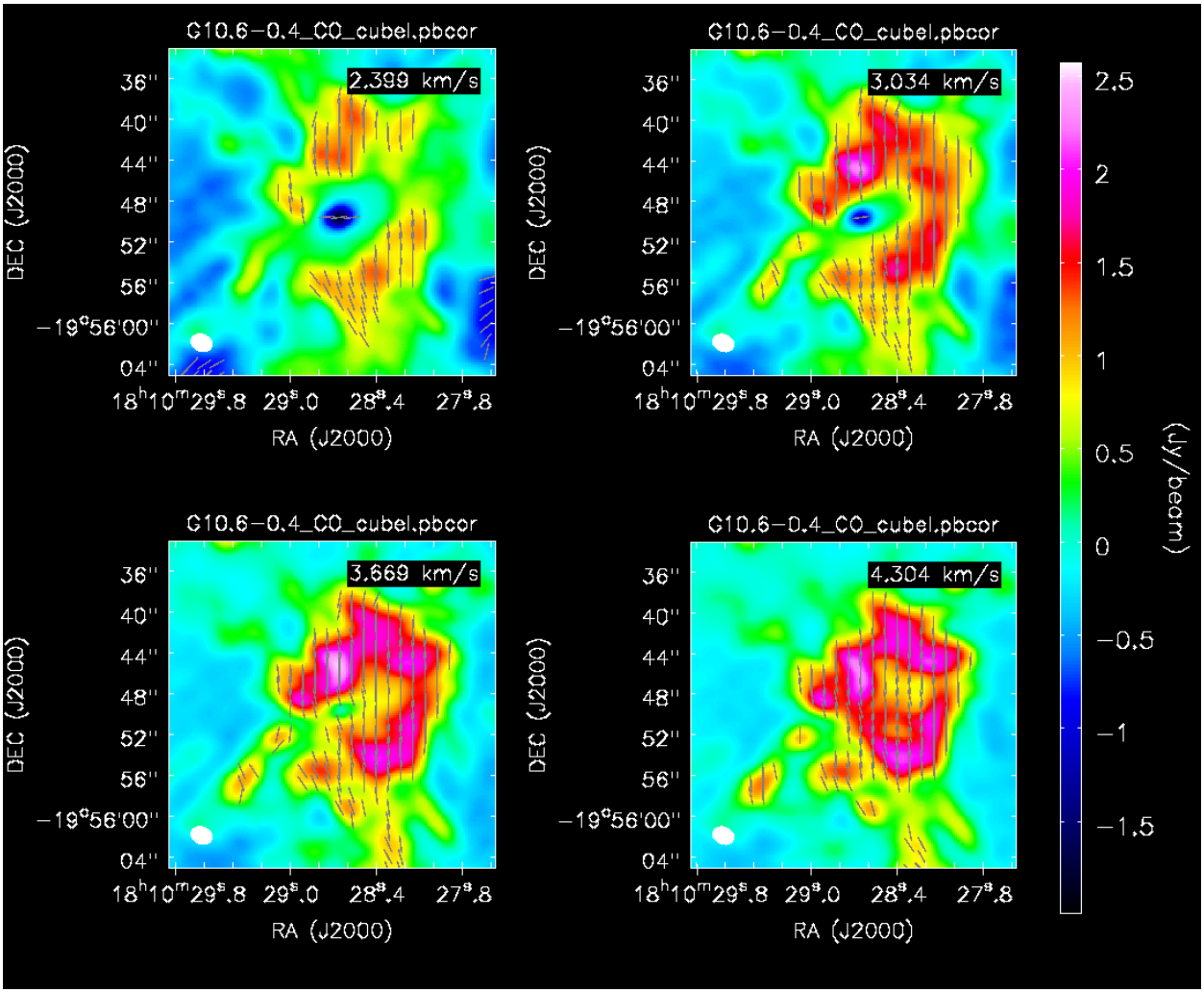

Figure 5.11: ALMA CO linear polarization channel maps part II: CO maps from velocity channel $v = 2.3$ km/s to 4.3 km/s. The CO total intensity is displayed in false colors, and the grey line segments indicate the EVPA orientation. EVPA vectors are not drawn for pixels with total intensity below $10\sigma_I$ or linear polarization intensity below $3\sigma_p$.

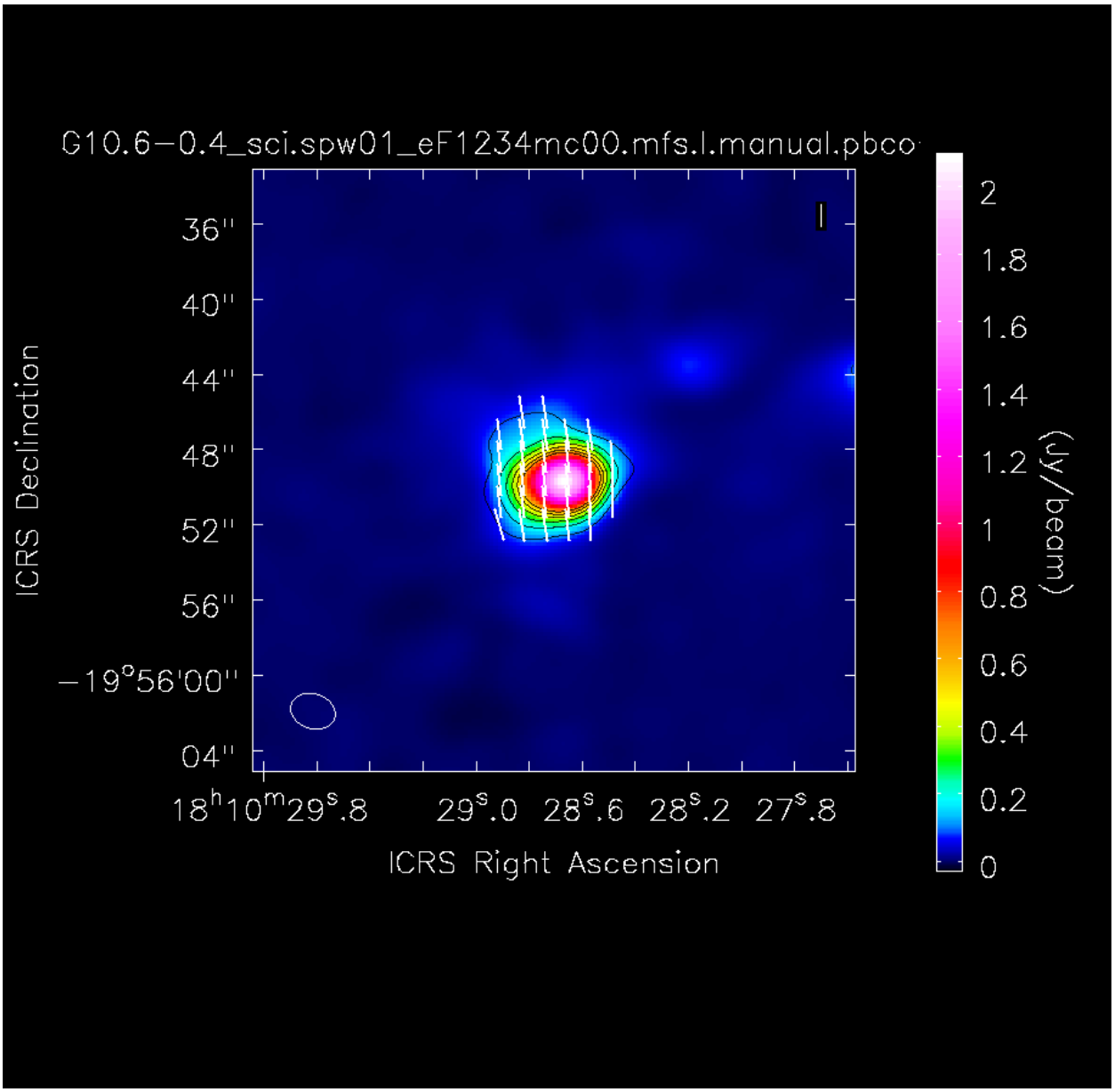

Figure 5.12: The ALMA dust continuum linear polarization map for G10.6-0.4. The continuum total intensity are displayed in false color, and white line segments indicate the EVPA orientation. EVPA vectors are not drawn for pixels with polarization intensity below $5\sigma_p$.

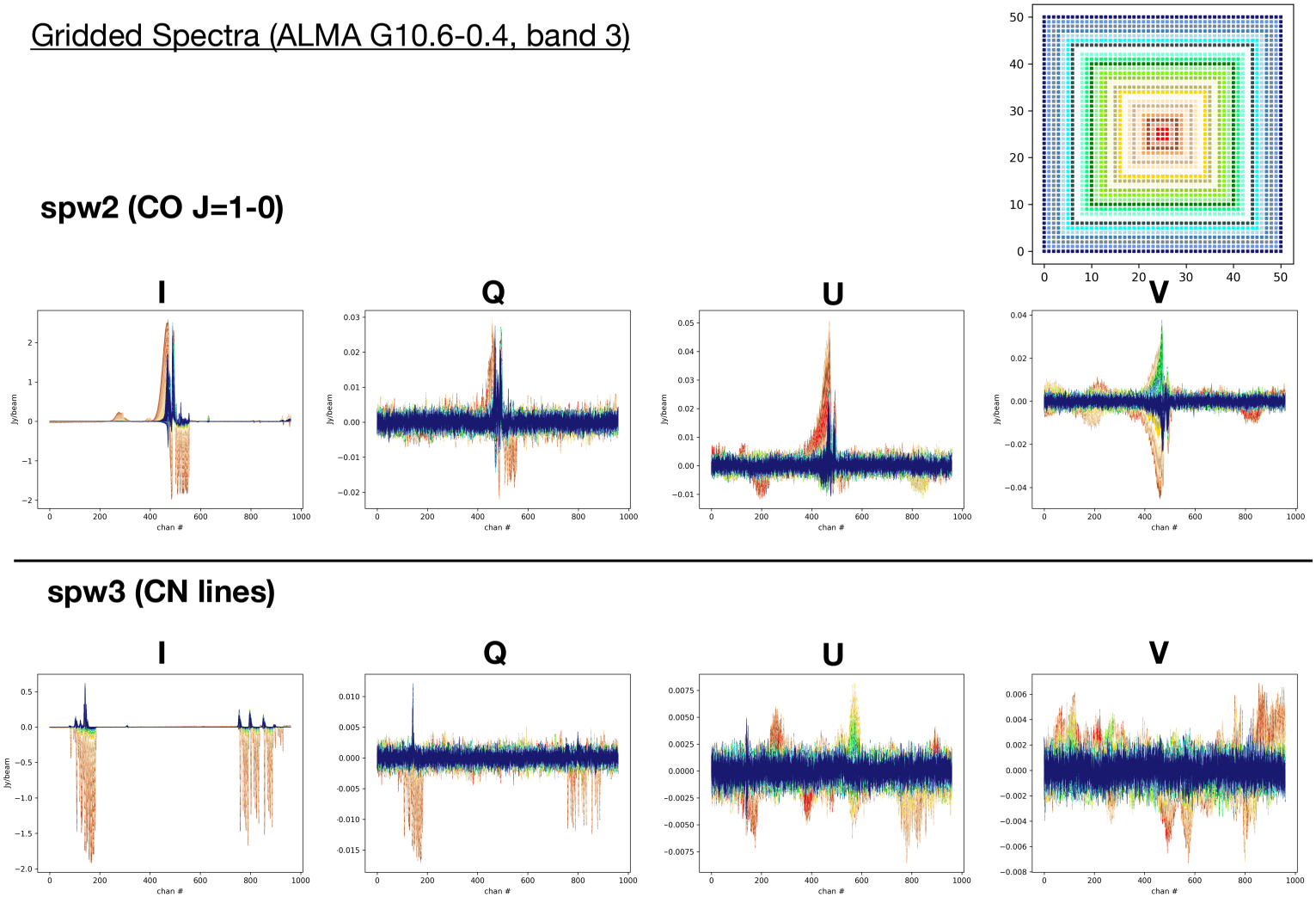

Figure 5.13: The grid Stokes IQUV spectra of G10.6-0.4 for both observed CO and CN line emission. A 50×50 pixel box in the image center was sampled to create this analysis, this corresponds to $10'' \sim 0.25$ pc scale. The CO results are displayed in the middle row. The CN results are displayed in the bottom row. The color arrangement is a general trend from red to blue, placed from the map phase center toward outer region as demonstrated in the square boxed region at the upper right corner.

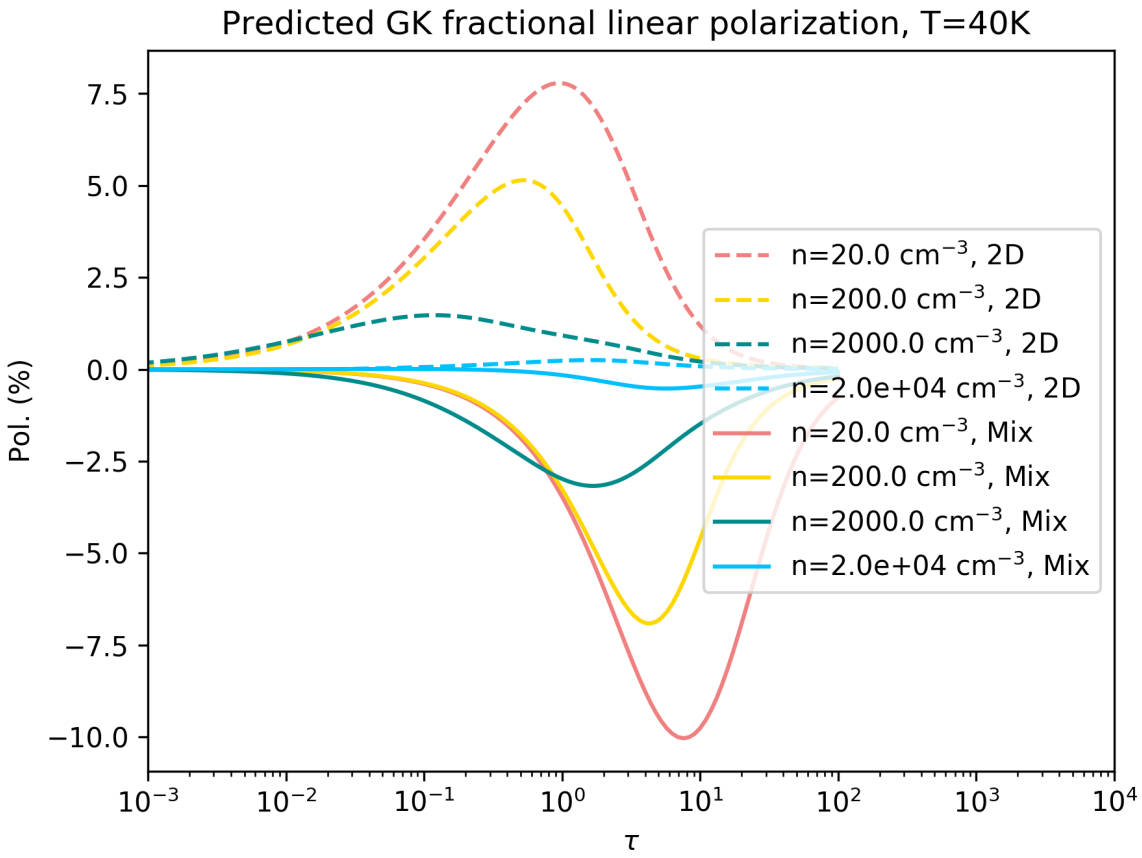

Figure 5.14: GK modeling with temperature of 40K using a density profile from 20 to 2.0×10^4 cm^{-3}. The model with different densities are marked with designated colors. The dashed lines mark the models with 2-D LVG geometry. The solid lines mark the models with mix(1-D + 2-D) LVG geometry.

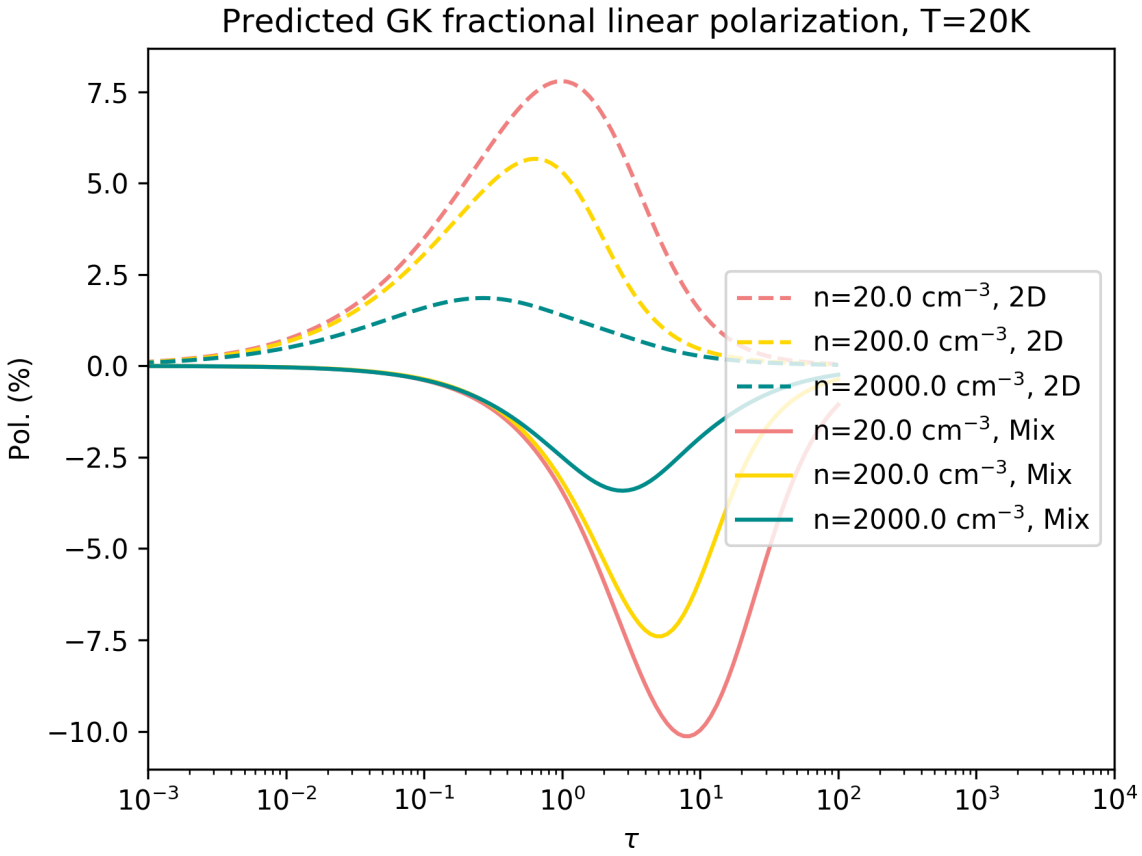

Figure 5.15: GK modeling with temperature of 20K using a density profile from 20 to 2.0×10^3 cm^{-3}. The model with different densities are marked with designated colors. The dashed lines mark the models with 2-D LVG geometry. The solid lines mark the models with mix(1-D + 2-D) LVG geometry.

Chapter 6

Summary- Conclusion and Future Work

Magnetic fields are ubiquitous in the universe yet present a perennial challenge to our detailed understanding of astrophysics in many environments. In this work, we have explored synergistic observational approaches to explore the magnetic field in late-type evolved stars and star-forming regions.

In the case of circumstellar magnetic fields of late-type evolved stars, there are key uncertainties concerning both the morphology and magnitude of circumstellar magnetic fields around these objects (Leal-Ferreira et al., 2013; Lèbre et al., 2014; Duthu et al., 2017) and the relative dynamical influence of magnetic fields in shaping AGB mass-loss outflows relative to other proposed mechanisms such as wind interaction models and binarity (García-Segura et al., 1999, 2014; Matt et al., 2000; Blackman et al., 2001; Soker, 2006; Kwok et al., 1978; Frank et al., 1993; Balick and Frank, 2002; Soker, 2004; García-Segura et al., 2018; Frank et al., 2018). The radial dependence of the magnetic field strength in the CSE of AGB stars and the measured power-law index of the magnetic field strength dependence on radius R have driven discussions of competing arguments concerning the magnitude and origin of circumstellar fields around late-type evolved stars and their global or local morphology and dynamical influence (Blackman et al., 2001; Thomas et al., 1995; Nordhaus and Blackman, 2006; Soker, 2006; Soker and Zoabi, 2002; Soker, 2002).

In the case of star-forming regions, magnetic fields are important both on different size scales and throughout evolutionary stages of star formation. The magnetic field and turbulence are considered the main agents that support the cloud from collapsing against self gravity (Krumholz and Tan, 2007). Whether either of the two mechanisms, or a hybrid mode of both governs the star-formation process remains a matter of continuing debate.

6.1 Conclusions

Detecting magnetic fields remains technically challenging observationally and requires careful scientific and theoretical inference. In this work, we have focused on complimentary techniques with different technical and scientific biases in order to strengthen their joint scientific constraints on estimates of magnetic field properties. We have mapped the magnetic fields in the CSE of two AGB stars using CARMA combining observations of maser polarization, polarized dust emission, and the G-K effect (Goldreich & Kylafis 1981), auxiliary VLA observations have also been performed. We have also presented the mapping of the magnetic

field in a massive star-forming region G10.6-0.4 using ALMA observation of the G-K effect in the $J = 2 - 1$ CO and $J = 2 - 1$ CN transition, as well as dust continuum polarization emission. We summarize our prior conclusions in the following subsections.

6.1.1 Magnetic Field Morphology in Evolved Stars

We have successfully detected the G-K effect in thermal $J = 2 - 1$ CO line emission from the CSE of the TP-AGB stars R Leo and R Crt in λ1.3 mm full-Stokes observations with CARMA (Huang et al., 2020). A circumstellar envelope (CSE) model profile and the associated parameters are estimated and used as input to a more detailed modeling of the predicted linear polarization from the G-K effect in the $J = 2 - 1$ CO transition (Huang et al., 2020). The fractional linear polarization measured in the $J = 2 - 1$ CO line for R Crt ($m_l \sim 3.1\%$) is consistent with the predicted signal strength from detailed G-K modeling, while for R Leo the measured fractional linear polarization ($m_l \sim 9.7\%$) is higher than expected perhaps due to spatial filtering in the Stokes I. Our G-K modeling is able to resolve the directional degeneracy, placing the measured EVPA parallel to the magnetic field lines. We also have detected linear polarization in the $v = 1, J = 5 - 4$ SiO maser line toward the CSE of R Crt and R Leo with values in the range $m_l \sim 17 - 34\%$. Combining the inferred magnetic field orientation from our G-K mapping using polarized $J = 2 - 1$ CO transition and other intrinsic alignments published for these sources in the literature suggest that there is a more confined or directed magnetic field geometry in R Crt. These results from CARMA with associated modeling demonstrate that the G-K effect is a viable means of extracting information concerning magnetic field morphology in the CSE around late-type evolved stars at various depths in the envelope. These observations are profoundly sensitivity-limited compared to modern telescopes such as ALMA but are the first such observations with CARMA. And this confirms the scientific importance of observations of this nature (Vlemmings et al., 2012). At greater sensitivity, future in-depth morphological mapping of the circumstellar magnetic field around late-type stars is possible using a range of molecular species and the associated transitions. In addition, these G-K observations are complemented by associated Zeeman and continuum observations. This is a significant future area for ALMA.

Observing at Q band (λ7mm) with VLA, we have used $v = 0, J = 1 - 0$ SiO and $v = 0, J = 1 - 0$ CS transitions as potential tracers of the magnetic field through the G-K effect and $v = 1, 2; J = 1 - 0$ SiO maser lines as tracers of the Zeeman effect (Huang and Kemball, in prep). We have detected SiO $v = 0, 1, 2; J = 1 - 0$ transitions and their associated polarization properties toward R Crt and R Leo. The detected high linear polarization fractions, accompanied by an analysis of brightness temperature and kinetic temperature in SiO $v = 0, J = 1 - 0$ transition for both R Crt and R Leo, suggests that this transition in both targets may involve maser features, limiting the usefulness as a G-K tracer. We also analyzed the spatial distribution of each spectral components for both targets for all three $v = 0, 1, 2$ transitions with the intent of understanding the spatial and spectral morphology. Our analysis shows that the $v = 0$ components

tend to be more extended spatially compared to other $v \geq 1$ counterparts.

6.1.2 Magnetic Field in Star-Forming Region

We have successfully detected dust continuum polarization and CO $J = 1 - 0$ linear polarization with ALMA in Band 3 toward a massive star-forming region G10.6-0.4. As noted earlier, we do not describe the associated CN data in the current work. The initial analysis has yielded rich scientific properties. The detected dust continuum polarization is of order $m_{\ell,p} \sim 1.52\%$, with a predominantly concentrated spatial structure, and an error-weighted PA $\sim 7.1^{\circ}$. The peak fractional linear polarization measured in the $J = 1-0$ CO line ($m_{\ell,p} \sim 2.28\%$) is consistent with the predicted signal strength from detailed G-K modeling. A highly structured total intensity CO line profile has also been revealed, where detailed properties will be the subject of future work.

6.2 Outlook for Future Work

6.2.1 ALMA G10.6-0.4 Polarization Observation

Dynamic and Kinetic Structure of G10.6-0.4

The dynamic and kinetic structure of G10.6-0.4 is of immediate future interest. The total intensity CO and CN line profiles revealed in our initial analysis will be compared with the apparent optical depth τ_{app} following Keto et al. (1987):

$$\tau_{app} = -\ln\left(1 + \frac{T_{line}}{T_{continuum}}\right) \tag{6.1}$$

as well as in work on associated radiative transfer analysis.

A specific focus is a comparison with the hierarchically organized structure in G10.6-0.4 from 0.1 to 10 pc scale revealed by Liu et al. (2012).

G-K Modeling Analysis and the Velocity Gradient Technique

We have earlier presented the G-K modeling analysis of expected linear polarization in the $J = 1 - 0$ CO line. The next goal is to model the $J = 1 - 0$ CN hyperfine lines in the G-K effect. The comparison between the magnetic field morphology revealed by the CN hyperfine lines versus the $J = 1 - 0$ CO transition will be scientifically important.

Current G-K modeling of the CO $J = 1-0$ transition is based on an initial exploration over a range of gas temperature and density derived by Keto (1990). We have multiple approaches that can potentially improve the current investigation. It is possible to conduct a radiative transfer analysis to obtain a more detailed view of the temperature and density profile over the regions where we have a G-K detection, especially comparing the regions of emission versus absorption. In addition, the G-K predicted linear polarization includes a

sign which indicates the relative alignment between the EVPA and the local magnetic field orientation (positive meaning perpendicular, negative meaning parallel). For example, as shown in Figure 5.15, the predicted EVPA alignment with respect to the local magnetic field for the 2-D and mix (1-D plus 2-D) LVG geometry are different. Thus we have the potential to constrain the local LVG geometry based on a more refined temperature and density profile. Moreover, we may follow Cortes et al. (2005) in adding the external continuum radiation source to represent emission from dust in a compact source. Our current G-K code (Huang et al., 2020) is based on the work by Yang and Lai (2010) and has been implemented with this feature in the current work, and we can explore this property in a systematic manner.

We have also planned through collaboration to compare the mapped magnetic field orientation of G10.6-0.4 by G-K effect with the predicted magnetic field orientation via the velocity gradient technique (VGT) (González-Casanova and Lazarian, 2017). It is proposed that strong Alfvénic turbulence develops eddy-like motions that are perpendicular to the orientation of local magnetic fields (González-Casanova and Lazarian, 2017). The velocity gradient developed from such local alignment will be perpendicular to the local magnetic field orientation (González-Casanova and Lazarian, 2017). Initial exploration of the method is underway.

CN Zeeman Effect

The CN Zeeman effect has been previously observed towards G10.6-0.4 by Crutcher et al. (1996) and remains a target of our future analysis of these data.

6.2.2 3-D Magnetic Field Morphology Mapping of AGB stars

The CSE of late-type stars contain a wealth of molecular species that can be used as tracers for multiple physical properties including the local magnetic field. As mentioned earlier, at greater sensitivity, future in-depth morphological mapping of the circumstellar magnetic field around late-type stars is possible using a range of molecular species and the associated transitions as tracers of the G-K effect. These molecular tracers can be sensitive to different physical scales in the CSE, depending on the synthesis and the dissociation of these molecules that occurs at different envelope scales. Given the relatively ordered LVG geometry in the CSE of AGB stars, a 3-D, layered G-K mapping of the magnetic is possible with facilities of exceptional sensitivity such as ALMA by observing even the weak molecular transitions in polarization studies.

In addition, these G-K observations are complemented by associated Zeeman and continuum observations as we have demonstrated in the current work.

6.2.3 The Molecular Environment of Nearby Galaxies

Molecules provide a unique and powerful probe of the complexity of the gas content, gas dynamics and kinematics in the cold part of our Universe across various physical scales. For nearby galaxies, molecular tracers have great potential in probing the dynamical and kinematic features, which will shed light on

the mechanism(s) at play that form substructures in the galaxies, and how the galaxies evolve through interactions with each other.

Through 3-D radiative transfer analysis (e.g. Lankhaar and Vlemmings (2020); Brinch and Hogerheijde (2010)), such observations have the potential to probe the dynamical and kinematic profile, and magnetic field morphology of the molecular environment in nearby galaxies in 3-D.

References

Agudo, I., Thum, C., Molina, S. N., Casadio, C., Wiesemeyer, H., Morris, D., Paubert, G., Gómez, J. L., and Kramer, C. (2018a). POLAMI: Polarimetric Monitoring of AGN at Millimetre Wavelengths - I. The programme, calibration and calibrator data products. , 474(2):1427–1435.

Agudo, I., Thum, C., Ramakrishnan, V., Molina, S. N., Casadio, C., and Gómez, J. L. (2018b). POLAMI: Polarimetric Monitoring of Active Galactic Nuclei at Millimetre Wavelengths - III. Characterization of total flux density and polarization variability of relativistic jets. , 473(2):1850–1867.

Akeson, R. L. (1997). *Millimeter Interferometric Polarimetry of Magnetic Field Structure in Protostellar Condensations*. PhD thesis, CALIFORNIA INSTITUTE OF TECHNOLOGY.

Arfken, G. B. and Weber, H. J. (2005). *Mathematical methods for physicists 6th ed.*

Balick, B. and Frank, A. (2002). Shapes and Shaping of Planetary Nebulae. , 40:439–486.

Beuther, H., Soler, J. D., Vlemmings, W., Linz, H., Henning, T., Kuiper, R., Rao, R., Smith, R., Sakai, T., Johnston, K., Walsh, A., and Feng, S. (2018). Magnetic fields at the onset of high-mass star formation. , 614:A64.

Beuther, H., Vlemmings, W. H. T., Rao, R., and van der Tak, F. F. S. (2010). Magnetic Field Structure in a High-mass Outflow/Disk System. , 724(1):L113–L117.

Blackman, E. G., Frank, A., Markiel, J. A., Thomas, J. H., and Van Horn, H. M. (2001). Dynamos in asymptotic-giant-branch stars as the origin of magnetic fields shaping planetary nebulae. , 409:485–487.

Boboltz, D. A. and Claussen, M. J. (2004). Ground-State SiO Maser Emission toward Evolved Stars. , 608(1):480–488.

Boboltz, D. A., Diamond, P. J., and Kemball, A. J. (1997). R Aquarii: First Detection of Circumstellar SiO Maser Proper Motions. , 487(2):L147–L150.

Born, M. and Wolf, E. (1959). *Principles of Optics Electromagnetic Theory of Propagation, Interference and Diffraction of Light*.

Bowen, G. H. (1988). Dynamical modeling of long-period variable star atmospheres. , 329:299–317.

Bower, G. C. (2014). G2 Monitoring at Submillimeter, Millimeter, and Radio Wavelengths. In *American Astronomical Society Meeting Abstracts #223*, volume 223 of *American Astronomical Society Meeting Abstracts*, page 108.02.

Brinch, C. and Hogerheijde, M. R. (2010). LIME - a flexible, non-LTE line excitation and radiation transfer method for millimeter and far-infrared wavelengths. , 523:A25.

Buhl, D., Snyder, L. E., Lovas, F. J., and Johnson, D. R. (1974). Silicon Monoxide: Detection of Maser Emission from the Second Vibrationally Excited State. , 192:L97–L100.

Bujarrabal, V., Planesas, P., and del Romero, A. (1987). SiO maser emission in evolved stars : relation to IR continuum. , 175:164–172.

Cantiello, M., Mankovich, C., Bildsten, L., Christensen-Dalsgaard, J., and Paxton, B. (2014). Angular Momentum Transport within Evolved Low-mass Stars. , 788(1):93.

Caselli, P. and Myers, P. C. (1995). The Line Width–Size Relation in Massive Cloud Cores. , 446:665.

Caswell, J. L., Murray, J. D., Roger, R. S., Cole, D. J., and Cooke, D. J. (1975). Neutral hydrogen absorption measurements yielding kinematic distances for 42 continuum sources in the galactic plan. , 45:239–258.

Chandrasekhar, S. and Fermi, E. (1953). Magnetic Fields in Spiral Arms. , 118:113.

Chen, Z., Nordhaus, J., Frank, A., Blackman, E. G., and Balick, B. (2016). Three-dimensional hydrodynamic simulations of L_2 Puppis. , 460:4182–4187.

Cherchneff, I., Barker, J. R., and Tielens, A. G. G. M. (1992). Polycyclic aromatic hydrocarbon formation in carbon-rich stellar envelopes. , 401:269–287.

Ching, T.-C., Lai, S.-P., Zhang, Q., Yang, L., Girart, J. M., and Rao, R. (2016). Helical Magnetic Fields in the NGC 1333 IRAS 4A Protostellar Outflows. , 819:159.

Churchwell, E. (2002). Ultra-Compact HII Regions and Massive Star Formation. , 40:27–62.

Cortes, P. and Crutcher, R. M. (2006). Interferometric Mapping of Magnetic Fields: G30.79 FIR 10. , 639(2):965–968.

Cortes, P. C., Crutcher, R. M., and Matthews, B. C. (2006). Interferometric Mapping of Magnetic Fields: NGC 2071IR. , 650(1):246–251.

Cortes, P. C., Crutcher, R. M., Shepherd, D. S., and Bronfman, L. (2008). Interferometric Mapping of Magnetic Fields: The Massive Star-forming Region G34.4+0.23 MM. , 676(1):464–471.

Cortes, P. C., Crutcher, R. M., and Watson, W. D. (2005). Line Polarization of Molecular Lines at Radio Frequencies: The Case of DR 21(OH). , 628:780–788.

Cotton, W. D., Ragland, S., Pluzhnik, E., Danchi, W. C., Traub, W. A., Willson, L. A., and Lacasse, M. G. (2009). SIO Masers in Asymmetric Miras. I. R Leonis. , 704:170–182.

Cox, N. L. J., Kerschbaum, F., van Marle, A.-J., Decin, L., Ladjal, D., Mayer, A., Groenewegen, M. A. T., van Eck, S., Royer, P., Ottensamer, R., Ueta, T., Jorissen, A., Mecina, M., Meliani, Z., Luntzer, A., Blommaert, J. A. D. L., Posch, T., Vandenbussche, B., and Waelkens, C. (2012). A far-infrared survey of bow shocks and detached shells around AGB stars and red supergiants. , 537:A35.

Crutcher, R. M. (2012). Magnetic Fields in Molecular Clouds. , 50:29–63.

Crutcher, R. M. and Kemball, A. J. (2019). Review of zeeman effect observations of regions of star formation. *Frontiers in Astronomy and Space Sciences*, 6:66.

Crutcher, R. M., Troland, T. H., Lazareff, B., and Kazes, I. (1996). CN Zeeman Observations of Molecular Cloud Cores. , 456:217.

Danilovich, T., Teyssier, D., Justtanont, K., Olofsson, H., Cerrigone, L., Bujarrabal, V., Alcolea, J., Cernicharo, J., Castro-Carrizo, A., García-Lario, P., and Marston, A. (2015). New observations and models of circumstellar CO line emission of AGB stars in the Herschel SUCCESS programme. , 581:A60.

Davis, L. (1951). The Strength of Interstellar Magnetic Fields. *Physical Review*, 81(5):890–891.

De Beck, E., Decin, L., de Koter, A., Justtanont, K., Verhoelst, T., Kemper, F., and Menten, K. M. (2010). Probing the mass-loss history of AGB and red supergiant stars from CO rotational line profiles. II. CO line survey of evolved stars: derivation of mass-loss rate formulae. , 523:A18.

de Vicente, P., Bujarrabal, V., Díaz-Pulido, A., Albo, C., Alcolea, J., Barcia, A., Barbas, L., Bolaño, R., Colomer, F., Diez, M. C., Gallego, J. D., Gómez-González, J., López-Fernández, I., López-Fernández, J. A., López-Pérez, J. A., Malo, I., Moreno, A., Patino, M., Serna, J. M., Tercero, F., and Vaquero, B. (2016). ^{28}SiO v = 0 J = 1-0 emission from evolved stars. , 589:A74.

Decin, L., De Beck, E., Brünken, S., Müller, H. S. P., Menten, K. M., Kim, H., Willacy, K., de Koter, A., and Wyrowski, F. (2010). Circumstellar molecular composition of the oxygen-rich AGB star IK Tauri. II. In-depth non-LTE chemical abundance analysis. , 516:A69.

Decin, L., Richards, A. M. S., Danilovich, T., Homan, W., and Nuth, J. A. (2018). ALMA spectral line and imaging survey of a low and a high mass-loss rate AGB star between 335 and 362 GHz. , 615:A28.

Deguchi, S. and Watson, W. D. (1984). Linear polarization of molecular lines at radio frequencies. , 285:126–133.

Diamond, P. J. and Kemball, A. J. (2003). A Movie of a Star: Multiepoch Very Long Baseline Array Imaging of the SiO Masers toward the Mira Variable TX Cam. , 599:1372–1382.

Diamond, P. J., Kemball, A. J., Junor, W., Zensus, A., Benson, J., and Dhawan, V. (1994). Observation of a ring structure in SiO maser emission from late-type stars. , 430:L61–L64.

Donati, J. F., Semel, M., Carter, B. D., Rees, D. E., and Collier Cameron, A. (1997). Spectropolarimetric observations of active stars. , 291(4):658–682.

Dorch, S. B. F. (2004). Magnetic activity in late-type giant stars: Numerical MHD simulations of non-linear dynamo action in Betelgeuse. , 423:1101–1107.

Downes, D., Wilson, T. L., Bieging, J., and Wink, J. (1980). H110alpha and H2CO survey of galactic radio sources. , 40:379–394.

Duari, D., Cherchneff, I., and Willacy, K. (1999). Carbon molecules in the inner wind of the oxygen-rich Mira IK Tauri. , 341:L47–L50.

Duthu, A., Herpin, F., Wiesemeyer, H., Baudry, A., Lèbre, A., and Paubert, G. (2017). Magnetic field in IRC+10216 and other C-rich evolved stars. , 604:A12.

Edwards, J. L., Cox, E. G., and Ziurys, L. M. (2014). Millimeter Observations of CS, HCO^+, and CO toward Five Planetary Nebulae: Following Molecular Abundances with Nebular Age. , 791:79.

Elitzur, M. (1980). The nature of SiO masers in late-type stars. , 240:553–566.

Elitzur, M. (1996). Polarization of Astronomical Maser Radiation. III. Arbitrary Zeeman Splitting and Anisotropic Pumping. , 457:415.

Etoka, S. and Le Squeren, A. M. (1997). OH eruptive Mira stars. , 321:877–887.

Feast, M. W., Glass, I. S., Whitelock, P. A., and Catchpole, R. M. (1989). A period-luminosity-colour relation for Mira variables. , 241:375–392.

Fiebig, D. and Guesten, R. (1989). Strong magnetic fields in interstellar H2O maser clumps. , 214:333–338.

Fish, V. L., Reid, M. J., Menten, K. M., and Pillai, T. (2006). Enhanced density and magnetic fields in interstellar OH masers. , 458:485–495.

Flower, D. R. (2001). The rotational excitation of CO by H_2. *Journal of Physics B Atomic Molecular Physics*, 34(13):2731–2738.

Forbrich, J., Wiesemeyer, H., Thum, C., Belloche, A., and Menten, K. M. (2008). Observations of the Goldreich-Kylafis effect in star-forming regions with XPOL at the IRAM 30 m telescope. , 492(3):757–766.

Frank, A., Balick, B., Icke, V., and Mellema, G. (1993). Astrophysical gasdynamics confronts reality - The shaping of planetary nebulae. , 404:L25–L27.

Frank, A., Chen, Z., Reichardt, T., De Marco, O., Blackman, E., and Nordhaus, J. (2018). Planetary Nebulae Shaped by Common Envelope Evolution. *Galaxies*, 6:113.

Frau, P., Girart, J. M., Zhang, Q., and Rao, R. (2014). Shaping a high-mass star-forming cluster through stellar feedback. The case of the NGC 7538 IRS 1-3 complex. , 567:A116.

Friedel, D. N. (2013). CADRE: The CArma Data REduction pipeline. *Astronomy and Computing*, 2:74–79.

Gaia Collaboration, Brown, A. G. A., Vallenari, A., Prusti, T., de Bruijne, J. H. J., Babusiaux, C., Bailer-Jones, C. A. L., Biermann, M., Evans, D. W., Eyer, L., Jansen, F., Jordi, C., Klioner, S. A., Lammers, U., Lindegren, L., Luri, X., Mignard, F., Panem, C., Pourbaix, D., Randich, S., Sartoretti, P., Siddiqui, H. I., Soubiran, C., van Leeuwen, F., Walton, N. A., Arenou, F., Bastian, U., Cropper, M., Drimmel, R., Katz, D., Lattanzi, M. G., Bakker, J., Cacciari, C., Castañeda, J., Chaoul, L., Cheek, N., De Angeli, F., Fabricius, C., Guerra, R., Holl, B., Masana, E., Messineo, R., Mowlavi, N., Nienartowicz, K., Panuzzo, P., Portell, J., Riello, M., Seabroke, G. M., Tanga, P., Thévenin, F., Gracia-Abril, G., Comoretto, G., Garcia-Reinaldos, M., Teyssier, D., Altmann, M., Andrae, R., Audard, M., Bellas-Velidis, I., Benson, K., Berthier, J., Blomme, R., Burgess, P., Busso, G., Carry, B., Cellino, A., Clementini, G., Clotet, M., Creevey, O., Davidson, M., De Ridder, J., Delchambre, L., Dell'Oro, A., Ducourant, C., Fernández-Hernández, J., Fouesneau, M., Frémat, Y., Galluccio, L., García-Torres, M., González-Núñez, J., González-Vidal, J. J., Gosset, E., Guy, L. P., Halbwachs, J. L., Hambly, N. C., Harrison, D. L., Hernández, J., Hestroffer, D., Hodgkin, S. T., Hutton, A., Jasniewicz, G., Jean-Antoine-Piccolo, A., Jordan, S., Korn, A. J., Krone-Martins, A., Lanzafame, A. C., Lebzelter, T., Löffler, W., Manteiga, M., Marrese, P. M., Martín-Fleitas, J. M., Moitinho, A., Mora, A., Muinonen, K., Osinde, J., Pancino, E., Pauwels, T., Petit, J. M., Recio-Blanco, A., Richards, P. J., Rimoldini, L., Robin, A. C., Sarro, L. M., Siopis, C., Smith, M., Sozzetti, A., Süveges, M., Torra, J., van Reeven, W., Abbas, U., Abreu Aramburu, A., Accart, S., Aerts, C., Altavilla, G., Álvarez, M. A., Alvarez, R., Alves, J., Anderson, R. I., Andrei, A. H., Anglada Varela, E., Antiche, E., Antoja, T., Arcay, B., Astraatmadja, T. L., Bach, N., Baker, S. G., Balaguer-Núñez, L., Balm, P., Barache, C., Barata, C., Barbato, D., Barblan, F., Barklem, P. S., Barrado, D., Barros, M., Barstow, M. A., Bartholomé Muñoz, S., Bassilana, J. L., Becciani, U., Bellazzini, M., Berihuete, A., Bertone, S., Bianchi, L., Bienaymé, O., Blanco-Cuaresma, S., Boch, T., Boeche, C., Bombrun, A., Borrachero, R., Bossini, D., Bouquillon, S., Bourda, G., Bragaglia, A., Bramante, L., Breddels, M. A., Bressan, A., Brouillet, N., Brüsemeister, T., Brugaletta, E., Bucciarelli, B., Burlacu, A., Busonero, D., Butkevich, A. G., Buzzi, R., Caffau, E., Cancelliere, R., Cannizzaro, G., Cantat-Gaudin, T., Carballo, R., Carlucci, T., Carrasco, J. M., Casamiquela, L., Castellani, M., Castro-Ginard, A., Charlot, P., Chemin, L., Chiavassa, A., Cocozza, G., Costigan, G., Cowell, S., Crifo, F., Crosta, M., Crowley, C., Cuypers, J., Dafonte, C., Damerdji, Y., Dapergolas, A., David, P., David, M., de Laverny, P., De Luise, F., De March, R., de Martino, D., de Souza, R., de Torres, A., Debosscher, J., del Pozo, E., Delbo, M., Delgado, A., Delgado, H. E., Di Matteo, P., Diakite, S., Diener, C., Distefano, E., Dolding, C., Drazinos, P., Durán, J., Edvardsson, B., Enke, H., Eriksson, K., Esquej, P., Eynard Bontemps, G., Fabre, C., Fabrizio, M., Faigler, S., Falcão, A. J., Farràs Casas, M., Federici, L., Fedorets, G., Fernique, P., Figueras, F., Filippi, F., Findeisen, K., Fonti, A., Fraile, E., Fraser, M., Frézouls, B., Gai, M., Galleti, S., Garabato, D., García-Sedano, F., Garofalo, A., Garralda, N., Gavel, A., Gavras, P., Gerssen, J., Geyer, R., Giacobbe, P., Gilmore, G., Girona, S., Giuffrida, G., Glass, F., Gomes, M., Granvik, M., Gueguen, A., Guerrier, A., Guiraud, J., Gutiérrez-Sánchez, R., Haigron, R., Hatzidimitriou, D., Hauser, M., Haywood, M., Heiter, U., Helmi, A., Heu, J., Hilger, T., Hobbs, D., Hofmann, W., Holland, G., Huckle, H. E., Hypki, A., Icardi, V., Janßen, K., Jevardat de Fombelle, G., Jonker, P. G., Juhász, Á. L., Julbe, F., Karampelas, A., Kewley, A., Klar, J., Kochoska, A., Kohley, R., Kolenberg, K., Kontizas, M., Kontizas, E., Koposov, S. E., Kordopatis, G., Kostrzewa-Rutkowska, Z., Koubsky, P., Lambert, S., Lanza, A. F., Lasne, Y., Lavigne, J. B., Le Fustec, Y., Le Poncin-Lafitte, C., Lebreton, Y., Leccia, S., Leclerc, N., Lecoeur-Taibi, I., Lenhardt, H., Leroux, F., Liao, S., Licata, E., Lindstrøm, H. E. P., Lister, T. A., Livanou, E., Lobel, A., López, M., Managau, S., Mann, R. G., Mantelet, G., Marchal, O., Marchant, J. M., Marconi, M., Marinoni, S., Marschalkó, G., Marshall, D. J., Martino, M., Marton, G., Mary, N., Massari, D., Matijevič,

G., Mazeh, T., McMillan, P. J., Messina, S., Michalik, D., Millar, N. R., Molina, D., Molinaro, R., Molnár, L., Montegriffo, P., Mor, R., Morbidelli, R., Morel, T., Morris, D., Mulone, A. F., Muraveva, T., Musella, I., Nelemans, G., Nicastro, L., Noval, L., O'Mullane, W., Ordénovic, C., Ordóñez-Blanco, D., Osborne, P., Pagani, C., Pagano, I., Pailler, F., Palacin, H., Palaversa, L., Panahi, A., Pawlak, M., Piersimoni, A. M., Pineau, F. X., Plachy, E., Plum, G., Poggio, E., Poujoulet, E., Prša, A., Pulone, L., Racero, E., Ragaini, S., Rambaux, N., Ramos-Lerate, M., Regibo, S., Reylé, C., Riclet, F., Ripepi, V., Riva, A., Rivard, A., Rixon, G., Roegiers, T., Roelens, M., Romero-Gómez, M., Rowell, N., Royer, F., Ruiz-Dern, L., Sadowski, G., Sagristà Sellés, T., Sahlmann, J., Salgado, J., Salguero, E., Sanna, N., Santana-Ros, T., Sarasso, M., Savietto, H., Schultheis, M., Sciacca, E., Segol, M., Segovia, J. C., Ségransan, D., Shih, I. C., Siltala, L., Silva, A. F., Smart, R. L., Smith, K. W., Solano, E., Solitro, F., Sordo, R., Soria Nieto, S., Souchay, J., Spagna, A., Spoto, F., Stampa, U., Steele, I. A., Steidelmüller, H., Stephenson, C. A., Stoev, H., Suess, F. F., Surdej, J., Szabados, L., Szegedi-Elek, E., Tapiador, D., Taris, F., Tauran, G., Taylor, M. B., Teixeira, R., Terrett, D., Teyssand ier, P., Thuillot, W., Titarenko, A., Torra Clotet, F., Turon, C., Ulla, A., Utrilla, E., Uzzi, S., Vaillant, M., Valentini, G., Valette, V., van Elteren, A., Van Hemelryck, E., van Leeuwen, M., Vaschetto, M., Vecchiato, A., Veljanoski, J., Viala, Y., Vicente, D., Vogt, S., von Essen, C., Voss, H., Votruba, V., Voutsinas, S., Walmsley, G., Weiler, M., Wertz, O., Wevers, T., Wyrzykowski, Ł., Yoldas, A., Žerjal, M., Ziaeepour, H., Zorec, J., Zschocke, S., Zucker, S., Zurbach, C., and Zwitter, T. (2018). Gaia Data Release 2. Summary of the contents and survey properties. , 616:A1.

Gail, H.-P. and Sedlmayr, E. (2013a). *Physics and Chemistry of Circumstellar Dust Shells*. Cambridge University Press.

Gail, H.-P. and Sedlmayr, E. (2013b). *Physics and Chemistry of Circumstellar Dust Shells*.

Garay, G. and Lizano, S. (1999). Massive Stars: Their Environment and Formation. , 111(763):1049–1087.

García-Segura, G., Langer, N., Różyczka, M., and Franco, J. (1999). Shaping Bipolar and Elliptical Planetary Nebulae: Effects of Stellar Rotation, Photoionization Heating, and Magnetic Fields. , 517:767–781.

García-Segura, G., López, J. A., and Franco, J. (2005). Magnetically Driven Winds from Post-Asymptotic Giant Branch Stars: Solutions for High-Speed Winds and Extreme Collimation. , 618:919–925.

García-Segura, G., Ricker, P. M., and Taam, R. E. (2018). Common Envelope Shaping of Planetary Nebulae. , 860:19.

García-Segura, G., Villaver, E., Langer, N., Yoon, S.-C., and Manchado, A. (2014). Single Rotating Stars and the Formation of Bipolar Planetary Nebula. , 783:74.

Girart, J. M., Crutcher, R. M., and Rao, R. (1999). Detection of Polarized CO Emission from the Molecular Outflow in NGC 1333 IRAS 4A. , 525(2):L109–L112.

Girart, J. M., Patel, N., Vlemmings, W. H. T., and Rao, R. (2012). Mapping the Linearly Polarized Spectral Line Emission around the Evolved Star IRC+10216. , 751:L20.

Glenn, J., Jewell, P. R., Fourre, R., and Miaja, L. (2003). A Polarization Survey of SiO Maser Variability in Evolved Stars. , 588:478–485.

Glenn, J., Walker, C. K., Bieging, J. H., and Jewell, P. R. (1997a). Millimeter-Wave Spectropolarimetry of Evolved Stars: Evidence for Polarized Molecular Line Emission. , 487(1):L89–L92.

Glenn, J., Walker, C. K., and Jewell, P. R. (1997b). HCO^+ Spectropolarimetry and Millimeter Continuum Polarimetry of the DR 21 Star-forming Region. , 479(1):325–331.

Gobrecht, D., Cherchneff, I., Sarangi, A., Plane, J. M. C., and Bromley, S. T. (2016). Dust formation in the oxygen-rich AGB star IK Tauri. , 585:A6.

Goldreich, P., Keeley, D. A., and Kwan, J. Y. (1973). Astrophysical Masers. 11. Polarization Properties. , 179:111–134.

Goldreich, P. and Kylafis, N. D. (1981). On mapping the magnetic field direction in molecular clouds by polarization measurements. , 243:L75–L78.

Goldreich, P. and Kylafis, N. D. (1982). Linear polarization of radio frequency lines in molecular clouds and circumstellar envelopes. , 253:606–621.

González-Casanova, D. F. and Lazarian, A. (2017). Velocity Gradients as a Tracer for Magnetic Fields. , 835(1):41.

González Delgado, D., Olofsson, H., Kerschbaum, F., Schöier, F. L., Lindqvist, M., and Groenewegen, M. A. T. (2003). "Thermal" SiO radio line emission towards M-type AGB stars: A probe of circumstellar dust formation and dynamics. , 411:123–147.

Gray, M. (2012). *Maser Sources in Astrophysics*.

Gray, M. D., Wittkowski, M., Scholz, M., Humphreys, E. M. L., Ohnaka, K., and Boboltz, D. (2009). SiO maser emission in Miras. *Monthly Notices of the Royal Astronomical Society*, 394(1):51–66.

Greaves, J. S., Holland, W. S., Friberg, P., and Dent, W. R. F. (1999). Polarized CO Emission from Molecular Clouds. , 512(2):L139–L142.

Greaves, J. S., Holland, W. S., and Ward-Thompson, D. (2001). Measurement of the Magnetic Field Direction in the NGC 2024 FIR 5 Protostellar Outflow. , 546(1):L53–L56.

Green, S. and Chapman, S. (1978). Collisional excitation of interstellar molecules: linear molecules CO, CS, OCS, and HC_3N. , 37:169–194.

Greenhill, L. J., Colomer, F., Moran, J. M., Backer, D. C., Danchi, W. C., and Bester, M. (1995). Interferometric Observations of the SiO Masers and Dust Shell of VX Sagittarii. , 449:365.

Guilloteau, S., Forveille, T., Baudry, A., Despois, D., and Goss, W. M. (1988). H2 CO and excited OH toward G 10.6-0.4 : another rotating disk ? , 202:189–202.

Habing, H. and Olofsson, H. (2004). *Asymptotic Giant Branch Stars*. Astronomy and Astrophysics Library. Springer.

Hacar, A., Tafalla, M., Forbrich, J., Alves, J., Meingast, S., Grossschedl, J., and Teixeira, P. S. (2018). An ALMA study of the Orion Integral Filament. I. Evidence for narrow fibers in a massive cloud. , 610:A77.

Hamaker, J. P., Bregman, J. D., and Sault, R. J. (1996). Understanding radio polarimetry. I. Mathematical foundations. , 117:137–147.

Han, J. L. (2017). Observing Interstellar and Intergalactic Magnetic Fields. , 55(1):111–157.

Haniff, C. A., Scholz, M., and Tuthill, P. G. (1995). New Diameter Measurements of 10 Mira Variables - Implications for Effective Temperatures Atmospheric Structure and Pulsation Modes. , 276:640.

Hartquist, T. W. and Dyson, J. E. (1997). The origin of strong magnetic fields in circumstellar SiO masers. , 319:589–592.

Herpin, F., Baudry, A., Thum, C., Morris, D., and Wiesemeyer, H. (2006). Full polarization study of SiO masers at 86 GHz. , 450:667–680.

Herwig, F. (2005). Evolution of Asymptotic Giant Branch Stars. , 43:435–479.

Hill, S. J. and Willson, L. A. (1979). Theoretical velocity structure of long-period variable star photospheres. , 229:1029–1045.

Hillwig, T. C., Jones, D., De Marco, O., Bond, H. E., Margheim, S., and Frew, D. (2016). Observational Confirmation of a Link Between Common Envelope Binary Interaction and Planetary Nebula Shaping. , 832:125.

Ho, P. T. P. and Haschick, A. D. (1981). Formation of OB clusters: VLA observations. , 248:622–637.

Ho, P. T. P., Haschick, A. D., Vogel, S. N., and Wright, M. C. H. (1983). Formation of OB clusters : OH maser observations. , 265:295–303.

Ho, P. T. P., Klein, R. I., and Haschick, A. D. (1986). Formation of OB Clusters: Radiation-driven Implosion? , 305:714.

Ho, P. T. P., Terebey, S., and Turner, J. L. (1994). The Rotating Molecular Core in G10.6-0.4: Synthesis Maps in 12C 18O. , 423:320.

Hoang, T. and Lazarian, A. (2008). Radiative torque alignment: essential physical processes. , 388:117–143.

Hoare, M. G., Kurtz, S. E., Lizano, S., Keto, E., and Hofner, P. (2007). Ultracompact Hii Regions and the Early Lives of Massive Stars. In Reipurth, B., Jewitt, D., and Keil, K., editors, *Protostars and Planets V*, page 181.

Höfner, S. and Olofsson, H. (2018). Mass loss of stars on the asymptotic giant branch. Mechanisms, models and measurements. , 26(1):1.

Houde, M., Hezareh, T., Jones, S., and Rajabi, F. (2013). Non-Zeeman Circular Polarization of Molecular Rotational Spectral Lines. , 764(1):24.

Hrivnak, B. J., Van de Steene, G., Van Winckel, H., Sperauskas, J., Bohlender, D., and Lu, W. (2017). Where are the Binaries? Results of a Long-term Search for Radial Velocity Binaries in Proto-planetary Nebulae. , 846:96.

Huang, K. Y., Kemball, A. J., Vlemmings, W. H. T., Lai, S. P., Yang, L., and Agudo, I. (2020). Mapping circumstellar magnetic fields of late-type evolved stars with the Goldreich-Kylafis effect: CARMA observations at λ1.3 mm of R Crt and R Leo. *arXiv e-prints*, page arXiv:2007.00215.

Hull, C. L. H. (2014). *From Cores to Envelopes to Disks: A Multi-scale View of Magnetized Star Formation*. PhD thesis, University of California, Berkeley.

Hull, C. L. H., Cortes, P. C., Le Gouellec, V. J. M., Girart, J. M., Nagai, H., Nakanishi, K., Kameno, S., Fomalont, E. B., Brogan, C. L., Moellenbrock, G. A., Paladino, R., and Villard, E. (2020). Characterizing the Accuracy of ALMA Linear-polarization Mosaics. , 132(1015):094501.

Hull, C. L. H. and Plambeck, R. L. (2015). The 1.3mm Full-Stokes Polarization System at CARMA. *Journal of Astronomical Instrumentation*, 4:1550005.

Humphreys, E. M. L., Gray, M. D., Yates, J. A., Field, D., Bowen, G., and Diamond, P. J. (1996). SiO masers in Mira variables at a single stellar phase. , 282(4):1359–1371.

Humphreys, E. M. L., Gray, M. D., Yates, J. A., Field, D., Bowen, G. H., and Diamond, P. J. (2002). Numerical simulations of stellar SiO maser variability. Investigation of the effect of shocks. *Astronomy and Astrophysics*, 386:256–270.

Ireland, M. J., Scholz, M., and Wood, P. R. (2008). Dynamical opacity-sampling models of Mira variables - I. Modelling description and analysis of approximations. , 391(4):1994–2002.

Ireland, M. J., Scholz, M., and Wood, P. R. (2011). Dynamical opacity-sampling models of Mira variables - II. Time-dependent atmospheric structure and observable properties of four M-type model series. , 418(1):114–128.

Ireland, M. J., Tuthill, P. G., Bedding, T. R., Robertson, J. G., and Jacob, A. P. (2004). Multiwavelength diameters of nearby Miras and semiregular variables. , 350:365–374.

Ishitsuka, J. K., Imai, H., Omodaka, T., Ueno, M., Kameya, O., Sasao, T., Morimoto, M., Miyaji, T., Nakajima, J.-I., and Watanabe, T. (2001). VLBI Monitoring Observations of Water Masers around the Semi-Regular Variable Star R Crateris. , 53:1231–1238.

Israel, F. P., Habing, H. J., and de Jong, T. (1973). Aperture synthesis observations of H II regions. I. A group of H II regions around l = 111 . , 27:143–160.

Jackson, J. D. (1998). *Classical Electrodynamics, 3rd Edition*.

Jewell, P. R., Snyder, L. E., Walmsley, C. M., Wilson, T. L., and Gensheimer, P. D. (1991). Observational properties of V = 1, J = 1 - 0 SiO masers. , 242:211.

Jorstad, S. and Marscher, A. (2016). The VLBA-BU-BLAZAR Multi-Wavelength Monitoring Program. *Galaxies*, 4:47.

Jorstad, S. G., Marscher, A. P., Morozova, D. A., Troitsky, I. S., Agudo, I., Casadio, C., Foord, A., Gómez, J. L., MacDonald, N. R., Molina, S. N., Lähteenmäki, A., Tammi, J., and Tornikoski, M. (2017). Kinematics of Parsec-scale Jets of Gamma-Ray Blazars at 43 GHz within the VLBA-BU-BLAZAR Program. , 846:98.

Kahn, F. D. (1974). Cocoons around early-type stars. , 37:149–162.

Kataoka, A., Muto, T., Momose, M., Tsukagoshi, T., Fukagawa, M., Shibai, H., Hanawa, T., Murakawa, K., and Dullemond, C. P. (2015). Millimeter-wave Polarization of Protoplanetary Disks due to Dust Scattering. , 809(1):78.

Kemball, A. J. and Diamond, P. J. (1993). VLBI spectral line polarization observations of the OH masers in the supergiant IRC+10420. In Clegg, A. W. and Nedoluha, G. E., editors, *Astrophysical Masers*, volume 412 of *Lecture Notes in Physics, Berlin Springer Verlag*, pages 369–372.

Kemball, A. J. and Diamond, P. J. (1997). Imaging the Magnetic Field in the Atmosphere of TX Camelopardalis. , 481:L111–L114.

Kemball, A. J., Diamond, P. J., and Cotton, W. D. (1995). Data reduction techniques for spectral line polarization VLBI observations. , 110:383.

Kemball, A. J., Diamond, P. J., Gonidakis, I., Mitra, M., Yim, K., Pan, K.-C., and Chiang, H.-F. (2009). Multi-Epoch Imaging Polarimetry of the SiO Masers in the Extended Atmosphere of the Mira Variable TX Cam. , 698:1721–1739.

Kemball, A. J. and Richter, L. (2011). Circular polarization measurement in millimeter-wavelength spectral-line VLBI observations. , 533:A26.

Keto, E. (2002). An Ionized Accretion Flow in the Ultracompact H II Region G10.6-0.4. , 568(2):754–760.

Keto, E. and Wood, K. (2006). Observations on the Formation of Massive Stars by Accretion. , 637(2):850–859.

Keto, E., Zhang, Q., and Kurtz, S. (2008). The Early Evolution of Massive Stars: Radio Recombination Line Spectra. , 672(1):423–432.

Keto, E. R. (1990). Radiative Transfer Modeling of Radio-Frequency Spectral Line Data: Accretion onto G10.6-0.4. , 355:190.

Keto, E. R., Ho, P. T. P., and Haschick, A. D. (1987). Temperature and Density Structure of the Collapsing Core of G10.6-0.4. , 318:712.

Keto, E. R., Ho, P. T. P., and Haschick, A. D. (1988). The Observed Structure of the Accretion Flow around G10.6-0.4. , 324:920.

Khouri, T., de Koter, A., Decin, L., Waters, L. B. F. M., Maercker, M., Lombaert, R., Alcolea, J., Blommaert, J. A. D. L., Bujarrabal, V., Groenewegen, M. A. T., Justtanont, K., Kerschbaum, F., Matsuura, M., Menten, K. M., Olofsson, H., Planesas, P., Royer, P., Schmidt, M. R., Szczerba, R., Teyssier, D., and Yates, J. (2014). The wind of W Hydrae as seen by Herschel. II. The molecular envelope of W Hydrae. , 570:A67.

Khouri, T., Vlemmings, W. H. T., Paladini, C., Ginski, C., Lagadec, E., Maercker, M., Kervella, P., De Beck, E., Decin, L., de Koter, A., and Waters, L. B. F. M. (2020). Inner dusty envelope of the AGB stars W Hydrae, SW Virginis, and R Crateris using SPHERE/ZIMPOL. , 635:A200.

Kim, D.-J., Cho, S.-H., Yun, Y., Choi, Y. K., Yoon, D.-H., Kim, J., Dodson, R., Rioja, M. J., Yang, H., and Yoon, S.-J. (2018). Simultaneous VLBI Astrometry of H_2O and SiO Masers toward the Semiregular Variable R Crateris. , 866:L19.

Kim, H., Trejo, A., Liu, S.-Y., Sahai, R., Taam, R. E., Morris, M. R., Hirano, N., and Hsieh, I.-T. (2017). The large-scale nebular pattern of a superwind binary in an eccentric orbit. *Nature Astronomy*, 1:0060.

Klaassen, P. D., Wilson, C. D., Keto, E. R., and Zhang, Q. (2009). Rotation of the Warm Molecular Gas Surrounding Ultracompact H II Regions. , 703(2):1308–1317.

Knight, W. R. (1966). A computer method for calculating kendall's tau with ungrouped data. *Journal of the American Statistical Association*, 61(314):436–439.

Krumholz, M. R. and Tan, J. C. (2007). Slow Star Formation in Dense Gas: Evidence and Implications. , 654(1):304–315.

Kudoh, T. and Basu, S. (2008). Three-dimensional Simulation of Magnetized Cloud Fragmentation Induced by Nonlinear Flows and Ambipolar Diffusion. , 679(2):L97.

Kwok, S. (1975). Radiation pressure on grains as a mechanism for mass loss in red giants. , 198:583–591.

Kwok, S., Purton, C. R., and Fitzgerald, P. M. (1978). On the origin of planetary nebulae. , 219:L125–L127.

Kylafis, N. D. (1983a). Linear polarization of interstellar radio-frequency absorption lines and magnetic field direction. , 275:135–144.

Kylafis, N. D. (1983b). Polarization of interstellar radio-frequency lines and magnetic field direction. , 267:137–150.

Lai, S.-P., Girart, J. M., and Crutcher, R. M. (2003). Interferometric Mapping of Magnetic Fields in Star-forming Regions. III. Dust and CO Polarization in DR 21(OH). , 598:392–399.

Lamers, H. J. G. L. M. and Cassinelli, J. P. (1999a). *Introduction to Stellar Winds*.

Lamers, H. J. G. L. M. and Cassinelli, J. P. (1999b). *Introduction to Stellar Winds*.

Lankhaar, B. and Vlemmings, W. (2019). Characterizing maser polarization: effects of saturation, anisotropic pumping, and hyperfine structure. , 628:A14.

Lankhaar, B. and Vlemmings, W. (2020). PORTAL: Three-dimensional polarized (sub)millimeter line radiative transfer. , 636:A14.

Lazarian, A. (2007). Tracing magnetic fields with aligned grains. , 106:225–256.

Leal Ferreira, M. L. (2014). *Magnetic Fields And The Formation Of Aspherical Planetary Nebulae*. PhD thesis, Argelander Institut für Astronomie, University of Bonn, Auf dem Hügel 71, 53121 Bonn, Germany.

Leal-Ferreira, M. L., Vlemmings, W. H. T., Kemball, A., and Amiri, N. (2013). Magnetic fields around evolved stars: further observations of H_2O maser polarization. , 554:A134.

Lèbre, A., Aurière, M., Fabas, N., Gillet, D., Herpin, F., Konstantinova-Antova, R., and Petit, P. (2014). Search for surface magnetic fields in Mira stars. First detection in χ Cygni. , 561:A85.

Lee, C.-F., Hwang, H.-C., Ching, T.-C., Hirano, N., Lai, S.-P., Rao, R., and Ho, P. T. P. (2018). Unveiling a magnetized jet from a low-mass protostar. *Nature Communications*, 9:4636.

Lee, C.-F., Rao, R., Ching, T.-C., Lai, S.-P., Hirano, N., Ho, P. T. P., and Hwang, H.-C. (2014). Magnetic Field Structure in the Flattened Envelope and Jet in the Young Protostellar System HH 211. , 797(1):L9.

Li, H.-B. and Henning, T. (2011). The alignment of molecular cloud magnetic fields with the spiral arms in M33. , 479:499–501.

Li, H.-B., Yuen, K. H., Otto, F., Leung, P. K., Sridharan, T. K., Zhang, Q., Liu, H., Tang, Y.-W., and Qiu, K. (2015). Self-similar fragmentation regulated by magnetic fields in a region forming massive stars. , 520(7548):518–521.

Li, S., Zhang, Q., Liu, H. B., Beuther, H., Palau, A., Girart, J. M., Smith, H., Hora, J. L., Lin, Y., Qiu, K., Strom, S., Wang, J., Li, F., and Yue, N. (2020). ALMA Observations of NGC 6334S. I. Forming Massive Stars and Clusters in Subsonic and Transonic Filamentary Clouds. , 896(2):110.

Lis, D. C., Goldsmith, P. F., Dickman, R. L., Predmore, C. R., Omont, A., and Cernicharo, J. (1988). Linear polarization of millimeter-wave emission lines in clouds without large velocity gradients. , 328:304–314.

Lister, M. L., Aller, H. D., Aller, M. F., Cohen, M. H., Homan, D. C., Kadler, M., Kellermann, K. I., Kovalev, Y. Y., Ros, E., Savolainen, T., Zensus, J. A., and Vermeulen, R. C. (2009). MOJAVE: Monitoring of Jets in Active Galactic Nuclei with VLBA Experiments. V. Multi-Epoch VLBA Images. , 137:3718–3729.

Liu, H. B., Ho, P. T. P., and Zhang, Q. (2010). The High-velocity Molecular Outflows in Massive Cluster-forming Region G10.6-0.4. , 725(2):2190–2208.

Liu, H. B., Quintana-Lacaci, G., Wang, K., Ho, P. T. P., Li, Z.-Y., Zhang, Q., and Zhang, Z.-Y. (2012). The Origin of OB Clusters: From 10 pc to 0.1 pc. , 745(1):61.

Liu, H. B., Zhang, Q., and Ho, P. T. P. (2011). An Overall Picture of the Gas Flow in a Massive Cluster-forming Region: The Case of G10.6-0.4. , 729(2):100.

Lovas, F. J., Bass, J. E., Dragoset, R. A., and Olsen, K. J. (2009). NIST recommended rest frequencies for observed interstellar molecular microwave transitions.

Luri, X., Brown, A. G. A., Sarro, L. M., Arenou, F., Bailer-Jones, C. A. L., Castro-Ginard, A., de Bruijne, J., Prusti, T., Babusiaux, C., and Delgado, H. E. (2018). Gaia Data Release 2. Using Gaia parallaxes. , 616:A9.

Mac Low, M.-M. and Klessen, R. S. (2004). Control of star formation by supersonic turbulence. *Reviews of Modern Physics*, 76(1):125–194.

Marco, O. D., Bond, H. E., Harmer, D., and Fleming, A. J. (2004). Indications of a large fraction of spectroscopic binaries among nuclei of planetary nebulae. *The Astrophysical Journal Letters*, 602(2):L93.

Matt, S., Balick, B., Winglee, R., and Goodson, A. (2000). Disk Formation by Asymptotic Giant Branch Winds in Dipole Magnetic Fields. , 545:965–973.

Matthews, L. D., Reid, M. J., Menten, K. M., and Akiyama, K. (2018). The Evolving Radio Photospheres of Long-period Variable Stars. , 156:15.

Maud, L. T., Tilanus, R. P. J., van Kempen, T. A., Hogerheijde, M. R., Schmalzl, M., Yoon, I., Contreras, Y., Toribio, M. C., Asaki, Y., Dent, W. R. F., Fomalont, E., and Matsushita, S. (2017). Phase correction for ALMA. Investigating water vapour radiometer scaling: The long-baseline science verification data case study. , 605:A121.

McKee, C. F. and Ostriker, E. C. (2007). Theory of Star Formation. , 45(1):565–687.

McKee, C. F. and Tan, J. C. (2002). Massive star formation in 100,000 years from turbulent and pressurized molecular clouds. , 416(6876):59–61.

Menten, K. M. and Melnick, G. J. (1991). 321 GHz submillimeter water masers around evolved stars. , 377:647–656.

Miyoshi, M., Matsumoto, K., Kameno, S., Takaba, H., and Lwata, T. (1994). Collisional pumping of SiO masers in evolved stars. , 371:395–397.

Moellenbrock, G. (2017). Synthesis Polarimetry Calibration. In *Submm/mm/cm QUESO Workshop 2017 (QUESO2017)*, page 19.

Monsch, K., Pineda, J. E., Liu, H. B., Zucker, C., How-Huan Chen, H., Pattle, K., Offner, S. S. R., Di Francesco, J., Ginsburg, A., Ercolano, B., Arce, H. G., Friesen, R., Kirk, H., Caselli, P., and Goodman, A. A. (2018). Dense Gas Kinematics and a Narrow Filament in the Orion A OMC1 Region Using NH_3. , 861(2):77.

Moran, J. M., Ball, J. A., Hansen, S. S., Huguenin, G. R., Lane, A. P., Predmore, C. R., and Reid, M. J. (1979). VLBI observations of SiO masers at a wavelength of 7 millimeters in late-type stars. , 231:L67–L71.

Morris, M., Lucas, R., and Omont, A. (1985). Molecular emission from expanding circumstellar envelopes Polarization and profile asymmetries. , 142:107–116.

Mouschovias, T. C. (1991). Cosmic Magnetism and the Basic Physics of the Early Stages of Star Formation. In Lada, C. J. and Kylafis, N. D., editors, *NATO Advanced Science Institutes (ASI) Series C*, volume 342 of *NATO Advanced Science Institutes (ASI) Series C*, page 61.

Mouschovias, T. C. and Ciolek, G. E. (1999). Magnetic Fields and Star Formation: A Theory Reaching Adulthood. In Lada, C. J. and Kylafis, N. D., editors, *NATO Advanced Science Institutes (ASI) Series C*, volume 540 of *NATO Advanced Science Institutes (ASI) Series C*, page 305.

Mueller, H. (1948). The Foundation of Optics (Abstract). *Journal of the Optical Society of America (J. Opt. Soc. Am.)*, 38:661.

Nagai, H., Nakanishi, K., Paladino, R., Hull, C. L. H., Cortes, P., Moellenbrock, G., Fomalont, E., Asada, K., and Hada, K. (2016). ALMA Science Verification Data: Millimeter Continuum Polarimetry of the Bright Radio Quasar 3C 286. , 824(2):132.

Nakamura, F. and Li, Z.-Y. (2005). Quiescent Cores and the Efficiency of Turbulence-accelerated, Magnetically Regulated Star Formation. , 631(1):411–428.

Nakamura, F. and Li, Z.-Y. (2008). Magnetically Regulated Star Formation in Three Dimensions: The Case of the Taurus Molecular Cloud Complex. , 687(1):354–375.

Nordhaus, J. and Blackman, E. G. (2006). Low-mass binary-induced outflows from asymptotic giant branch stars. , 370:2004–2012.

Nordhaus, J., Blackman, E. G., and Frank, A. (2007). Isolated versus common envelope dynamos in planetary nebula progenitors. , 376:599–608.

Omodaka, T., Kobayashi, H., Kitamura, Y., Nakano, M., and Ishiguro, M. (1992). The Massive Star-Forming Region: G10.6-0.4 Molecular Cloud. , 44:447–457.

Padoan, P. and Nordlund, Å. (1999). A Super-Alfvénic Model of Dark Clouds. , 526(1):279–294.

Paladini, C., Klotz, D., Sacuto, S., Lagadec, E., Wittkowski, M., Richichi, A., Hron, J., Jorissen, A., Groenewegen, M. A. T., Kerschbaum, F., Verhoelst, T., Rau, G., Olofsson, H., Zhao- Geisler, R., and Matter, A. (2017). The VLTI/MIDI view on the inner mass loss of evolved stars from the Herschel MESS sample. , 600:A136.

Pardo, J. R., Alcolea, J., Bujarrabal, V., Colomer, F., del Romero, A., and de Vicente, P. (2004). ^{28}SiO v = 1 and v = 2, J = 1-0 maser variability in evolved stars. Eleven years of short spaced monitoring. , 424:145–156.

Parke, Nathan G., I. (1948). *Matrix-Optics*. PhD thesis, MASSACHUSETTS INSTITUTE OF TECHNOLOGY.

Pascoli, G. (1997). On Circumstellar Envelope Formation. , 489:946–950.

Pearson, K. (1895). Note on Regression and Inheritance in the Case of Two Parents. *Proceedings of the Royal Society of London Series I*, 58:240–242.

Perrin, F. (1942). Polarization of Light Scattered by Isotropic Opalescent Media. , 10(7):415–427.

Petit, P., Aurière, M., Konstantinova-Antova, R., Morgenthaler, A., Perrin, G., Roudier, T., and Donati, J. F. (2013). *Magnetic Fields and Convection in the Cool Supergiant Betelgeuse*, page 231.

Pillai, T., Kauffmann, J., Wiesemeyer, H., and Menten, K. M. (2016). CN Zeeman and dust polarization in a high-mass cold clump. , 591:A19.

Pirogov, L., Zinchenko, I., Caselli, P., Johansson, L. E. B., and Myers, P. C. (2003). N_2H^+(1-0) survey of massive molecular cloud cores. , 405:639–654.

Plambeck, R. L. and Wright, M. C. H. (2016). ALMA Observations of Orion Source I at 350 and 660 GHz. , 833(2):219.

Plambeck, R. L., Wright, M. C. H., Friedel, D. N., Widicus Weaver, S. L., Bolatto, A. D., Pound, M. W., Woody, D. P., Lamb, J. W., and Scott, S. L. (2009). Tracing the Bipolar Outflow from Orion Source I. , 704(1):L25–L28.

Proust, D., Ochsenbein, F., and Pettersen, B. R. (1981). A catalogue of variable-visual binary stars. , 44:179–187.

Qiu, K., Zhang, Q., Menten, K. M., Liu, H. B., Tang, Y.-W., and Girart, J. M. (2014). Submillimeter Array Observations of Magnetic Fields in G240.31+0.07: An Hourglass in a Massive Cluster-forming Core. , 794(1):L18.

Ramstedt, S., Doan, L., Danilovich, T., Lindqvist, M., Saberi, M., Vlemmings, W. H. T., Olofsson, H., Beck, E. D., Groenewegen, M. a. T., Hfner, S., Kastner, J. H., Kerschbaum, F., Khouri, T., Maercker, M., Montez, R., Quintana-Lacaci, G., Sahai, R., Tafoya, D., and Zijls, A. (2020). DEATHSTAR: Nearby AGB stars with the atacama compact array. i. CO envelope sizes and asymmetries: A new hope for accurate mass-loss-rate estimates. Publisher: EDP Sciences.

Ramstedt, S. and Olofsson, H. (2014). The $^{12}CO/^{13}CO$ ratio in AGB stars of different chemical type. Connection to the $^{12}C/^{13}C$ ratio and the evolution along the AGB. , 566:A145.

Reid, M. J. (1990). Masers and stellar magnetic fields. In Beck, R., Kronberg, P. P., and Wielebinski, R., editors, *Galactic and Intergalactic Magnetic Fields*, volume 140 of *IAU Symposium*, pages 21–24.

Reid, M. J. (2007). IAU 242 closing summary. In Chapman, J. M. and Baan, W. A., editors, *Astrophysical Masers and their Environments*, volume 242 of *IAU Symposium*, pages 522–529.

Reid, M. J. and Menten, K. M. (2007). Imaging the Radio Photospheres of Mira Variables. , 671:2068–2073.

Reid, M. J. and Moran, J. M. (1981). Masers. , 19:231–276.

Reid, M. J., Moran, J. M., Leach, R. W., Ball, J. A., Johnston, K. J., Spencer, J. H., and Swenson, G. W. (1979). Stellar OH masers and magnetic fields - VLBI observations of U Orionis and IRC +10420. , 227:L89–L92.

Reid, M. J., Schneps, M. H., Moran, J. M., Gwinn, C. R., Genzel, R., Downes, D., and Roennaeng, B. (1988). The Distance to the Center of the Galaxy: H 2O Maser Proper Motions in Sagittarius B2(N). , 330:809.

Richter, L., Kemball, A., and Jonas, J. (2016). Simultaneous VLBA polarimetric observations of the v = {1,2} J = 1-0 and v = 1, J = 2-1 SiO maser emission towards VY CMa II: component-level polarization analysis. , 461:2309–2327.

Robinson, S. E. and van Blerkom, D. J. (1981). A mechanism for producing ground vibrational state SiO masers. , 249:566–571.

Robishaw, T. (2008). *Magnetic fields near and far: Galactic and extragalactic single-dish radio observations of the Zeeman effect*. PhD thesis, University of California, Berkeley.

Robishaw, T. and Heiles, C. (2018). The Measurement of Polarization in Radio Astronomy. *arXiv e-prints*, page arXiv:1806.07391.

Rüdiger, G., Hollerbach, R., and Kulsrud, R. M. (2005). The Magnetic Universe: Geophysical and Astrophysical Dynamo Theory. *Physics Today*, 58(11):56–56.

Rybicki, G. B. and Lightman, A. P. (1979). *Radiative processes in astrophysics*.

Sabin, L., Zhang, Q., Zijlstra, A. A., Patel, N. A., Vázquez, R., Zauderer, B. A., Contreras, M. E., and Guillén, P. F. (2014). Submillimetre polarization and magnetic field properties in the envelopes of protoplanetary nebulae CRL 618 and OH 231.8+4.2. , 438:1794–1804.

Samus', N. N., Kazarovets, E. V., Durlevich, O. V., Kireeva, N. N., and Pastukhova, E. N. (2017). General catalogue of variable stars: Version GCVS 5.1. *Astronomy Reports*, 61:80–88.

Sanhueza, P., Jackson, J. M., Foster, J. B., Garay, G., Silva, A., and Finn, S. C. (2012). Chemistry in Infrared Dark Cloud Clumps: A Molecular Line Survey at 3 mm. , 756(1):60.

Sanna, A., Reid, M. J., Menten, K. M., Dame, T. M., Zhang, B., Sato, M., Brunthaler, A., Moscadelli, L., and Immer, K. (2014). Trigonometric Parallaxes to Star-forming Regions within 4 kpc of the Galactic Center. , 781(2):108.

Sault, R. J., Hamaker, J. P., and Bregman, J. D. (1996). Understanding radio polarimetry. II. Instrumental calibration of an interferometer array. , 117:149–159.

Sault, R. J., Teuben, P. J., and Wright, M. C. H. (1995). A Retrospective View of MIRIAD. In Shaw, R. A., Payne, H. E., and Hayes, J. J. E., editors, *Astronomical Data Analysis Software and Systems IV*, volume 77 of *Astronomical Society of the Pacific Conference Series*, page 433.

Schöier, F. L., Ramstedt, S., Olofsson, H., Lindqvist, M., Bieging, J. H., and Marvel, K. B. (2013). The abundance of HCN in circumstellar envelopes of AGB stars of different chemical type. , 550:A78.

Schöier, F. L., van der Tak, F. F. S., van Dishoeck, E. F., and Black, J. H. (2005). An atomic and molecular database for analysis of submillimetre line observations. , 432:369–379.

Shinnaga, H., Moran, J. M., Young, K. H., and Ho, P. T. P. (2004). Interferometric Observation of the Highly Polarized SiO Maser Emission from the v = 1, J = 5-4 Transition Associated with VY Canis Majoris. , 616(1):L47–L50.

Shirley, Y. L., Evans, Neal J., I., Young, K. E., Knez, C., and Jaffe, D. T. (2003). A CS J=5–>4 Mapping Survey Toward High-Mass Star-forming Cores Associated with Water Masers. , 149(2):375–403.

Shu, F. H., Adams, F. C., and Lizano, S. (1987). Star formation in molecular clouds: observation and theory. , 25:23–81.

Sobolev, V. V. (1960). *Moving envelopes of stars*.

Soker, N. (2002). Local circumstellar magnetic fields around evolved stars. , 336:826–830.

Soker, N. (2004). Shaping Planetary Nebulae and Related Objects. In Meixner, M., Kastner, J. H., Balick, B., and Soker, N., editors, *Asymmetrical Planetary Nebulae III: Winds, Structure and the Thunderbird*, volume 313 of *Astronomical Society of the Pacific Conference Series*, page 562.

Soker, N. (2004). Why a single-star model cannot explain the bipolar nebula of carinae. *The Astrophysical Journal*, 612(2):1060.

Soker, N. (2006). Why magnetic fields cannot be the main agent shaping planetary nebulae. *Publications of the Astronomical Society of the Pacific*, 118(840):260.

Soker, N. and Zoabi, E. (2002). Turbulent dynamo in asymptotic giant branch stars. , 329:204–208.

Sokolov, V., Wang, K., Pineda, J. E., Caselli, P., Henshaw, J. D., Barnes, A. T., Tan, J. C., Fontani, F., Jiménez-Serra, I., and Zhang, Q. (2018). Subsonic islands within a high-mass star-forming infrared dark cloud. , 611:L3.

Soleillet, P. (1929). Sur les paramètres caractérisant la polarisation partielle de la lumière dans les phénomènes de fluorescence. *Annales de Physique*, 10(12):23–97.

Sollins, P. K. and Ho, P. T. P. (2005). The Molecular Accretion Flow in G10.6-0.4. , 630(2):987–995.

Sollins, P. K., Zhang, Q., Keto, E., and Ho, P. T. P. (2005). Spherical Infall in G10.6-0.4: Accretion through an Ultracompact H II Region. , 624(1):L49–L52.

Soria-Ruiz, R., Alcolea, J., Colomer, F., Bujarrabal, V., Desmurs, J. F., Marvel, K. B., and Diamond, P. J. (2004). High resolution observations of SiO masers: Comparing the spatial distribution at 43 and 86 GHz. *Astronomy and Astrophysics*, 426:131–144.

Spruit, H. C. (2002). Dynamo action by differential rotation in a stably stratified stellar interior. , 381:923–932.

Stokes, G. G. (1851). On the Composition and Resolution of Streams of Polarized Light from different Sources. *Transactions of the Cambridge Philosophical Society*, 9:399.

Szymczak, M., Cohen, R. J., and Richards, A. M. S. (1999). MERLIN polarimetry of the OH maser emission from R Crateris. , 304:877–882.

Taylor, J. R. (1996). *An Introduction to Error Analysis: The Study of Uncertainties in Physical Measurements 2nd Edition*. University Science Books.

Teyssier, D., Hernandez, R., Bujarrabal, V., Yoshida, H., and Phillips, T. G. (2006). CO line emission from circumstellar envelopes. , 450:167–179.

Thomas, J. H., Markiel, J. A., and van Horn, H. M. (1995). Dynamo Generation of Magnetic Fields in White Dwarfs. , 453:403.

Thompson, A. R., Moran, J. M., and Swenson, Jr., G. W. (2017). *Interferometry and Synthesis in Radio Astronomy, 3rd Edition*.

Tilley, D. A. and Pudritz, R. E. (2007). The formation of star clusters - II. 3D simulations of magnetohydrodynamic turbulence in molecular clouds. , 382(1):73–94.

van Langevelde, H., Quiroga-Nuñez, L. H., Vlemmings, W. H. T., Loinard, L., Honma, M., Nakagawa, A., Immer, K., Burns, R. A., Pihlstrom, Y., Sjouwerman, L., Natarajan, I., Rich, R. M., and Deane, R. (2018). The Synergy between VLBI and Gaia astrometry. In *14th European VLBI Network Symposium & Users Meeting (EVN 2018)*, page 43.

van Marle, A. J., Cox, N. L. J., and Decin, L. (2014). Eyes in the sky. Interactions between asymptotic giant branch star winds and the interstellar magnetic field. , 570:A131.

Vasyunina, T., Linz, H., Henning, T., Zinchenko, I., Beuther, H., and Voronkov, M. (2011). Chemistry in infrared dark clouds. , 527:A88.

Vázquez-Semadeni, E., Banerjee, R., Gómez, G. C., Hennebelle, P., Duffin, D., and Klessen, R. S. (2011). Molecular cloud evolution - IV. Magnetic fields, ambipolar diffusion and the star formation efficiency. , 414(3):2511–2527.

Vinokur, M. (1965). Optimisation dans la recherche d'une sinusoïde de période connue en présence de bruit. Application à la radioastronomie. *Annales d'Astrophysique*, 28:412.

Vlemmings, W. (2019). Magnetic fields of AGB and post-AGB stars. In Kerschbaum, F., Groenewegen, M., and Olofsson, H., editors, *IAU Symposium*, volume 343 of *IAU Symposium*, pages 19–26.

Vlemmings, W. H. T., Diamond, P. J., and Imai, H. (2006). A magnetically collimated jet from an evolved star. , 440:58–60.

Vlemmings, W. H. T., Humphreys, E. M. L., and Franco-Hernández, R. (2011). Magnetic Fields in Evolved Stars: Imaging the Polarized Emission of High-frequency SiO Masers. , 728(2):149.

Vlemmings, W. H. T., Khouri, T., Martí-Vidal, I., Tafoya, D., Baudry, A., Etoka, S., Humphreys, E. M. L., Jones, T. J., Kemball, A., O'Gorman, E., Pérez-Sánchez, A. F., and Richards, A. M. S. (2017). Magnetically aligned dust and SiO maser polarisation in the envelope of the red supergiant VY Canis Majoris. , 603:A92.

Vlemmings, W. H. T., Khouri, T., and Olofsson, H. (2019). Resolving the extended stellar atmospheres of asymptotic giant branch stars at (sub)millimetre wavelengths. , 626:A81.

Vlemmings, W. H. T., Ramstedt, S., Rao, R., and Maercker, M. (2012). Polarization of thermal molecular lines in the envelope of IK Tauri. , 540:L3.

Wang, Y., Zhang, Q., Pillai, T., Wyrowski, F., and Wu, Y. (2008). NH_3 Observations of the Infrared Dark Cloud G28.34+0.06. , 672(1):L33.

Wannier, P. G., Scoville, N. Z., and Barvainis, R. (1983). The polarization of millimeter-wave emission lines in dense interstellar clouds. , 267:126–136.

Wardle, J. F. C. and Kronberg, P. P. (1974). The linear polarization of quasi-stellar radio sources at 3.71 and 11.1 centimeters. , 194:249–255.

Watson, W. D. (2009). Magnetic Fields and the Polarization of Astrophysical Maser Radiation: A Review. In *Revista Mexicana de Astronomia y Astrofisica Conference Series*, volume 36 of *Revista Mexicana de Astronomia y Astrofisica Conference Series*, pages 113–120.

Whitelock, P. and Feast, M. (2000). Hipparcos parallaxes for Mira-like long-period variables. , 319:759–770.

Wiesemeyer, H., Thum, C., Baudry, A., and Herpin, F. (2009). Precessing planetary magnetospheres in SiO stars?. First detection of quasi-periodic polarization fluctuations in R Leonis and V Camelopardalis. , 498:801–810.

Willson, L. A. and Bowen, G. H. (1986). *Stellar Pulsation, Atmospheric Structure, and Mass Loss*, volume 254, page 385.

Wittkowski, M., Chiavassa, A., Freytag, B., Scholz, M., Höfner, S., Karovicova, I., and Whitelock, P. A. (2016). Near-infrared spectro-interferometry of Mira variables and comparisons to 1D dynamic model atmospheres and 3D convection simulations. , 587:A12.

Wong, W.-H. and An, T. (2018). SMA molecular line survey towards the massive star-forming region G10.6-0.4 in W31 complex. *Research in Astronomy and Astrophysics*, 18(11):134.

Wood, D. O. S. and Churchwell, E. (1989). The Morphologies and Physical Properties of Ultracompact H II Regions. , 69:831.

Xu, S., Zhang, B., Reid, M. J., Zheng, X., and Wang, G. (2019). Comparison of Gaia DR2 Parallaxes of Stars with VLBI Astrometry. , 875(2):114.

Yang, L. and Lai, S. P. (2010). Probing the magnetic field structure in star-forming regions through molecular line polarization. In *ASRROC 2010 Symposium Proceedings: Probing the magnetic field structure in star-forming regions through molecular line polarization*, volume 8 of *JTAM*.

Yates, J. A., Cohen, R. J., and Hills, R. E. (1995). Submillimetre water masers in circumstellar envelopes. , 273:529–548.

Yoon, D.-H., Cho, S.-H., Yun, Y., Choi, Y. K., Dodson, R., Rioja, M., Kim, J., Imai, H., Kim, D., Yang, H., and Byun, D.-Y. (2018). Astrometrically registered maps of H_2O and SiO masers toward VX Sagittarii. *Nature Communications*, 9:2534.

Zhang, Q., Qiu, K., Girart, J. M., Liu, H. B., Tang, Y.-W., Koch, P. M., Li, Z.-Y., Keto, E., Ho, P. T. P., Rao, R., Lai, S.-P., Ching, T.-C., Frau, P., Chen, H.-H., Li, H.-B., Padovani, M., Bontemps, S., Csengeri, T., and Juárez, C. (2014). Magnetic Fields and Massive Star Formation. , 792(2):116.

Zhang, Y. (2017). Molecular studies of Planetary Nebulae. In Liu, X., Stanghellini, L., and Karakas, A., editors, *Planetary Nebulae: Multi-Wavelength Probes of Stellar and Galactic Evolution*, volume 323 of *IAU Symposium*, pages 141–149.

Ziurys, L. M. (2006). Interstellar Chemistry Special Feature: The chemistry in circumstellar envelopes of evolved stars: Following the origin of the elements to the origin of life. *Proceedings of the National Academy of Science*, 103:12274–12279.

Ziurys, L. M., Tenenbaum, E. D., Pulliam, R. L., Woolf, N. J., and Milam, S. N. (2009). Carbon Chemistry in the Envelope of VY Canis Majoris: Implications for Oxygen-Rich Evolved Stars. , 695(2):1604–1613.

Zwillinger, D. and Kokoska, S. (1999). *CRC standard probability and statistics tables and formulae.*